UNIVERSITY OF GAZİANTEP
GRADUATE SCHOOL OF
NATURAL & APPLIED SCIENCES

DEVELOPING A NEW LINEAR INDUCTION MOTOR DRIVE WITH Z-SOURCE INVERTER USING A DSP

Ph.D. THESIS
IN
ELECTRICAL AND ELECTRONICS ENGINEERING

BY
BERRİN SÜSLÜOĞLU ETOĞLU
MARCH 2011

Developing a New Linear Induction Motor Drive with Z-Source Inverter Using a Dsp

Ph.D. Thesis
in
Electrical and Electronics Engineering
University of Gaziantep

Supervisor:
Assist. Prof. Dr. Vedat Mehmet KARSLI

by
Berrin SÜSLÜOĞLU ETOĞLU
March 2011

Name of the thesis : Developing a new linear induction motor drive with z-source inverter using a DSP
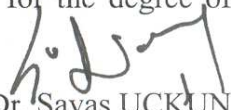
Name of the student: Berrin Süslüoğlu Etoğlu

Exam date : 17.03.2011

Approval of the Graduate School of Natural and Applied Sciences

Prof. Dr. Ramazan KOÇ
Director

I certify that this thesis satisfies all the requirements as a thesis for the degree of Doctor of Philosphy.

Prof. Dr. Savaş UÇKUN
Head of Department

This is to certify that we have read this thesis and that in our opinion it is fully adequate, in scope and quality, as a thesis for the degree of Doctor of Philosphy.

Yrd. Doç. Dr. Vedat Mehmet KARSLI
Supervisor

Examining Committee Members   Signature

1. Prof. Dr. M.Cengiz TAPLAMACIOĞLU...

2. Prof. Dr. Celal KORAŞLI...

3. Prof. Dr. Arif NACAROĞLU...

4. Prof. Dr. Ergun ERÇELEBİ...

5. Yrd. Doç. Dr. Vedat Mehmet KARSLI...

ABSTRACT

**DEVELOPING A NEW LINEAR INDUCTION MOTOR DRIVE
WITH Z-SOURCE INVERTER USING A DSP**

SÜSLÜOĞLU ETOĞLU, Berrin

Ph.D. in Electrical & Electronics Eng.
Supervisor: Assist. Prof. Dr. Vedat Mehmet Karslı

March 2011, 186 pages

The main focus of this thesis is to develop a linear induction motor drive hardware and software control system with Z-source inverter. Within this framework, the study involves the analysis and Matlab/Simulink computer simulation of the mathematical representation of the linear induction motor including end-effect, direct thrust control, and space vector modulation technique for Z-source inverter.

This thesis proposes an improvement in flux estimation algorithm by taking into end effect. Improved accuracy of the estimated flux linkage is shown to obtain a more accurate electromagnetic thrust model using direct thrust controller. To estimate the stator flux and thrust correctly, a discrete form of the low-pass filter including magnitude and phase errors compensation terms is used instead of a pure integrator to prevent the integral instability.

The real-time experiments have been carried out by the use of Texas Instruments TMS320F2812 digital signal processor and "Code Composer Studio" software tools. The recently developed Z-source inverter provides a way of boosting the input voltage, a condition that cannot be obtained in the traditional inverters. It also allows the use of the shoot-through switching state, which eliminates the need for dead-times that are used in the traditional inverters to avoid the risk of damaging the inverter circuit.

The results obtained from the simulations and experiments conducted in this study illustrate that it has been possible to increase the inverter bridge voltage about 90% above the input dc link voltage by controlling its shoot-through period.

Keywords: linear induction motor, end effect, direct thrust control, z-source inverter

ÖZET

EMPEDANS BESLEMELİ İNVERTERİ OLAN YENİ BİR LİNEER ASENKRON MOTOR SÜRÜCÜSÜNÜN DSP KULLANILARAK GELİŞTİRİLMESİ

SÜSLÜOĞLU ETOĞLU, Berrin

Doktora Tezi, Elektrik-Elektronik Mühendisliği
Tez yöneticisi: Yrd. Doç. Dr. Vedat Mehmet. Karslı

Mart 2011, 186 sayfa

Bu tezin hedefi Z-beslemeli evirici ile doğrusal asenkron motorun sürücü sisteminin, donanım ve yazılım kontrol sistemini geliştirmektir. Bu çerçevede, çalışma, uç etkili lineer asenkron motorun matematiksel modelinin, doğrudan itme kuvveti kontrol yönteminin ve Z-beslemeli inverter için uzay vektör modülasyon tekniği de dahil olmak üzere analizlerini ve Matlab / Simulink bilgisayar benzetimlerini içerir.

Bu tezde doğrusal asenkron motorun uç etkisi göz önüne alınarak akı tahmini algoritmasında iyileşme önerilmiştir. Akı tahminindeki iyileşme itme kuvveti tahmininde iyileşmeye de sebep olmuştur. Stator akı tahmininde integral kararsızlığını önlemek için büyüklük ve faz kompanzasyon terimleri eklenmiş alçak geçiren dijital filtre kullanılmıştır.

Gerçek zamanlı deneyler Texas Instruments TMS320F2812 dijital sinyal işlemcisi ve "Code Composer Studio" yazılım araçları kullanılarak yapılmıştır. Yakın tarihte geliştirilen Z-beslemeli evirici ile dc bara geriliminde, geleneksel eviriciler ile elde edilemeyen artış sağlanabilir. Aynı bacaktaki anahtarlama elemanlarının aynı an kapalı olmasına izin veren bu topoloji sayesinde geleneksel eviricilerde evirici devresinin bozulma riskini önlemek için kullanımı zorunlu olan ölü zaman ihtiyacını ortadan kaldırır.

Elde edilen benzetim ve deney sonuçlarında kısa devre süresi kontrol edilerek evirici geriliminde, giriş dc gerilimine oranla yaklaşık %90 artış elde edilmiştir.

Anahtar kelimeler: doğrusal hareketli asenkron motor, doğrudan itme kuvveti kontrolü, uç etkisi, z-beslemeli evirici

ACKNOWLEDGMENTS

CONTENTS

LIST OF FIGURES

LIST OF TABLES

LIST OF SYMBOLS /ABREVIATIONS

d: direct axis

q: quadrature axis

v_s: primary voltage

v_r: secondary voltage

i_{sa}:   stator a phase current

i_{sb}:   stator b phase current

i_{sc}:   stator c phase current

i_{sd}:   d component of stator current

i_{sq}:   q component of stator current

i_{rd}:   d component of rotor current

R_s: primary resistance

R_r: secondary resistance referred to the pimary

L_{ls}:   per phase stator winding leakage inductance

L_{lr}:   per phase rotor winding leakage inductance

L_{ss}:   self inductance of the stator winding

L_{rr}:   self inductance of the rotor winding

L_{sm}:   mutual inductance between stator windings

L_{rm}:   mutual inductance between rotor windings

L_{sr}:   peak value of the stator to rotor mutual inductance

Ψ: flux linkage

J: moment of inertia

D: damping constant

τ: pole pitch

v_r: electrical linear speed

v_s: linear synchronous speed

v_m: mechanical linear speed

F_e: electromagnetic thrust

F_L: external force disturbance

P: number of poles

1/p: integration

$S_k(t)$: the switching functions of each leg of the VSI where k:a, b,c

HB_ψ: hysteresis band width for flux

HB_{Fe}: hysteresis band width for thrust

h_{Fe}: thrust hysteresis comparator output

h_φ: flux hysteresis comparator output

T_{sh}: shoot through time duration

T_s: sampling period interval

M: modulation index

D_{sh}: shoot through duty cycle

B: boost factor

V_{DC}: dc supply voltage

v_i: dc link voltage across the inverter bridge terminals

V_C: capacitor voltage of z-source inverter

R_g: gate resistor

LIM: linear induction motor

RIM: rotary induction motor

DTC: direct torque control (RIM), direct thrust control (LIM)

PWM: pulse width modulation

SVM: space vector modulation

VSI: voltage source inverter

ZSI: impedance source inverter

LPF: low pass filter

IGBT: insulated gate bipolar transistor

DSO: digital storage oscilloscope

DSP: digital signal processing

ADC: analogue-to-digital converter

A/D: analogue to digital

EMI: electromagnetic interference

ESR: equivalent series resistance

CW: clockwise

CCW: counterclockwise

p.u.:   per unit

ISR: interrupt service routine

CHAPTER 1

INTRODUCTION

Linear induction motors (LIMs) are recently used in many industrial applications, including transportation, conveyor systems, material handling, sliding door closers, etc., with satisfactory performance. The most obvious advantage of linear motors is that they have no gears, and require no mechanical rotary-to-linear converters. The other advantages of LIM are reduction of mechanical losses, silence, high starting thrust force, and easy maintenance, repairing, and replacement [1].

A linear induction motor is a kind of special electrical machine that converts electrical energy directly into the mechanical energy of linear motion. The construction of a LIM is similar to a rotary induction motor (RIM) with cut open and rolled flat; with RIMs stator viewed as the primary and its rotor as the secondary for LIM. Therefore, LIM keeps on having both non-linear, time varying, coupled model of RIM. As distinct from RIM, LIM has an open magnetic circuit. When the primary of a LIM moves, the eddy currents are formed on the surface of its secondary to resist a sudden increasing and disappearing fluxes. This non-uniform flux distribution further complicates the modeling, speed control and parameter determination of LIM. To resolve the end effect problem, speed dependent scaling factors are introduced to the magnetizing branch in the d-axis equivalent circuit of RIM [2]. Moreover, a thrust correction coefficient may also be introduced to calculate the actual thrust [3, 4].

The driving principles of the LIM are similar to the traditional RIM, but its control characteristics are more complicated than RIM due to end effect and the difficulty in parameter determination. Field-oriented control (FOC) of LIM in [5-7] achieved decoupled torque and flux dynamics leading to independent control of the torque and flux as for a separately excited DC motor. However, FOC requires magnetizing

inductance and secondary resistance and inductance. Although the parameters of the simplified equivalent circuit model of a LIM can be measured by no-load and locked secondary tests, due to limited length of the motor, the realization of the no-load test is impossible. Hence, the conventional method for calculating the equivalent circuit parameters of LIM is limited. In order to measure these parameters, application of the finite element method has been proposed in [8, 9]. Another proposed method is removal of the secondary of LIM [10]. The first one requires complex calculations and the second one has mechanical hardness furthermore it is not practical also. Moreover, even if the steady-state equivalent circuit parameters are found with one of these methods, the estimation of the secondary side resistance and inductance parameters are more difficult since they may change as time varies due to the change of operating conditions, such as speed of mover and temperature.

In the last ten years, the applications of intelligent methods to the LIM control system take attention. Neural network, fuzzy and genetic algorithm based control algorithms have been employed for this purpose [11-14].

Compared with FOC and intelligent methods, direct thrust control (DTC) for LIMs has been less researched. DTC was applied to LIM by [4, 40- 41] as the Direct Thrust and Flux Control. In contrast to field-oriented control, DTC requires the accurate knowledge of the stator resistance, the stator flux and thrust estimations. For the reasons mentioned above, while selecting the controller method, only the primary voltage, current, winding resistance and speed dependent method, direct thrust control is preferred. DTC uses motor electric torque and stator flux linkage directly as control variables, whether traditional field oriented current vector control uses currents as control variables to indirectly influence on the electric torque of the machine. The main advantage of this method is small torque response time [35]. Furthermore, coordinate transformation from rotating reference frame is not used which will decrease the complexity of the control scheme and save the operation of the DSP. However, it suffers from initial value and dc offset problems in the flux linkage integration. The flux estimation techniques can be classified mainly in three groups: model reference adaptive (MRAS) based [15] and observer-based [16] and back- electromotive force EMF based [17-19] estimators.

2

The first category is based on model reference adaptive (MRAS) techniques, which uses a speed independent model as the reference model and a speed dependent model. The error from the two models is forced to zero by an adjusting mechanism, which gives the estimated speed. The second estimation technique is based on the linearized state-space model. The states of the drive, including the rotor speed are estimated by comparing variables in the model and from experimental data.

The first two techniques are computationally intensive and difficult for the implementation in a low cost fixed-point DSP's. In this thesis, the emf based flux estimator is used. Due to the problems of pure integrator, the stator flux is estimated by using low-pass filter (LPF) approach. The stator flux compensation method in [18] is also adopted for gain and phase errors of LPF. In the thesis, flux estimator of LIM is improved by considering the end effect in its flux linkage equations and discussed in chapter 4.

Another problem normally associated with DTC drive is the high thrust ripple. Ideally, small torque hysteresis band will produce small torque ripple. However, for DSP-based implementation, if the hysteresis band is too small, the possibility for the torque to touch the upper band is increased. High switching frequency can be selected to prevent incorrect voltage vector selection hence torque ripple reduces. There are numerous techniques proposed to reduce the torque ripple such as, Space Vector Modulation (SVM) [20], fuzzy logic control [21], [22] and by using multilevel inverter [23]. Most of these operations are complicated than usual. In such situations, the overall performance and the efficiency of the fixed point DSP-based motor driver system may be deteriorated. For this reason, in thesis, in contrary to classical DTC, the duration for the application of the voltage vector is determined according to the conditions of the flux and thrust errors to reduce thrust ripples.

The voltage-source (v-source) inverter based adjustable speed drive system has certain limitations and problems. Obtainable output voltage is limited quite below the input line voltage. To avoid short circuiting of damaging dead time is allowing which provides a delay time between gating signals but it causes waveform distortion. The Z-source inverter (ZSI) is an alternative topology that can boost the dc link voltage using passive components. It uses a Z-shaped LC impedance network for coupling the inverter circuit to the power source, which provides a way of boosting the input

voltage. This is the condition that cannot be obtained in the traditional inverters. It also eliminates the need for dead-times that are used in the traditional inverters to avoid the risk of damaging the inverter circuit. z-source inverter based LIM drive was not dealt with before in the literature. This thesis presents the z- source inverter based LIM drive system.

1.1 Scope of the Thesis

This work aims the analysis, the design and the implementation of a LIM drive system with Z-source inverter based topology using ezDSPTMS320F2812. At first, the dynamic modelling of LIM with/without end effect is developed and simulated with MATLAB/SIMULINK. Next, DTC of LIM is mathematically investigated, modelled and simulated by using MATLAB/SIMULINK SimPowerSystem Toolbox. Then, a new flux estimator for DTC is proposed in considering the end effect phenomenon of LIM. DTC using the proposed estimator is then simulated to show its effectiveness.

The steady state mathematical analysis of z-source inverter is derived. The Matlab/Simulink model of a modified space vector modulation technique for z-source inverter is developed and the related Matlab/Simulink simulation is carried out. The z-source inverter based LIM drive system has several advantages that are desirable for many drive systems; producing any desired output ac voltage even greater than the line voltage and the increased reliability of the inverter due to needless of dead times.

A prototype hardware LIM drive system including the both power circuit and isolation circuits is designed and constructed to test the control algorithms. The experimental realization for the investigated algorithms is developed on ezDSPTMS320F2812 using C coding.

Finally, the experimental results for the developed system are presented. With the developed z-source inverter based on V/Hz control, the AC voltage applied to LIM is no longer limited and is boosted 90% which is beyond the limit achieved by conventional v-source inverter.

The contributions of this thesis may be summarized as follow:

- Flux estimator of LIM is improved by considering the end effect in its flux linkage equations. It is verified by using MATLAB/SIMULINK SimPowerSystem toolbox.
- An experimental set-up is developed to study LIM drive system
- The realization of z-source inverter based speed drive system is developed to boost up the supply voltage

1.2 Overview of the Chapters

A brief review of the contents of this thesis is given as follows:

Chapter 2: Dynamic model of a linear induction motor is given. Also, MATLAB/SIMULINK modeling of LIM is presented.

Chapter 3: This chapter explains the direct thrust control generalities. Furthermore MATLAB/SIMULINK modeling for direct thrust control of LIM is given. The performance of direct thrust controlled LIM drive with different hysteresis band amplitudes for thrust and stator flux is simulated with MATLAB/SIMULINK and the obtained simulation results are shown.

Chapter 4: Dynamic model of a linear induction motor including the end effect is introduced. The performed simulations concerning the end effect problems are given. Direct thrust control of LIM is improved by considering the end effect in its flux and thrust estimator parts and the related simulation results are presented.

Chapter 5: It mentions about the problems that may be encountered in implementation of DTC. These are pure integration problems due to the presence of noise and dc offsets, stator resistance variations, dead time effects, current limiting and thrust ripples.

Chapter 6: Z-source inverter operation stages, mathematical analysis and dimensioning of passive elements are mentioned. It also presents the modulation model for z-source inverter. Matlab/Simulink dynamic modeling is also performed and a control structure in closed loop is proposed for LIM and the related simulation results are given.

Chapter 7: The developed experiment set-up is described by giving detailed information of each hardware components.

Chapter 8: The brief explanations of the developed software programs are given.

Chapter 9: The experimental results and the problems encountered are given**.**

Chapter 10: The results and contribution of this study for linear induction motor drive system are summarized. Furthermore, the recommendations for future research are presented.

CHAPTER 2

LIM BASICS

The history of linear induction motor (LIM) goes back to the 19th century. The idea of linear induction motor was patented by Charles Wheatstone in 1845. In 1905, a new project is described for traction purposes. In 1945 Westinghouse Company of America built a aircraft launcher, called as "Electropult", by constructing a flat, single-sided LIM with a moving primary [24]. After 1950, there have been rapid advances in linear induction motor technology.

There are few researchers in literature, whose names link to LIM study. E.R.Laithwaite is the first one. He analyzed linear induction motors according to their configurations and associated applications and published them in his 1966 book. Yamamura and Poloujadoff studied the theoretical aspects of LIM in detail, especially the influence of end effects. Both works are primarily concerned with theoretical analysis of single and double-sided linear induction motors. Nasar and Boldea also did extensive research on especially single-sided LIMs. The most recent book on LIMs, by Gieras, covers all aspects of LIM subject, including constructional features, applications, electromagnetic effects, controller and design.

Nowadays, the linear induction motor has been widely used in a variety of applications especially in transportation, but also in conveyor systems, actuators, material handling, pumping of liquid metal, sliding door closers, curtain pullers, robot base movers, office automation, drop towers, elevators, etc. [1,24]

Linear induction motors can have various configurations according to its air-gap geometry which may be flat or cylindrical. They can be also single-sided or double-sided with either the primary or the secondary being the mover. This thesis concerns about the control of a single-sided LIM having a short moving primary and flat air-gap.

The operation principle of a single-sided LIM is the same as that of a rotary induction motor. It is basically obtained by opening the rotating squirrel cage induction motor and laying it flat as shown in Figure 2.1. In LIMs, as in rotary induction motors, the armature constitutes the primary and the field the secondary. The primary usually contains a three phase winding in the uniform slots of the laminated core. The primary windings are distributed such that, when excited by a three phase supply, they generate a travelling linear magnetic field.
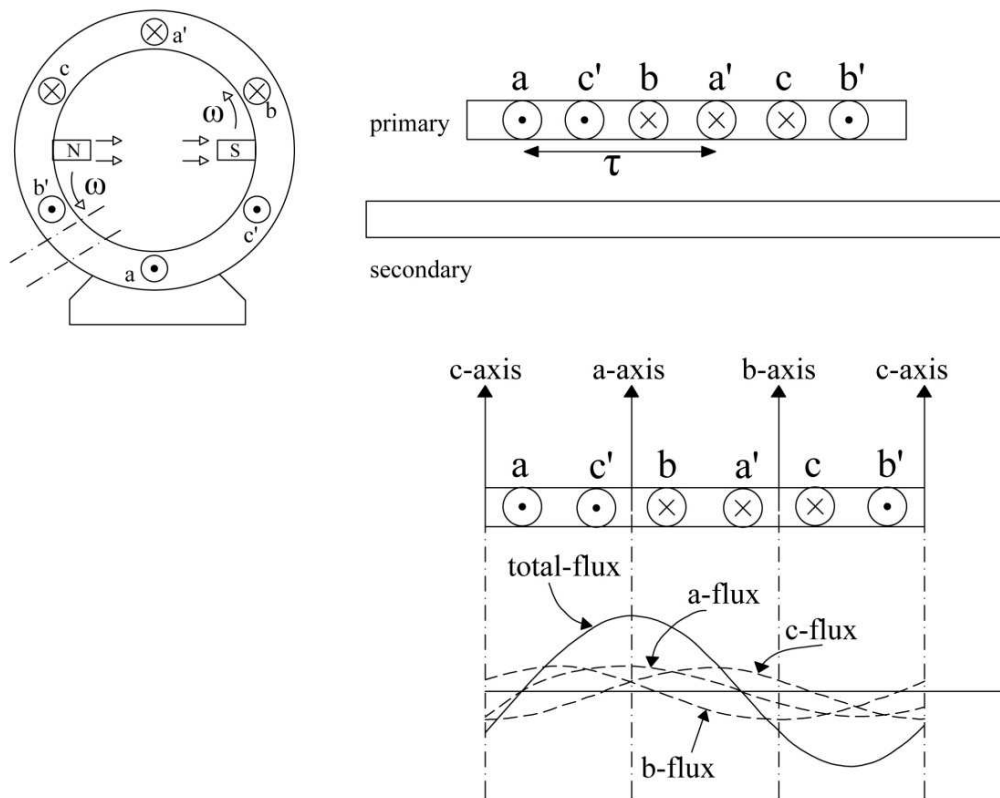
Figure 2.1. The linear induction motor configuration and its flux distribution

The secondary of the LIM, or rotor, which is an aluminum sheet or copper, with or without a solid back iron plate completes the magnetic circuit and creates the magnetic flux linkage across the air gap. This in turn induces a voltage on the conductive part, which generates an eddy current in the conducting outer layer of the secondary. The interaction between the eddy current and the changing electromagnetic field generates electromagnetic thrust on the plate.

LIMs operate at a constant velocity from zero to full load, and the speed is frequency driven. The cheapest model is a moving short primary and stationary long secondary because of the expensive copper windings in the primary and cheap secondary.

Apparently the LIM operates as its rotary counterpart does, with thrust instead of torque and linear speed instead of angular speed, based on the principle of travelling field in the airgap.

However, in reality there is an important difference between linear and rotary IMs. It is the open magnetic circuit of LIMs at the ends. Especially for short primaries (with 2, 4 poles), this result in the non-uniform magnetic flux distribution. There are also current asymmetries between phases due to the fact that one phase has a position closer to the middle [24, 26].

The differences of LIM come out the following main advantages and disadvantages [27]:

Advantages:
   •Direct electromagnetic thrust propulsion with no mechanical transmission,
   •Ruggedness; very low maintenance costs,
   •Separate cooling of primary and secondary if required,
   •All advanced drive technologies for rotary IMs may be applied without notable changes to LIMs.

Disadvantages:
   •Due to large airgap, the power factor and efficiency tend to be lower than with rotary IMs. However, the efficiency should be compared with the combined efficiency of rotary motor including its mechanical transmission counterpart.
   •Efficiency and power factor are further reduced by end effects. Fortunately, these effects are notable only in high speed low pole count LIMs. Therefore, they may be limited to some extent.

2.1 Basic Principle of Operation of Three-Phase Linear Induction Motor

The operation principle of a three phase induction motor is based upon Faraday's Law and the Lorentz force on a conductor [28]. Faraday's law of electromagnetic induction states that if the flux linking a loop varies as a function of time, a voltage is

induced between its terminals. The value of the induced voltage is proportional to the rate of change of flux. Lorentz force on a conductor states that when a current-carrying conductor is placed in a magnetic field, it is subjected to an electromagnetic force. When three-phase voltage is applied to the primary copper windings, a magnetic field is created. If a secondary conductive plate is placed near this primary magnetic field, a traveling magnetic flux is produced which constitutes an electromagnetic thrust. The traveling magnetic field and developed thrust are shown in Figure 2.2
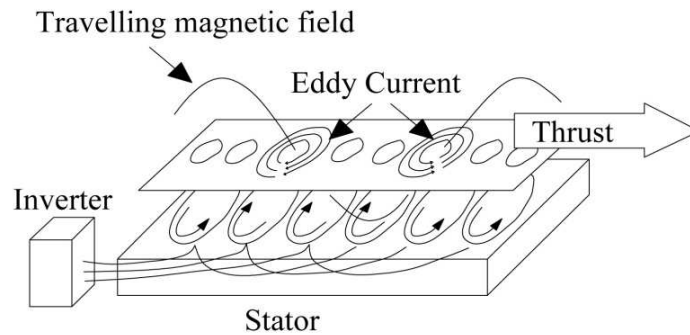
Figure 2.2. Traveling magnetic field and thrust created when primary is energized

The traveling wave of flux travels continuously from one end of the stator to the other. The flux moves from left to right and cuts off at the edges of the stator, but it builds up again at the left. The traveling flux travels at a synchronous speed given by equation (2.1).

$$v_s = \frac{2\tau}{T} = 2\tau f = 2\tau \frac{\omega_s}{2\pi} = \frac{\tau}{\pi}\omega_s \qquad\qquad (2.1)$$

where v_s is the linear synchronous speed (m/s), τ is the width of one pole pitch (m), and f is the frequency (Hz).

It is important to note that the linear speed is a function of the frequency and the pole pitch and not the number of poles as in a rotary induction motor. Therefore it is possible for a 4-pole LIM to have the same synchronous linear speed as that of a 6-pole, provided that they have the same pole pitch.

2.2 Mathematical Modeling of Linear Induction Motor

The derivation of the mathematical modelling of LIM is necessary for developing LIM drive system. Model equations are derived on an analogy between RIMs and LIMs.

According to the Kirchoff's Laws, the voltage equations of the magnetically coupled stator and rotor circuit of RIM can be written as in (2.2) and (2.3) [29, 30] with reference to Figure 2.3.
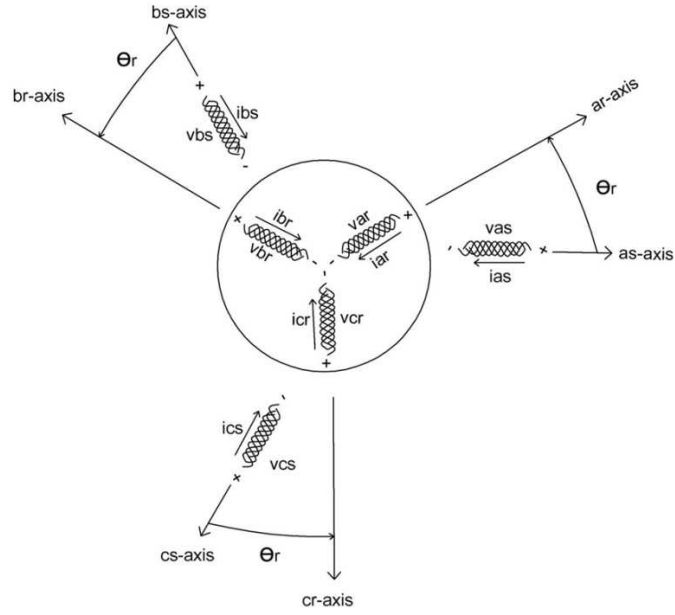
Figure 2.3. Axes of three-phase induction motor

Stator Voltage Equations:

$$v_{as} = i_{as}R_s + \frac{d}{dt}\psi_{as}$$

$$v_{bs} = i_{bs}R_s + \frac{d}{dt}\psi_{bs}$$

$$v_{cs} = i_{cs}R_s + \frac{d}{dt}\psi_{cs} \tag{2.2}$$

Rotor Voltage Equations:

$$v_{ar} = i_{ar}R_r + \frac{d}{dt}\psi_{ar}$$

$$v_{br} = i_{br}R_r + \frac{d}{dt}\psi_{br}$$

$$v_{cr} = i_{cr}R_r + \frac{d}{dt}\psi_{cr} \tag{2.3}$$

In matrix notation, the flux linkages of the stator and rotor windings, in terms of the winding inductances and currents, may be written compactly as in (2.4).

$$\begin{bmatrix} \psi_s^{abc} \\ \psi_s^{abc} \end{bmatrix} = \begin{bmatrix} L_{ss}^{abc} & L_{sr}^{abc} \\ L_{rs}^{abc} & L_{rr}^{abc} \end{bmatrix} \begin{bmatrix} i_s^{abc} \\ i_r^{abc} \end{bmatrix} \tag{2.4}$$

where $\psi_s^{abc} = \left(\psi_{as}, \psi_{bs}, \psi_{cs} \right)^T, \psi_r^{abc} = \left(\psi_{ar}, \psi_{br}, \psi_{cr} \right)^T$

$$i_s^{abc} = \left(i_{as}, i_{bs}, i_{cs} \right)^T, \qquad i_r^{abc} = \left(i_{ar}, i_{br}, i_{cr} \right)^T$$

where the superscript T denotes the transpose of the array.

The sub-matrices of the stator-to-rotor and rotor-to-rotor winding inductances are shown in (2.5).

$$L_{ss}^{abc} = \begin{bmatrix} L_{ls} + L_{ss} & L_{sm} & L_{sm} \\ L_{sm} & L_{ls} + L_{ss} & L_{sm} \\ L_{sm} & L_{sm} & L_{ls} + L_{ss} \end{bmatrix}$$

$$L_{rr}^{abc} = \begin{bmatrix} L_{lr} + L_{rr} & L_{rm} & L_{rm} \\ L_{rm} & L_{lr} + L_{rr} & L_{rm} \\ L_{rm} & L_{rm} & L_{lr} + L_{rr} \end{bmatrix} \tag{2.5}$$

where L_{ls} is the per phase stator winding leakage inductance, L_{lr} is the per phase rotor winding leakage inductance, L_{ss} is the self inductance of the stator winding, L_{rr} is the self inductance of the rotor winding, L_{sm} is the mutual inductance between stator windings, L_{rm} is the mutual inductance between rotor windings, and L_{sr} is the peak value of the stator to rotor mutual inductance

However, the mathematical model based on equations (2.2) through (2.5) is very complex. This motor model in abc axis is described by six first-order differential equations. These differential equations are coupled to one another through the mutual inductance between the windings. In particular, the primary-to-secondary mutual inductances are dependent on the mover position so they vary with time.

Using the d-q axis coordinate transformation proposed by R.H.Park which is given in Appendix A, the analysis of LIM modeling becomes more convenient [31]. The basic idea is the translation of the three-phase system variables onto the orthogonal two-axis d-q frame by using simple matrix calculations [29, 30]. This transformation can facilitate the computation of the transient solution of the above linear induction motor model by transforming the differential equations with time-varying inductances to differential equations with constant inductances.

The two commonly used reference frames in the analysis of induction machine are the stationary and synchronously rotating frames [30]. For transient studies of adjustable speed drives, it is usually more convenient to simulate an induction machine and its converter on a stationary reference frame [29]. Moreover, calculations with stationary reference frame are less complex due to zero frame speed since some terms cancelled. In the stationary rotating reference, the dq variables of the machine are in the same frame as those normally used for the supply system. Furthermore, the stationary reference model is more suitable for DTC method. Considering the mentioned advantages, the stationary reference frame modelling of LIM is preferred in this study. The developed LIM motor model in stationary frame is shown in Figure 2.4.

While the mathematical model of a LIM is created using the aid of electrical and mechanical equations, the following assumptions are made:

- only the fundamental harmonic of MMF exists
- there are no end effects
- the airgap is uniform
- magnetizing circuit is unsaturated
- the primary windings are symmetrical
- LIM is connected to an infinite bus.
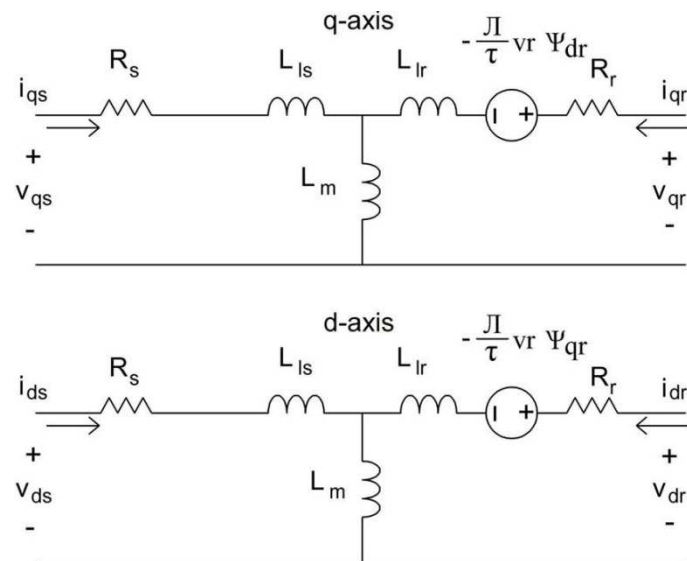
Figure 2.4. Equivalent circuit of a linear induction motor in the stationary frame

The corresponding model equations are given by (2.6) through (2.9).

Electric formula**:**

Primary side d-q voltage equations:

$$v^s{}_{ds} = R_s i^s{}_{ds} + \frac{d}{dt}\psi^s{}_{ds}$$

$$v^s{}_{qs} = R_s i^s{}_{qs} + \frac{d}{dt}\psi^s{}_{qs} \tag{2.6}$$

Secondary side d-q voltage equations:

$$v^s{}_{dr} = R_r i^s{}_{dr} + \frac{\pi}{\tau} v_r \psi^s{}_{qr} + \frac{d}{dt}\psi^s{}_{dr}$$

$$v^s{}_{qr} = R_r i^s{}_{qr} - \frac{\pi}{\tau} v_r \psi^s{}_{dr} + \frac{d}{dt}\psi^s{}_{qr} \tag{2.7}$$

where the subscript s corresponds to stator, r corresponds to rotor, d corresponds to direct axis, q corresponds to quadrature axis, ψ corresponds to flux.

Thrust formula**:**

$$F_e = \frac{3}{2}\frac{\pi}{\tau}\frac{P}{2}\left(\psi^s{}_{ds}i^s{}_{qs} - \psi^s{}_{qs}i^s{}_{ds}\right) \tag{2.8}$$

where P is the number of poles.

Mechanical formula:

$$F_e - F_L = J\frac{d}{dt}v_m + Bv_m \tag{2.9}$$

where F_e is the electromagnetic thrust, F_L is external force disturbance, J is the mechanical inertia, B is the natural damping and v_m is the mechanical speed.

2.3 Matlab/Simulink Modelling of LIM

Matlab/Simulink model of LIM is developed by using (2.6)-(2.9) and SimPowerSystem Toolbox. While modeling these equations, the derivative is not used. Since some signals may have discontinuities and that would result in spikes when differentiated. Instead the integral form is preferred. The simulation model is formed by choosing flux-linkage as a state variable rather than currents. Since the easy way of successfully solving this system is to use the flux-linkage as the tool. What remains is to find the currents from the flux-linkages. By this way, the dynamics of LIM can be expressed as a combination of fourth order electrical

differential equations and a first order mechanical differential equation. The final equations used in implemented model are shown in (2.10).

$$\psi^s{}_{ds} = \frac{1}{p}\left(v^s{}_{ds} - R_s i^s{}_{ds}\right)$$

$$\psi^s{}_{qs} = \frac{1}{p}\left(v^s{}_{qs} - R_s i^s{}_{qs}\right)$$

$$\psi^s{}_{dr} = \frac{1}{p}\left(v^s{}_{dr} - R_r i^s{}_{dr} - \frac{\pi}{\tau} v_r \psi^s{}_{qr}\right)$$

$$\psi^s{}_{qr} = \frac{1}{p}\left(v^s{}_{qr} - R_r i^s{}_{qr} + \frac{\pi}{\tau} v_r \psi^s{}_{dr}\right)$$

$$v_r = \frac{1}{p}\left(\frac{P}{2J}\left(F_e - F_L\right)\right) \tag{2.10}$$

where 1/p stands for integral operation.

The simulation model used to evaluate LIM model consists of a three phase LIM block and a three phase voltage source. The masked Simulink model is given in Figure 2.5. In the developed model, the inputs through LIM are three-phase voltage and the load torque. On the other hand, the outputs are three-phase currents, the electromagnetic thrust and the mover speed. The secondary is short circuited in the model. The open model used for simulation of the LIM is shown in Figure 2.6. In this model, three-phase voltages applied to the input are converted into d-q stationary reference frame voltages. Once d-q phase voltages obtained, using the equations associated flux and current are calculated and then applied to electromechanical and mechanical torque equations to obtain torque-speed responses.

2.4 Summary

The operation principle of a single-sided LIM including its advantages/disadvantages is briefly explained. Since LIM operates as its rotary counterpart does, with thrust instead of torque and linear speed instead of angular speed, based on the principle of travelling field in the airgap, LIM mathematical model equations are derived on an analogy between RIMs and LIMs. The ideal motor model is described by six first-order differential equations, one for each winding. However, these differential equations are coupled to one another through the mutual inductance between the windings and the coupling terms are time varied. The orthogonal two axis dq transformation makes easier the modelling of the motor by transforming the

differential equations with time-varying inductances to differential equations with constant inductances.

Dynamic model of LIM in stationary reference frame is preferred due to its less complexity and convenience for DTC. The open form of the developed MATLAB/SIMULINK modeling of LIM is also presented.
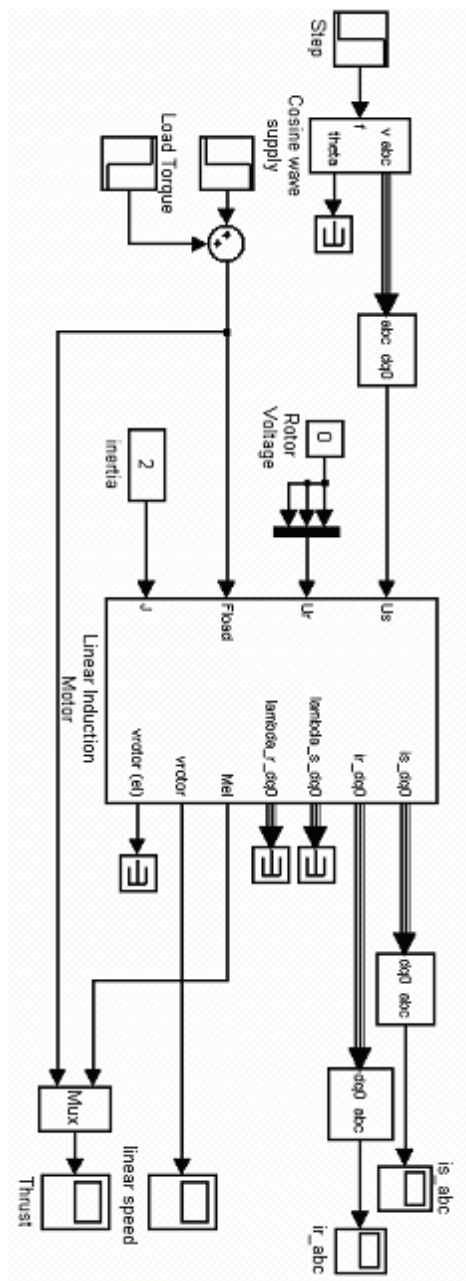
Figure 2.5. LIM masked model in Simulink
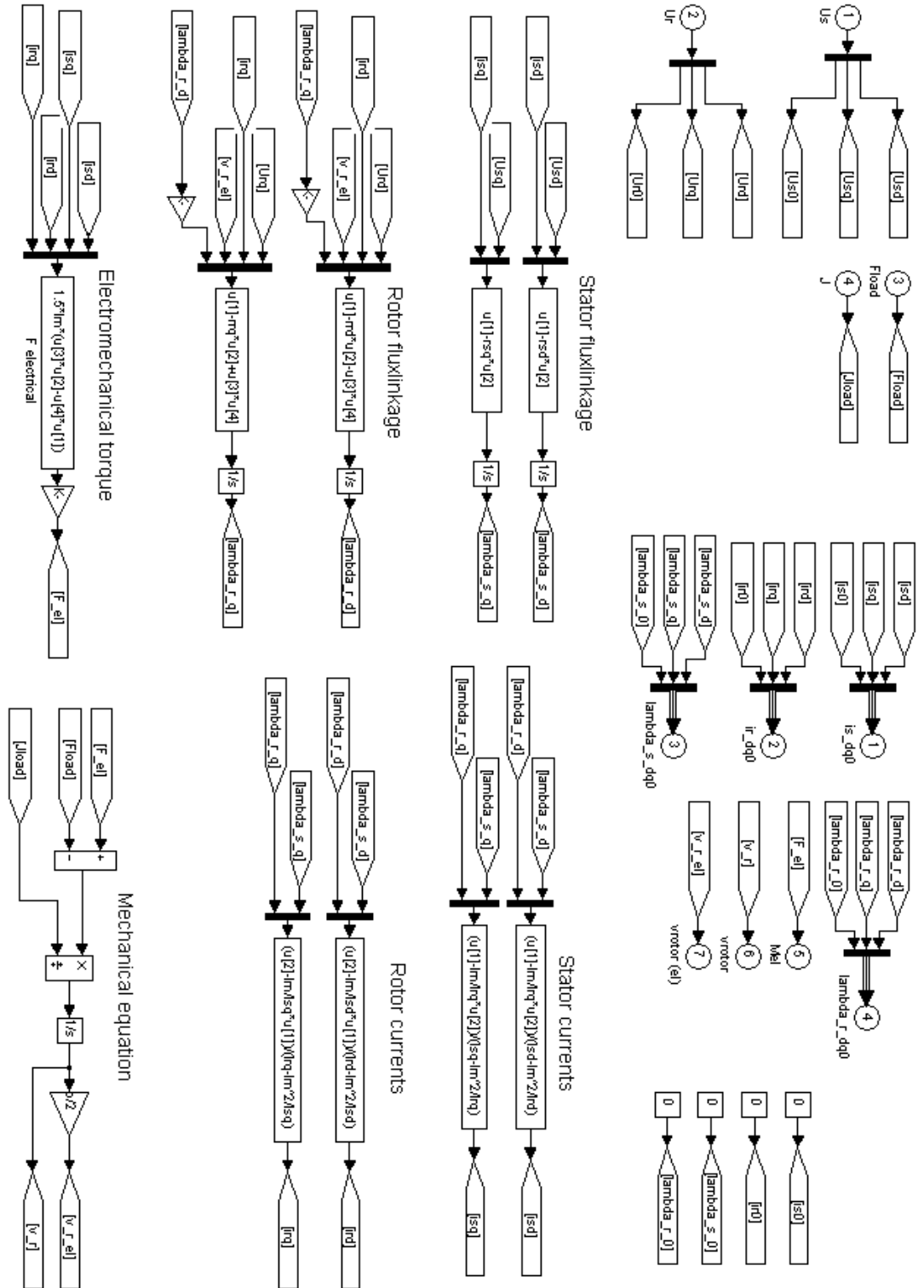
Figure 2.6. LIM model implementation in Matlab/Simulink

CHAPTER 3

DIRECT TORQUE CONTROL PRINCIPLES

In the 1980s, an advanced control technique direct torque control (DTC) was introduced by Takahashi [32] and Depenbrock [33] for voltage-fed PWM inverter drives as an alternative to field-oriented control [34]. DTC technology was first used commercially by ABB in 1995, and rapidly became the favorite control method for AC drives, especially for demanding or critical applications [35]. Compared to the field oriented control, DTC method has the following features [34].

- There no current control loop, the current is controlled indirectly.
- Coordinate transformation is not required.
- It is not sensible to machine parameter variation except the stator resistance.
- Response time for torque is small.

The driving principles of the linear induction motor (LIM) are similar to the traditional rotary induction motor (RIM) but its control characteristics are more complicated than the RIM [36]. High performance control of LIM by vector control mostly carried out in secondary flux oriented scheme has been presented in many works [37- 40]. However, field oriented control (FOC) is complicated and requires machine parameters. Compared with RIM, DTC for LIMs have been less researched. DTC was applied to LIM by [8, 40- 41] as the Direct Thrust and Flux Control. In contrast to field-oriented control, DTC requires the accurate knowledge of the stator resistance, the stator flux and thrust estimations. The control algorithm of DTC makes it practical to implement on a microcontroller embedded in the drive.

The chapter is organized as follows. At first, the basic principles of voltage space vectors for 3-phase voltage source inverter (VSI) are given. Next, the principles of the direct thrust control are introduced. Then, a step by step Matlab/Simulink modeling of the direct thrust controlled LIM drive is shown. Finally, simulation results and some conclusions are presented.

3.1 Mathematical Model of VSI Using Space Vector Approach

Representing three phase quantities as space vectors is particularly useful for power electronic applications [30, 44]. Essentially this methods defines a three phase system with a single unity vector $u = 1 + a + a^2$, where a=exp(2π/3).
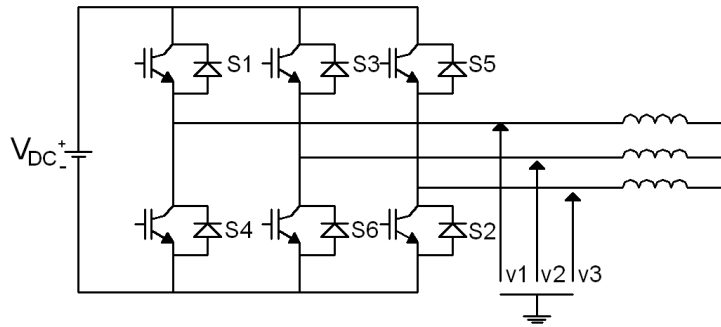
Figure 3.1. Three phase voltage source inverter

In Figure 3.1, the voltage vector representing the triplet v1,v2, v3, can be drawn by summing three vectors (length proportional to amplitude) directed as three 120° shifted axes (a, b, c) as shown in Figure 3.2.
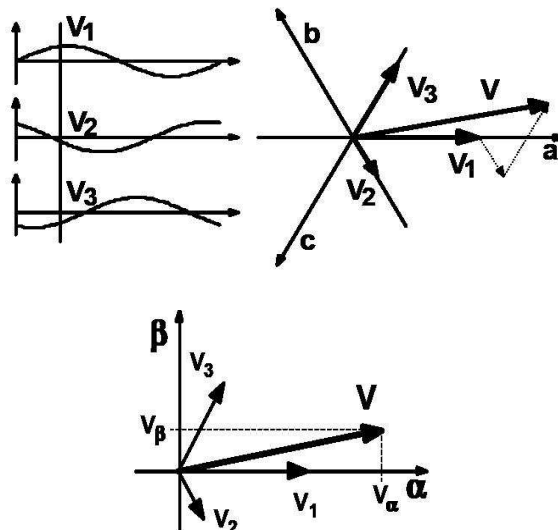
Figure 3.2. Vector representation of inverter output voltages

19

By using the space vector transformation defined in Appendix A, the three-phase axes are defined by the unity vectors 1, a, a^2, where a=exp($2\pi/3$)

$$\vec{V} = \frac{2}{3}\left(V_1 + aV_2 + a^2 V_3\right)$$ (3.1)

The voltage source inverter topology given by Figure 3.1 imposes some constraints:

- Switches 1 and 4 (leg 1), 3 and 6 (leg 2) or 5 and 2 (leg 3) should not be simultaneously on at the same time since the dc cannot be shorted.

- The output of the inverter must not be opened due to its inductive load. Therefore at least one switch in each leg must be closed at any moment.

By the above constraints, there exist eight valid switch combinations for the inverter. These states are shown in Figure 3.3.

Six out of these eight topologies called non-zero (active) switching states produce a nonzero output voltage. The remaining two topologies known as zero switching states produce zero output voltage hence zero ac line current.

Assuming the switching states for the VSI, (3.1) can be given by (3.2).

$$\vec{V}_s(t) = \frac{2}{3}V_{dc}\left(S_a + aS_b + a^2 S_c\right)$$ (3.2)

where $S_a(t)$, $S_b(t)$ and $S_c(t)$ are the switching functions of each leg of the VSI, such that, when upper switch is on $S_{a,b,c}$ is 1; when lower switch is on $S_{a,b,c}$ is 0.

Conceptually, a set of three phase waveforms can be represented by a single rotating vector with angular speed ω as given by (3.3).

$$\vec{V}_k = \sqrt{\frac{2}{3}}V_{DC} \cdot e^{j\frac{(k-1)\pi}{3}} \quad \text{with (k=1,...,6)}, \qquad V_7 = V_8 = 0$$ (3.3)
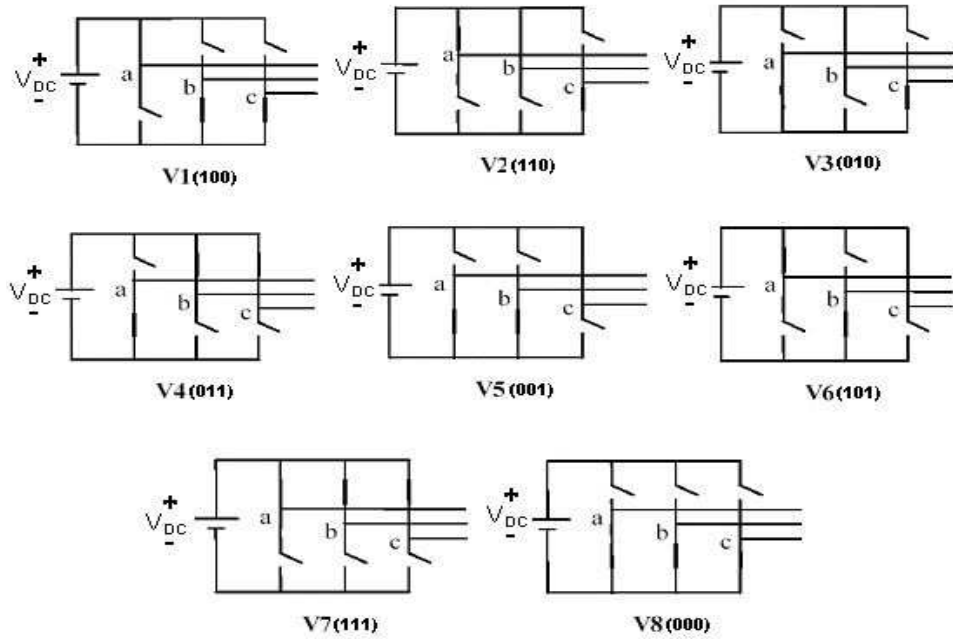
Figure 3.3. Possible states of three phase three wire inverter

Table 3.1. Possible switching vectors of three phase, three wire inverter

k	SA	SB	SC	V_a	V_b	V_c	V_α	V_β
1	1	0	0	$2/3$	$-1/3$	$-1/3$	$\sqrt{2/3}$	0
2	1	1	0	$1/3$	$1/3$	$-2/3$	$\sqrt{1/6}$	$\sqrt{1/2}$
3	0	1	0	$-1/3$	$2/3$	$-1/3$	$-\sqrt{1/6}$	$\sqrt{1/2}$
4	0	1	1	$-2/3$	$1/3$	$1/3$	$-\sqrt{2/3}$	0
5	0	0	1	$-1/3$	$-1/3$	$2/3$	$-\sqrt{1/6}$	$-\sqrt{1/2}$
6	1	0	1	$1/3$	$-2/3$	$1/3$	$\sqrt{1/6}$	$-\sqrt{1/2}$
7	1	1	1	0	0	0	0	$\sqrt{1/2}$
8	0	0	0	0	0	0	0	0

Positions of the six non-zero voltage vectors (V_1-V_6) is presented in Figure 3.4. The tips of these vectors form a regular hexagon shown by dotted line. It is defined that the area enclosed by two adjacent vectors, within the hexagon, as a sector. Thus there are six sectors numbered as 1-6. Each vector lies in the center of a sector of 60° with named as S1 to S6 according to the voltage vector it contains.

21
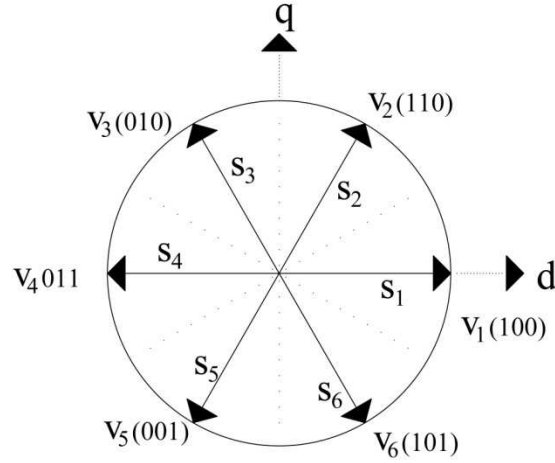
Figure 3.4. Output voltage space vector of the three phase three wire inverter in d-q coordinates

Considering the last two states in Table 3.1, it can be seen that the output line voltages generated by this topology are given by $V_a=V_b=V_c=0$. These are represented as vectors which have zero magnitude and hence are referred to as zero-switching state vectors or zero voltage vectors. They assume the position at origin in the α-β, plane.

3.2 Principles of Direct Torque Control

The basic idea of the DTC method is coming from Faraday's induction law in the calculation of the motor flux linkage vector. The induction law gives a connection between the voltage vectors and the flux linkage vector by using (3.4)[30].

$$\psi_s = \int (v_s - i_s R_s) dt \tag{3.4}$$

This equation is also known as "the voltage model" of the motor. Assuming the voltage drop on the stator resistance small, (3.4) can be rewritten as in (3.5).

$$\Delta \overline{\psi}_s = v_s \Delta t \tag{3.5}$$

From equation (3.5) and Figure 3.4, it can be seen that the inverter voltage directly force the stator flux to trace the required stator flux locus by choosing the appropriate inverter switching state.

The idea of the torque control in DTC is based on the fact that the rotor and air gap flux linkages have quite long time constants. In an analogy for RIM, the electromagnetic thrust in three-phase LIM is derived as in (3.6).

$$F_e = \frac{3}{2} \frac{\pi}{\tau} \frac{P}{2} \frac{L_m}{L_s L_r - L_m^2} |\overline{\psi}_s| |\overline{\psi}_r| \sin(\rho_s - \rho_r)$$

(3.6)

where the subscript s corresponds to stator, r corresponds to rotor.

According to (3.6), at any time, the thrust is proportional to the magnitude of the stator and the rotor fluxes and the sine of angle between them. The rotor flux is low-pass filtered form of the stator flux with a rotor time constant. Therefore, a quick change in stator flux is traced very slowly by the rotor flux due to its large time constant [30, 42, 43]. The rotor flux can be assumed constant as long as the switching time is very smaller then the rotor time constant. By using this assumption; if the stator flux magnitude is kept constant, then the electromagnetic thrust can be controlled by changing the angle between stator and the rotor fluxes. The angular speed of the stator flux can be changed by choosing the suitable inverter states. This is the tangential component of the applied voltage vector that determines the angular speed of the stator flux.

A general approach for selecting the right voltage vector is determined by using Figure 3.5. According to this figure, the stator flux vector lying on the sector k can be increased by selecting v_k, v_{k+1}, v_{k-1}; whereas it can be decreased by the v_{k+2}, v_{k+3}, v_{k-2}. The zero vectors short the machine terminals and keeps the flux unchanged neglecting the voltage drop on the stator resistance. Thus, by selecting step by step the appropriate stator voltage vector, it is then possible to change the stator flux in the required way as shown in Figure 3.6 [30].

In reference to Figure 3.5, if the stator flux vector lies in the k-th sector, then the electromagnetic thrust can be increased by selecting v_{k+1}, v_{k+2}; whereas it can be decreased by the v_{k-1}, v_{k-2}. The states of v_k and v_{k+3} are not considered because of their effects can change depending on the stator flux position at the same sector [44].
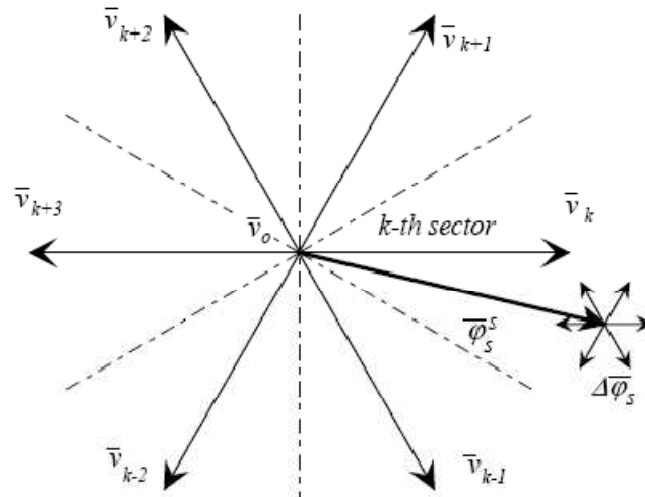
Figure 3.5. Stator flux vector with different possible switching vectors
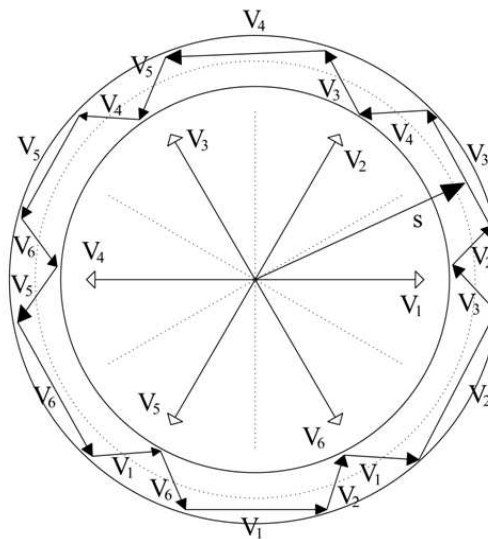
Figure 3.6. Stator flux-linkage vector trajectory by applying the proper voltage vector

A stator flux vector trajectory given in Figure 3.7 shows the stator and air gap flux vectors rotating in counter clockwise direction at an angular frequency of ω. The dotted lines denote the hysteresis band for the stator flux vector magnitude. Although it couldn't be shown in the figure, the torque has also its own hysteresis limit. The selection of the voltage vector is made to restrict the flux and torque error within their respective flux and torque hysteresis bands to obtain the fastest response and highest efficiency at every instant [30]. When the upper or lower hysteresis limit for thrust and flux is reached, a new voltage vector is applied. Assumed that flux vector

lies in sector one and it is integrated with V_3 until the lower limit is reached or the torque reaches its upper limit. If these cases happen simultaneously, they are kept inside the hysteresis band by using the voltage vectors V_6.
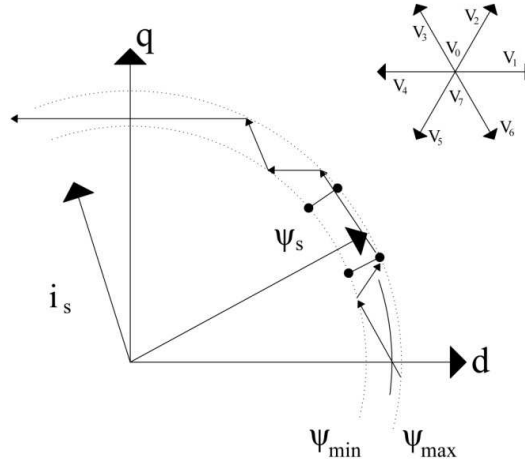
Figure 3.7. A stator flux trajectory with selected voltage vectors in DTC

All the switching possibilities for the above mentioned selection procedures can be tabulated in the switching table given in Table 3.2. At every modulation instant, it selects the most suitable voltage vector to meet the flux and torque control requirements relative to the stator flux linkage orientation. In the optimal switching table, there is no unnecessary switching take place.

Table 3.2. Switching table for DTC

Sector		1	2	3	4	5	6
Flux	Thrust						
$h_\varphi = 1$	$h_{Fe} = 1$	V2	V3	V4	V5	V6	V1
	$h_{Fe} = 0$	V7	V 0	V7	V0	V7	V0
	$h_{Fe} = -1$	V6	V 1	V2	V3	V4	V5
$h_\varphi = -1$	$h_{Fe} = 1$	V3	V4	V5	V6	V1	V2
	$h_{Fe} = 0$	V0	V7	V0	V7	V0	V7
	$h_{Fe} = -1$	V5	V6	V1	V2	V3	V4

According to Table 3.2 and Figure 3.8, the required hysteresis comparator for thrust is a three-valued and for the flux is a two-valued. The thrust hysteresis comparator output h_{Fe} can take (-1, 0, 1), flux hysteresis comparator output h_{φ} can take (0, 1) as given in Figure 3.8. The meaning of each output is given according to the following cases:
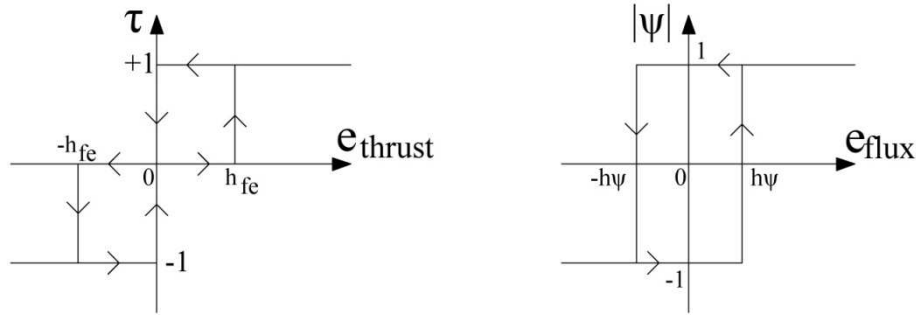
Figure 3.8. Hysteresis comparators for thrust and stator flux respectively

$h_{Fe} = -1$: the actual value of the torque is higher than the reference and out of the defined hysteresis limit; the torque must be reduced;

$h_{Fe} = 1$: the actual value of the torque is below the reference and out of the hysteresis limit; the torque must be increased;

$h_{Fe} = 0$: the actual value is inside the hysteresis limit.

$h_{\psi} = -1$: the actual value of the flux linkage is above the reference and out of the hysteresis limit; the flux must be reduced;

$h_{\psi} = 1$: the actual value of the flux linkage is lower than the reference and out of the defined hysteresis limit; the flux must be increased.

3.3 Modelling of DTC for LIM

A simulation for conventional direct thrust control of LIM drive is carried out using Matlab/Simulink simulation package. The developed direct thrust control scheme is shown in Figure 3.9. The drive model is implemented by five main blocks: LIM model, inverter model, thrust and stator flux estimator, speed controller part to obtain thrust reference value and finally hysteresis controllers to obtain necessary switching state. The following subsections briefly explain the details of each block.

26
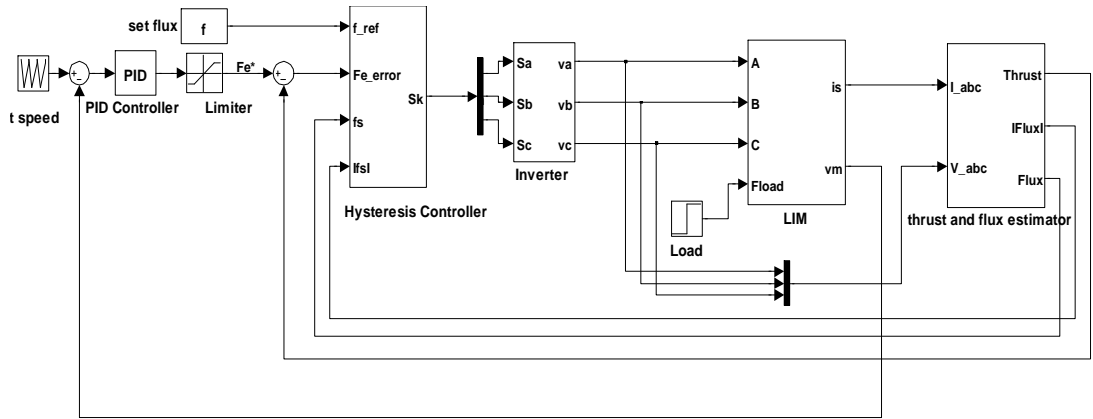
Figure 3.9. Matlab/Simulink model of a DTC LIM drive

LIM Block:

LIM is a voltage controlled system. The Matlab/Simulink modelling of the LIM was given in Figure 2.5.

Inverter Block:

The inverter applies three-phase voltage signals to LIM determined according to the switching states. The developed Simulink model for the inverter is shown in Figure 3.10. For modelling the three-phase, three-wire inverter (3.7) is used.

$$v_a = V_{DC} \frac{(2S_a - S_b - S_c)}{3}$$ (3.7.a)

$$v_b = V_{DC} \frac{(2S_b - S_a - S_c)}{3}$$ (3.7.b)

$$v_c = V_{DC} \frac{(2S_c - S_a - S_b)}{3}$$ (3.7.c)

where V_{DC} is dc link voltage.
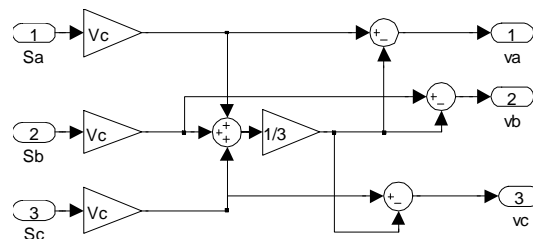
Figure 3.10. Matlab/Simulink model for inverter

Stator Flux and Thrust Estimator Block:

LIM mathematical model in stationary reference frame is used to estimate the stator flux and the electrical thrust. From the VSI state and having the value of dc link voltage, the voltage in each phase can be deduced. Once the voltages and currents are obtained, they are transformed in d and q components by means of Park transformation. In reference to equation (3.4), having the stator resistance value, the stator flux components are expressed by (3.8.a) and (3.8.b).

$$\overline{\psi}_{sd} = \int\left(\overline{v}_{sd} - R_s \, \overline{i}_{sd} \right) dt \qquad\qquad (3.8.a)$$

$$\overline{\psi}_{sq} = \int\left(\overline{v}_{sq} - R_s \, \overline{i}_{sq} \right) dt \qquad\qquad (3.8.b)$$

The stator flux linkage magnitude is given by (3.9).

$$\left|\overline{\psi}_s\right| = \sqrt{\psi^2_{sd} + \psi^2_{sq}} \qquad\qquad (3.9)$$

Finally, the thrust estimation is obtained by using equation (3.10).

$$F_e = \frac{3}{2}\frac{\pi}{\tau}\frac{P}{2}(\overline{\psi}_{sd}\overline{i}_{sq} - \overline{\psi}_{sq}\overline{i}_{sd}) \qquad\qquad (3.10)$$

where d corresponds to direct axis, q corresponds to quadrature axis.

The overall Simulink model for stator flux and thrust estimator is shown in Figure 3.11.
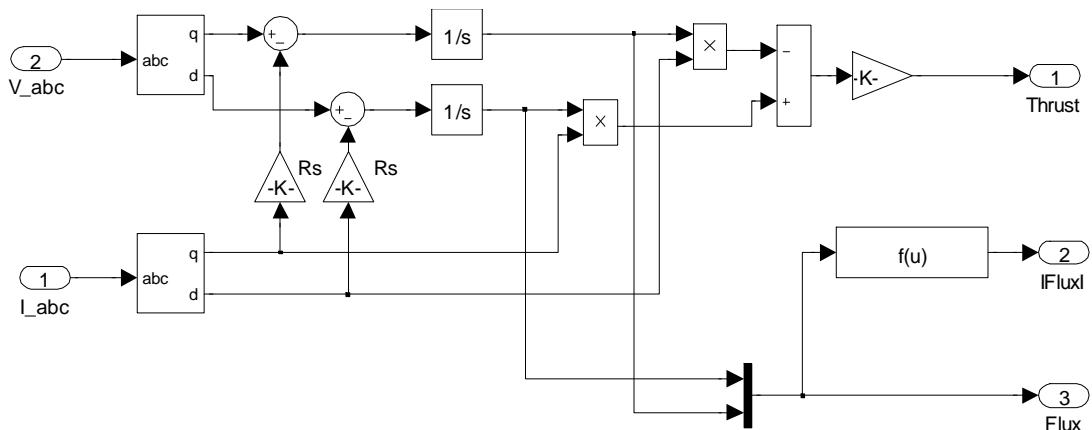
Figure 3.11. Matlab/Simulink model for stator flux and thrust estimator

Speed Controller Part:

The speed control loop uses a proportional-integral (PI) controller to produce thrust reference for the controller. Output of PI controller has been limited.

Controller Block:

The block diagram of the hysteresis controller is shown in Figure 3.12. There are two loops corresponding to the magnitudes of the stator flux and thrust. The reference values for the flux and thrust are compared with their actual values, and the resulting error values are fed into two and three-level hysteresis blocks respectively.
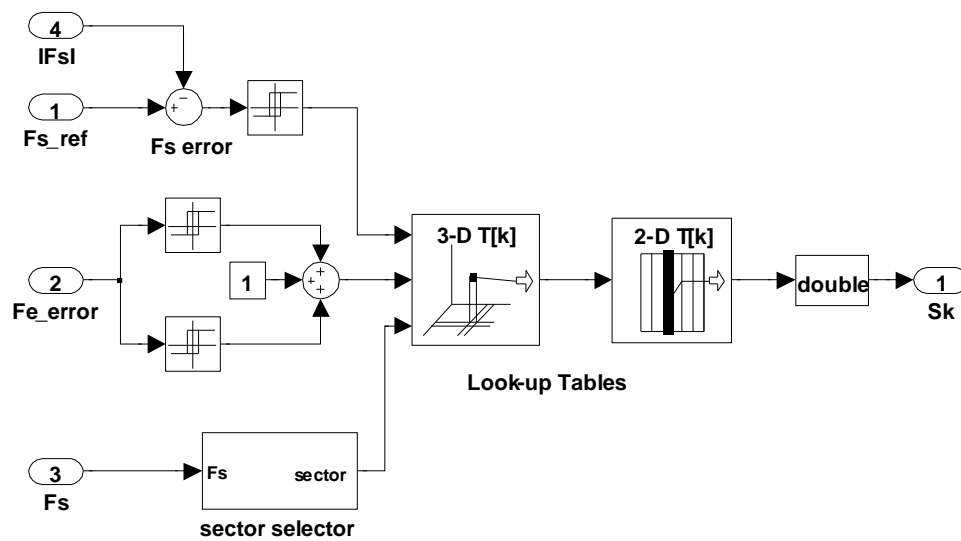
Figure 3.12. Hysteresis controller and switching vector selector block

Sector selector block calculates the position of the stator flux vector corresponding to the six regions of voltage vectors.

The outputs of two hysteresis blocks, the position of the stator flux are used as inputs of the three-dimensional look-up table. Switching table is embedded in three-dimensional look-up table. The number of the appropriate voltage vector is the input through the two-dimensional look-up table, while switching vector is its output.

3.4 Simulation Results

All simulations are done in Matlab/Simulink using SimPowerSystem Toolbox. Linear induction motor parameters used to test the DTC strategy for LIM are given in Table 3.3.

Table 3.3. LIM parameters

Number of poles	2
Primary resistance-Rs	2.82 Ω
Secondary resistance-Rr	48.84 Ω
Primary inductance-Ls	0.0452 H
Secondary inductance-Lr	0.0301 H
Magnetizing inductance-Lm	0.0262 H
Pole pitch-τ	0.06 m
Moving mass	0.5 kg

Simulations are carried on for three cases by selecting the different hysteresis bands for stator flux and thrust as shown in Table 3.4.

Table 3.4. Simulated hysteresis band width for flux and thrust

	Case I	**Case II**	**Case III**
HB_ψ	%0.03	%0.003	%0.003
HB_{Fe}	%0.001	%0.001	%0.05

In all case, a step change of thrust command is applied at 0.1 second from zero to 60 N.m. At the same time, the triangular wave speed reference with amplitude of 5.85 m/s and the stator flux reference with amplitude of 0.96 Wb are applied to the LIM drive. Closed loop performance of the direct thrust control method for three cases are compared in terms of thrust response, speed and stator flux reference tracking, flux trajectories, stator currents and phase-a stator voltage that are given in Figure 3.13, Figure 3.14, Figure 3.15, Figure 3.16, Figure 3.17 and Figure 3.18 in respectively.
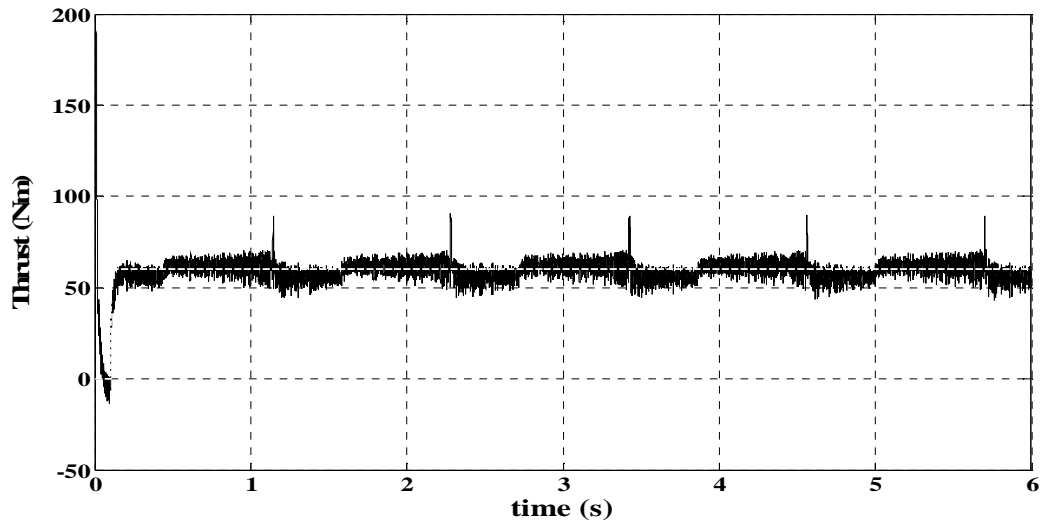
Figure 3.13.a. Thrust response of the DTC in LIM for case I
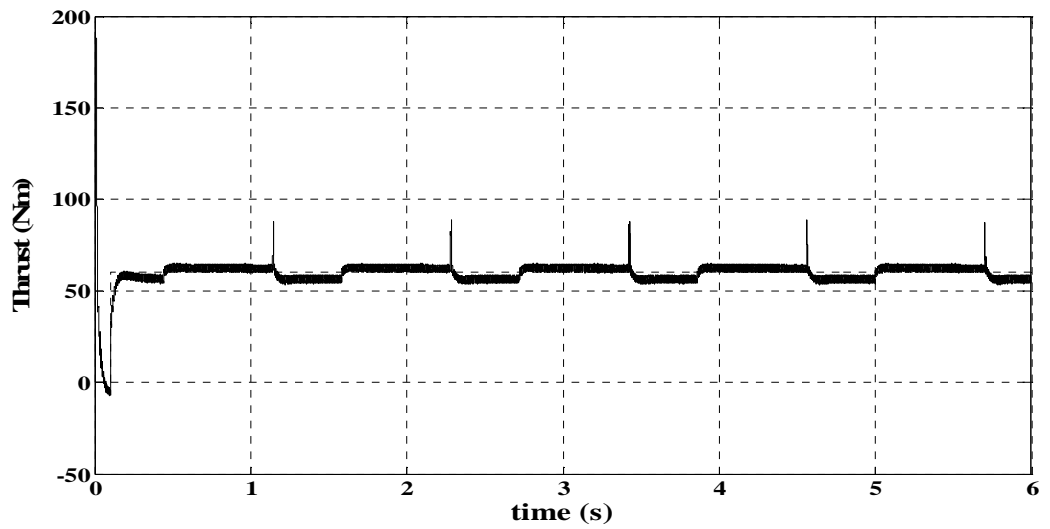
Figure 3.13.b. Thrust response of the DTC in LIM for case II
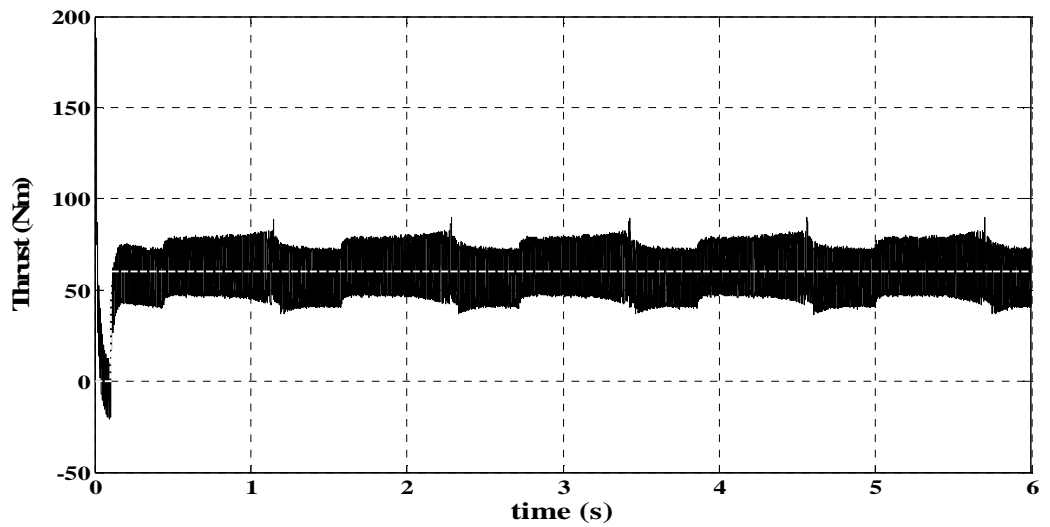
Figure 3.13.c. Thrust response of the DTC in LIM for case III

31
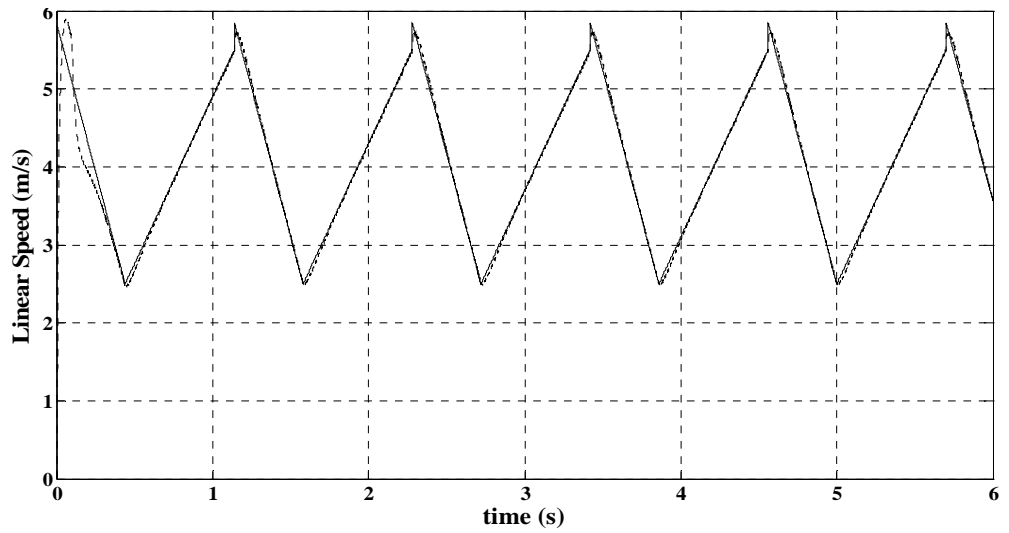
Figure 3.14.a. Speed reference tracking of the DTC in LIM for case I
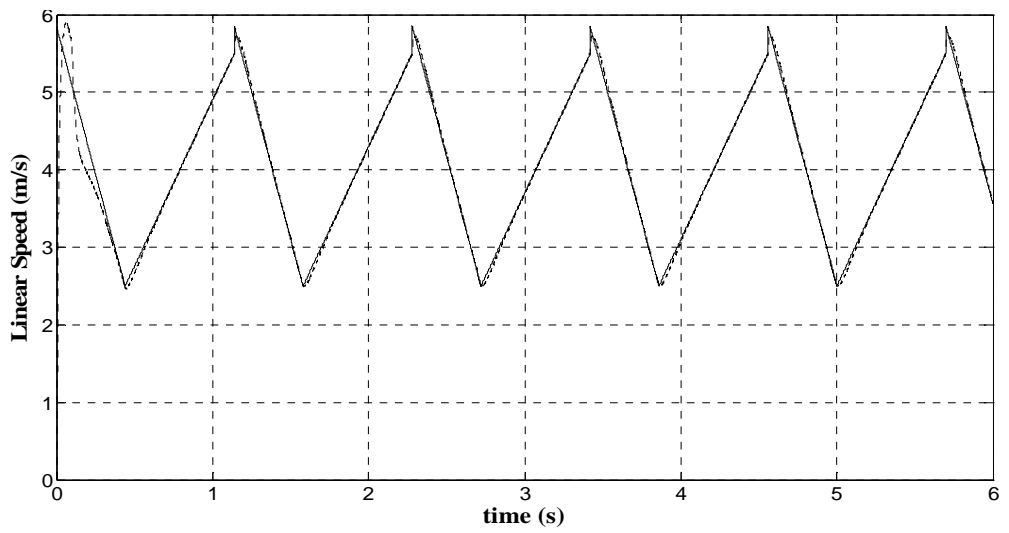
Figure 3.14.b. Speed reference tracking of the DTC in LIM for case II
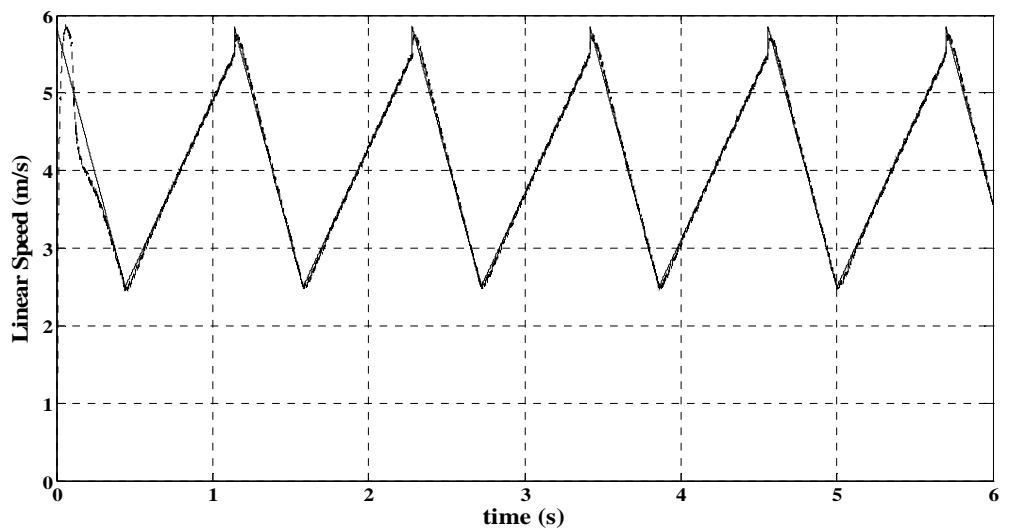
Figure 3.14.c. Speed reference tracking of the DTC in LIM for case III

32
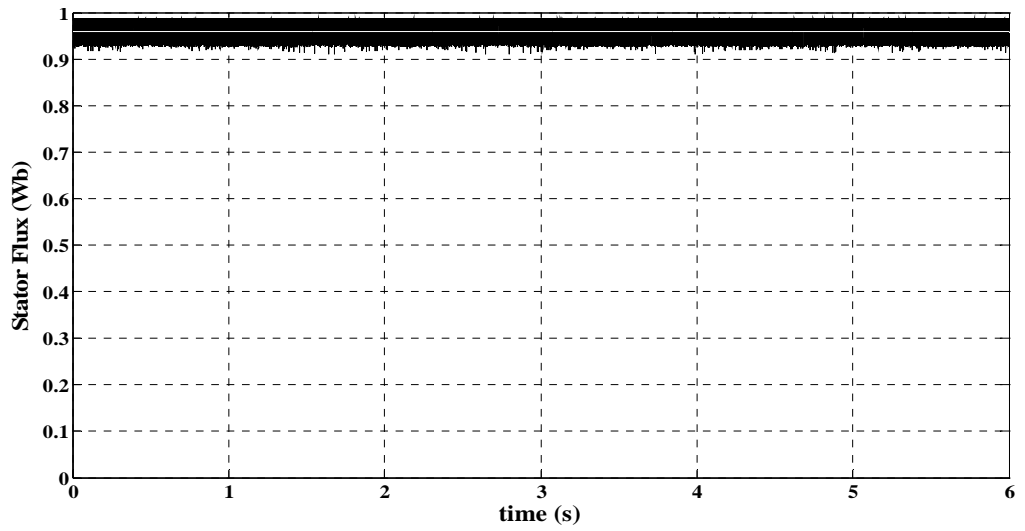
Figure 3.15.a. Stator flux reference tracking of the DTC in LIM for case I
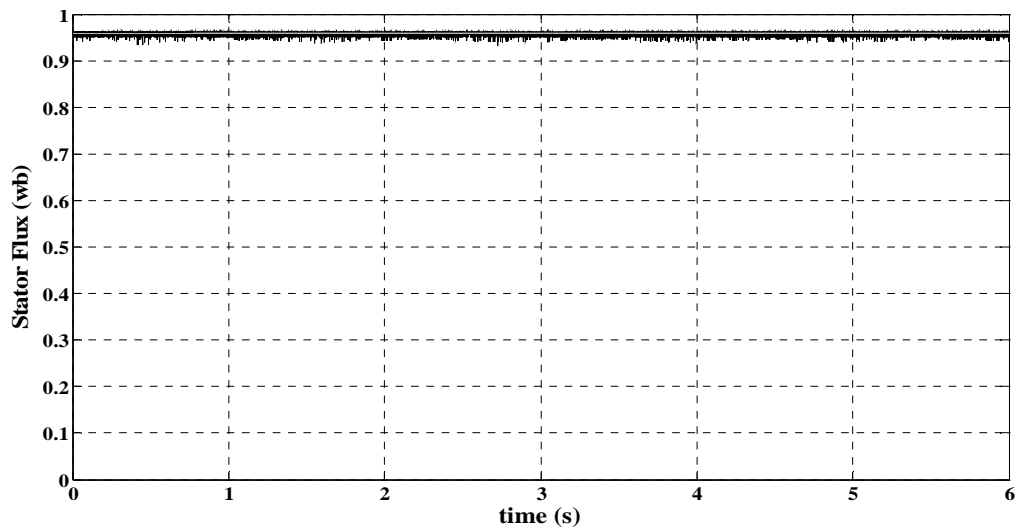
Figure 3.15.b. Stator flux reference tracking of the DTC in LIM for case II
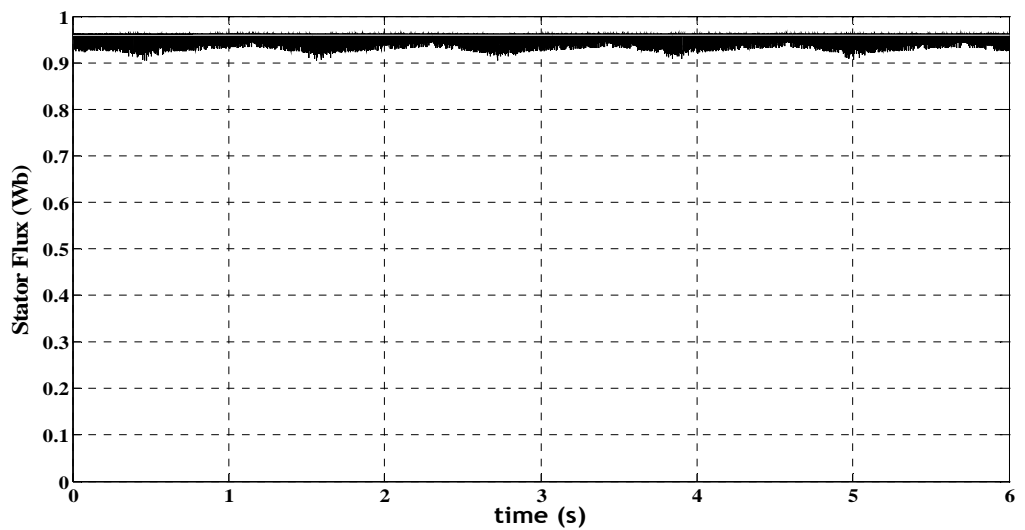
Figure 3.15.c. Stator flux reference tracking of the DTC in LIM for case III

33
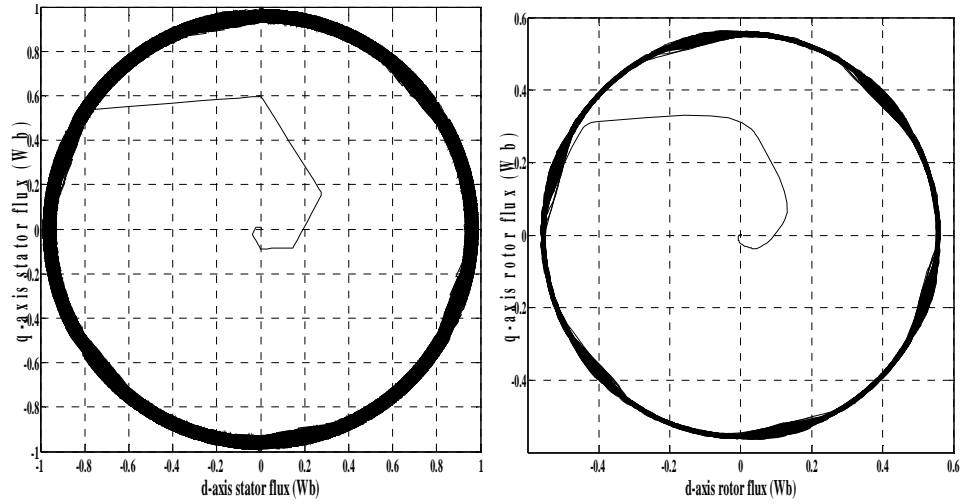
Figure 3.16.a. Stator flux and rotor flux trajectories of the DTC in LIM for case I
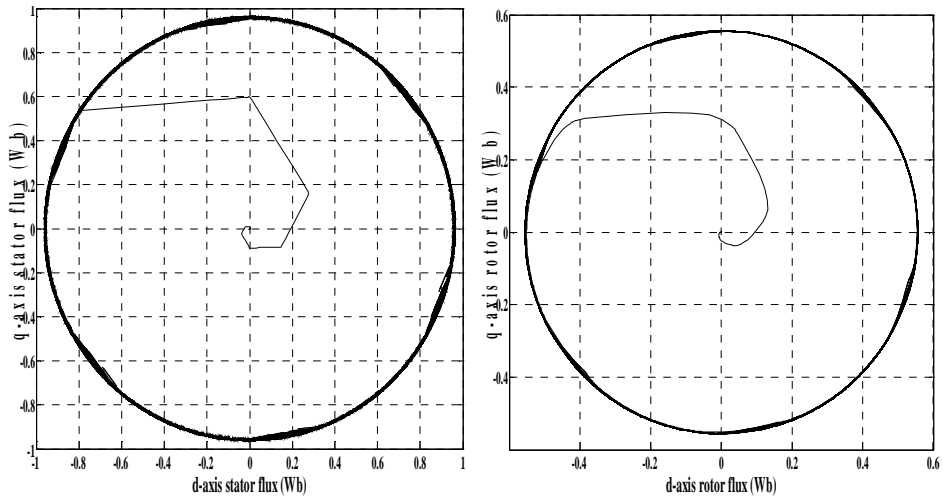
Figure 3.16.b. Stator flux and rotor flux trajectories of the DTC in LIM for case II
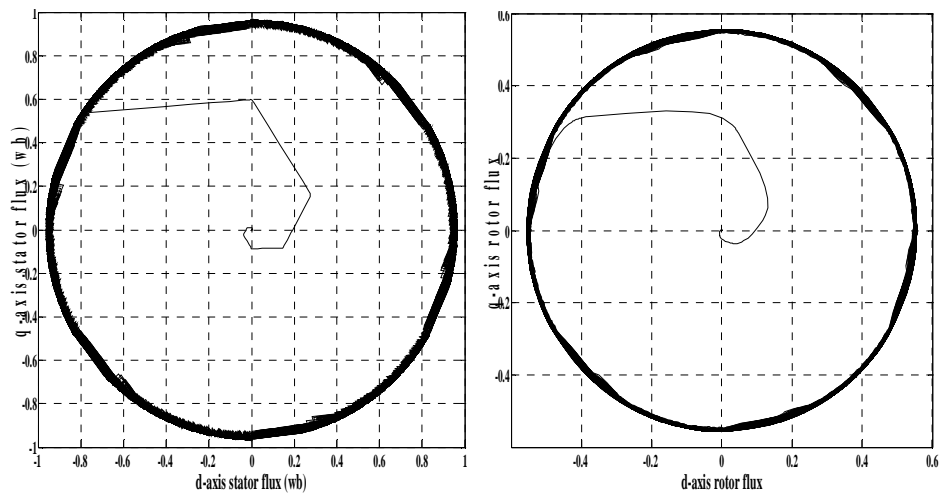
Figure 3.16.c. Stator flux and rotor flux trajectories of the DTC in LIM for case III
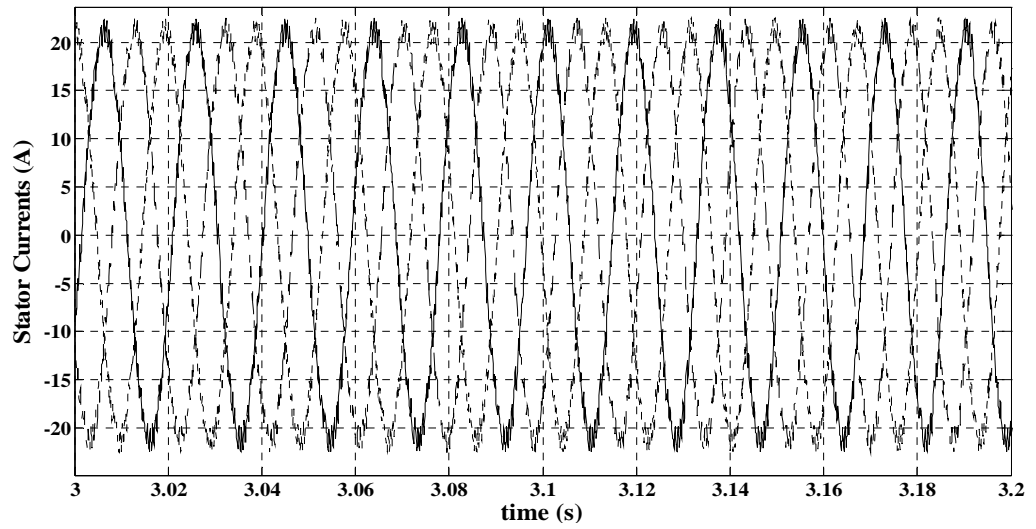
Figure 3.17.a. Three-phase stator currents of the DTC in LIM for case I
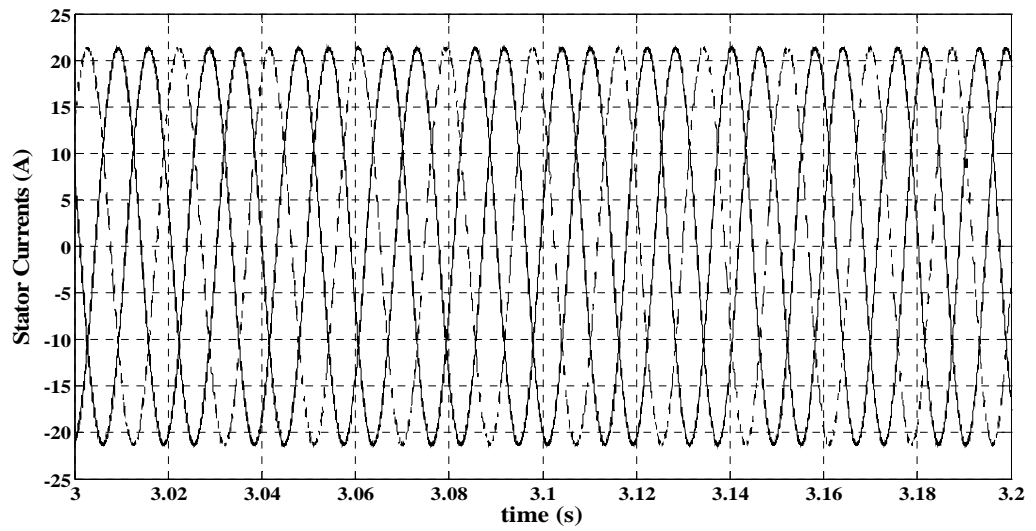
Figure 3.17.b. Three-phase stator currents of the DTC in LIM for case II
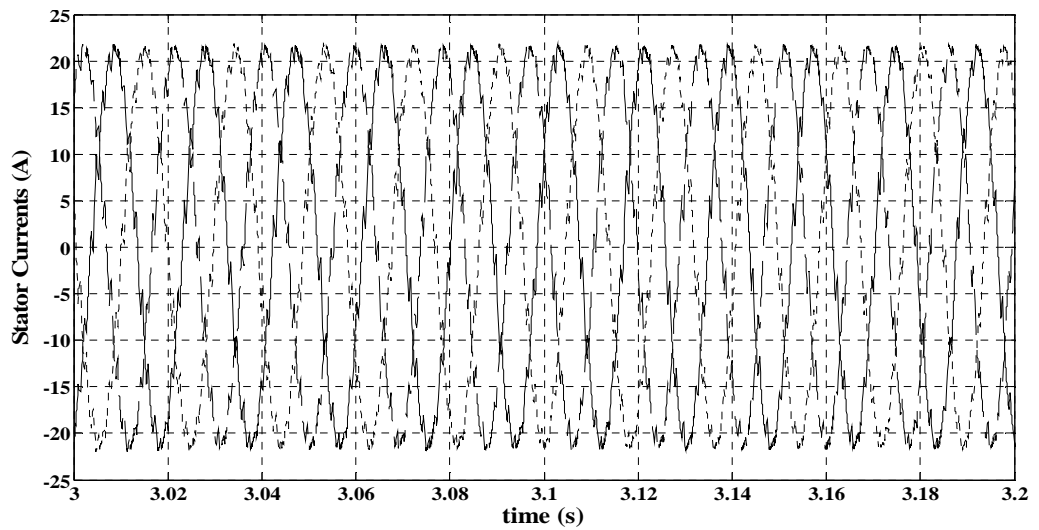
Figure 3.17.c. Three-phase stator currents of the DTC in LIM for case III
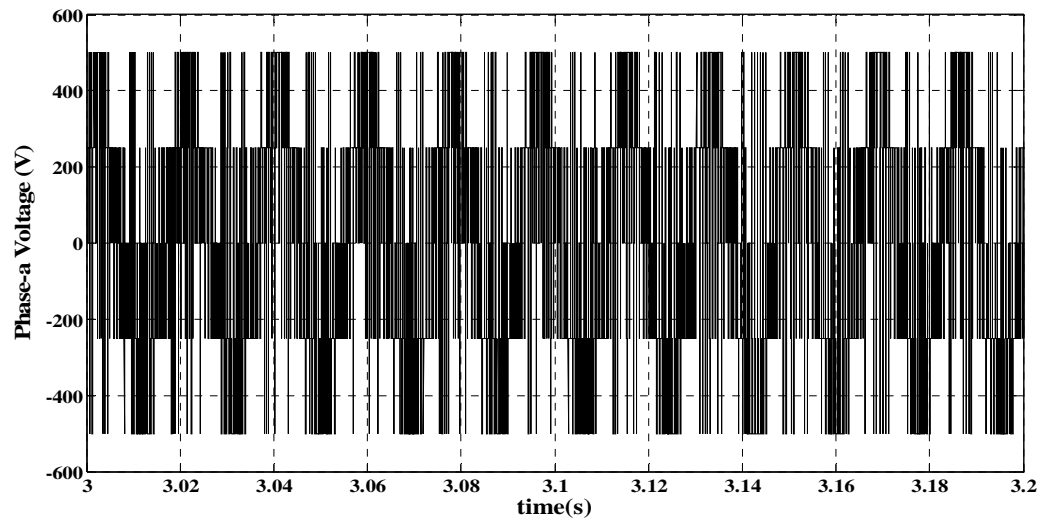
Figure 3.18.a. Phase-a stator voltage of the DTC in LIM for case I
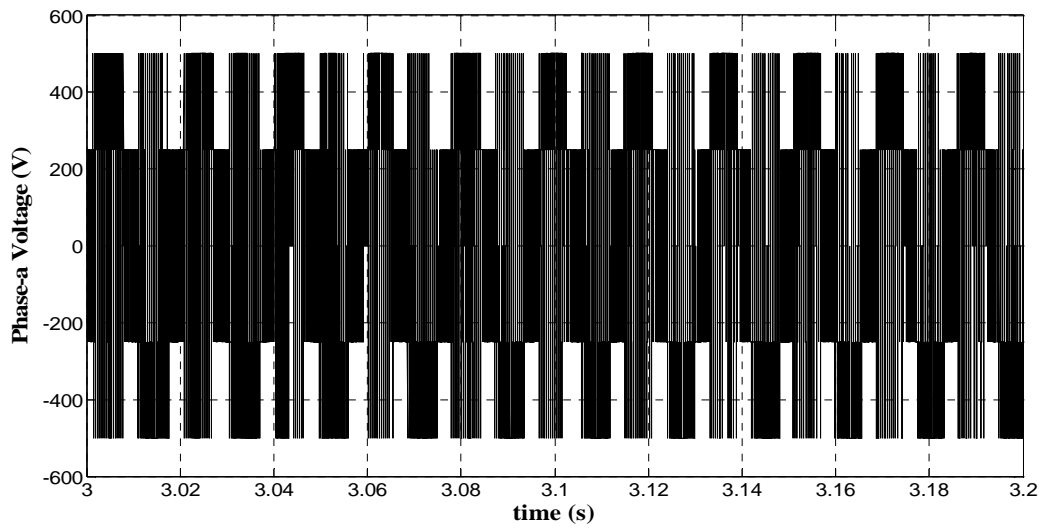
Figure 3.18.b. Phase-a stator voltage of the DTC in LIM for case II
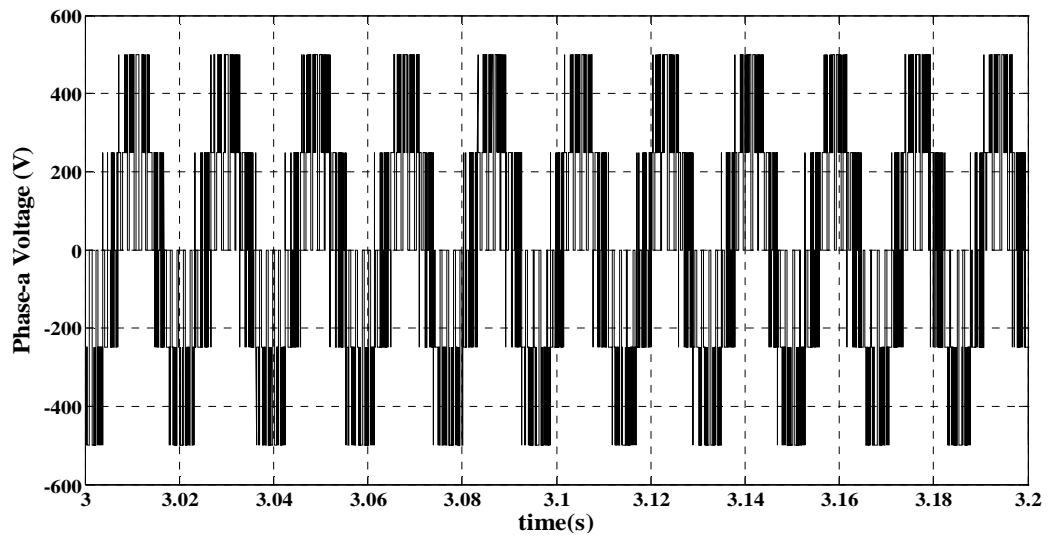
Figure 3.18.c. Phase-a stator voltage of the DTC in LIM for case III

36

As presented in Figure 3.14, for all cases, the measured and the reference speed are very close to each other.

For all cases, the stator and rotor flux vectors follow a circular trajectory as shown by Figure 3.16.

Comparing the Figure 3.15.a with Figure 3.15.b, it can be said that increasing the stator flux hysteresis band results in ripples in stator flux. Furthermore, Figure 3.17.a and Figure 3.17.b show that the current distortion increases with increasing the flux hysteresis band width. On the other hand, as the flux hysteresis band width is increased, the switching frequency decreases which is shown in Figure 3.18.a.

Comparison of Figure 3.18.b and Figure 3.18.c shows that the switching frequency is strongly decreases with decreasing the thrust hysteresis band. However, thrust, speed, stator and rotor flux ripples increases as shown in Figure 3.13.c, Figure 3.14.c, Figure 3.16.c. Furthermore, by comparing Figure 3.17.c and Figure 3.17.b, it can be said that stator currents get distorted with decreasing thrust hysteresis band.

According to simulation results small hysteresis band for flux should be chosen to reduce the current harmonics for considering the heating effect of harmonics and small hysteresis band for thrust should be chosen to reduce thrust pulsations, with using high-speed switching devices and processors.

3.5 Summary

In the chapter, the main principles of DTC is explained and direct thrust controlled LIM drive has been modelled. The performance of the direct thrust controlled LIM drive with different hysteresis band amplitudes for thrust and stator flux is simulated and compared using Matlab/Simulink. Simulation results verifies that the width of the hysteresis bands may influence the drive performance in terms of flux and torque ripples, current harmonics and switching frequency of the power device [45-48]. Hysteresis band for stator flux mainly influences the stator current on the other hand hysteresis band for thrust mainly affects the switching frequency.

CHAPTER 4

DIRECT TORQUE CONTROL of LIM INCLUDING END-EFFECT

The linear induction motor operates as its rotary counterpart does, with thrust instead of torque and with linear speed instead of angular speed. In a LIM, the primary winding corresponds to the stator winding of a rotary induction motor (RIM), while the secondary corresponds to the rotor. The main difference between RIM and LIM is the finite length of LIM's primary. As the primary of LIM moves, a new flux is continuously developed at the entry of the primary side, while the existing flux disappears at the exit side [24, 48, 49]. This non-uniform distribution of airgap flux causes flux and thrust attenuations. This phenomenon is called 'end effect' and it was proved experimentally in [50]. The end effect problem becomes more severe as the speed increases.

In literature, most researchers used magnetic field theory to analyze the end effects. However, the magnetic field approach is not suitable in modeling and vector controller design of LIM. To resolve the end effect problem in LIM control, the speed dependent factors are introduced into the magnetizing branch of its d-axes equivalent circuit [4, 5, 48].

Although the driving principles of the linear induction motor are similar to the traditional rotary one, its control characteristics are much more complicated than RIM owing to its end effect problem. In literature, high performance vector control of LIM mostly carried out in secondary flux oriented scheme [5, 34, 37, 39, 51]. However, field oriented control is complicated and requires accurate knowledge of the motor parameters. In contrast to field-oriented control, the traditional, direct torque control (DTC) does not require the information of the inductance only requires the stator resistance of LIM. The control algorithm of DTC makes it suitable for practical implementation for LIM drive systems. As compared with RIM, DTC for LIM has been less researched.

In the papers studying Direct Thrust Control (DTC) for LIM [7, 40, 41], the end effect was included in the form of thrust correction coefficient. The thrust correction coefficient was obtained by using the finite element analysis in starting conditions considering only the static end effect. However, in this thesis, flux and thrust estimations are improved in a simple manner to reduce the error caused by the end effect by using the equivalent circuit model of LIM rather than using Maxwell equations.

4.1 LIM Mathematical Model Including End Effect

As the primary of LIM moves, a new magnetic field continuously is formed in the secondary around entry region but the existing field disappears at the exit region. Lenz Law states that, these sudden field changes will be resisted by the rapidly growing eddy currents in the secondary side. Hence, the reduction field at the exit end will face a sudden increase in flux and the field increase at the entry end will lead to a decrease. The decay speed of the eddy current is dependent on secondary time constants, whereas the growth speed is related to the sheet leakage time constant [48]. Since the leakage time constant is very small, the eddy current at the entry end grows very rapidly in respect to the primary current causing flux to be more distorted at the entry region [5,48, 52] as shown in Figure 4.1.
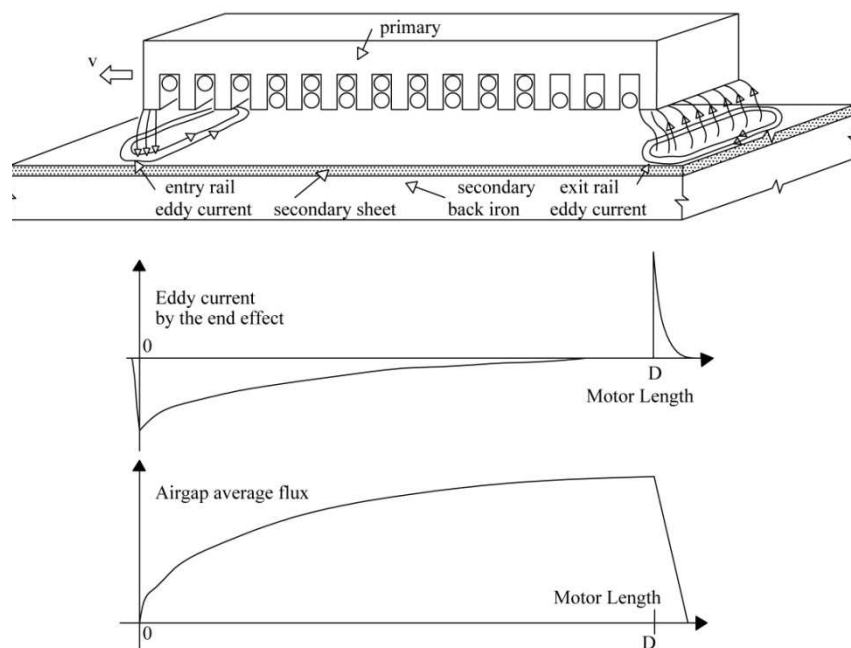
Figure 4.1. Eddy Current generation and air gap flux profile of LIM due to end effect [5]

39

First, Duncan [48] developed the per phase equivalent circuit of LIM considering the end effect by modifying the magnetizing branch of the equivalent circuit of the RIM shown in Figure 4.2.
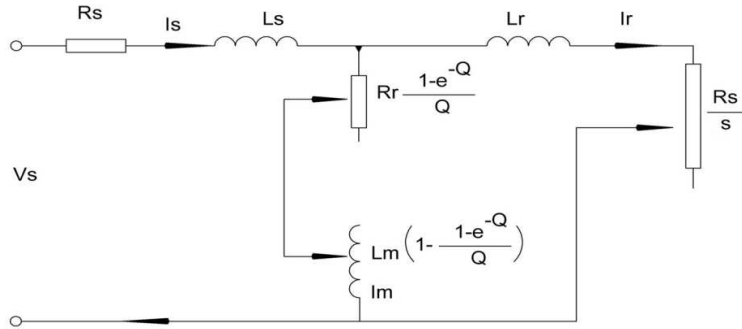
Figure 4.2. Duncan's equivalent circuit of linear induction motor [48]

Duncan's model was transformed into d-q model in a synchronous frame by [5, 40, 51, 52]. To resolve the end effect problem, speed dependent scaling factors are introduced to the magnetizing inductance and series resistance in the d-axis equivalent circuit of RIM. To study the dynamic behavior of the linear induction motor both under transient and steady state conditions, the existed model for LIM is adapted into the stationary reference frame in this thesis. Figure 4.3 shows the developed d-q equivalent circuit of the LIM including the end effect in stationary frame, in which only the magnetization branch in d-axis equivalent circuit is different from RIM model.
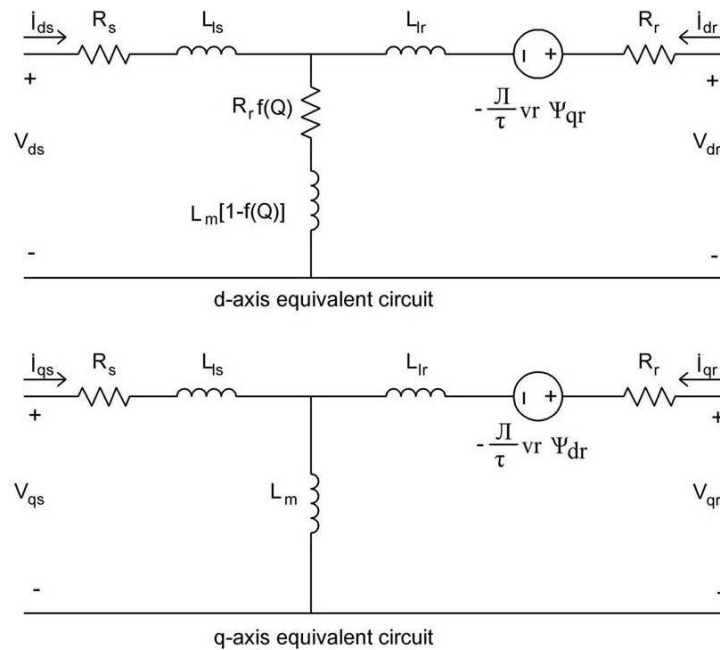
Figure 4.3. d-q equivalent circuit of the LIM including the end effect in stationary frame

40

The speed dependent factor to express the end effect on magnetization branch is related to a function given by (4.1) [5]. This function is inversely proportional to the motor speed.

$$f(Q) = \frac{1 - e^{-Q}}{Q} \qquad (4.1)$$

where $Q = {PDR_r}\Big/{2v_r L_r}$, D is motor primary length.

From the d-q equivalent circuit of LIM shown in Figure 4.2, the primary and secondary voltage and flux linkage equations in stationary reference frame are developed by (4.2), (4.3) and (4.4), respectively.

d-q axis primary voltage equations:

$$v_{ds} = R_s i_{ds} + R_r f(Q)(i_{ds} + i_{dr}) + \frac{d}{dt}\psi_{ds}$$

$$v_{qs} = R_s i_{qs} + \frac{d}{dt}\psi_{qs} \qquad (4.2)$$

d-q axis secondary voltage equations:

$$v_{dr} = R_r i_{dr} + \frac{\pi}{\tau} v_r \psi_{qr} + R_r f(Q)(i_{ds} + i_{dr}) + \frac{d}{dt}\psi_{dr}$$

$$v_{qr} = R_r i_{qr} - \frac{\pi}{\tau} v_r \psi_{dr} + \frac{d}{dt}\psi_{qr} \qquad (4.3)$$

where the subscript s corresponds to primary, r corresponds to secondary, d corresponds to direct axis, q corresponds to quadrature axis, R_s, R_r the primary and the secondary resistances, τ is pole pitch and v_r is the electrical speed.

Flux linkage equations are given by (4.4).

$$\psi_{ds} = L_{ls} i_{ds} + L_m (1 - f(Q))(i_{ds} + i_{dr})$$
$$\psi_{qs} = L_{ls} i_{qs} + L_m (i_{qs} + i_{qr})$$
$$\psi_{dr} = L_{lr} i_{dr} + L_m (1 - f(Q))(i_{ds} + i_{dr})$$
$$\psi_{qr} = L_{lr} i_{qr} + L_m (i_{qs} + i_{qr}) \qquad (4.4)$$

where L_{lr}, L_{ls}, L_m refer to the leakage inductance of secondary, leakage inductance of primary and magnetizing inductance, respectively.

The thrust force is calculated by (4.5).

$$F_e = \frac{3}{2} \frac{\pi}{\tau} \frac{P}{2} \left(\psi_{ds} i_{qs} - \psi_{qs} i_{ds} \right)$$ (4.5)

The LIM motion dynamics is expressed by (4.6).

$$F_e - F_L = J \frac{d}{dt} \frac{2}{P} v_r + B \frac{2}{P} v_r$$ (4.6)

where P is the number of poles, F_e is the electromagnetic thrust, F_L is the external force, J is the mechanical inertia, B is the natural damping.

4.2 Direct Thrust Control Modelling of LIM Including End Effect

The DTC for LIM can be analyzed in the same way as that for RIM. For the good performance of DTC, the accurate prediction of the thrust and stator flux is important. One problem in the case of LIM with end effect is that a new speed dependent resistance and inductance parameters are included in the magnetization branch. However, it cannot be ignored since the end effect influences the thrust and flux characteristics of LIM. This makes it necessary to modify the flux and thrust estimations. The developed Matlab/Simulink modeling for DTC for LIM including end effect is given in Figure 4.4.

The drive model is implemented by five main blocks: LIM model, inverter model, thrust and stator flux estimator, speed controller part to obtain thrust reference value and finally switching vector selector to obtain necessary switching state for the inverter.
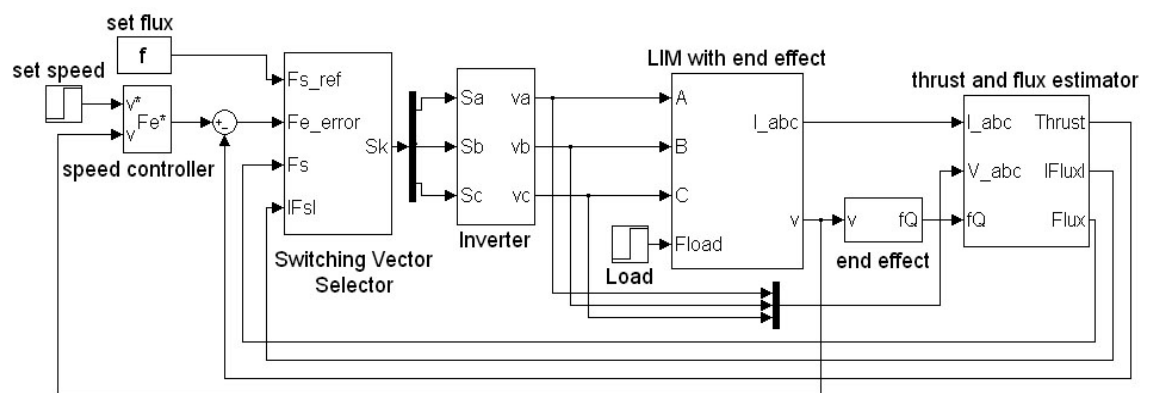
Figure 4.4. Block diagram of DTC for LIM including end effect

42

The measured input values into the DTC control are the motor speed, currents and voltages. The input reference values are the linear speed and the magnitude of the stator flux. The PI type speed controller is used to produce the thrust reference command for the drive. The end effect factor f(Q), voltage and current signals are inputs to the flux and thrust estimator block, which produces the values of stator flux and thrust. Thrust and flux hysteresis comparators compare the actual values of the thrust and the flux with their reference values. Depending on the outputs from these comparators, the switching table logic directly determines the optimum inverter voltage vector and inverter switching directly controls the motor flux and thrust.

The application of the traditional stator flux estimation principle for LIM that considers voltage drop only on the stator resistance causes errors on flux and thrust estimations. Due to end effect property of LIM, it is more accurate to use equation (4.7) for primary flux estimation including with the speed dependent coefficient.

$$\psi^s{}_{ds} = \int \left(v^s{}_{ds} - R_s i^s{}_{ds} - R_r f(Q)\left(i^s{}_{ds} + i^s{}_{dr} \right) \right) dt \tag{4.7}$$

It is reasonable to ignore d-axis rotor current due to its measurement difficulty and less effect on the flux estimation. Then, flux estimate is obtained by (4.8) considering partial end effect.

$$\psi^s{}_{ds} = \int \left(v^s{}_{ds} - R_s i^s{}_{ds} - R_r f(Q) i^s{}_{ds} \right) dt \tag{4.8}$$

The thrust value considering end effect is estimated by (4.9).

$$F_e = \frac{3}{2}\frac{\pi}{\tau}\frac{P}{2} L_m \left(-f(Q)i_{ds}i_{qs} + (1 - f(Q))i_{dr}i_{qs} - i_{qr}i_{ds} \right) \tag{4.9}$$

4.3 Simulation Results

The simulation study consists of two parts. In the first part, a simulation study of direct-on-line starting both under no-load and load is presented to show the application of the dynamic model of the LIM.

In the second part, the validity of the proposed thrust and flux estimators is examined and also, the closed loop performance of DTC employing this improved thrust and flux estimator is shown.

Throughout the simulation study, linear induction motor parameters used to test the DTC strategy for LIM are given in section 3, in Table 3.3. All simulations are done in Matlab/Simulink using SimPowerSystem Toolbox.

4.3.1 Simulation results of LIM modeling including end-effect

For the first case, at standstill, LIM is connected to a 380V, 50 Hz supply. The simulation results of free-acceleration characteristics are plotted in Figure 4.5 and Figure 4.6.
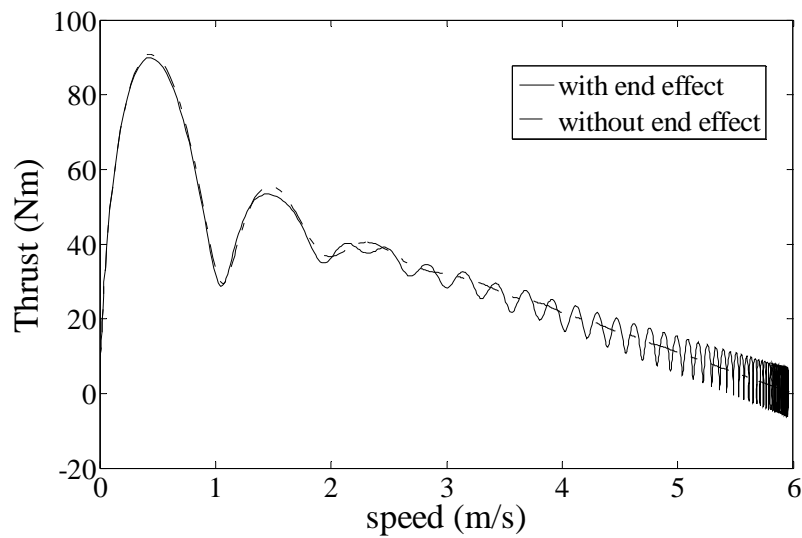
Figure 4.5. Free-acceleration linear speed versus thrust characteristic
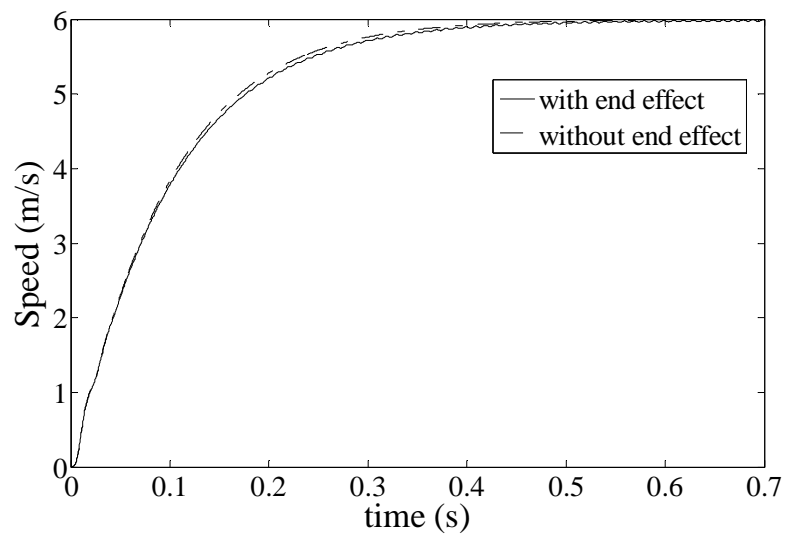
Figure 4.6. No-load speed characteristic

From the Figure 4.6, the end effect has a reducing effect on peak thrust.

In the second case of the simulation study, a step change of thrust command is applied at 0.6 second from zero to 40 Nm. The plots of the thrust against speed and the speed against time are given in Figure 4.7 and Figure 4.8, respectively. Thrust response with end effect is smaller than the thrust response without end effect and the difference between them is the required end effect compensation. It can be seen that when the load is added the speed drops and the required load thrust can be generated successfully.
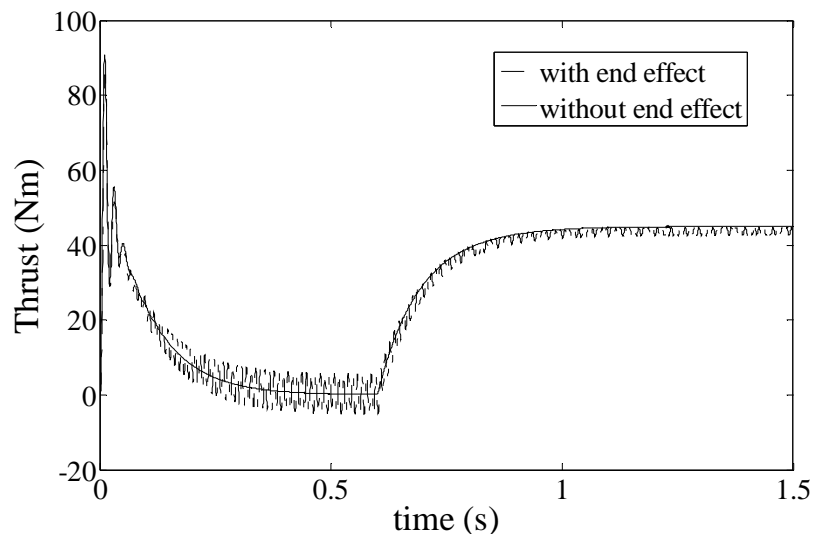
Figure 4.7. No-load thrust versus linear speed characteristic
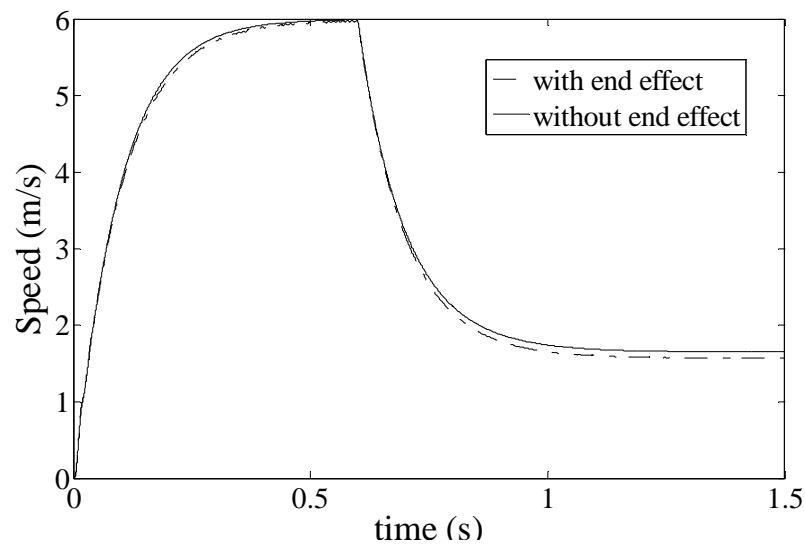
Figure 4.8. No-load linear speed characteristic

The d-axis magnetizing inductance versus speed graph is shown in Figure 4.9. At 0.1 second, at which the speed is around 4-5m/s, noticeable reduction is observed in this inductance which proves that the end effect increases. Furthermore, at Figure 4.10, the unbalanced three phase currents are observed even under the balanced three phase voltage conditions resulted from the unbalanced inductance distribution.
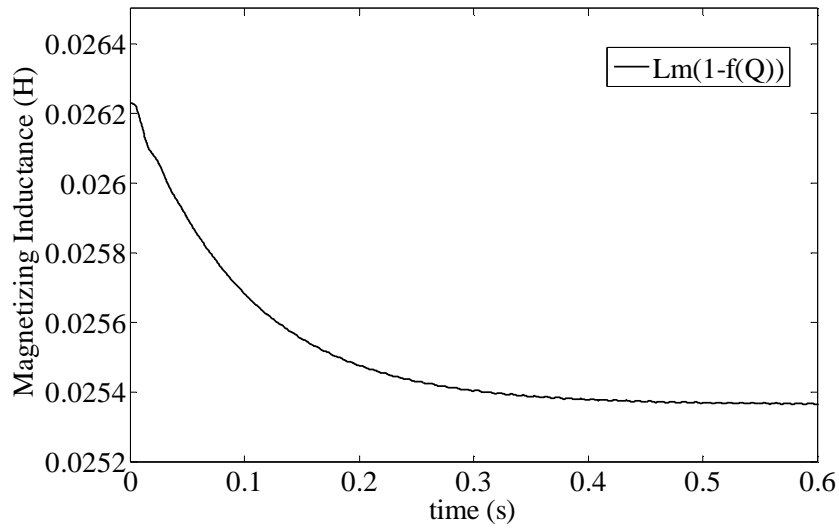
Figure 4.9. d-axis magnetizing inductance characteristic at no-load
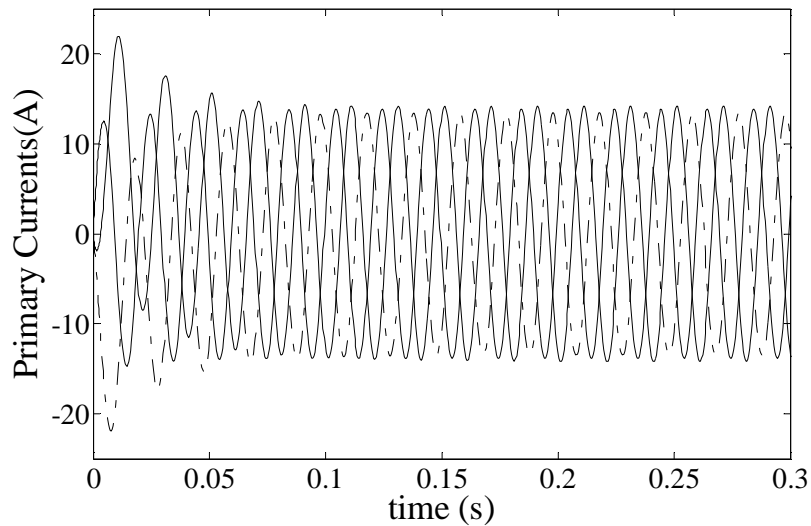
Figure 4.10. Three-phase primary currents of LIM

The influence of the seconder resistance on the end effect is presented in Figure 4.11 and Figure 4.12 by reducing its rated value to its half and later to its one fourth, respectively. According to these figures, it can be said that, the lower value of the seconder resistance strengthens the end effect. To reduce the end effect, the usage of a thin seconder conductor sheet is proposed but this result in a reduction in motor performance and causes in mechanical weakness.
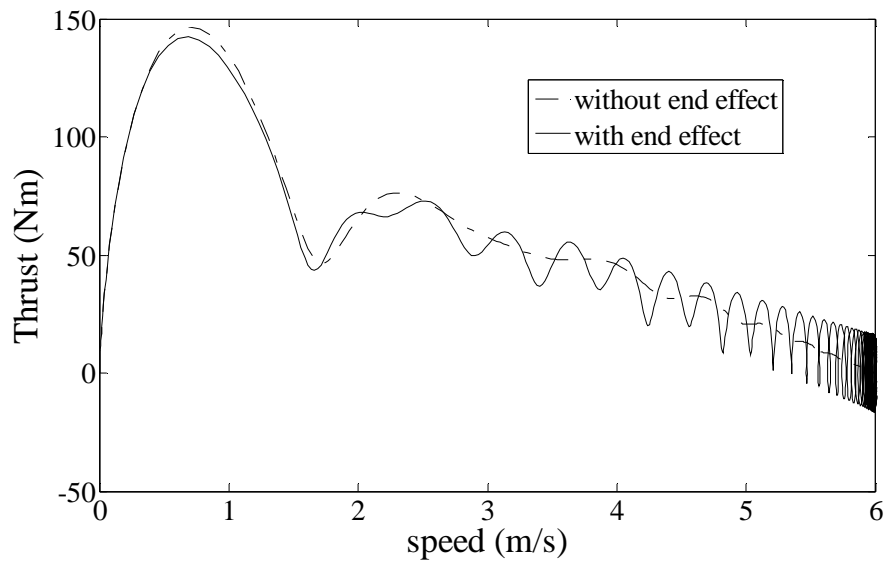
Figure 4.11. No-load speed characteristic with Rr= 24.42Ω
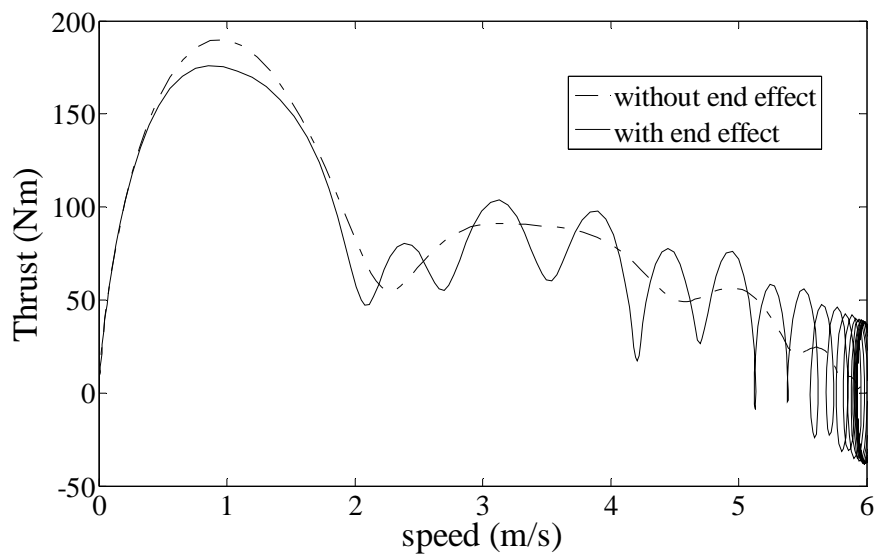
Figure 4.12. No-load speed characteristic with Rr= 12.21Ω

47

The influence of frequency on the end effect is also simulated and the simulation results for the frequencies of 150 Hz and 300 Hz are presented in Figure 4.13 and Figure 4.14, respectively. From the simulation results, it is confirmed that working at the high frequencies increases the severity of the end effect problem.
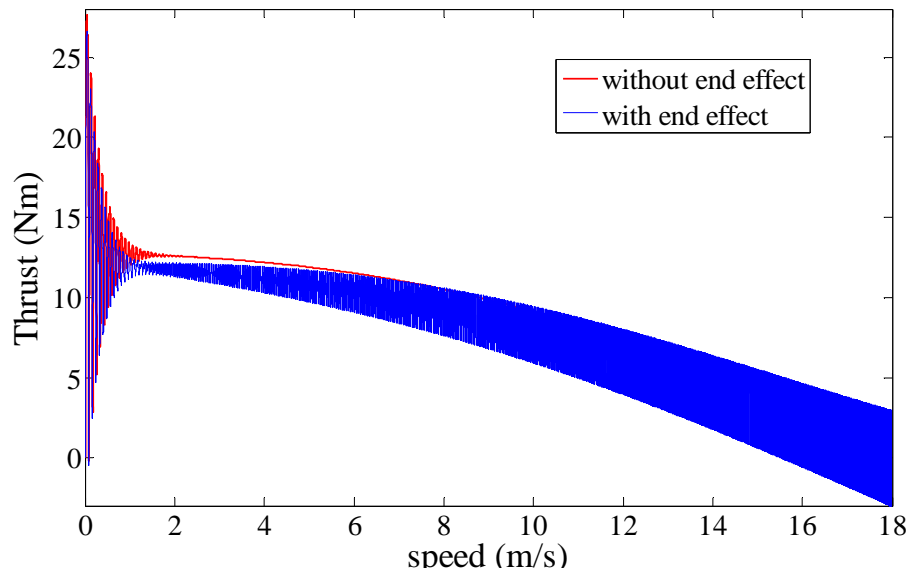
Figure 4.13. No-load speed characteristic with f=150 Hz
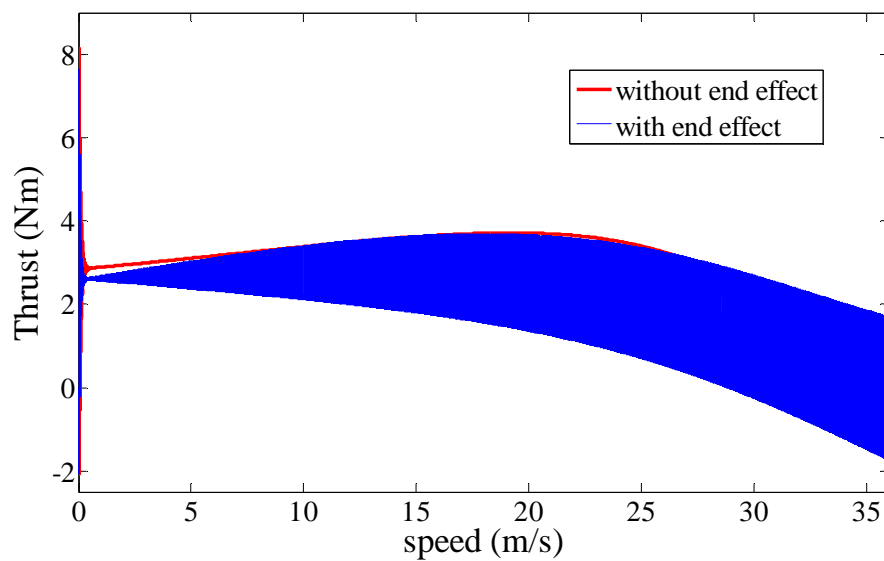
Figure 4.14. No-load speed characteristic with f=300 Hz

4.3.2 Simulation results for DTC of LIM including end-effect

In this part of the simulation study, a step change of thrust command is applied at 0.4 second from zero to 30 Nm. The applied stator flux reference has the amplitude of 0.96 Wb. The performance of the estimators without considering end effect, with fully considering end effect and with partially considering end effect is observed in Figure 4.15, Figure 4.16, and Figure 4.17, respectively.
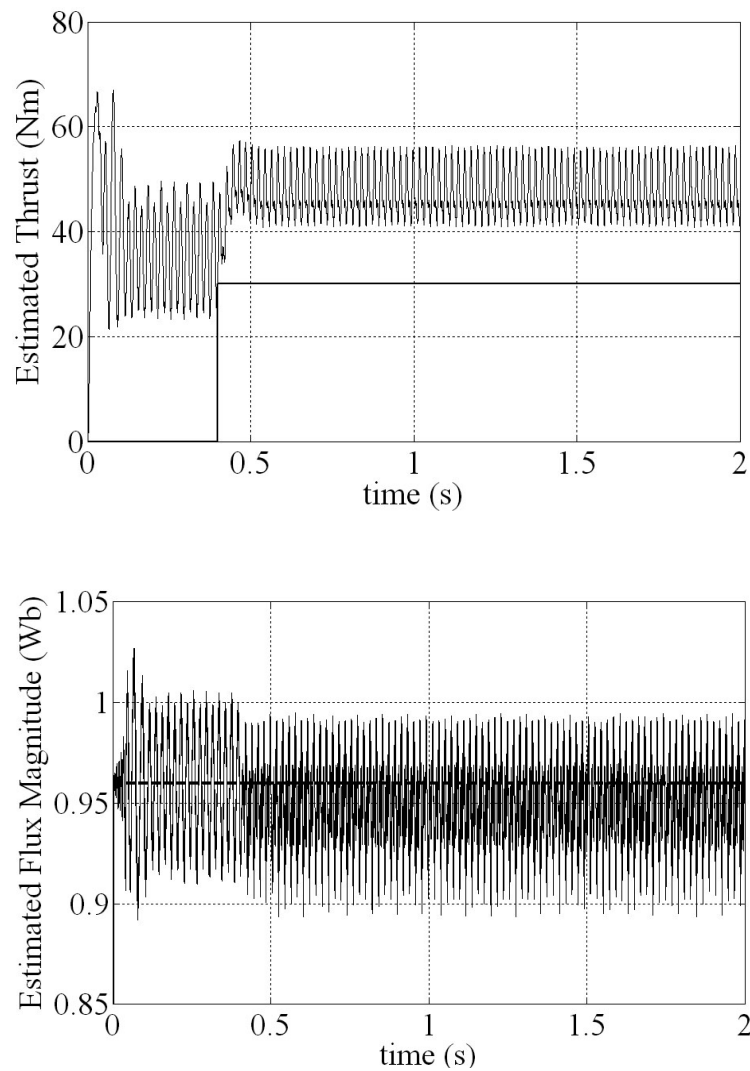
Figure 4.15. Estimated thrust and flux waveforms without considering end effect
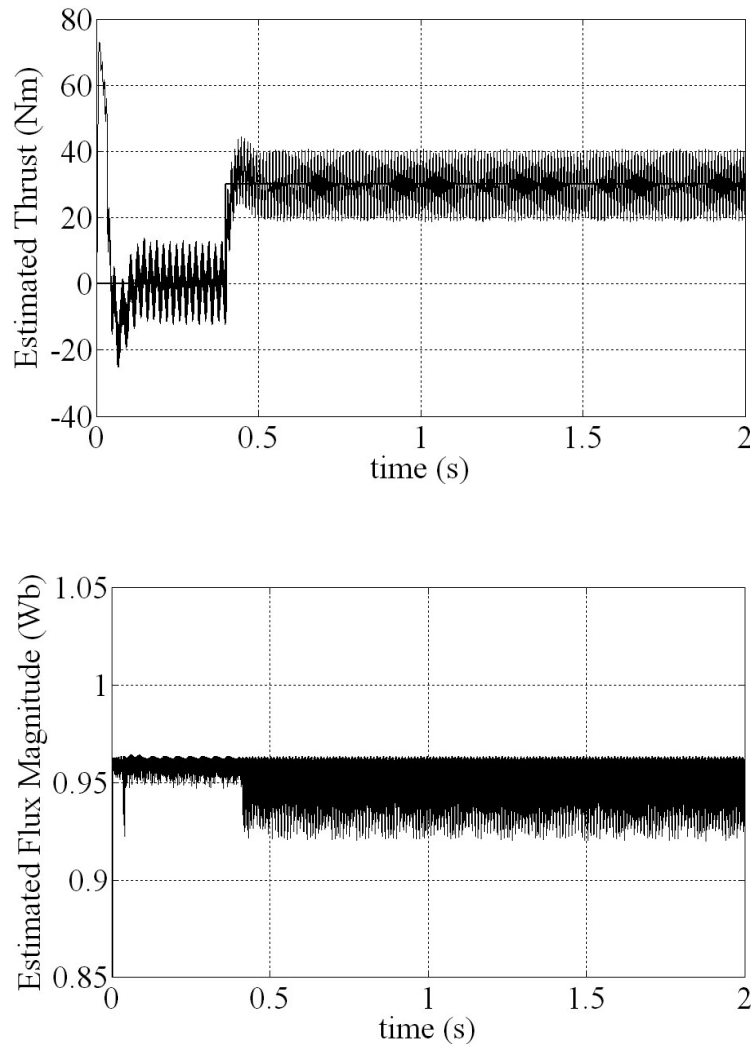
Figure 4.16. Improved estimated thrust and flux waveforms with fully considering end effect

In Figure 4.15 and Figure 4.16, the thrust and flux estimations show satisfactory results. However, without considering end effect, thrust estimation does not reach the expected value as shown in Figure 4.13. The results will become worse with the increase of speed.
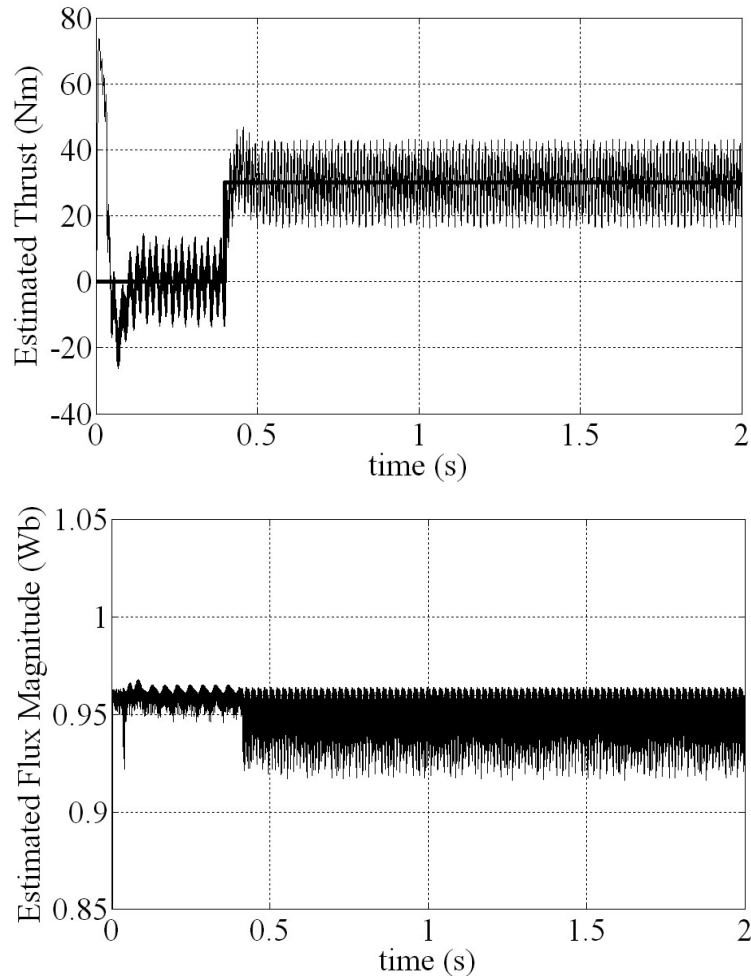
Figure 4.17. Estimated thrust and flux waveforms with partially considering end effect

The closed loop performance of DTC strategy with given improvement is also examined by putting a step change of thrust command at 0.4 second from zero to 30 Nm, when the triangular wave shaped speed reference with amplitude of 3.5 m/s and the stator flux reference with amplitude of 0.96 Wb are applied to the LIM drive.

Figure 4.18, Figure 4.19, Figure 4.20 and Figure 4.21 show the speed, thrust, flux linkage trajectory and three-phase primary currents, respectively.
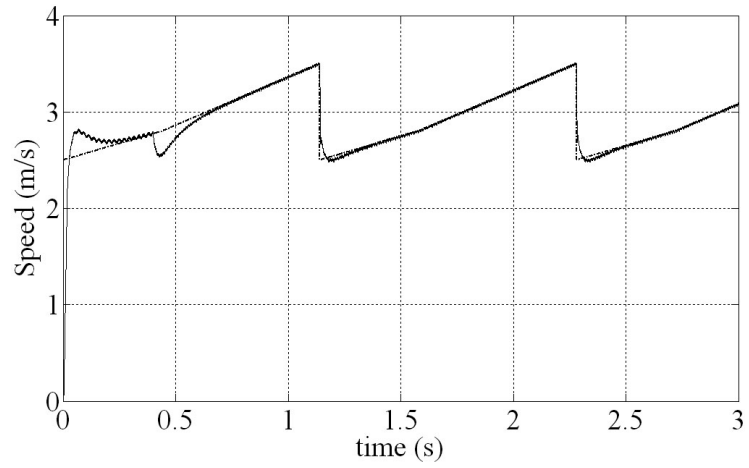
Figure 4.18. Speed reference tracking of the DTC in LIM
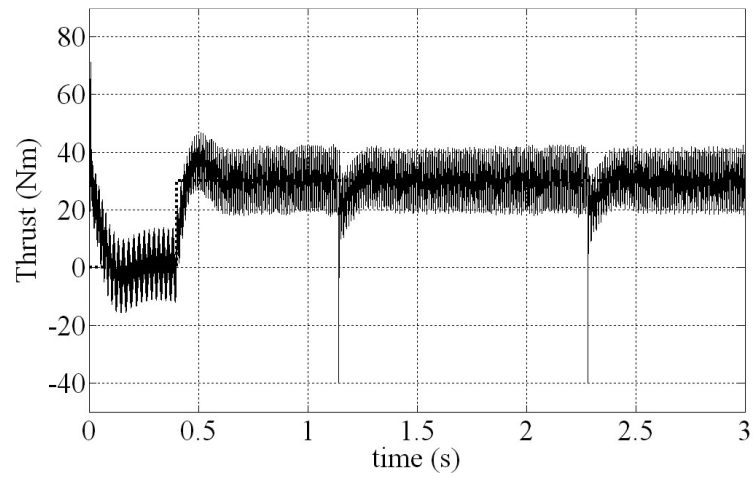
Figure 4.19. Thrust response of the DTC in LIM
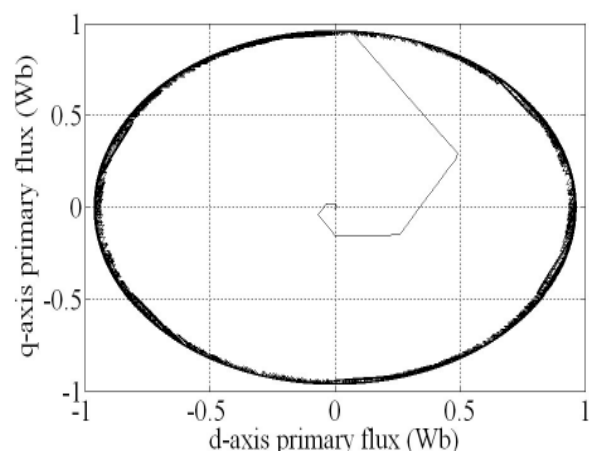
Figure 4.20. Primary flux trajectory of the DTC in LIM
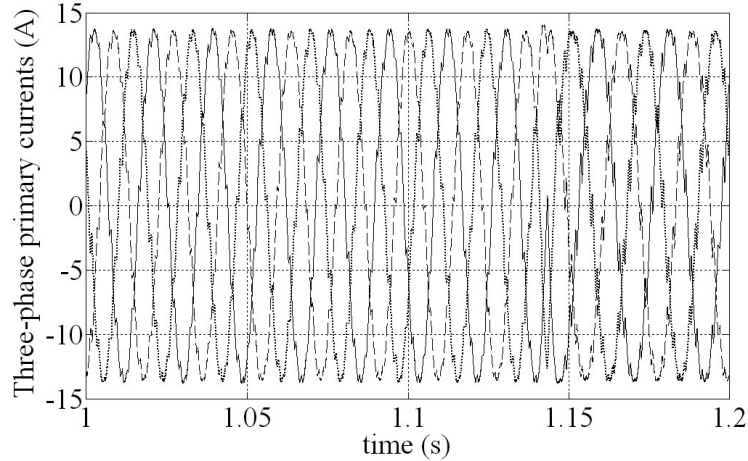
Figure 4.21. Three-phase primary currents

It can be seen from simulation results that direct thrust control system follows the imposed references with high performance and fast response. According to the simulation results, it is important not to ignore the end effect in flux and thrust estimation part in DTC strategy for LIM. To achieve good response, the thrust and flux estimator for DTC of LIM is improved by taking into account end effect. The given improvement is validated by the simulation results. The method used has been found satisfactory and can be applied in real situation using a DSP system. However, the improved flux and thrust equations require the primary and secondary resistance values. Furthermore, the simplicity of the conventional DTC method comes with the disadvantage of thrust ripples. Researchers can choose modified versions of DTC for reducing thrust ripples [53].

4.4 Summary

The LIM mathematical model with end-effect is developed in stationary reference frame and the developed model is simulated by using MATLAB/SIMULINK. The detractive influence of the increased supply frequency, the decreased seconder resistance on thrust is shown by means of simulation results. A method for better flux/thrust estimation for DTC is proposed in considering the end effect phenomenon of LIM and its viability is proven by using MATLAB/SIMULINK.

CHAPTER 5

PROBLEMS COUNTERED IN REALIZATION OF DTC

This chapter mentions about the problems that encountered in the implementation of DTC. These are pure integration problems due to the presence of noise and dc offsets, stator resistance variations, dead time effects, current limiting and torque ripple.

5.1 Stator Flux Estimation Problems

DTC performance is dependent on how precisely the stator flux is constructed. Practically, flux estimation algorithm that has been developed under ideal conditions does not work well and must be modified to work on a real system [54-57]. Stator flux estimation is related to the voltage drop on the stator resistance. At high speed region, the voltage drop on the stator resistance can be neglected comparing with the stator input voltage. Consequently, the estimated torque is the same as the actual torque and DTC switching table can output a proper voltage vector. On the other hand, at low speed region, the voltage drop on the stator resistance is comparable with the stator voltage. Therefore, it becomes difficult to estimate the stator flux correctly. The lower stator flux brings about a lower value of induced torque. Besides, the open-loop integration based flux estimation suffers from instability problems. In real world, especially at low speeds, these problems arise from a variety of factors including noise in measurements, digital approximation errors, dc offset in the measurements.

Initial value problems and the dc offset in measurements cause open loop integral to give erroneous results. They can be analyzed mathematically as in the following. Let's say a signal X is fed to an integrator and then the output signal Y is obtained by this integration process as shown by (5.1):

$$Y = \int X dt \qquad \text{where } X = A_m \sin(wt) \tag{5.1}$$

$$Y = \frac{1}{w}(-A_m \cos(wt) + A_m \cos(wt)\big|_{t=0}) \tag{5.2}$$

As indicated by equation (5.2), the initial value problem at t=0 results in an error. This error is simulated in Matlab/Simulink and the resulted flux trajectory with non-zero initial condition is shown in Figure 5.1. As seen in Figure 5.1, there is a drift in the flux trajectory.
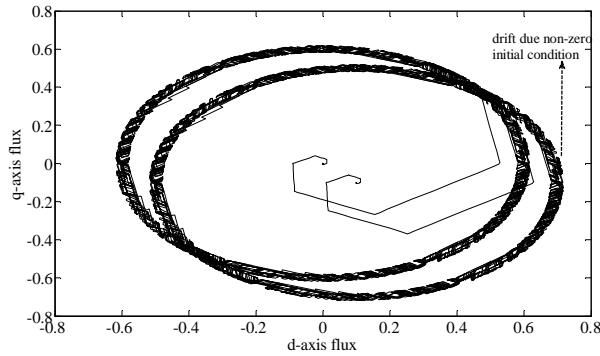
Figure 5.1. Drift in the flux trajectory due to non-zero initial condition of integrator

If the input signal has an offset represented by (5.3) then the output signal is obtained by (5.4).

$$X = A_m \sin(wt) + A_{dc} \tag{5.3}$$

$$Y = \frac{1}{w}\left(-A_m \cos(wt) + A_m\right) + tA_{dc} \tag{5.4}$$

In equation (5.4), there is an additional term (tA_{dc}) which is increasing with time related with input offset. This offset value causes the output to be ramp function looking. Figure 5.2 shows the integrator output with 1 % small dc offset is added to its input.
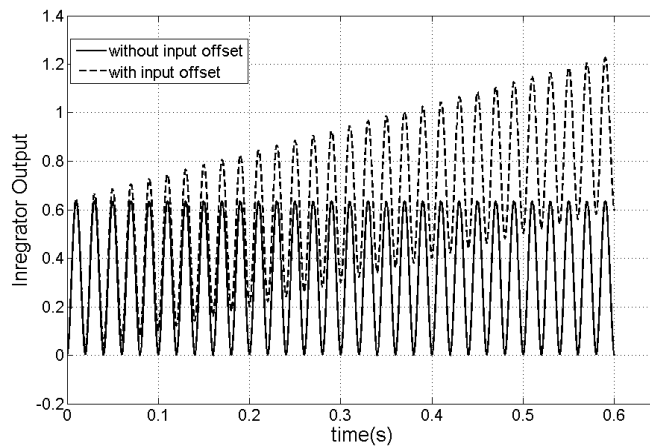
Figure 5.2. Integrator output with and without input dc offset

55

Whatever how small the offset available in the input, the ramp signal will eventually drive the integrator into saturation with time as presented in Figure 5.3 which is obtained by Matlab/Simulink.
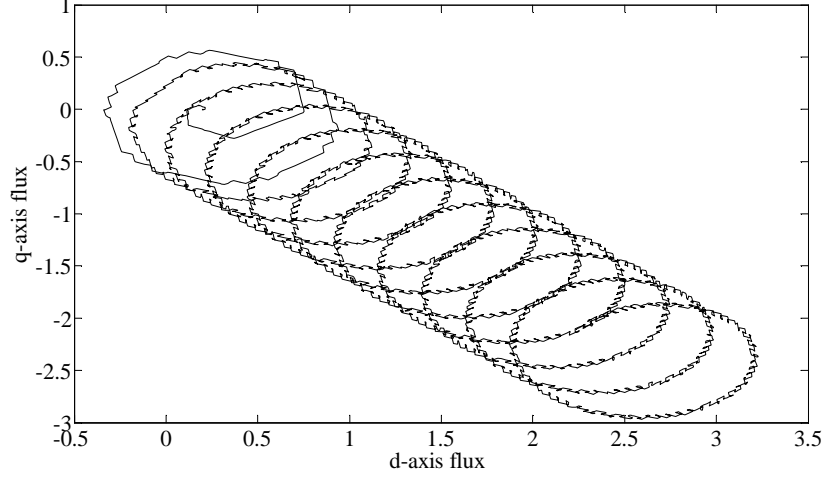
Figure 5.3. Flux trajectory due to dc offset

As a result, the stator flux estimation based on a voltage model with open loop integrator is not capable of achieving high performance especially at low speeds. To overcome this problem, some researchers used theoretical approaches like extended Kalman filters [59], and nonlinear observers [60]. The other ones preferred low-pass filter instead of pure integrator [54-58] and some others incorporate the advantages of the both voltage and current model to improve the stator flux estimation [62, 63].

In current model, at first, the rotor flux linkage equation (5.7) is obtained from the flux linkage and voltage equations of the rotor given by (5.5) and (5.6). Then the stator flux linkage equation (5.8) is derived.

$$\overline{\psi}_r = L_r \overline{i}_r + L_m \overline{i}_s \tag{5.5}$$

$$0 = R_r \overline{i}_r + \frac{d}{dt} \overline{\psi}_r + j\omega_r \overline{\psi}_r \tag{5.6}$$

$$\overline{\psi}_r = \int (\frac{R_r}{L_r}(L_m i_s - \overline{\psi}_r) - j\omega_r \overline{\psi}_r)dt \tag{5.7}$$

$$\overline{\psi}_s = \frac{L_m}{L_r} \overline{\psi}_r + L_s' \overline{i}_s \tag{5.8}$$

where $L_s' = L_s - \frac{L_m^2}{L_r}$ is the stator transient inductance.

56

Notice that, equation (5.7) represents a closed-loop integral that causes the current model to be more stable than the open loop voltage model since the offset errors naturally diminish. However, the current model is dependent on the inductance parameters of the motor model and rotor speed information. If they are erroneous, they will cause magnitude and phase errors in rotor flux estimation so in stator flux estimation. Especially, at high speeds, numerical errors in measuring speed and deviations in inductance parameters of the motor distort the estimation accuracy.

In this thesis, among the above mentioned methods, low-pass filter based voltage model is preferred to estimate the stator flux. The simple method to remove the dc component caused by the pure integration algorithm is to remove by a high-pass filter, as shown in Figure 5.4 where $\bar{v}_{emf} = \bar{v}_s - R_s \bar{i}_s$ is back- emf, $\bar{\psi}^{est}$ is the estimating flux, ω_c is the cut-off frequency. By combination of the pure integrator block and high-pass filter block in Figure 5.4 together, a low-pass filter is formed as given in (5.9).

$$\bar{\psi}_s^{est} = \frac{1}{s + \omega_c} \bar{v}_{emf} \tag{5.9}$$
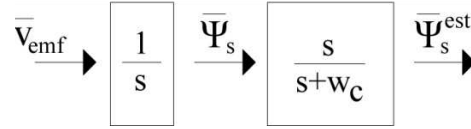
Figure 5.4. High-pass filter of flux linkage

As shown in Figure 5.5, the estimated flux can be acquired by simply getting the back emf through a one-order low-pass filter.
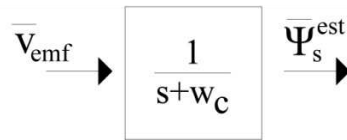
Figure 5.5. Low-pass filter of back emf

By using equation (5.9);

$$\bar{\psi}_s^{est}(s + \omega_c) = \bar{V}_s - \bar{I}_s R_s \tag{5.10}$$

Digital implementation of equation (5.10) can be written by (5.11).

$$\overline{\psi}_{s(k)}{}^{est} = \frac{1}{1+T_s\omega_c}((\overline{V}_s - \overline{I}_s R_s)T_s + \overline{\psi}_{s(k-1)}{}^{est}) \tag{5.11}$$

if $\omega_c << \omega_e$ (ω_e stands for the frequency of the stator flux) offset removal capability of LPF is reduced. Selection of an appropriate cutoff frequency is done by experimental trials; the values in the range of 2-3 Hz are sufficient.

Amplitude and phase response of the one-order low-pass filter are expressed by (5.12).

$$Gain\angle Phase = \frac{1}{\sqrt{\omega_e{}^2 + \omega_c{}^2}} \angle -\tan^{-1}(\omega_e/\omega_c) \tag{5.12}$$

Equation (5.12) shows that when the frequency of the stator flux is very high, the amplitude attenuation and phase shift are not important, and the flux can be estimated accurately, thus the expected motor operation behavior is achieved. But if the motor operates at low speed, the flux amplitude attenuation and phase shift become serious which leads to inaccurate estimation of flux and deterioration in DTC performance. Therefore, the amplitude and phase of the flux must be compensated during low speed operation.

5.1.1 Compensation of the stator flux estimation

In thesis, the amplitude and phase errors of the flux estimation are compensated based on the fact that the back emf is orthogonal to the stator voltage [54].

The stator flux estimation under sinusoidal steady-state condition can be written as,

$$\overline{\psi}_s = \frac{\overline{V}_s - \overline{I}_s R_s}{j\omega_e} \tag{5.13}$$

In (5.13), it is clear that the stator flux is lagging the back emf by 90 electrical degrees. By using LPF approach, the equation (5.13) becomes:

$$\overline{\psi}_s{}^{est} = \frac{\overline{V}_s - \overline{I}_s R_s}{\omega_c + j\omega_e} \tag{5.14}$$

Figure 5.6 shows the phasor diagram of the actual and estimated stator flux basing on (5.13) and (5.14).
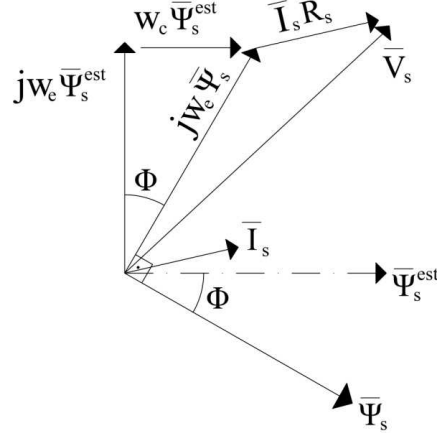
Figure 5.6. Phasor diagram for steady state operation of induction machine showing the actual and estimated stator flux based on LP filter [54]

By equating (5.13) and (5.14), the actual stator flux is obtained as,

$$\overline{\psi}_s = \overline{\psi}_s^{\,est} - j\frac{\omega_c}{\omega_e}\overline{\psi}_s^{\,est} \tag{5.15}$$

According to equation (5.13), other than $\omega_e >> \omega_c$ LPF approximation requires magnitude and phase compensation which is determined by using (5.16).

$$\frac{\psi_s^{\,est}}{\psi_s}\angle\theta^{est} - \theta = \frac{\omega_e}{\sqrt{\omega_e^{\,2} + \omega_c^{\,2}}}\angle\frac{\pi}{2} - \tan^{-1}(\omega_e/\omega_c) \tag{5.16}$$

where $\overline{\psi}_s^{\,est} = \psi_s^{\,est}\angle\theta^{est}$ and $\overline{\psi}_s = \psi_s\angle\theta$.

From equation (5.16), it is clear that the estimated stator flux leads the actual stator flux by an angle depending on the selected cut-off and the stator flux frequency. In addition to this, its magnitude is always smaller than the actual one. This causes the magnitude of the actual stator flux becomes larger than its reference value during DTC which may result in saturation.

The estimated and the actual stator flux vector are given in the d-q reference frame by Figure 5.7.
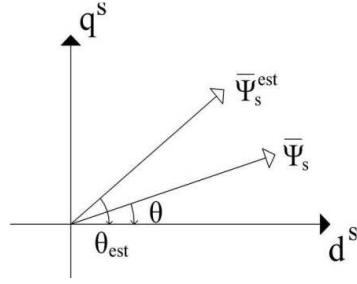
Figure 5.7. The estimated and the actual stator flux vectors given in d-q reference frame

The d-q components of the actual stator flux in terms of the d-q components of the estimated flux, cut-off frequency of LPF and the rotational speed of the stator flux are given by equations (5.17) through (5.23) [54].

$$\psi_{ds} = \psi_s \cos(\theta_{est} - \gamma) \tag{5.17}$$

where $\gamma = \frac{\pi}{2} - \tan^{-1}(\omega_e / \omega_c)$

Assuming $\gamma' = \tan^{-1}(\omega_e / \omega_c)$, then,

$$\psi_{ds} = \psi_s \sin(\theta_{est} + \gamma') \tag{5.18}$$

By using trigonometric relations;

$$\psi_{ds} = \psi_s \left(\frac{\psi_{qs}^{est}}{\psi^{est}} \frac{\omega_c}{\sqrt{\omega_c^2 + \omega_e^2}} + \frac{\psi_{ds}^{est}}{\psi^{est}} \frac{\omega_e}{\sqrt{\omega_c^2 + \omega_e^2}} \right) \tag{5.19}$$

where $\psi_s = \frac{\sqrt{\omega_c^2 + \omega_e^2}}{\omega_e} \psi_s^{est}$

$$\psi_{ds} = \psi_{qs}^{est} \frac{\omega_c}{\omega_e} + \psi_{ds}^{est} \tag{5.20}$$

Similarly, for q axis;

$$\psi_{qs} = -\psi_s \cos(\theta_{est} + \gamma) \tag{5.21}$$

$$\psi_{qs} = \psi_s \left(-\frac{\psi_{ds}^{est}}{\psi^{est}} \frac{\omega_c}{\sqrt{\omega_c^2 + \omega_e^2}} + \frac{\psi_{qs}^{est}}{\psi^{est}} \frac{\omega_e}{\sqrt{\omega_c^2 + \omega_e^2}} \right) \tag{5.22}$$

$$\psi_{qs} = -\psi_{ds}^{est} \frac{\omega_c}{\omega_e} + \psi_{qs}^{est} \tag{5.23}$$

60

By using equations (5.20) and (5.23), the performance of the flux estimator can be improved by compensating for the magnitude and phase errors.

The position of stator flux space vector is calculated by (5.24) using the stator flux representation on d-q frame:

$$\theta_s = \tan^{-1}(\psi_{qs}/\psi_{ds}) \tag{5.24}$$

Then, the synchronous speed is obtained by taking the derivative of (5.24). The resulted expression related to the frequency of stator flux is given by (5.25).

$$\omega_e = \frac{d}{dt}\theta_s = \frac{d}{dt}\tan^{-1}(\psi_{qs}/\psi_{ds}) = \frac{\dot{\psi}_{qs}\psi_{ds} - \dot{\psi}_{ds}\psi_{qs}}{\psi_{ds}^2 + \psi_{qs}^2} \tag{5.25}$$

Digital implementation of equation (5.25) can be written as:

$$\omega_{e(k)} = \frac{\psi_{ds(k-1)}\psi_{qs(k)} - \psi_{ds(k)}\psi_{qs(k-1)}}{(\psi_{ds}^2 + \psi_{qs}^2)T_s} \tag{5.26}$$

5.2 Stator Resistance Variation

The stator resistance is the only parameter used for the well-known voltage model stator flux estimation. Its measurement is much easier and accurate than the inductance measurement and the only variation is due to change in temperature. In literature, the effect of stator resistance variation on the DTC performance was investigated [63-64]. According to [64], it is possible to use the stator current to track the change in stator resistance. The error between the measured stator current and the reference current is processed through PI controller to compensate the change in stator resistance until the error in current becomes zero. The reference current is derived from the reference torque and stator-flux information. In this thesis, PI controller based complex stator resistance estimation is not preferred, since it cancels the inherent simplicity of DTC.

The stator resistance is updated according to the temperature variation. This technique is simple and straightforward assuming that the temperature dependency of the stator resistance is given by (5.27) [65].

$$R_s = R_{so}(1 + \alpha(T - T_o)) \tag{5.27}$$

where R_{so} is the stator resistance measures at the room temperature To and α is the temperature coefficient (=0.004041 for an copper conductor) of the conductor material.

For a class A motor, the maximum winding temperature is specified as 105ºC [66]. When the winding temperatures rise up to maximum temperature, Rs differs by up to 35%.

5.3 Current Limiting

By using equation (5.8), the stator current is defined by equation (5.28).

$$\bar{i}_s = \frac{1}{L'_s}(\overline{\psi}_s - \frac{L_m}{L_r}\vec{\psi}_r) \tag{5.28}$$

where $L'_s = L_s - \frac{L_m^2}{L_r}$ is the stator transient inductance.

According to (5.28), the stator current depends on both stator and rotor flux. Therefore, an important difference between the stator and the rotor flux causes the increment of stator current rapidly.

Regarding that the stator time constant is smaller than the rotor mechanical time constant, even the selection of tangential voltage vector to reduce the stator flux amplitude may result in a fast variation of the stator current.

In DTC, while following the flux and torque set commands, the stator current magnitude can exceed the upper limit of IGBTs of the inverter. Consequently, current limiting is necessary for both flux and torque forming stages. Two different strategies were proposed to limit the stator current for DTC [67]. In the first one, the zero voltage vector is applied so that the resulting stator flux and torque reducement lower the stator current amplitude [68]. In the second one, a non-zero voltage vector V_{k+2} tangential vector is chosen in sector k to reduce the stator flux magnitude and so does the stator current.

During DTC implementation for current limiting purpose, at first stator flux forming stage is completed then the torque set-up is. The applied procedure is given in Figure 5.8. At starting, considering the rotor mechanical constant, V1 is applied until the stator flux attains its reference value. During this period, if the stator current approaches its

limiting value, zero voltage vector is applied to the inverter. After completed the flux tuning, the torque is tune-up. To increase the torque, V_{k+1} is applied until the current limit is reached. After then V_{k+2} or zero vector are selected to limit the current.
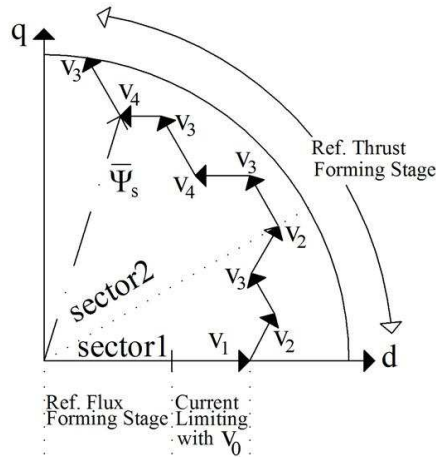
Figure 5.8. DTC starting procedure with current limiting

Furthermore, in realization, ramp looking reference settings for flux is preferred. Therefore, the possibility of occurance of overcurrent condition is alleviated by gradually increasing the flux.

5.4 Dead Time Effect

In an ideal situation, the states of two switches in an inverter leg are allowed to change simultaneously from on to off and vice versa. However, any type of power electronic switch has finite turn-on and turn-off times, in practice. Therefore, it is necessary to include a protection time to avoid a short circuit in the DC link even with the fastest type semiconductors. A dead-time (blanking time, lock-out time) should be included in the software before the turn-on of the other switch [69].

The dead time effect for one phase leg of an inverter is shown by Figure 5.9. According to this figure, the dead-time counts from the time instant at which one semiconductor switch in a leg turns off and terminates when the opposite switch is turned on.

63
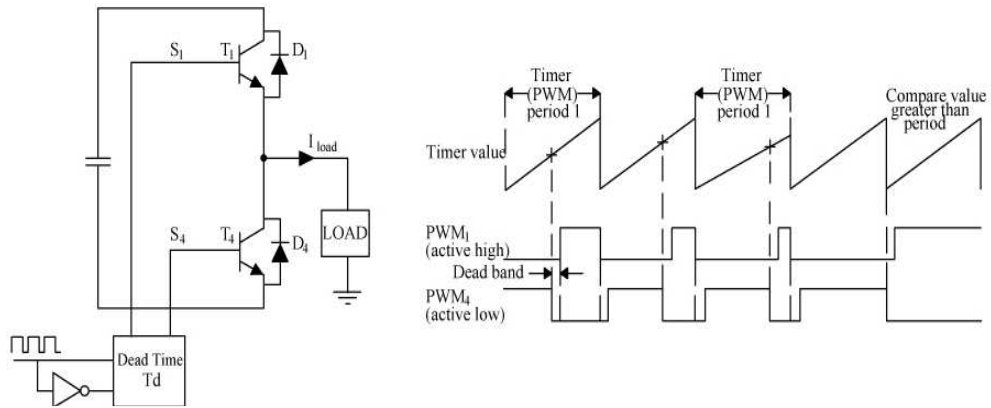
Figure 5.9. Dead time effect for one phase leg of an inverter

Consequently, the time duration of real drive signal for upper transistor gets shorter than ideal signal and for lower transistor gets longer than ideal. During the dead-time duration, since both switches in each leg are in the off-state, the output voltage is dependent on the direction of the output current. As a consequence of this, when the phase current I_{load} is positive, the output voltage is reduced, and when the current I_{load} is negative the output voltage is increased. Since this is repeated for every switching operation, these effects become significant in high switching frequency operation. This is a temporary loss of DTC. One another consequence of including dead time is the appearance of undesirable harmonics [70, 71]. To further minimize the adverse effects of the dead time, it is selected as small as possible in software implementation.

If the applied stator voltages are calculated from the voltage vector demand and the DC bus voltage measurement, the obtained voltage signals are not exactly equal to the real voltages applied to the motor. Because they are free from dead time effects and harmonics. Instead of this method, the stator voltage is measured directly through signal conditioning and filtering circuit.

5.5 Torque Ripple Minimization

The hysteresis based direct torque control has the disadvantage of the torque and flux ripples [34]. The usage of small hysteresis band and high switching frequency with a fast processor are solutions. However, if the hysteresis band is selected as too small, the problems of overshoot/undershoot occur. Whereas the high switching frequency causes

increased switching losses leading to worse efficiency and increased stress on inverter switches. The selected voltage vector is applied for the entire switching period in the conventional DTC. In Figure 5.10, T_0 means no more torque is needed and thus the zero voltage vector should be selected. Then, the actual value of the torque falls slowly until below the value Tref - Δh. After that, an appropriate voltage vector is selected in order to increase the torque. If the stator flux vector lies in sector k with a magnitude greater than its reference value, then the voltage vector V_{k+2} is selected to increase torque. While during this stage, the actual torque value gets close to its reference so there is decrescent torque error. By applying the same selected voltage vector for the whole switching period, assuming it is not small enough, may cause the electromagnetic torque exceeding its reference value before the end of the switching period. This process goes on with high torque and current ripple.
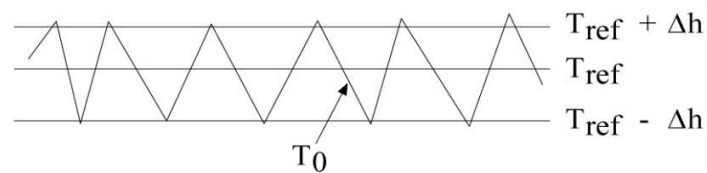
Figure 5.10. Hysteresis control of torque where Tref is torque reference and Te is actual torque and hb is hysteresis band

In order to overcome torque ripple problem, a number of methods are proposed. In [72, 73], adaptive hysteresis band comparator is designed maintaining constant switching frequency. There are some methods to reduce the torque ripple by removing the hysteresis comparators, such as fuzzy logic [74], [75], predictive control [76]. Another approach is to use space vector modulation (SVM) technique to synthesize the desired stator voltage. In [20, 34, 77], a conventional SVM is used. Nonetheless, there exist other solutions, involving complex calculations and these will increase the complexity of the DTC drive. This defeats the purpose of the basic DTC philosophy of simple implementation. In contrary to classical DTC, in this thesis, the duration for the application of the voltage vector is determined according to the conditions of the flux and thrust errors to reduce these ripples. During the application of the zero voltage vector, no power is absorbed by the machine so stator flux and torque are only decreased slightly. If the selected non-zero voltage vector is applied for a portion of the switching

period and the zero voltage vector is applied for the rest of the switching period then these ripples can be reduced. The portion of the time named as duty ratio is determined according to the decrease or increase in the flux and thrust errors for example if the thrust and flux errors are increasing, then the duty ratio is set as big rather than small as shown in Table 5.1.

Table 5.1. Duty ratio selection according to the thrust/flux errors

Thrust Error \ Flux Error	Positive, increasing	Positive, decreasing	Negative, increasing	Negative, decreasing
Positive, increasing	%55	%75	%75	%55
Positive, decreasing	%75	%95	%95	%75
Negative, increasing	%75	%95	%95	%75
Negative, decreasing	%55	%75	%75	%55

5.6 Summary

In this chapter, an analysis of the effect of the non-idealities on the DTC implementation and their solutions are mentioned. The effect of offset and gain errors in the measured current and voltage signals are analyzed. They cause an error in the estimated stator flux linkage hence in thrust estimates and, further on according to the characteristic properties of the control system. The flux estimation based on low-pass filter approach including the stator flux magnitude and phase angle errors compensation is effectively eliminate the errors in calculated flux. Under this structure, a better flux correction gives an effective improvement for a motor's output torque. The current limiting algorithm while following the flux and torque set commands is also mentioned in this chapter. Finally, the method for achieving torque ripple minimization is suggested by arranging the duty ratio of the selected voltage vectors depending on the torque/flux error status for every sampling period. This can be accomplished by using fast digital signal processor TMS320F2812.

CHAPTER 6

Z-SOURCE INVERTER

The traditional pwm inverter has been widely used in adjustable speed drives, uninterruptible power supply applications [30]. However, it has some limitations. Obtainable output voltage is quite below the input line voltage [78, 79]. This problem is mostly solved by using a dc-dc boost converter with an extra cost. In 2002, Peng F. Z. proposed a new type of power inverter. To differentiate this new inverter from conventional voltage source inverter (VSI) and current source inverter (CSI), the author called it as impedance source (Z-source) inverter (ZSI). The main circuit and its operating principle have been described in [80].

In the traditional 3-phase voltage source inverter (VSI), the shoot through states in which both switches in a leg are in the on state, are strongly forbidden. However, miss-gating from EMI can cause shoot-through that leads to destruction of the inverter. The dead time that is needed to avoid shoot-through which creates distortion and unstable operation at low speeds. However, in the case of z-source inverter, in addition to the eight vectors of traditional VSI, one more vector is defined which is called as "shoot through zero vector". The z-source inverter makes use of this vector to boost the DC link voltage without using a boost DC/DC converter. Moreover, it reduces harmonic current [82]. To utilize these advantages, ZSI was applied to the adjustable speed drives, fuel cell applications, UPS systems [78, 79, 82- 84].

Figure 6.1 shows the general structure of the VSI based Z-source inverter. Although DC/AC conversion is the most common application of the Z-source topology, it can also be applied to AC/DC and AC/AC power conversions [85-86]. The X shape impedance is the Z-source network which is composed of two inductors and two capacitors to provide a coupling between the DC source and the inverter bridge.
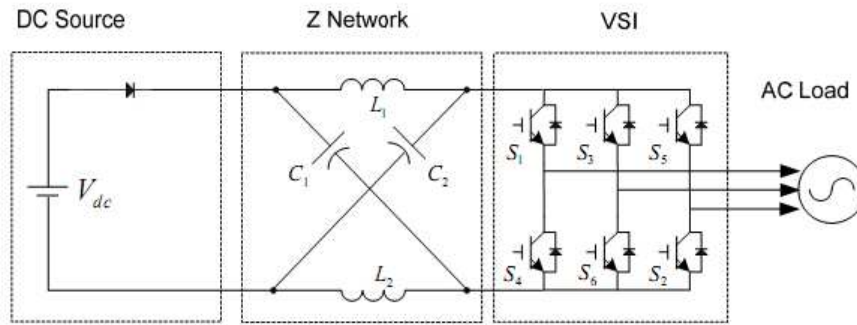
Figure 6.1. Block diagram of VSI based Z-source inverter

6.1 Steady State Circuit Analysis

The ZSI has two operating modes: non-shoot through mode and shoot through mode. To perform the circuit analysis of ZSI, the equivalent circuit models belonging to these modes are constituted by looking from the dc link side in Figure 6.1. Figure 6.2(a) shows the equivalent circuit of ZSI in non-shoot through mode, while Figure 6.2(b) shows the equivalent circuit in shoot through mode [80]. As can be seen from these figures, in the shoot-through state, the Z-source network is shorted and in the active state, the Z-source network sees the load voltage.

(a)

(b)
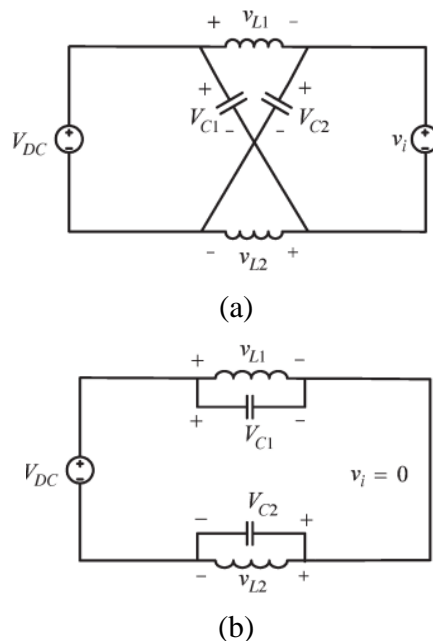
Figure 6.2. Equivalent circuits of ZSI: (a) Non–shoot-through mode (b) Shoot- through model

For simplicity, the inductors L_1 and L_2 and capacitors C_1 and C_2 are assumed as to have the same inductance L and capacitance C, respectively [80]. As a result of this assumption, the Z-source topology becomes symmetrical giving rise to the following equation (6.1).

$$V_{C1} = V_{C2} = V_C \qquad\qquad v_{L1} = v_{L2} = v_L \tag{6.1}$$

The inverter bridge is assumed in the shoot-through mode for an interval of T_{sh} and in the non- shoot-through mode for an interval of T_{nsh} during the switching period of Ts.

$$T_s = T_{sh} + T_{nsh} \tag{6.2}$$

Mode 1: shoot through mode

In mode 1, the energy transferred from source to load equals to zero. From Figure 6.2(b), the inductor voltage and the input voltage of the inverter can be written as:

$$v_L = V_C \qquad\qquad V_{DC} = 2V_C \qquad\qquad v_i = 0 \tag{6.3}$$

Mode 2: non-shoot through mode

In mode 2, real energy transfers between the source and load. From Figure 6.2(a), the inductor voltage and the input voltage of the inverter can be written in (6.4).

$$v_L = V_{DC} - V_C \qquad\qquad v_i = V_c - v_L = 2V_C - V_{DC} \tag{6.4}$$

Since the average voltage of the inductors over one switching period should be zero in steady state, the inductor and capacitor voltages are derived as in (6.5) and (6.6), respectively.

$$V_L = \bar{v}_L = \int_0^{} v_L dt = \frac{T_{sh}V_C + T_{nsh}(V_{DC} - V_C)}{T_s} = 0 \tag{6.5}$$

$$V_C = \frac{T_s - T_{sh}}{T_s - 2T_{sh}} V_{DC} \tag{6.6}$$

As can be understood from equation (6.6), the steady state capacitor voltage is only dependent on the shoot through time. However, the relationship between them is not linear as shown in Figure 6.3. This nonlinearity may deteriorate the transient response of capacitor voltage especially when the shoot through time duty ratio is bigger than 0.4.
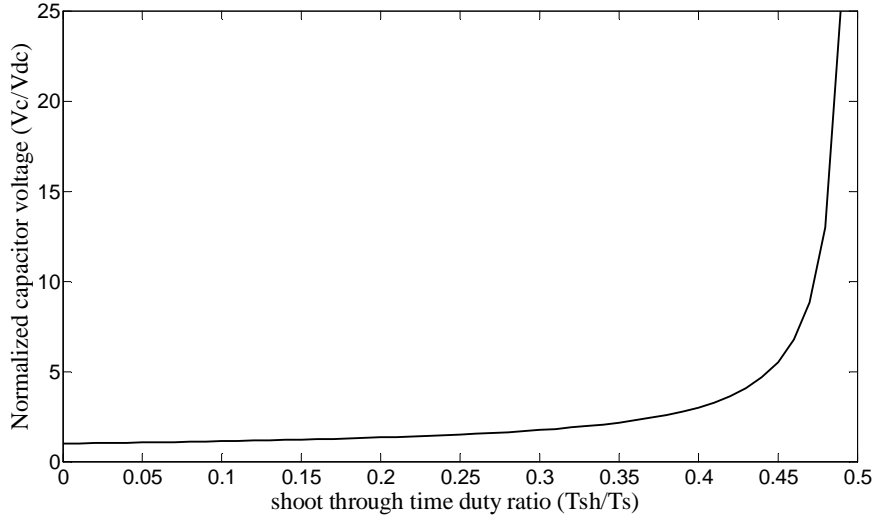
Figure 6.3. Relationship between the capacitor voltage and shoot through time

Similarly, the average dc link voltage across the three phase inverter can be found by (6.7). The average of the dc link voltage is equal to the capacitor voltage.

$$V_i = \bar{v}_i = \int_0^{} v_i dt = \frac{T_{sh}0 + T_{nsh}(2V_C - V_{DC})}{T_s} = \frac{T_s - T_{sh}}{T_s - 2T_{sh}} V_{DC} = V_C \tag{6.7}$$

It can be understood from (6.3) and (6.4), the dc-link voltage of the inverter has a pulsating nature. The peak value of the pulsating dc-link voltage is expressed in (6.4) and it can be rewritten in steady state as given by (6.8).

$$\widehat{v}_i = V_C - v_L = \frac{T_s}{T_s - 2T_{sh}} V_{DC} = B.V_{DC} \tag{6.8}$$

Notice that, the boost factor denoted by B in equation (6.8) is always bigger than 1 and can take any value between one and infinity.

6.2 Improved Z-Source Converter

In traditional type of Z-source inverter, at start-up, the capacitors are charged to half of the input dc voltage over the free-wheeling diodes or snubbers of IGBTs immediately. This phenomenon results in surge current and voltage in the filter inductors as shown in Figure 6.4 by using Matlab/Simulink.

70
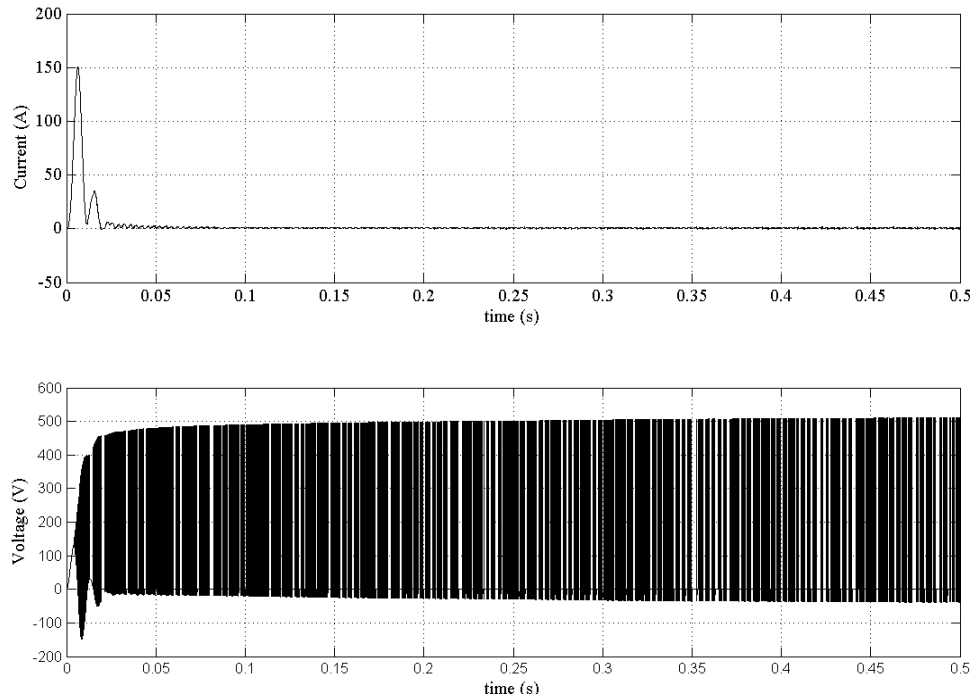
Figure 6.4. Current and voltage waveforms of an inductor with traditional topology

These problems can be overcome using series ZSI which is proposed in [91]. The modified topology is given in Figure 6.5 in which the X-shaped LC network is connected in series with dc voltage supply and the three-phase inverter.
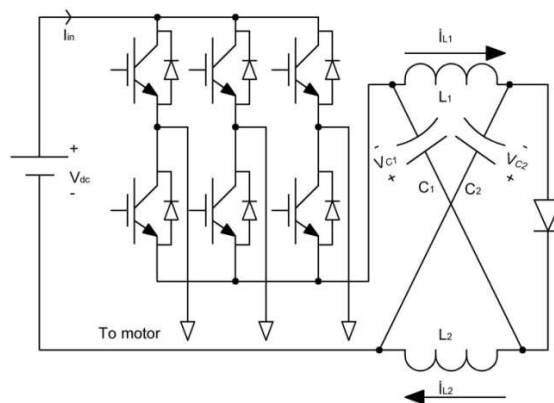
Figure 6.5. Improved Z-source inverter [91]

With the modified topology, the surge current through the filter inductor is obtained by using Matlab/Simulink as shown in Figure 6.6. Obviously, it is considerably smaller than the one with the traditional topology.

71
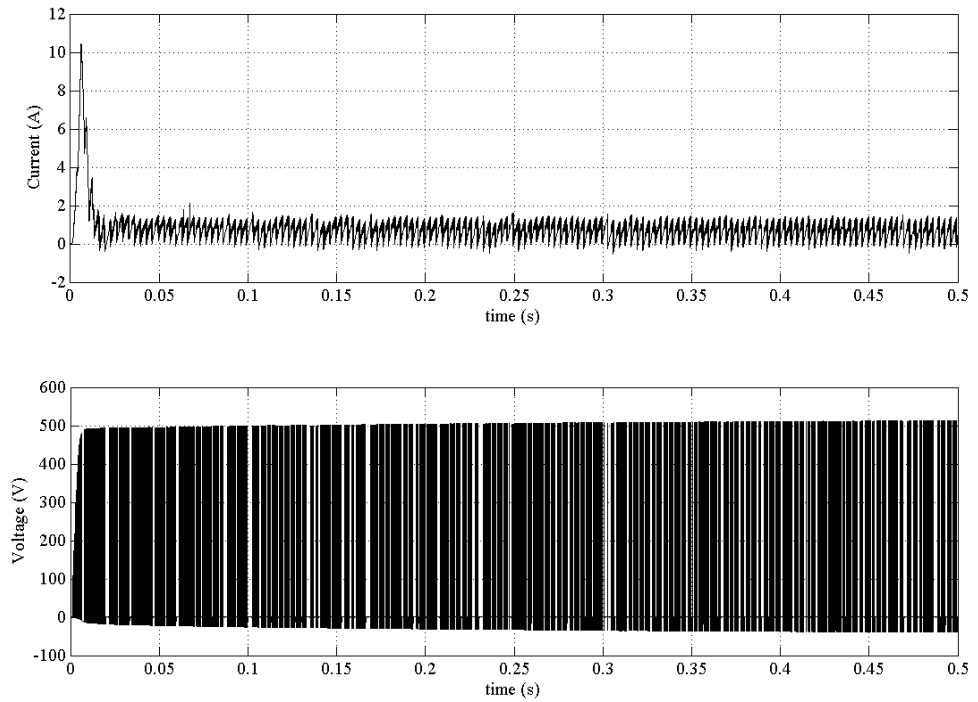
Figure 6.6. Current and voltage waveforms of an inductor with modified topology

In principle, the improved Z-source inverter has also two operation modes; the non-shoot through mode and the shoot-through mode as shown in Figure 6.7.
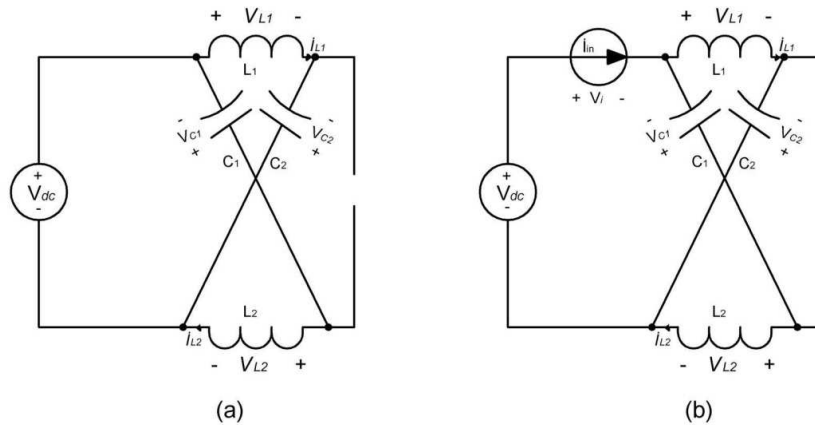
Figure 6.7. Equivalent circuit of improved Z-source inverter [91]
(a) shoot-through mode. (b) non-shoot-through mode.

In the shoot through mode, the diode is open circuited, the inductors are charged and the capacitors are discharged.

$$v_L = V_C + V_{DC} \qquad i_C = i_L \quad i_{in} = 2i_L \quad v_i = 0$$

(6.9)

When in the non-shoot through mode, the energy is transferred between the dc supply and the load, the inductors are discharged and the capacitors are charged.

$$v_L = -V_C \qquad v_i = V_{DC} - 2v_L = V_{DC} + 2V_C$$

(6.10)

Assuming sinusoidal steady state conditions, the inductor and capacitor voltages are derived as in (6.11) and (6.12), respectively.

$$V_L = \bar{v}_L = \int_0^T v_L dt = \frac{T_{sh}(V_C + V_{DC}) + T_{nsh}(-V_C)}{T_s} = 0$$

(6.11)

$$V_C = \frac{T_{sh}}{T_s - 2T_{sh}} V_{DC}$$

(6.12)

As can be understood from equation (6.12), the steady state capacitor voltage is less than the the capacitor voltage with the traditional ZSI. Furthermore, it is zero when the shoot through time is zero. Figure 6.8 shows the ratio of the capacitor voltage to the dc supply voltage with respect to the shoot through duty ratio for both topologies.
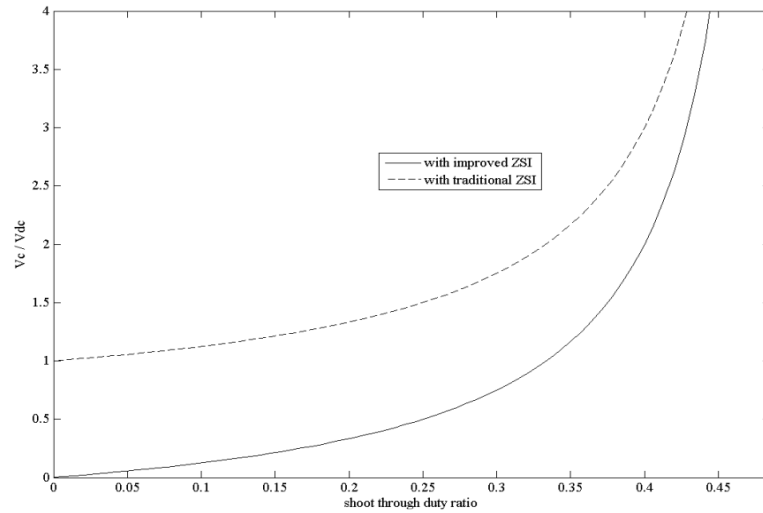
Figure 6.8. The ratio of the capacitor voltage to the dc supply voltage with respect to the shoot through duty ratio for both topologies

With the improved topology, the capacitor voltage stress is less than the traditional one as expected. Notice that, the boost factor denoted by B in equation (6.13) is always bigger than 1 as in the case of traditional topology.

$$\widehat{v}_i = V_{DC} + 2V_C = \frac{T_s}{T_s - 2T_{sh}} V_{DC} = B.V_{DC}$$

<div align="right">(6.13)</div>

The modulation scheme and the voltage boost capability are the same with the traditional topology but with reduced cost due to low voltage stress on the capacitors and lower inrush current.

6.3 State-Space Model of Improved ZSI

A state –space averaging technique is widely used in modeling of power converters. Since power converters are high frequency switching circuits, in a well-designed converter operating in Continuous Conduction Mode (CCM), the switching ripple is low and the switching frequency is much higher than the natural frequencies of the converter.

Hence, a possible simplification of a power converter model could be obtained by ignoring the switching ripple and averaging the circuit waveforms over the switching period.

For a z-source inverter operating in a continuous conduction mode, there are two circuit states one state corresponds to a shoot-through state and the other one to non-soot through state. During each state, the linear circuit is described by means of a state vector consisting of the inductor current and the capacitor voltage. Equations (6.14) and (6.15) constitute the state space model of the improved z-source inverter.

$$\begin{bmatrix} L1 & 0 & 0 & 0 & 0 \\ 0 & L2 & 0 & 0 & 0 \\ 0 & 0 & C1 & 0 & 0 \\ 0 & 0 & 0 & C2 & 0 \\ 0 & 0 & 0 & 0 & Ll \end{bmatrix} \begin{bmatrix} \dot{i}_{L1} \\ \dot{i}_{L2} \\ \dot{v}_{C1} \\ \dot{v}_{C2} \\ \dot{i}_{in} \end{bmatrix} = \begin{bmatrix} 0 & 0 & 0 & 1 & 0 \\ 0 & 0 & 1 & 0 & 0 \\ -1 & 0 & 0 & 0 & 0 \\ 0 & -1 & 0 & 0 & 0 \\ 0 & 0 & 0 & 0 & -Rl \end{bmatrix} \begin{bmatrix} i_{L1} \\ i_{L2} \\ v_{C1} \\ v_{C2} \\ i_{in} \end{bmatrix} + \begin{bmatrix} 1 \\ 1 \\ 0 \\ 0 \\ 0 \end{bmatrix} V_{DC}$$

$$K\dot{x}(t) = A_1 x(t) + B_1 u(t)$$

<div align="right">(6.14)</div>

$$\begin{bmatrix} L1 & 0 & 0 & 0 & 0 \\ 0 & L2 & 0 & 0 & 0 \\ 0 & 0 & C1 & 0 & 0 \\ 0 & 0 & 0 & C2 & 0 \\ 0 & 0 & 0 & 0 & Ll \end{bmatrix} \begin{bmatrix} \dot{i}_{L1} \\ \dot{i}_{L2} \\ \dot{v}_{C1} \\ \dot{v}_{C2} \\ \dot{i}_{in} \end{bmatrix} = \begin{bmatrix} 0 & 0 & -1 & 0 & 0 \\ 0 & 0 & 0 & -1 & 0 \\ 1 & 0 & 0 & 0 & -1 \\ 0 & 1 & 0 & 0 & -1 \\ 0 & 0 & 1 & 1 & -Rl \end{bmatrix} \begin{bmatrix} i_{L1} \\ i_{L2} \\ v_{C1} \\ v_{C2} \\ i_{in} \end{bmatrix} + \begin{bmatrix} 0 \\ 0 \\ 0 \\ 0 \\ 1 \end{bmatrix} V_{DC}$$

$$K\,\dot{x}(t) = A_2 x(t) + B_2 u(t) \tag{6.15}$$

Using the state space model, the model can be averaged over the switching cycle provided that the natural frequencies of the converter are much slower than the switching frequency. This is called the state space averaging and the results of it are the state space equations of the equilibrium (or steady state) and the AC small signal model [92]. The state space averaged model that describes the converter in equilibrium is given in (6.16).

$$0 = A\,X + BU \tag{6.16}$$

where the averaged matrices are

$$A = D_{sh}A_1 + (1-D_{sh})A_2 \qquad\qquad B = D_{sh}B_1 + (1-D_{sh})B_2$$

$$\begin{bmatrix} 0 \\ 0 \\ 0 \\ 0 \\ 0 \end{bmatrix} = \begin{bmatrix} 0 & 0 & D_{sh}-1 & D_{sh} & 0 \\ 0 & 0 & D_{sh} & D_{sh}-1 & 0 \\ -2D_{sh}+1 & 0 & 0 & 0 & D_{sh}-1 \\ 0 & -2D_{sh}+1 & 0 & 0 & D_{sh}-1 \\ 0 & 0 & -D_{sh}+1 & -D_{sh}+1 & -Rl \end{bmatrix} \begin{bmatrix} i_{L1} \\ i_{L2} \\ v_{C1} \\ v_{C2} \\ i_{in} \end{bmatrix} + \begin{bmatrix} D_{sh} \\ D_{sh} \\ 0 \\ 0 \\ -D_{sh}+1 \end{bmatrix} V_{DC}$$

$$\tag{6.17}$$

The equilibrium dc components are X:equilibrium (dc) state vector, U: equilibrium (dc) input vector. Solution for X=-A^{-1}BU is given in (6.18).

$$V_C = \frac{D}{1-D}V_{DC} \qquad\qquad I_L = \left(\frac{1-D}{1-2D}\right)^2 \frac{V_{DC}}{Rl} \qquad\qquad I_l = \left(\frac{1-D}{1-2D}\right) \frac{V_{DC}}{Rl} \tag{6.18}$$

6.4 Dimensioning of Capacitors and Inductors

During the design of the z-source inverter, the determination of the inductance and capacitance values are challenging. These values should be determined according to the selected boost factor.

The purpose of the inductors is to limit current ripple through the system. During shoot-through mode, the inductor current increases during non-shoot through period it decreases. The average current through the inductor can be defined in terms of total power P and the input dc voltage as shown by (6.19).

$$I_{L,ave} = \frac{S}{V_{DC}}$$
(6.19)

For an 10KVA system with 350V input dc, the average current is about 30A. The maximum current through the inductor is maximum at shoot through. In the design procedure, 30% peak to peak current ripple through the inductors was chosen. Therefore, the allowed ripple current (Δi_L) is 9A, the maximum current through the inductor is about 35A.

Assuming the capacitance value as high enough to keep V_C as constant during changing states, the inductor value can be expressed by (6.20) in non-shoot through state in which the inductor current decreases and by (6.21) in shoot through state in which the inductor current increases.

$$L = \frac{(1 - D_{sh})V_C}{f \cdot \Delta i_L}$$
(6.20)

$$L = \frac{D_{sh}(V_C + V_{DC})}{f \cdot \Delta i_L}$$
(6.21)

where $V_C = \frac{D_{sh}}{1 - 2D_{sh}} V_{DC}$

(6.20) and (6.21) show that the current ripple is the same for both state.

With ZSI operating at 15kHz with 0.23 shoot through mode duty ratio and 350V dc input voltage, to keep the ripple less than 9A , the required inductance should be no less than (6.22).

$$L \geq \frac{D_{sh}(1 - D_{sh}) \cdot V_{DC}}{(1 - 2D_{sh}) \cdot f \cdot \Delta i_L} = 0.85mH$$

(6.22)

where f is the operating frequency of the ZSI.

The main purpose of the capacitors in the z-link is to limit voltage ripple and also absorb the current ripple. The voltage ripple across the capacitor can be roughly calculated by using (6.23).

$$\Delta V_C = \frac{\Delta t \cdot I_{L,ave}}{C}$$

(6.23)

where Δt is the shoot period.

To limit the capacitor voltage ripple to 3% at peak power, the minimum value of the required capacitance is given by

(6.24).

$$C \geq \frac{30 \cdot 0.23}{15000 \cdot 150 \cdot 3\%} = 103uF$$

(6.24)

6.5 Modulation of the Z-Source Inverter

Although other than space vector pulse-width modulation (SVPWM) techniques like sinusoidal PWM, hysteresis based modulation can be used to realize the z-source inverter modulation [87, 88], in the thesis, SVPWM is preferred because of lower harmonic content and more efficient use of supply voltage [89].

As mentioned in section 3.1, the eight inverter switching vectors, six of them called active vectors and rest of two zero vectors, are used in SVPWM. The objective of SVPWM is to approximate the reference voltage vector by a combination of these eight vectors.

To implement a SVPWM, first, the desired three phase voltages at the output of the inverter in the abc reference frame is transformed into a vector in the stationary d-q frame. In this way, it could be represented by an equivalent vector $\vec{V}_{ref}$. The mean desired reference voltage vector that is defined over a sufficiently small switching period can be considered approximately constant during the switching period (T_S) [89]. If this reference vector is defined between the vectors of V_k and V_{k+1}, the reference vector can be written in terms of these vectors and the zero vectors as given in (6.25) [89].
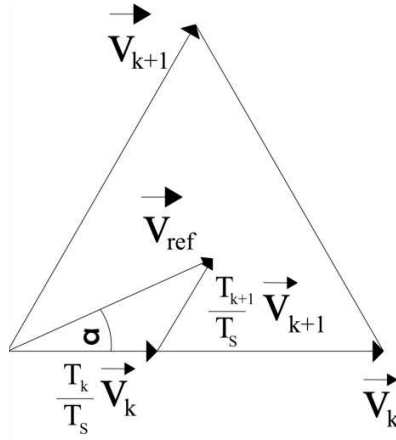
Figure 6.9. Decomposition of the reference voltage for sector k

$$\int_0^{\frac{T_S}{2}} \vec{V}_{ref}\,dt = \int_0^{\frac{T_0}{2}} \vec{V}_8\,dt + \int_{\frac{T_0}{2}}^{\frac{T_0}{2}+T_k} \vec{V}_k\,dt + \int_{\frac{T_0}{2}+T_k}^{\frac{T_0}{2}+T_k+T_{k+1}} \vec{V}_{k+1}\,dt + \int_{\frac{T_0}{2}+T_k+T_{k+1}}^{\frac{T_S}{2}} \vec{V}_7\,dt \qquad (6.25)$$

$$T_0 + T_k + T_{k+1} = \frac{T_S}{2}$$

where T_k denotes half the on-time of vector $\vec{V}_k$ and T_0 is half the zero-state time.

Since $\vec{V}_7$ and $\vec{V}_8$ are equal to zero, $\vec{V}_{ref}$ is assumed constant and $\vec{V}_k$, $\vec{V}_{k+1}$ are characteristically constant vectors, (6.25) takes the following form:

$$\vec{V}_{ref}\frac{T_S}{2} = \vec{V}_k T_k + \vec{V}_{k+1} T_{k+1} \qquad (6.26)$$

Splitting this vectorial equation (6.26) into its real and imaginary components, (6.27) is obtained.

$$\begin{pmatrix} V_{ref,d} \\ V_{ref,q} \end{pmatrix} \frac{T_s}{2} = \frac{2}{3} V_{DC} \begin{bmatrix} \cos\dfrac{(k-1)\pi}{3} & \cos\dfrac{k\pi}{3} \\ \sin\dfrac{(k-1)\pi}{3} & \sin\dfrac{k\pi}{3} \end{bmatrix} \begin{pmatrix} T_k \\ T_{k+1} \end{pmatrix} \tag{6.27}$$

By using (6.27), each switching time interval calculated as follows:

$$\begin{pmatrix} T_k \\ T_{k+1} \end{pmatrix} = \frac{\sqrt{3} T_S}{2 V_{DC}} \begin{bmatrix} \sin\dfrac{k\pi}{3} & -\cos\dfrac{k\pi}{3} \\ -\sin\dfrac{(k-1)\pi}{3} & \cos\dfrac{(k-1)\pi}{3} \end{bmatrix} \begin{pmatrix} V_{ref,d} \\ V_{ref,q} \end{pmatrix}$$

$$T_0 = \frac{T_S}{2} - T_k - T_{k+1} \tag{6.28}$$

Based on the above conventional SVPWM technique for traditional VSI, a shoot through duration should be added for ZSI. Figure 6.10 shows SVPWM patterns for both conventional VSI and ZSI, respectively [84].
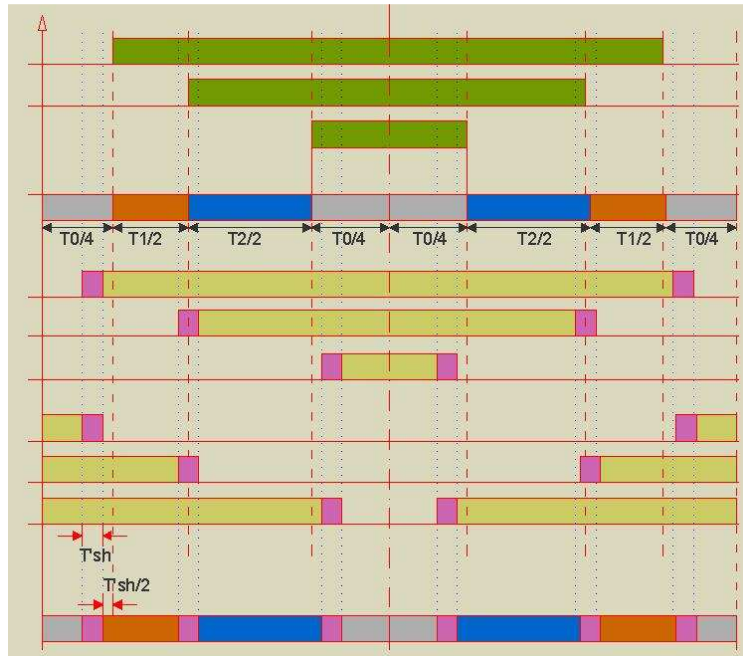
Figure 6.10. SVPWM implementation for VSI and ZSI for sector 1 [84]

As can be seen from Figure 6.5, these shoot through states are evenly and symmetrically located in each phase, without changing active state times T_k and T_{k+1}. The zero vector time limits the shoot through state time. Even if the dc link voltage can be controlled by adjusting shoot through time, the maximum shoot through time is restricted by zero vector duration depending upon the modulation index.

6.6 Matlab/Simulink Modelling of SVPWM for ZSI

The block diagram of the developed model of SVPWM for ZSI is given in Figure 6.11.
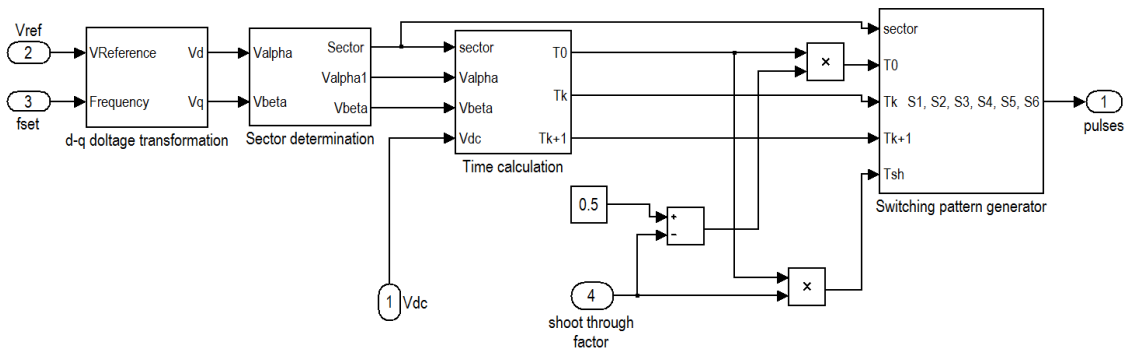
Figure 6.11. Block diagram of the developed SVPWM for ZSI

Modelling of the SVPWM technique involves three main stages:

- Determining the sector of reference space vector:
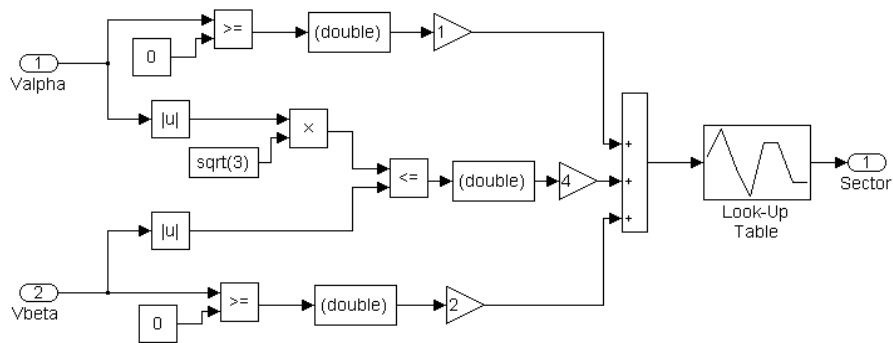
Figure 6.12. Modelling of the space vector sector determination

One of the features of the modelling shown in Figure 6.7 is the ease of sector determination which is determined by two sign check and one comparison, $V_\alpha \overset{?}{\geq} 0$, $V_\beta \overset{?}{\geq}$ 0 and $\sqrt{3}|V_\alpha| \overset{?}{\leq} |V_\beta|$. The obtained numerical values are stored in look-up table to find the sector number.

- Calculating the time intervals:

By using (6.28), the necessary time intervals are calculated as shown in Figure 6.13. The detection of a reference vector outside the hexagon is also done by checking the sum of T_k and T_{k+1}. If the sum is greater than the half of the switching period then the reference vector must be scaled back to fit within the hexagon.
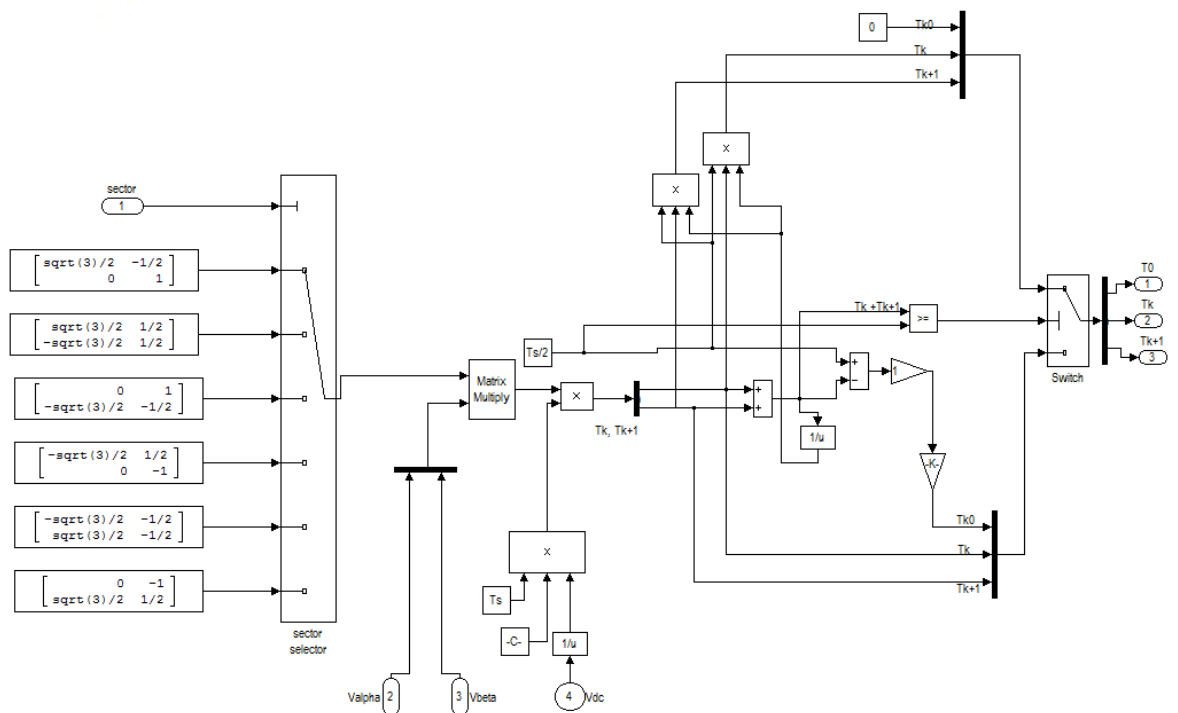
Figure 6.13. Modeling of finding time intervals

- Switching pattern generator:

The switching pattern of SVPWM of ZSI is generated by using the Table 6.1 [84]. Note that, when the shoot through time duration (Tsh) is equal to zero, the switching time durations are the same as that for the traditional VSI.

Table 6.1. Switching time durations in each sector

Sector	S1, S3, S5	S2, S4, S6
1	S1=T1+T2+ Tsh +T0/2 S3= T2+ T0/2 S5= T0/2-Tsh	S4= T0/2 S6=T1+ Tsh+T0/2 S2=T1+T2+2Tsh+ T0/2
2	S1= T2+T0/2 S3= T2+T3+Tsh+ T0/2 S5= T0/2-Tsh	S4= T3+Tsh+T0/2 S6= T0/2 S2=T2+T3+2Tsh+ T0/2
3	S1= T0/2-Tsh S3= T3+T4+Tsh+ T0/2 S5= T3+T0/2	S4= T3+T4+2Tsh+ T0/2 S6= T0/2 S2=T3+Tsh+ T0/2
4	S1= T0/2-Tsh S3= T4+ T0/2 S5= T4+T5+Tsh+T0/2	S4= T4+T5+2Tsh+ T0/2 S6= T5+Tsh+T0/2 S2= T0/2
5	S1= T6+T0/2 S3= T0/2-Tsh S5= T5+T6+Tsh+T0/2	S4= T5+Tsh+ T0/2 S6= T5+T6+2Tsh+T0/2 S2= T0/2
6	S1= T6+T1+Tsh+ T0/2 S3= T0/2-Tsh S5= T6+T0/2	S4= T0/2 S6 = T6+T1+2Tsh+T0/2 S2= T1+Tsh+T0/2

The developed model for this part is given in Figure 6.14.
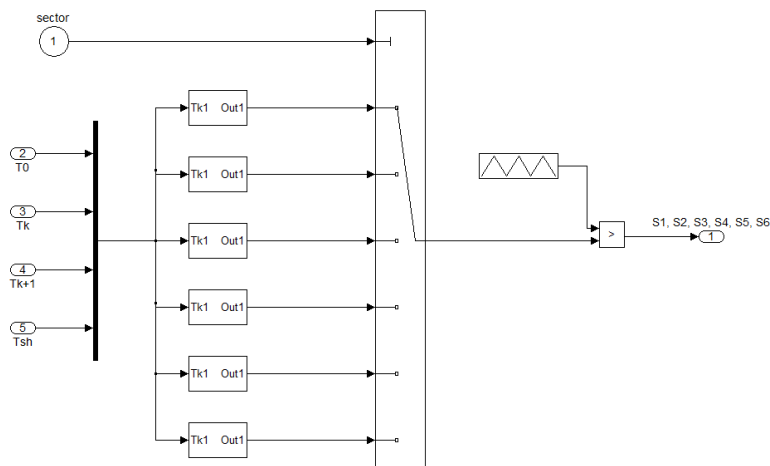
Figure 6.14. PWM generation

6.7 Simulation Results

In order to verify the boosting performance of the ZSI, simulation study using Matlab/Simulink is carried out. The applied control method is based on measuring the capacitor voltage which equals to the average value of the inverter input voltage, and from this measurement estimation of the necessary boost ratio [90]. The simulated system consists of a dc voltage source, a diode, three-phase z-source inverter and a LIM as shown in Figure 6.15 and the system parameters are given in Table 6.2.
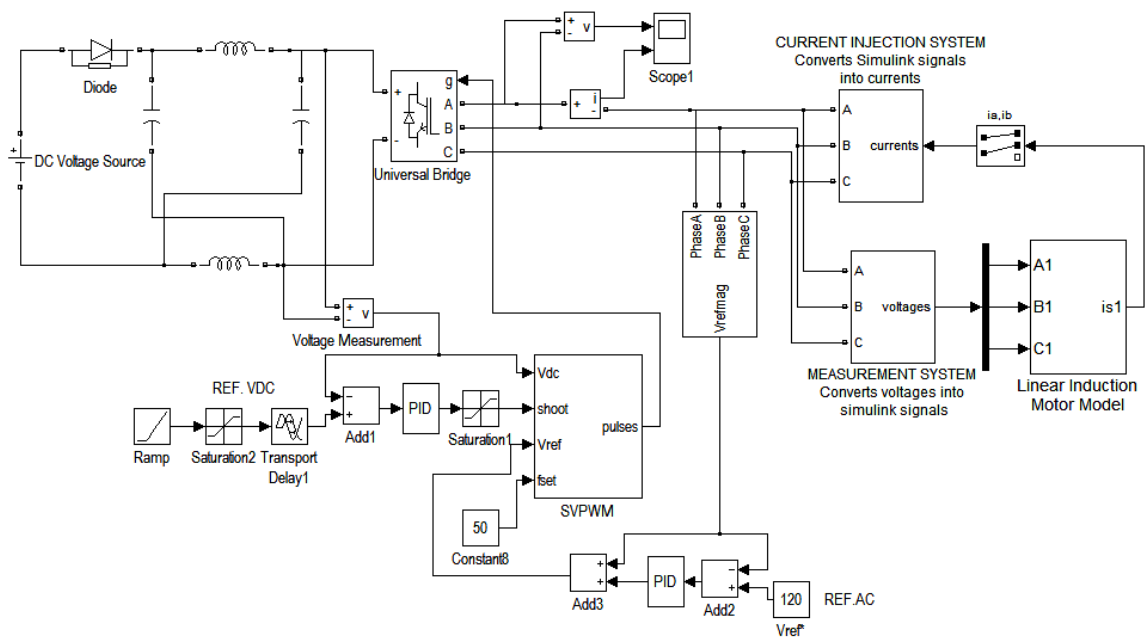
Figure 6.15. Matlab/Simulink block diagram for voltage control of ZSI

Table 6.2. System parameters for simulation

DC supply voltage	400V
L1=L2	3mH
C1=C2	2250μF
Reference peak output voltage	120V
Sampling period	1ms

During simulation, a ramp change of capacitor voltage command is applied starting at 0.55 second from 400V to end with 700V at 0.7second. Figure 6.16 shows the transient response of the capacitor voltage with %57 boosting operation. The capacitor voltage finally reaches its desired boost value after 0.1 sec delay.
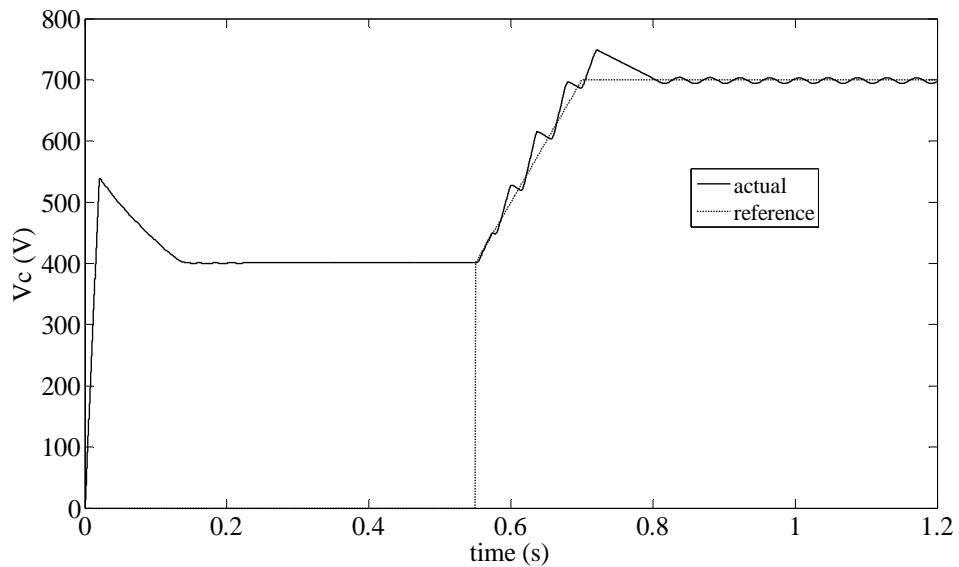
Figure 6.16. Capacitor voltage versus time

Figure 6.16 shows the transient response of the ac peak output voltage magnitude. It follows its reference value of 120V.
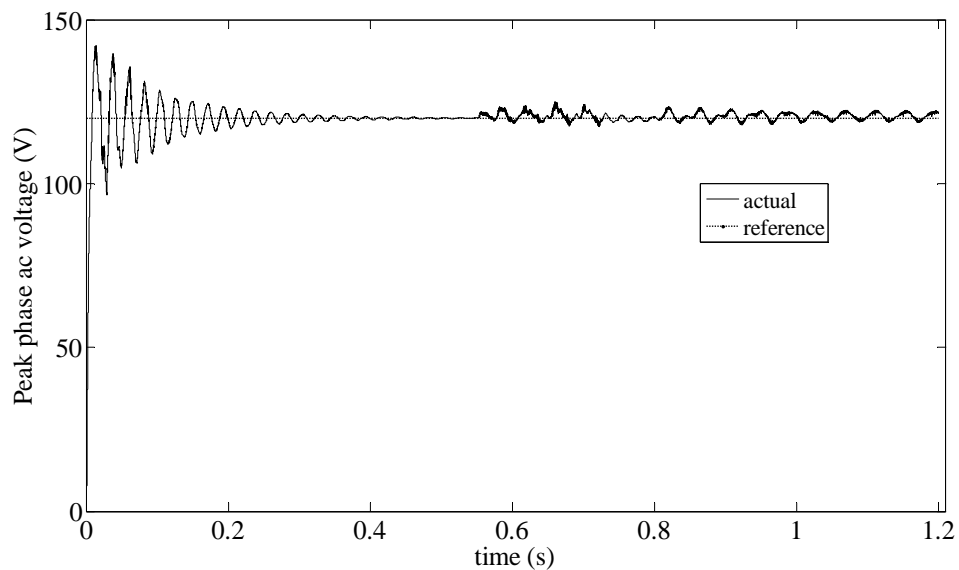
Figure 6.17. Peak phase voltage versus time

To achieve the necessary voltage boost level, the maximum shoot-through time is increased gradually starting from 0.55 sec. to 0.7 sec. As can be seen from Figure 6.18, after 0.8 sec. the maximum of the shoot through duty ratio is kept constant since reference capacitor voltage is kept constant after that period.
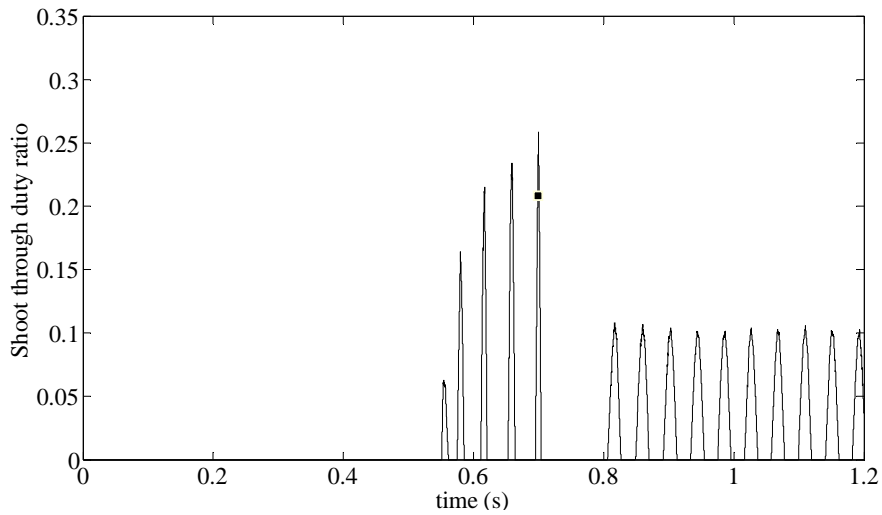
Figure 6.18. Shoot through duty ratio

Figure 6.19 shows the PWM signals of six power switches while boosting the dc link voltage.
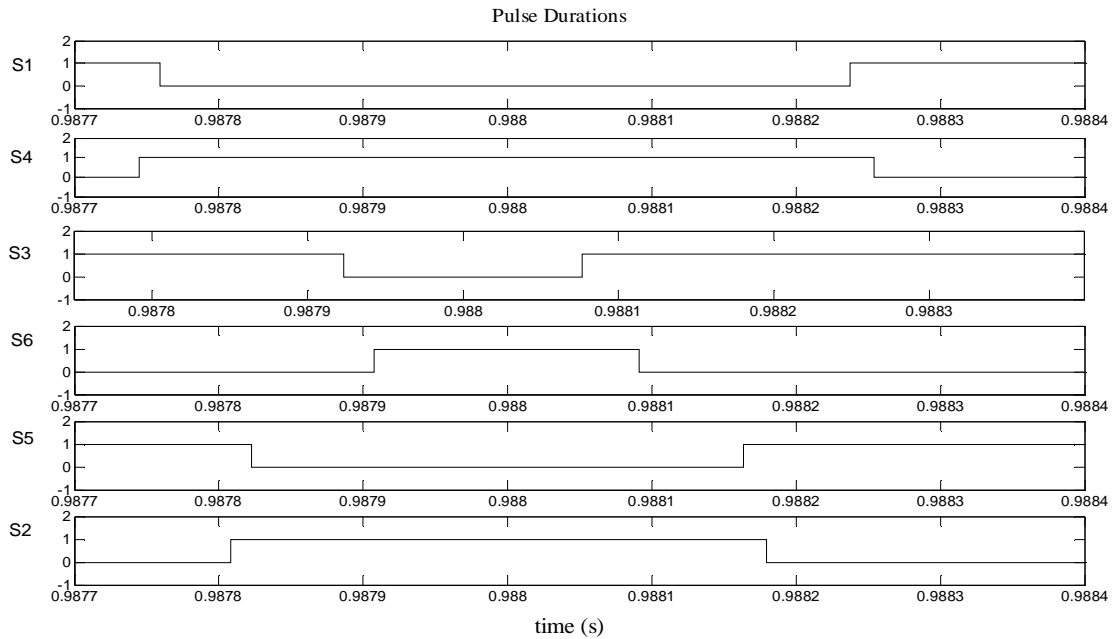
Figure 6.19. Six PWM signal during shoot-through state

85

The simulation result related to the phase A inverter current is shown in Figure 6.20. It suffers from switching ripples due to low switching frequency selection during simulation study. They are suppressed by selecting a switching frequency above 15 kHz and well designed inverter output filter.
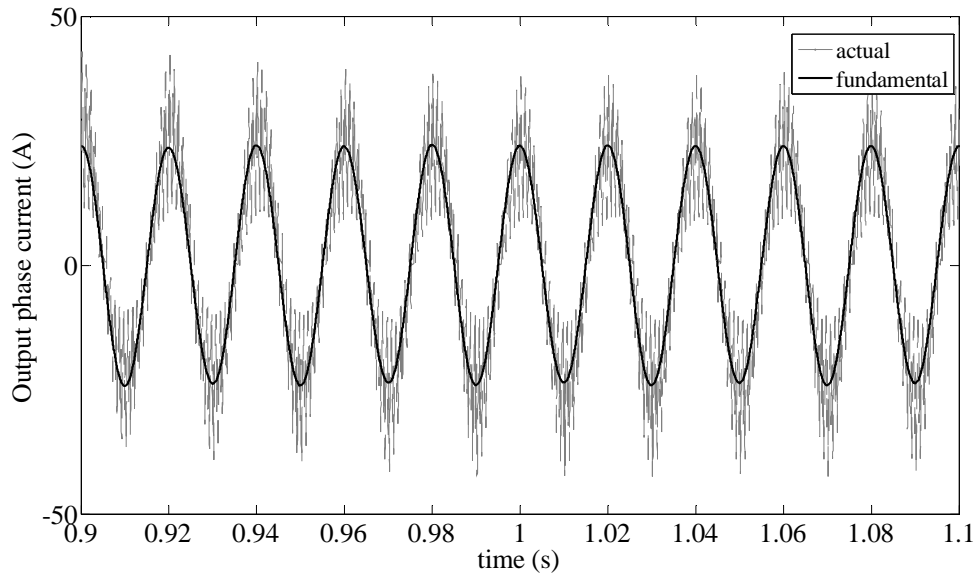
Figure 6.20. Phase A inverter current together with its fundamental part

Figure 6.21 shows the line-to-line voltage of the inverter and its fundamental component during normal duration. Notice that, the peak value of the fundamental part of the line-line voltage is square root three times of the defined reference voltage of 120V. Also the peak value of the line-line voltage is equal to dc link voltage of 400V.

Similarly, Figure 6.22 shows the the line-to-line voltage of the inverter and its fundamental component during boosting period. Again the peak value of the fundamental part of the line-line voltage is 207V as expected. However, the peak value of the line-line voltage swings between ±1000V. It is because of the pulsating nature of the input voltage of the z-source inverter satisfied by equations (6.4) and (6.5).
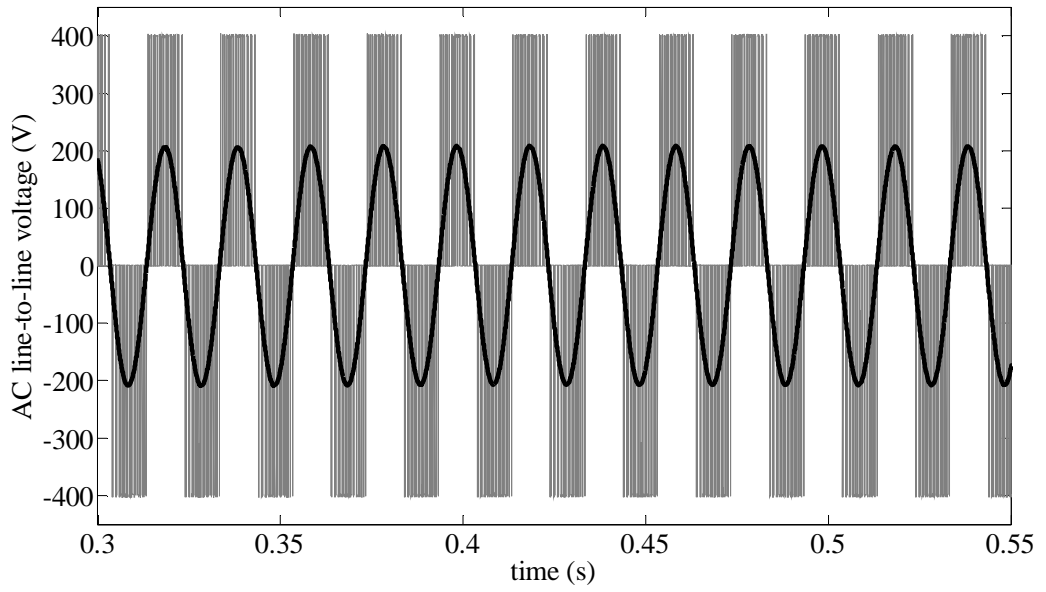
Figure 6.21. V$_{AB}$ line-to-line voltage
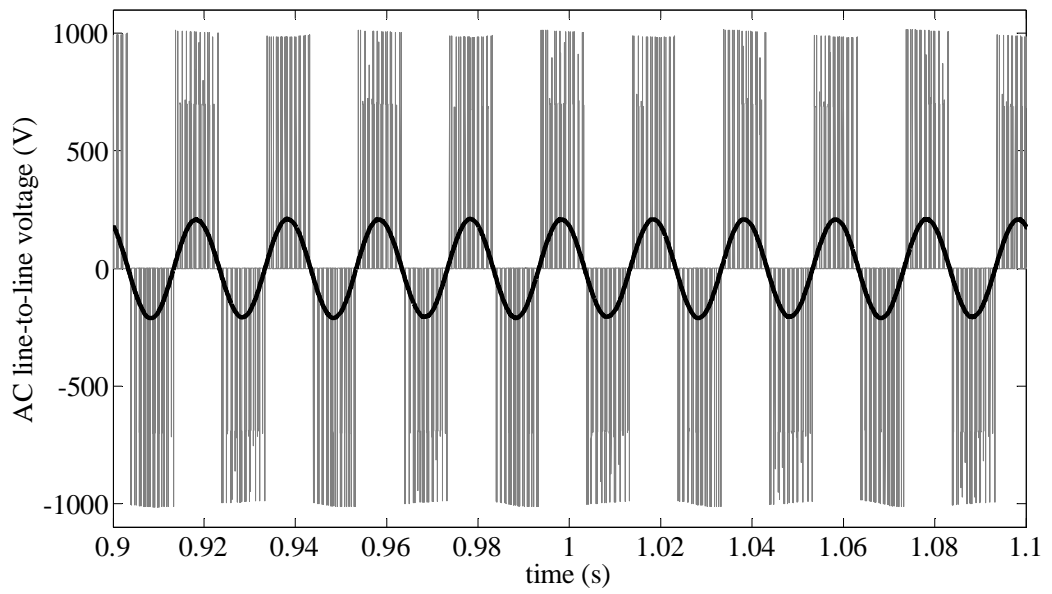
Figure 6.22. V$_{AB}$ line-to-line voltage during voltage boosting stage

87

The simulated ZSI control system follows the imposed references with acceptable performance. After doing the necessary design modifications like z-source component selections, suppressing the switching ripples and limiting ac voltage distortions, it is applied in V/Hz control of LIM using a DSP system.

6.8 Summary

This chapter is related with mathematical analysis and simulation of the z-source inverter. First, a brief introduction for the z-source inverter is given. Then, the steady state relations are derived and boost factor is given based on the simplified circuit of the z-source inverter. Next, the z-source inverter is compared to its series connected modified version. The dimensioning of the inductance and capacitance values are mentioned. Then, a modified space vector modulation technique and the related Matlab/Simulink model are explained. In modelling, the shoot-through states are distributed among the traditional space vector modulation pattern in such a way that the active states are kept the same. Following that, the simulation results obtained with z-source inverter based LIM are presented. The simulation results verified that the dc link voltage can be boosted to any value irrespective of input voltage by changing the shoot-through period of z-source inverter. It is concluded that the LIM drive is suitable for this topology as a step up converter in the dc link which converts the input dc voltage to a higher output dc voltage for three phase inverter bridge.

CHAPTER 7

INTRODUCTION TO LIM DRIVE HARDWARE

LIM drive hardware is formed by two main parts: power circuit part and interface circuits part. The interface section contains all the low voltage, high speed logic and signal conversion electronics, whereas the power section includes the high voltage and high current power semiconductors. The overall schematic diagram of the experimental set-up is given in Figure 7.1.
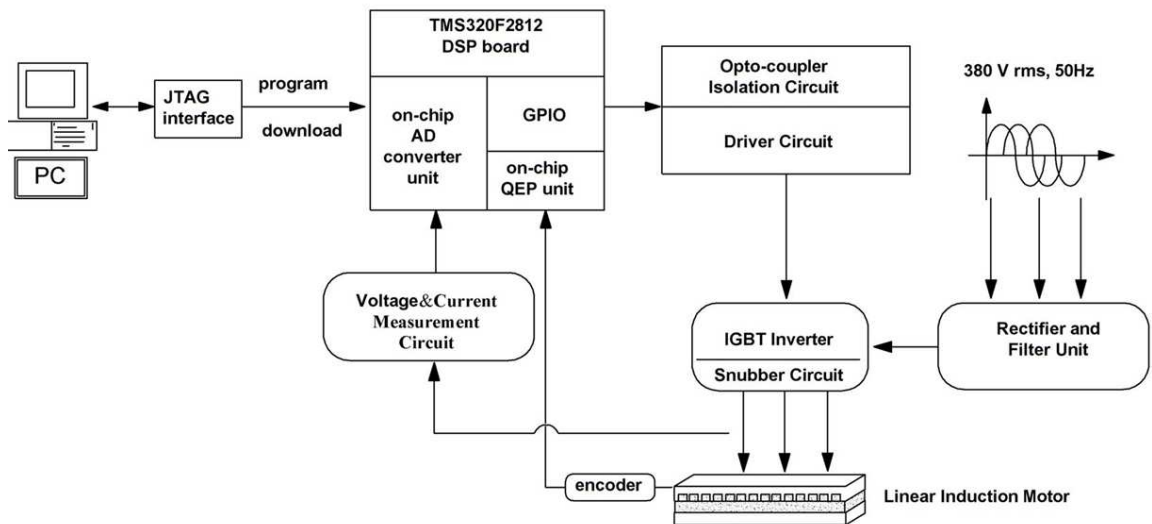
Figure 7.1. System block diagram of the experimental set-up

The interface circuit part involves the voltage and current measurement circuits, input/output optocoupler isolation circuits, gate driver circuits, fault detection circuits and digital signal processor (DSP). The power circuit part is composed of ac reactor, rectifier, its filter unit, the IGBT inverter and its snubber circuit.

The interface circuits communicate with the power circuit by the signals flowing between them through DSP.

7.1 Power Circuit Part

The power circuit part can be divided into five main groups:

- Mains choke
- Three-phase rectifier
- Dc link inrush limiter, dc link filter
- Three-phase inverter & snubber.

The overall power circuit diagram is given in Figure 7.2. From left to right, the AC line choke, the three-phase bridge rectifier, the dc link which is composed of the pre-charge resistance, inductance and capacitors, and the inverter which is composed of six IGBTs with diodes are shown.
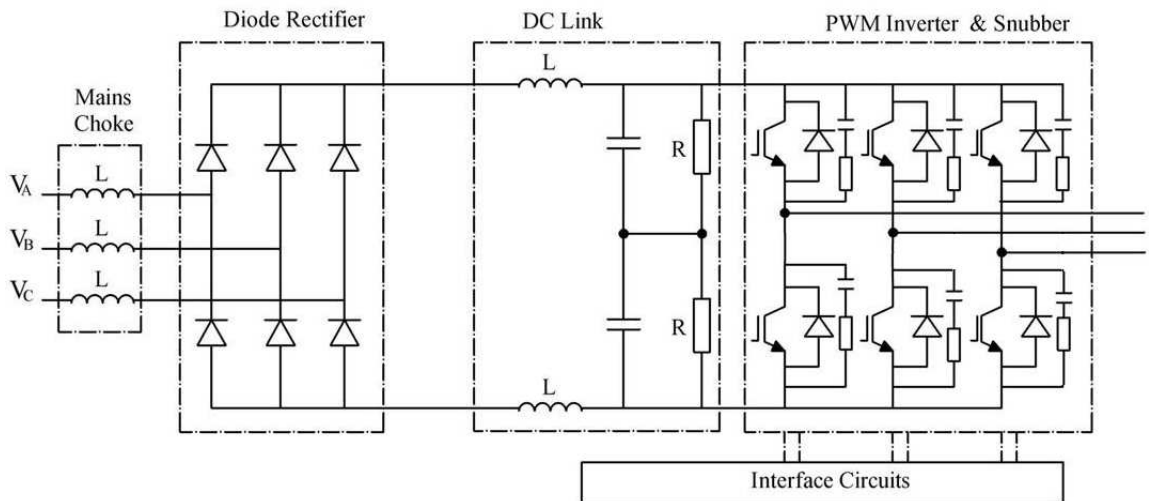
Figure 7.2. Power circuit diagram with snubber

The mains choke also called line reactor is connected in series to the mains side. It limits any current peaks caused by surge currents or switching operations. It also reduces the harmonics and increases the lifespan of the DC link capacitors hence the lifespan of the inverter. Since 3% line reactor is enough to provide line buffering [93], the commercially available the line reactor of 1.85 mH is chosen in reference to (7.1).

$$3\% \, L_{linereactor} = 0.03xL_{base} = 0.03x\frac{V^2{}_{ll}}{S}x\frac{1}{2\pi f} = \frac{(380V)^2}{(10KVA)^2 2\pi 50} = 1.38mH \tag{7.1}$$

In order to obtain DC link voltage level for the inverter, three phase line voltage, 380 Vrms is converted to DC by using standard 3-phase uncontrolled bridge rectifier with filter capacitor and inductor to eliminate its voltage and current ripples.

The mean voltage on the DC bus is 1.654 times the mains phase peak voltage. Therefore, a diode bridge rectifier will produce mean 514V DC bus voltage when the input AC line to line voltage is 380V. Uncontrolled bridge rectifier used in the power circuit of LIM drive is selected as SKD 160/12 of the Semikron Semiconductors having a rating of 1200 V, 160 A. The voltage range is chosen well above the maximum dc link voltage, since the voltage across this device during turn-off will be much higher than the DC bus voltage due to stray inductances in the circuit. This design point is specified in [93] as "..Under worst case conditions, the amplitude of the reflected voltage pulse can be 2 to 2.5 times the inverter DC bus voltage".

Before the filter unit, charging resistor should be inserted between the rectifier output and the capacitor to limit the inrush current when power is first applied [69, 94-95]. When power is switched on for the first time, the energy storage capacitors are initially fully discharged; it is practically a short circuit. Without using a current limiting circuit, the storage capacitors will draw a large amount of charging current from source which in turn may give harm to the rectifier.

There are two main approaches to solve the problem of inrush current:
- Using pre-charge resistors, with a bypass contactor, either on AC side or DC side of the AC/DC rectifier bridge
- Preferring a controlled AC/DC bridge rectifier instead of an uncontrolled ones [94].

The first method, shown in Figure 7.2, is the most common and the practical method. The resistor used to prevent the inrush current at starting is specified at the worst case conditions. The worst case occurs when the rectifier is connected to the supply at its maximum voltage. The worst-case inrush current can be estimated from (7.2) [95].

$$I_{inrush} = \frac{V_m}{R_{sec} + R_{ESR}} \tag{7.2}$$

where R_{sec} is the equivalent resistance looking from the transformer secondary and R_{ESR} is the equivalent series resistance (ESR) of the filtering capacitor.

The Maximum Allowable Surge Current (IFSM) rating of the employed diodes is 1600A for an interval of 10ms. IFSM rating of the employed diodes must be higher than the inrush current. Assuming the ESR of filtering capacitor as zero, minimum 0.6 Ω R_{inrush} resistor should be added for controlling inrush current.

The LC filter which is used after the rectifier was designed in order to minimize the ripple on DC link. Harmonic representation of rectifier with LC filter is given in Figure 7.3 where $V_n(n\omega)$ is a harmonic voltage source and n is the harmonic order of the rectifier output voltage at the filter terminals [95].
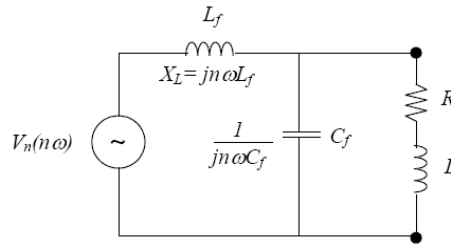
Figure 7.3. Harmonic representation of rectifier with LC filter [95]

The dominant output voltage harmonic number is 6 for three-phase bridge rectifier [95]. For good filtering, the impedance of the load should be larger in comparison to the impedance offered by the filter capacitor to the *6*-th harmonic voltage harmonic. The equation using this assumption is given in (7.3).

$$C_f = \frac{10}{6w\sqrt{R^2 + (6wL)^2}}$$

(7.3)

Using the voltage divider rule, the rms value of the *6*-th harmonic voltage across the load is given by (7.4).

$$V_{O6} = \frac{1}{(6w)^2 L_f C_f - 1} V_6 = RFxV_{DC}$$

(7.4)

where RF is the ripple factor, $V_6 \left(=1.654\dfrac{V_{peak(phase)}}{\sqrt{2}}\dfrac{2}{35} \right)$ is the dominant output harmonic voltage rms value and $V_{DC}\left(=1.654V_{peak(phase)} \right)$ is the output voltage mean value.

Assuming RF as 0.05, it is reasonable to use 1mH inductor and two capacitors connected in series each has a rating of 4700 µF, 600 V to eliminate voltage/current ripples in DC link. In addition, a resistor of 47 kΩ, 15W is connected across each capacitor to balance the voltage on them. The lower the value of the sharing resistor is the better the sharing and the smaller the discharging time of capacitors will be, but this will also increase drive losses.

The three phase inverter was designed to drive a 7kW linear induction motor with 535V DC link voltage. Hence the maximum peak line to line voltage achievable is 535V.

Assuming motor power factor is as 0.5, the peak current is calculated in (7.5).

$$
\sqrt{3}x V_{rms(line-line)} x I_{rms(line)} x 0.5 = 7000W
$$
$$
V_{rms(line-line)} = \frac{535}{\sqrt{2}} = 378V
$$
$$
I_{line(rms)} = 21.5A
$$
$$
I_{line(peak)} = 30A \tag{7.5}
$$

In the design, the considered maximum current value that IGBT can carry is about 30 A (peak). However, the current rating was selected as 60 A because of the consideration of 100 % safety margin. This margin has been selected for considering thermal safety.

During switching of IGBTs, the stray inductances and capacitances in the circuit may cause resonances. These resonances can cause up to 100 % voltage overshoots during the worst case condition. Therefore, it is wise to select IGBT voltage ratings as 1200V.

According to mentioned demands, the co-pack IGBT with an ultra fast soft recovery diode IRGPS60B120KD is used to build the inverter. The voltage rating of this IGBT is at 1200V, while the switching frequency is up to 40 kHz.

Snubber circuit design is very important in drive system, especially for applications of high current and high stray inductances. When an IGBT is suddenly turned off, trapped energy in the stray inductance of the circuit is dissipated in the IGBT causing voltage overshoot across the switch. The magnitude of overvoltage transient is proportional to the value of the main circuit stray inductance and the rate of fall of turn-off current of IGBT. The situation gets worse for higher switching speed of IGBT. Snubber circuits can be used to protect fast switching IGBT's from the overvoltage transients. They are available in various configurations, RC snubber circuit, RCD charge-discharge snubber circuit, RCD-clamp snubber circuit as shown in Figure 7.4.a, Figure 7.4.b and Figure 7.4.c, respectively [95].
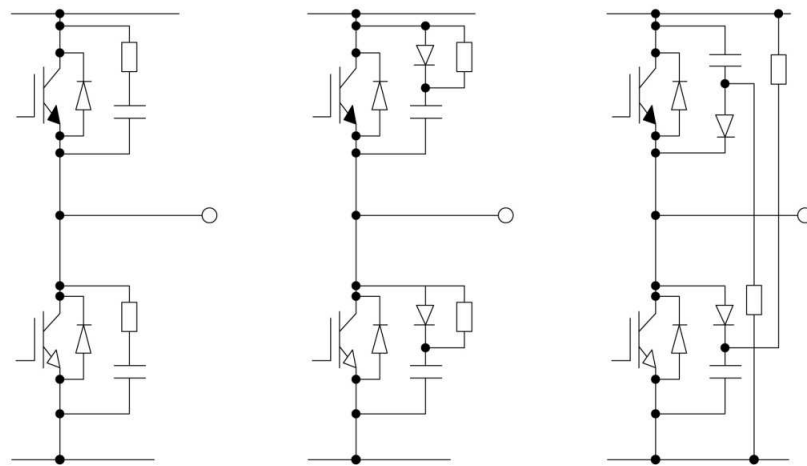
a) RC snubber circuit   b) Charge and discharge c) Discharge suppressing
                                  RCD snubber circuit   RCD snubber
                                  circuit

Figure 7.4. Snubber circuits [96]

In the developed prototype inverter, RCD-clamp snubber circuit is used since it is more suitable in high current applications [97]. At turn-off, the snubber diode is forward biased and the snubber is activated. The energy stored in stray inductance is absorbed by the snubber capacitor. The diode block oscillations and the snubber resistor consume the energy of the snubber capacitor. During turn-on the snubber capacitors are fully charged to the dc bus voltage. Their discharge path is provided through the free-wheeling diode, IGBT and the snubber resistor.

Care should be taken to choose the appropriate value of R and C to optimize the snubber performance. Normally, the calculation of R and C should be based on the property of the physical circuit. The energy stored in the stray inductance should be absorbed in the snubber capacitor by (7.6).

$$\frac{1}{2}L_{stray}i^2 \leq \frac{1}{2}C_s v^2 \tag{7.6}$$

The snubber capacitor computation was based on an initial estimation value of circuit stray inductance as 250nH, an acceptable overvoltage fluctuation as 22V, peak current as 30A as shown in (7.7).

$$C_s = \frac{L_{stray}}{\Delta V_{dc}^2}I_p^2 = \frac{250.10^{-9}.30^2}{22^2} \approx 0.47\,\mu F \tag{7.7}$$

As C_s larger, the peak power and the switching loss will be lower. However, larger C_s causes greater loss on the snubber resistor, since the energy stored in the snubber capacitor should be discharged over a snubber resistor. Another criterion is the time constant produced by the snubber capacitor with the snubber resistor. The RC time constant of the snubber should be small compared to the switching period but long compared to the voltage rise time. Given the time constant of the snubber is equal to (R_sxC_s) and the initial capacitor voltage is equal to V_{dc}, the voltage must fall to 0.1V dc within the time period ton [97] as shown in (7.8).

$$t_{on} > 2.3R_s C_s \tag{7.8}$$

RC time constant should be at least 1/3 of the switching cycle ($\tau = T/3 = 1/3f$). A smaller value of the resistance requires a higher withstanding power but serves a faster discharge and a more effective snubber. If the snubber resistor is chosen as too low, the snubber circuit current will oscillate and the peak current of IGBT at turn-off will increase. Rs calculation is given in (7.9).

$$R_s = \frac{1}{6.C_s.f_{sw}} = 47\,ohm \tag{7.9}$$

where f_{sw}=20kHz and C_s=470nF

Irrespective of the resistance, the power dissipation loss P_{RS} is calculated as follows.

$$P_{Rs} = \frac{1}{2}LI_p^{\,2}f_{sw} = \frac{1}{2}250.10^{-9}.30^2.20.10^3 = 2.25W \qquad (7.10)$$

The designed snubber circuit schematic is given in Figure 7.5.
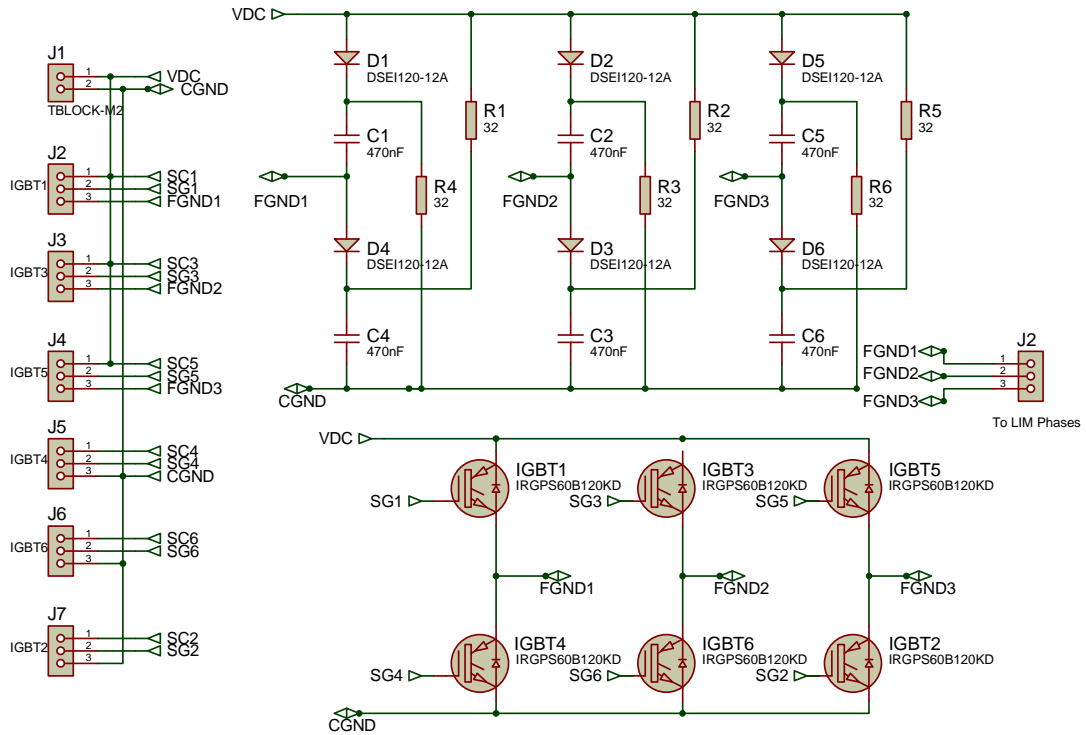
Figure 7.5. The designed snubber circuit

The chosen snubber diode has a low transient forward voltage, short reverse recovery time and a soft recovery.

The leads in the DC-link between the input filter capacitor and the power semiconductor devices have stray inductances. These inductances may cause voltage spikes on the power semiconductors and huge peak output currents especially at turn-off of IGBTs. To reduce this stray inductance, connections between the inverter and the dc link should be as close as possible.

7.2 Interface Circuits Part

The main purpose of the interface circuits is to produce the gate signals (PWM) which are required for controlling IGBTs in the power circuit. The main part of interface circuits is the software which is embedded into the DSP microcontroller. The interface part of LIM drive follows the primary currents and voltages of LIM, dc link voltages and currents, fault signals from protection cards and finally motor speed continuously.

It is developed in six main stages as given in the following:

- Measurement and signal conditioning circuits,
- Fault detection circuits,
- Gate drive circuit,
- Input/output opto-coupler isolation circuits,
- Power supply circuits.
- DSP board, using TMS320F2812 DSP Controller,
- Embedded control software running on TMS320F2812 DSP controller, using code composer studio.

7.2.1 Measurement and signal conditioning circuit

The high accuracy current and voltage measurement has primary importance for acceptable performance of the drive control system. However, the sensing techniques not only pick up the measurements but also the noise of the power system. Therefore, proper signal conditioning techniques must be applied to alleviate the noise and high frequency interference inherent in raw measurements. Signal conditioning is further necessary for filtering non-electrical signals coming from the environment, mainly switching action of IGBTs in the sensed current and voltage signals as mentioned before.

Furthermore, since the voltage range of the analog-to-digital converters in ezDSP TMS320F2812 is between 0 to 3 V, signal scaling and shifting circuit is also necessary.

According to the Nyquist's Sampling Theorem, in order to obtain a correct and unique digital representation of sampled signals, the maximum frequency of the analog signal

must be less than half of the sampling rate. Failure to satisfy this requirement will result in aliasing of higher frequency components, meaning that these components will appear to have frequencies lower than their true values. Therefore, it is necessary to pass the signal of interest through a proper low-pass filter which is tuned for a cut-off around maximum half of the sampling frequency. This operation eliminates the signal aliasing phenomenon. For getting more signal information, a wider bandwidth of anti-aliasing filter is preferred. These filters are placed at the beginning of the signal conditioning board.

In the developed hardware set-up, the analog voltage and current signals measurement circuits were developed. Each circuit has an anti-aliasing filter. In the following sections, the hardware platforms for the current and voltage measurements are described.

7.2.1.1 Current measurement circuit

Three techniques are used commonly for current sensing: shunt resistors, current transformers and Hall Effect sensors. The considered criterions for choosing current sensor should be galvanic isolation, accuracy, ease of implementation and robustness [98].

Shunt resistor is a small value resistor inserted in series with the specified current loop. Since the load current flows through the resistor, according to the ohm's law, a voltage drop proportional to the current value will be generated. Given the resistance known, after we measure the voltage drop, we can get the sensed current value. The merits of shunt resistor are simple structure and low cost. But it suffers from the absence of galvanic isolation. Moreover, the current shunt resistor produces small voltages. It always needs an amplifier to magnify this voltage signal, which makes this technique more complicated.

Current transformers are relatively simple to implement. The primary current will generate a magnetic field that is coupled into a secondary coil by Faraday's Law. The magnitude of the secondary current is proportional to the number of turns in the coil, which is typically as high as >1000 A. The secondary current is then sensed through a sense resistor to convert the output into a voltage. However, in reality, a part of primary

current is used to magnetize the core. Thus less than the actual primary ampere-turns are to be transformed into the secondary ampere-turns. This introduces an error especially in the measurement of small current since a relatively large part of the current is utilized for magnetization. However, it is appropriate for large current application.

Another popular technology used in current measurement is the Hall-effect sensor. The current flowing through a semi-conductor material establishes a magnetic field in a plane perpendicular to the current, which forces the moving carriers to crowd to one side of the conductor. As a result of this crowding, a Hall voltage will develop perpendicular to both the current and the magnetic field. The main advantage of the closed-loop method is high accuracy and repeatability over a large signal range [94].
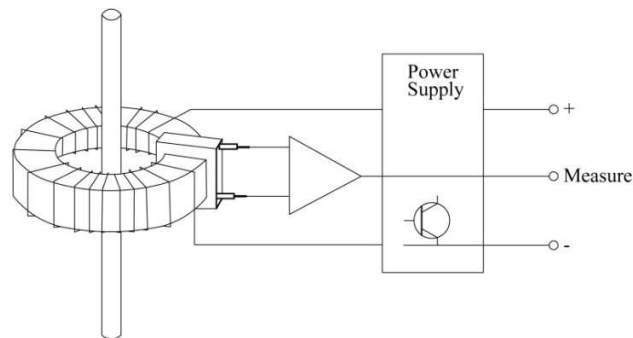
Figure 7.6. Principle of the LEM Hall effect current sensor [95]

These models also have significant power supply requirements, as the secondary winding current will be related to the maximum primary current times the turns ratio. The LEM usually requires a DC power supply of about 15 V DC in order to achieve a high rate of change of current in the secondary winding. This high *di/dt* is also necessary to maintain high bandwidth.

Among three of the current measurement methods, Hall sensor has a relatively high performance. It can provide galvanic isolation, high accuracy and ease of use.

In the thesis, Hall Effect sensors LA 100-P is selected for current sensing. These sensors are capable of sensing AC, DC and mixed current waveforms. The output of these

sensors is between 0-5V and unipolar. The specifications of LA 100-P and its connection diagram is given in Table 7.1 and Figure 7.7, respectively.
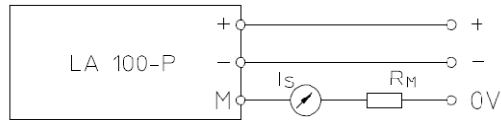
Figure 7.7. Connection diagram of current sensing circuit

Table 7.1. Specifications of the current sensor

Current Sensor LEM LA 100-P	
Primary nominal rms current	100A
Primary current measuring range	±150A
Secondary nominal rms current	50mA
Conversion ratio	1:2000
Design temperature	85°
Supply voltage	±15V
Measuring resistance (max)	102Ω

The output voltage of the Hall effect current sensor can be expressed by (7.11).

$$V_m = i_1 \frac{N_1}{N_2} Rm \tag{7.11}$$

where, i_1 is the stator current, N1 is the external turns number, 1/N2 is the internal turn ratio and Rm is the external measuring resistance.

The internal turn ratio for the chosen LEM is 1/2000 and the numbers of winding turns depend on the chosen LIM current range. In any case, to improve the sensitivity of the current measurement, a few numbers of turns should be passed through the Hall effect sensor, since its accuracy is maximum around the primary nominal current of the Hall sensor.

Concerning a maximum 25A LIM current flowing through the Hall Effect current sensor, four numbers of turns are to be passed through the Hall Effect sensor to improve the sensitivity of the current measurement. In this case, the induced secondary current is equal to 50mA. Then it passes through the variable resistor (Rm) of 100Ω and the output voltage is equal to ±5V which is the measure of the LIM current.

Since the ADCs on the DSP board cannot sense the negative voltage and requires signal between 0-3V, the current sensors needs extra hardware. An offset voltage is added to the AC current signals to compensate the negative parts. Later, in the software, this amount is subtracted. Furthermore, the current signals must be normalized between the 0-3V range using amplifiers before the ADCs. The zener diodes are also used to prevent burning the TMS320F2812 DSP in case of ripples in the current. All of these procedures are combined in the signal conditioning circuit before ADC unit of DSP in two parts: a filtering subcircuit and a shifting and scaling subcircuit. The shifting and scaling subcircuit scales the signals coming out of LEM unit into analog signals of level 0-3V which are required by the ADC unit of DSP. The antialiasing filter subcircuit buffers and filters the ADC from the sensing unit and minimizes the interaction between them.

In the prototype study, the anti-aliasing filter is realized by using unity gain Sallen-Key type of second order low pass filter as recommended in [99]. The circuit diagram of this filter is given in Figure 7.8.
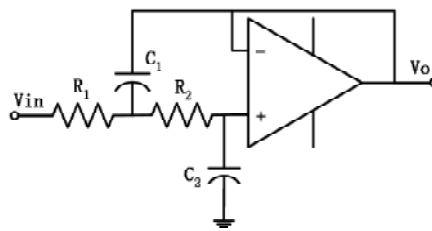
Figure 7.8. 2-pole, unity gain, Sallen-Key type low-pass filter

The operation of filter can be described in [99]. At low frequencies, where C1 and C2 appear as open circuits, the signal is buffered to the output. At high frequencies, where C1 and C2 appear as short circuits, the signal is shunted to ground at the amplifier's input, and the signal does not appear at Vo. Near the cut-off frequency, where the

impedance of C1 and C2 is on the same order as R1 and R2, positive feedback through C2 provides bandwidth enhancement of the signal.

The overall current measurement and signal conditioning circuit design is shown in Figure 7.9. First, the current signals must be filtered from the noise of the power system. Then, the resulted signals are normalized between the ±1.5V range using amplifiers. Furthermore, an offset voltage of 1.5V is added to the AC current signals to compensate the negative parts. The zener diodes 1N4728A are used to prevent current ripple which is greater than 3V before the ADC inputs including 100Ω protection resistor. All of these procedures are combined in the signal conditioning circuit before ADC unit of DSP in two parts: an antialiasing filter and isolation subcircuit, a scaling and shifting subcircuit.

The antialiasing filter component values will be calculated with using Texas Instruments FilterPro filter design program [100].
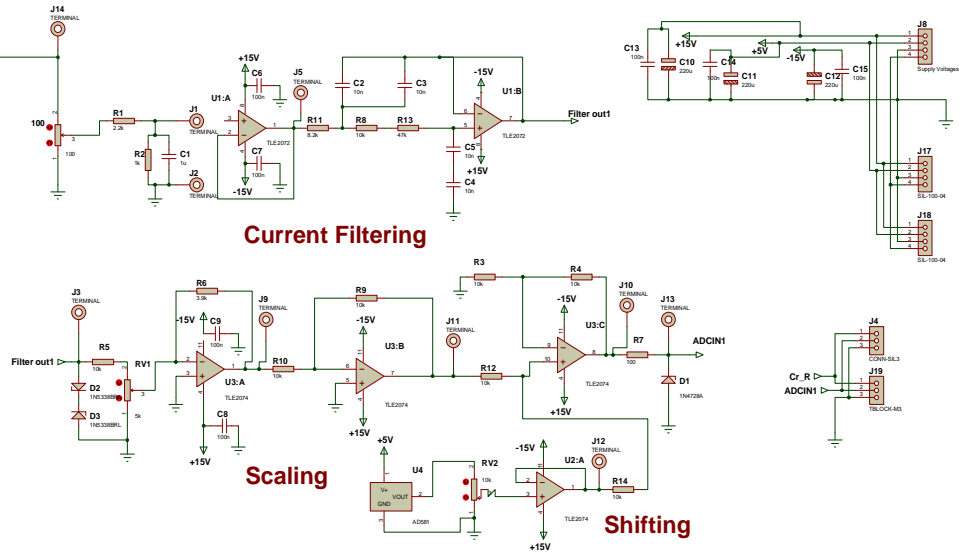
Figure 7.9. Current measurement circuit

7.2.1.2 Voltage measurement circuit

The dc link can be measured with a simple voltage divider but its accuracy may not be satisfactory. The voltage transducers also provide galvanic isolation between the high

voltage circuit and the low voltage measurement circuit. For this reason in order to get reliable voltage measurement results without any noise problems, LEM LV-25P voltage transducer will be used instead of a voltage divider as the sensing device in the study. The insulation property of the voltage sensor is quite sufficient to protect the digital circuit and low voltage analog circuit from high voltage part. The specifications of LV 25-P and its connection diagram is given in Table 7.2 and Figure 7.10, respectively.

Table 7.2. Specifications of the voltage sensor

Voltage Sensor LEM LV 25-P	
Primary nominal rms current	10mA
Primary current measuring range	±14mA
Secondary nominal rms current	25mA (max 35mA)
Conversion ratio	2500:1000
Accuracy	± 0.8 %
Supply voltage	±15V
Measuring resistance (±14mA)	100-190Ω
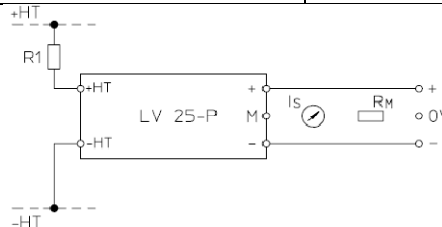
Figure 7.10. Connection diagram of voltage sensing circuit

In the Figure 7.10, R1 is the resistance necessary to convert voltage signal to a current signal, Rm is the measurement resistance. +HT, -HT entries represent the difference of the tension, i.e. signal to be measured, terminals +and – are the supply voltages and Is is the current output signal proportional to the input signal.

The input voltage range pf LV 25-P is defined as 10V to 500V. Conversion resistance R1 is calculated in (7.12) assuming maximum value of 400V for phase voltages of LIM. The chosen maximum primary current is 14mA.

$$R_1 = \frac{400V}{14mA} \qquad (7.12)$$

Considering 25% variation in voltage and compliance with a commercial value, R1 is chosen as 47 kΩ.

Rm can be calculated by using the max secondary current of 35mA and the output voltage value of ±5V as given by (7.13).

$$R_m = \frac{5V}{35mA} \qquad (7.13)$$

Rm is chosen as 150Ω which is compatible with the LV 25-P specification for measurement resistance range of 100-190 Ω. Remember that, the output voltage cannot be chosen as ±3V because of the ADC voltage specifications. Therefore, the usage of similar scaling and shifting circuit as in the current measurement is necessary before the ADC pins of TMS320F2812 DSP. The overall voltage measurement and signal conditioning circuit design is shown in Figure 7.11.
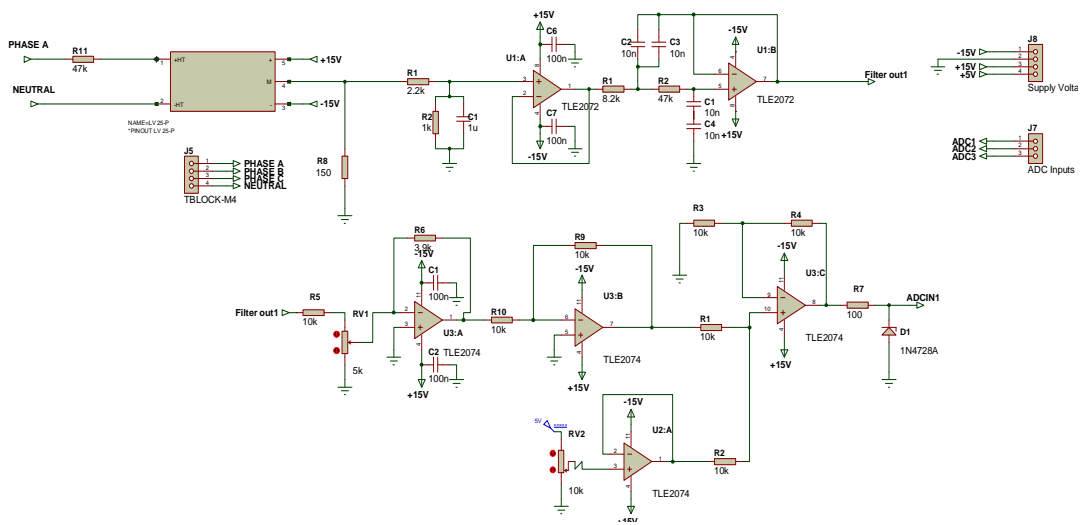
Figure 7.11. Phase voltage measurement circuit

7.2.1.3 DC link voltage measurement circuit

Each of the dc link voltage on the terminals of z-shaped LC circuit is to be measured with respect to the negative dc link by using an isolated voltage amplifier. The isolated voltage amplifier chosen is HCPL-7800A which can measure the actual high voltage and

translate it into a low level signal. According to its datasheet, it requires two isolated +5V dc voltage supplies.

The developed circuit is given in Figure 7.12. For proper operation of the HCPL-7800A, the input voltage of the isolation amplifier should be kept around 200mV range by using nine series connected 250mW resistors and one trimmer. Since the isolated amplifier has a gain of nearly eight, the output is about 1,6 V. In order to get a max 3V signal from the dc link, an additional gain stage is developed using an operational amplifier.
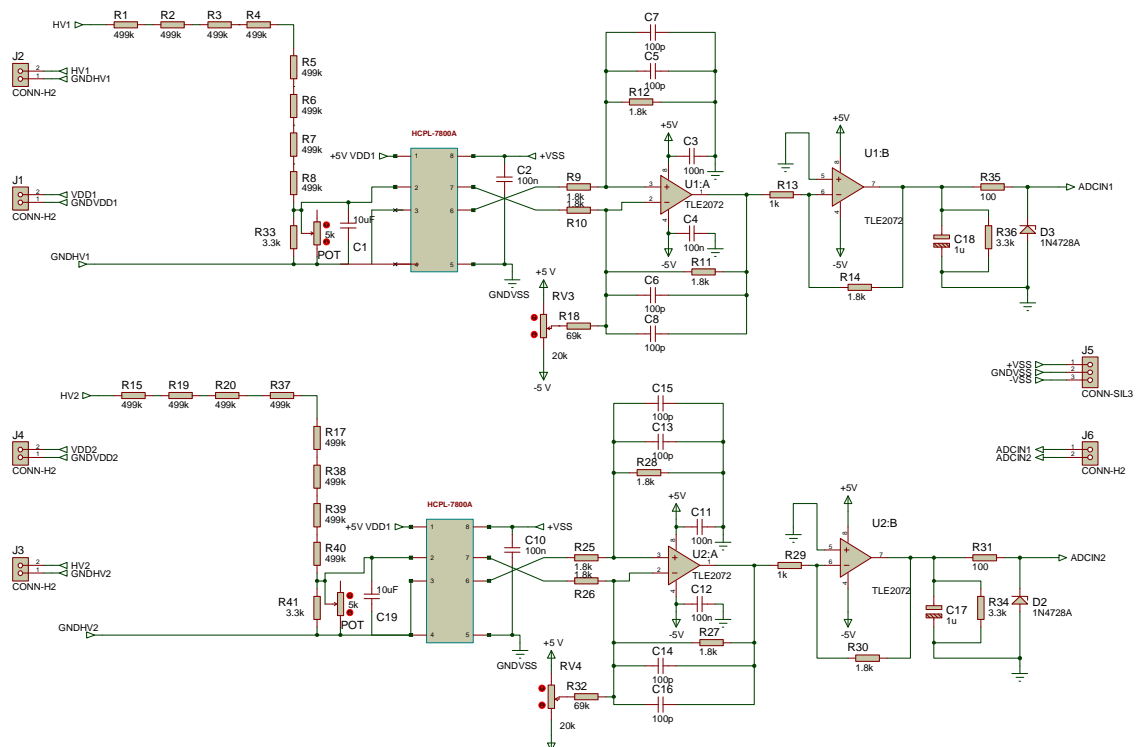
Figure 7.12. DC link voltage measurement circuit

The designed circuit was calibrated under between the 400V-800V dc voltage ranges. At first, the offset compensation was done. The dc terminals was shorted, the measured signal was adjusted to 0V by using 20kΩ trimmer. Then the short was removed and 785V was applied to the dc link and by using 5kΩ pot, the voltage signal at the input of HCPL-7800A was adjusted as 200mV.

7.2.2 Gate Drive Circuit

The gate drive circuit is the board between the PWM output isolation circuit and the inverter circuit. The main functions of this board are;

- To provide isolation in transmitting the PWM signals from DSP to the gate of all IGBTs,
- To change the level of PWM signals, provide high current, high voltage to turn on and off IGBTs quickly since PWM signals generated by DSP are at 3 V level,
- To transmit error signals from inverter to DSP board; provide short circuit protection.

Figure 7.13 illustrates a basic IGBT gate drive circuit, which converts PWM output signals into appropriate voltage and current that can drive the IGBTs reliably and efficiently. The conversion is performed by a pair of transistors connecting the IGBT's gate to the appropriate V_{on} and V_{off} voltages. For rapid turn-on and turn-off process, the applied voltages should be bipolar. The gate resistor is selected to generate a proper peak current for charging or discharging the IGBT's gate.
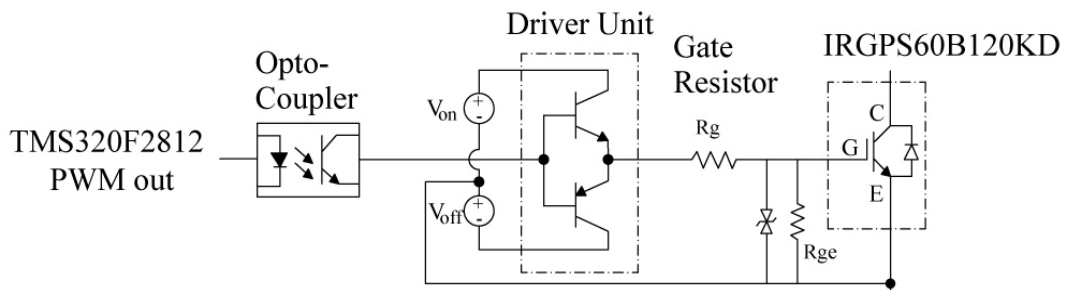
Figure 7.13. A basic date driver circuit

Gate drive circuitry and IGBTs are the source of both radiated and conducted EMI noise [94, 101]. When the upper IGBTs are turning on, the whole gate drive makes a voltage swing of DC-link voltage in a few nanoseconds. Large *dv/dt* can create significant common-mode noise currents through the parasitic capacitive coupling paths, while *di/dt* creates noise through inductive coupling paths. Therefore, in order to minimize *dv/dt* and *di/dt* propagations, several design considerations have to be taken into account. Optocouplers that isolate gate-drives from DSP show great importance in reducing

common-mode noise. It will be a good design consideration to use of an optocoupler having a common mode rejection ratio of 15000 V/us.

The designed gate drive circuit consists of two parts: The first stage consists of 6N137 optocoupler and CD74HCT04E hex schmitt inverter. 6N137 optocoupler is used to provide electrical isolation between the interface circuit and the power circuit because of its high speed and high-common mode noise rejection. CD74HCT04E hex schmitt inverter strengthens the drive current.

In the second part, the optical coupler Drive Circuit HCPL-316J is chosen as the driver of IGBT due to its functions, such as fast switch speed (500ns), optical isolation, the feedback of fault situation, wide operating voltage (15V-30V), automatic reset and automatic close down etc. In addition, it has a smaller footprint size than older drivers a 16 pins surface-mount part. The chip takes logic-level switching signals, and outputs gate signals for the power electronics devices.

According to the internal circuitry of HCPL-316J given in Appendix B, Vout is determined by VCC2 minus three diode drops. In this work, we set Vout = 18-(3x0,7) = 15,9 V and VEE = -5 V. These voltages are used to drive the IGBTs. The gate drive circuit is developed according design hints given in its datasheet. The driver circuit receives the gating signals from the DSP through output isolation circuit. The gate signals are applied to its positive gate signal input pin. Therefore, IGBT turns on only when its positive pin is at logic high, and its negative pin at logic low.

The collector-to-emitter voltage of the IGBT is monitored by DESAT pin of HCPL-316J and IGBT will be slowly turned-off if Vdesat exceeds a threshold of 7V. Correspondingly, a fault signal is propagated to the input side to notify the DSP for detected fault condition, as shown in Figure 7.14. This FAULT output remains low until the RESET is brought low.
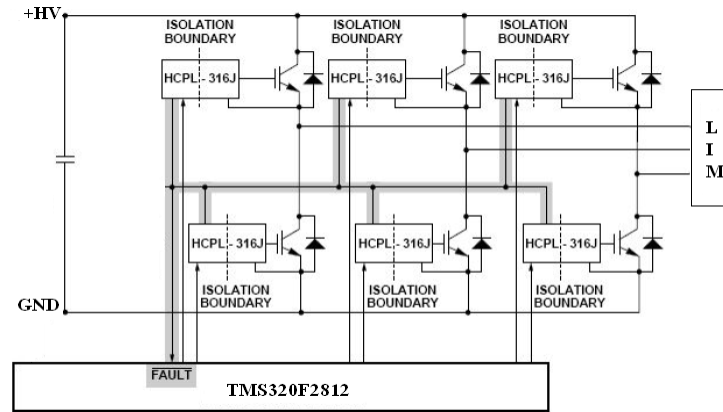
Figure 7.14. Schematic of the gate driver

The following steps are considered in IGBTs gate drive design:

- Gate resistor-Rg

The gate resistance has a significant effect on the dynamic performance of IGBTs. A smaller gate resistor charges and discharges the input capacitance of IGBT faster reducing switching times and losses. However, faster switching leads to higher *di/dt*, which leads to higher voltage spikes and oscillations on the DC bus as well as increased EMI contributions. A larger value of the gate resistance limits voltage transients and reduces the oscillation. Choosing a more accurate value is a trade off. From equation (7.14) the gate resistance value is estimated.

$$Rg \geq \frac{\left(V_{CC2} - V_{EE} - V_{OL} - 1\right)}{I_{OLpeak}} = \frac{18 - (-5) - 1.5 - 1}{2.0} = 10,25\Omega \qquad (7.14)$$

where V_{OL} is low level output voltage at the peak current of 2.5A

A larger gate drive resistor will reduce the *di/dt* of the inverter which in turn reduces the peak diode reverse recovery. However, this results in higher duty cycle loss because the device takes longer to turn on. More accurate resistance value is found by practical tests depending on the different switching frequency, switching time, slope of *dv/dt* and the parasitic components originating from the circuit layout. In the experimental study, 20Ω gate drive resistors are used.

- *Gate-Emitter resistor-R_{ge}*

Rge of 10 kΩ is installed to prevent IGBT from being destroyed if gate circuit is bad or if the gate circuit is not operating and a voltage is applied to the power circuit.

- *Gate-Emitter overvoltage protection*

The absolute maximum rating of gate-to-emitter voltage is given as ±20V for IRGPS60B120KD. Therefore zener diode protection is necessary in the case of a possibility that a voltage greater than ±20V is applied.

- *Isolated power supply*

The driver provides a bipolar output of +15/-5 V for rapid turn-on and turn-off of IGBTs. Since the potentials on the motor terminals of the inverter are floating relative the ground level, each of the upper side IGBTs need separate voltage supplies. For this reason the driver circuit card is be equipped with four dc power supply, three for upper side IGBTs and common for the lower ones.
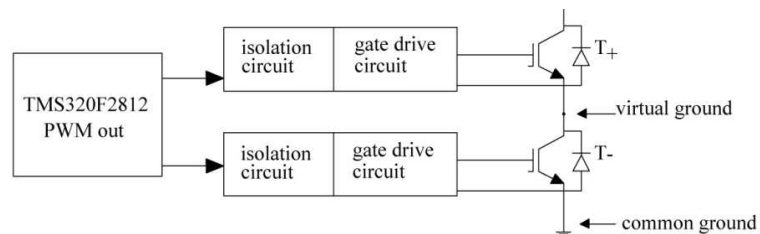
Figure 7.15. Electrical isolation between the base drive circuitry and the logic level control circuitry

- *Printed circuit board consideration*

Special attention should be given to minimize the stray inductance in the drive circuit. If the wiring between the drive circuit and the IGBT is long, the IGBT may be in a malfunction due to gate signal oscillation or induced noise. Twisted wiring is used as shown in Figure 7.16 as recommended in [69, 101,102]. The gate wiring and IGBT control circuit wiring is separated from each other as much as possible.
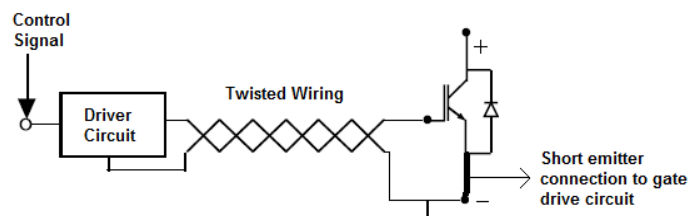
Figure 7.16. Printed circuit board considerations in connecting gate drive circuit to IGBT

The designed schematic of the gate driver part is shown in Figure 7.17. Each IGBT has its own gate drive circuit which basically consists of a single chip HCPL-316J with some external components.
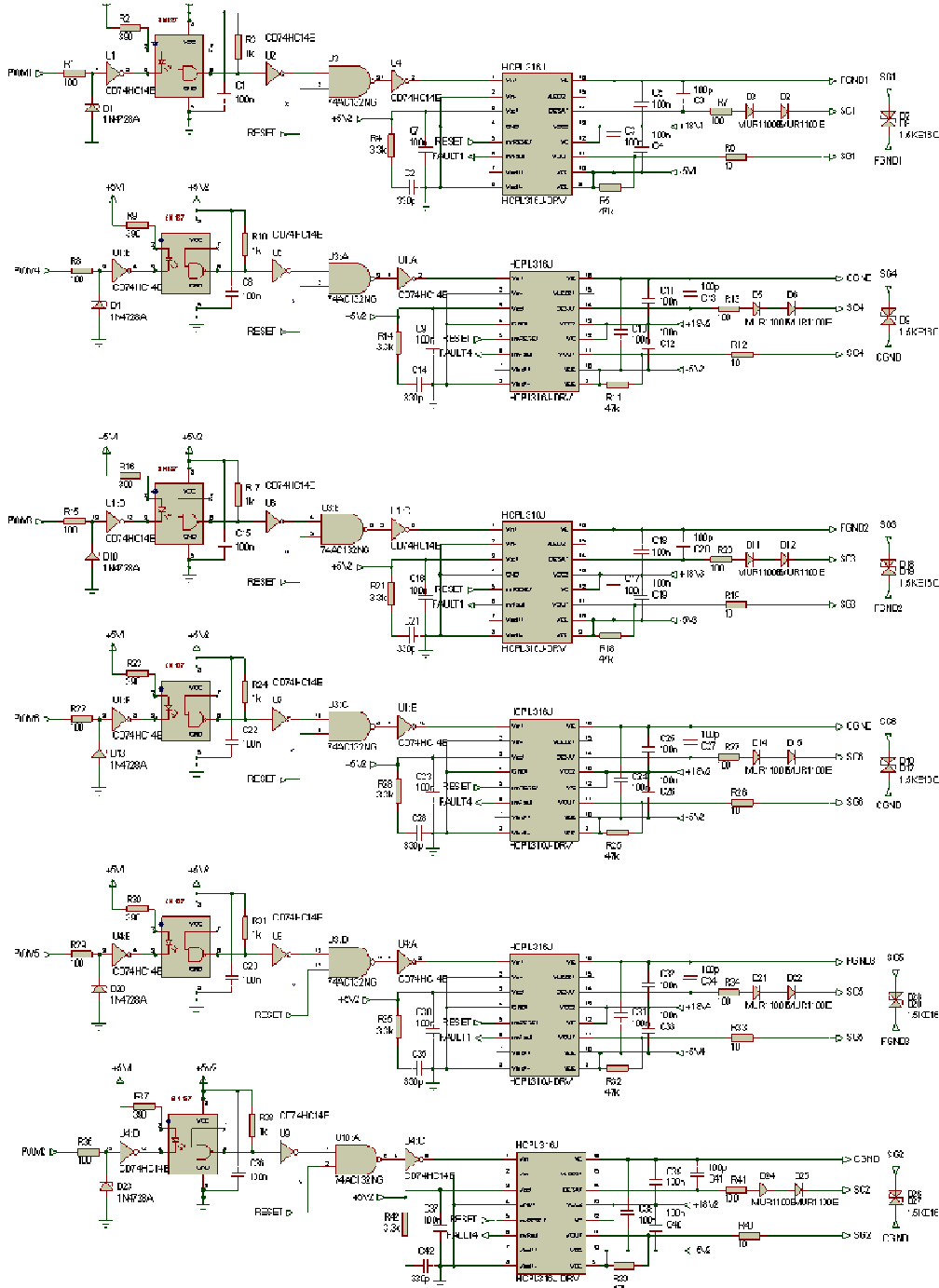
Figure 7.17. Layout of the overall gate driver circuit

7.2.3 Protection circuits

Three causes of damage to IGBTs are over current, over voltage and over temperature [103]. Therefore these three fault conditions should be monitored by using:

- Over current detection circuit
- Over voltage detection circuit
- Over temperature detection circuit

Over current and overvoltage detection circuits are used in order to detect over current and overvoltage in the three phases of the inverter and in the dc link. When a fault is detected, the priority is to turn off all of the switching devices. The second priority is to alert the DSP via the FAULT signal. The third priority is to indicate the fault by an LED indicator.

The over current fault for the IGBTs are traced by the HCPL-316J driver by measuring the saturation voltage VCE(sat) of the IGBT. When VCE exceeds a predefined voltage an over current fault signal is indicated and a shutdown sequence is initiated by its soft turn-off property.

7.2.3.1 Phase over current/ over voltage detection circuit

The input signals for phase over current detection circuit originate from the output of current and voltage sensors. The developed circuit schematic is given in Figure 7.18. The amplifiers do the action of precision rectifier. If the rectified input signal is larger than predefined threshold, it means that the faults happen in the main circuit.
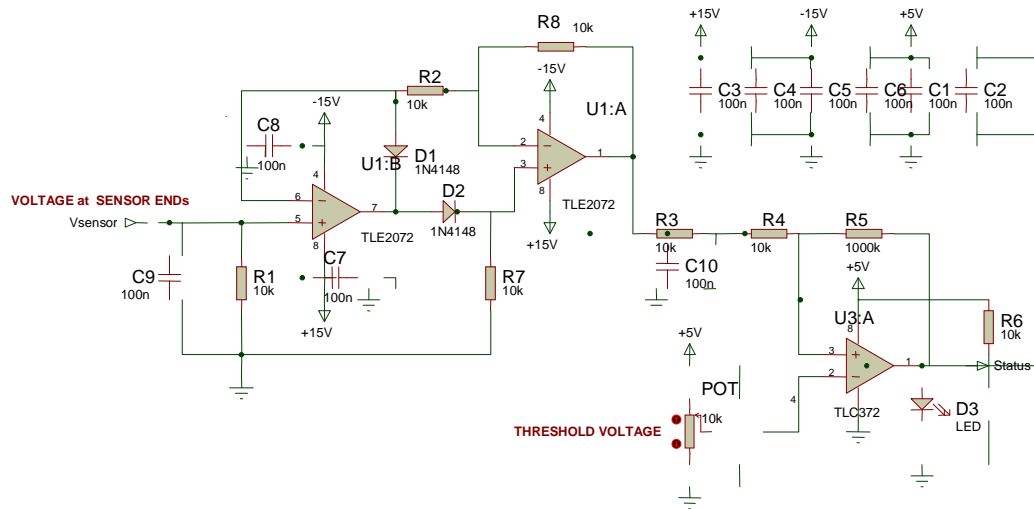
Figure 7.18. Phase overvoltage detection circuit

7.2.3.2 Over temperature detection circuit

The temperature sensor is used for monitoring the temperature of the IGBT. Although the IGBT can tolerate a junction temperature of 150°C, the over temperature protection is to be adjusted for a temperature of 75°C. The LM35 precision integrated-circuit temperature sensor is used, whose output voltage is linearly proportional to the Centigrade temperature. It is in a TO-92 package, which has a 10 mV/°C output signal.

The developed temperature fault detection circuit is given in Figure 7.19. The signal out of LM35 is amplified such that 75°C corresponding to 5 V. All temperature fault indication signals are OR gated with the other OR gate fault signals to feed back to the DSP, where it could be monitored and the inverter can be disabled if the temperature is too high.
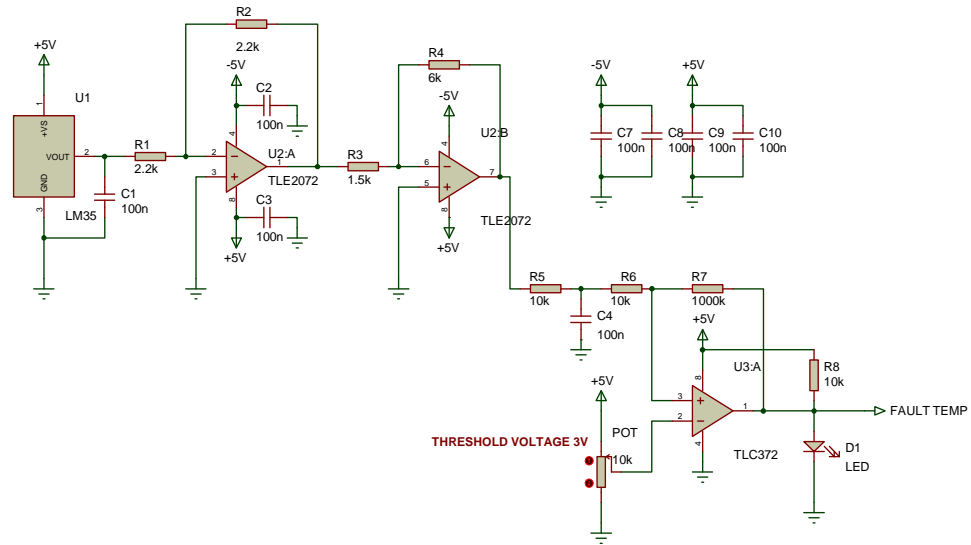
Figure 7.19. Over temperature detection circuit

Together with the over current fault created by HCPL 316j, all fault indication signals are proceeded to OR gate, the output from this OR gate is fed to the DSP's PdpintA interrupt pins through input isolation circuit. When the fault signal pin carry a falling edge signal, PdpintA is enabled and put PWM output pins in the high-impedance state, which disables the PWM signals within 200 nanoseconds using internal hardware logic within the DSP. This state can only be reset by a RESET CPU command from the DSP, or the built-in reset-button from the power stage.

7.3 Summary

In this chapter, the general architecture and the electrical details of the developed hardware set-up are described in order to implement the previously mentioned control algorithms for LIM. The developed hardware mainly grouped in two categories: power circuit part and the interface part. The power circuit part consists of ac side choke, EMI filter, three phase diode bridge rectifier, dc link circuit, three phase bridge IGBT inverter and its snubber circuit and LC filter circuit. Six IGBTs (three legs) are used to obtain bridge inverter. The isolation circuit part consists of voltage and current measurement circuits, input/output optocoupler isolation circuits, fault detection circuits and gate driver circuits. The design details and the complete schematics of the developed circuits

are given. The interface circuits communicate with the power circuit by the signals flowing between them through DSP. eZdsp F2812 DSP board can be regarded the "brain" of the system. All the gate signals for the IGBTs, the fault signals from the driver boards, the signals for system reset and all the measurements are processed by the controller. The produced gate signals have 0-3.3 Vpeak value. These signals are amplified to 0-5 V and connected to IGBT driver circuit. The driver circuit changes the amplitudes of the signals to (-5 Vpeak)-(15 Vpeak) and one driver circuit is required for each IGBT. The amplified signals are given to Gate-Emitter of each IGBT to constitute the required three phase sinusoidal voltages.

The developed experimental set-up is adaptable to any DSP controlled motor control system.

CHAPTER 8

DSP IMPLEMENTATION

This chapter explains how to implement and realize the algorithms mentioned in the preceding chapters. The term 'Implementation' refers to writing program codes at the registers of the digital signal controller to make the developed hardware system to work according to a signal from the computer.

Power electronics systems typically consist of nonlinear switching elements working at a high-frequency. Therefore, real-time power electronics systems demand the use of high-speed data acquisition and control. TMS320F2812 DSP based controller meet these requirements. In this thesis, all experiments have been implemented on this fixed-point processor, so-called eZdsp2812 board.

8.1 Specification of ezDSPTMF2812

This 32-bit DSP is highlighted by 150MHz CPU, 12-bit, 80ns A/D converter, 32-bit timers and real-time code debugging capability. The ADC channels offer a fast conversion rate of 80ns at 25 MHz clock speed. The sixteen ADC channels can be either operated as an auto-sequenced cascaded sequencer or two independent dual sequencers. The ADC conversion can be triggered by a variety of sources including hardware, software and a number of timer events in the DSP to synchronize with different events easily.

Two modules (Event Manager A and B) can generate 16 PWM pulses either independently or synchronized to each other. The PWM pulses generated by the compare units on each module are suitable for control of two three-phase full bridge inverters simultaneously. A dead-band for the gate signals can be introduced for these pulses on their rising edge. The EVs and ADC can be easily synchronized by selecting the suitable interrupts.

eZDSPTMF2812 also offers a pair of hardware interrupt based power drive protection pins (PDPINTA and PDBINTB for EVA and EVB respectively) for protecting the inverters in case of faulty conditions. Two dedicated GPIO pins can be configured for this purpose and can be controlled by external fault logic. Whenever a 'low' is sensed by the DSP on these ports, an interrupt of the highest priority is triggered. All PWM channels are immediately sent into a high-impedance state and with suitable pull down resistors connected externally, these PWM pins are kept at 'low' state during this interrupt period. More detailed description of the DSP functionalities can be found in [102-105].

TMS320F2812 supports the 32-bits fixed-point format. The IQmath library developed by Texas Instruments helps the programmers in writing algorithms as if they were written in the floating point. To show the easiness of "IQmath" approach, a simple equation implementation for three different approaches is given in Table 8.1 [106].

Table 8.1. Illustration of "IQmath" approach comparing with traditional fixed-point and floating-point approaches in C language

	Data type	C implementation
Floating point	float y,m,x,b;	y=m*x+b;
Traditional fixed-point	long y,m,x,b;	y=(long64)(m*x)>>GLOBAL_Q+b;
"IQMath"	_iq y,m,x,b;	y=_IQmpy(m,x)+b;

The data type "_iq" seen in Table 8.1 is used to identify the variables in GLOBAL_Q format. The GLOBAL_Q value indicates the number of fractional bits. It should be adjusted basing on the needs of dynamic range and numerical resolution [106]. The dynamic range is defined as the ratio between the largest and smallest numbers that is formulated in dB unit by (8.1) [107].

$$dynamic\_range_{dB} = 20\log\frac{l\arg est\_number}{smallest\_number}$$

(8.1)

The dynamic range of the floating-point processor is very high, thus allowing representation of both very small and large numbers with excellent accuracy. In contrast to floating point processor, for fixed point ones, the dynamic range is much smaller but it is cost effective due to its inexpensive architecture.

116

Resolution and dynamic range requirement is application dependent [108]. Higher precision selection results in a lower dynamic range as illustrated by Table 8.2. Hence, there must be a tradeoff between the range and the resolution while specifying the IQ format. It is recommended to check the application performance with different numerical precisions for achieving the best performance [108].

Table 8.2. Smallest, least negative, largest positive numbers, and dynamic range among 16-bit fixed-point, 32-bit fixed-point, and 32-bit floating-point representation

	Resolution	Least negative number	Largest positive number	Dynamic range (dB)
16-bit fixed-point; Q15	2^{-15}	-1	$1-2^{-15}$	90
32-bit fixed-point; Q31	2^{-31}	-1	$1-2^{-31}$	187
32-bit floating-point	2^{-127}	-2^{-128}	2^{128}	1535

While working with fixed point processor, one must ensure that the sign of variables is retained and products don't overflow i.e. during multiplication. Otherwise, the coming situation is equivalent to changing the direction of the control since the contents of associated registers wrap around. By using pu concept, this handicap is blocked since two pu numbers can be multiplied together without overflow. Another benefit is that it allows the same controller to be used for any motor regardless of its parameters. In the program, IQ24 was chosen as the default IQ format.

In the case of reading from ADC registers, to increase the accuracy, one must reserve as many bits as possible to floating part. For that reasons, parameters such as motor currents, voltages are stored as a Q15 fraction in programs. By this way, parameters are converted between -1 and 0.99999 with a resolution of 2^{-15}. However, PU values should be selected carefully depending on the operating conditions. If the rated values are chosen as base values, the amount of states may exceed unity in transient regions that is also equivalent to changing the direction of the control. Therefore the base values should be chosen according to the transient state peak values. However, this will give harm to the accuracy of the steady state computations. The amount of transient peak state is system dependent but it is a good starting point to select as 1.2 times of rated value.

In the thesis, the channels of A/D function and GPIO function are applied to achieve the experiment system. The A/D function is used to obtain the measured three-phase LIM primary currents, voltages and DC link voltage from Hall effect sensors. The GPIO function is employed to deliver the 6 PWM switching signals to the gate drive circuit, to detect fault from error sensing cards, to measure the speed using CAP function and sending enable/disable signals for PWM generation and relay operation.

The resolution of ADC in TMS320F2812 gives a maximum accuracy of 7.3 mA for a maximum current of 30 A. The digital output of ADC can be described by (8.2).

$$ADC_{out} = \frac{4096}{3}(Gain_{ADC}V_{input} + Offset_{ADC}) \qquad (8.2)$$

Practically, the gain of the ADC is not equal to "1" and it's offset to zero and also sensors used may have dc bias that result in errors in the measurements. To improve the reading of ADC a software routine was used to estimate the offset for each ADC channel depending upon the type of the signal whether ac or dc. The input signals of ADC was summed-up 5000 times before the inverter energized and then the average offset value is obtained and each ADC channel was compensated according to this obtained average offset value.

Throughout this thesis, the developed programs are written in C and compiled using Code Composer Studio (CCStudio). The CCStudio provides the tools for code generation with basic real-time analysis and debug. The verification of software implementation is carried through graphics and visualization instantaneous variables. To develop a program using CCStudio, it is necessary to create a project. This project is divided into folders and each file type has a folder. The programming environment and the project structure are shown in Figure 8.1. It is necessary to indicate to the compiler the directory of the each file which is used in the project; otherwise the compilation cannot be performed.
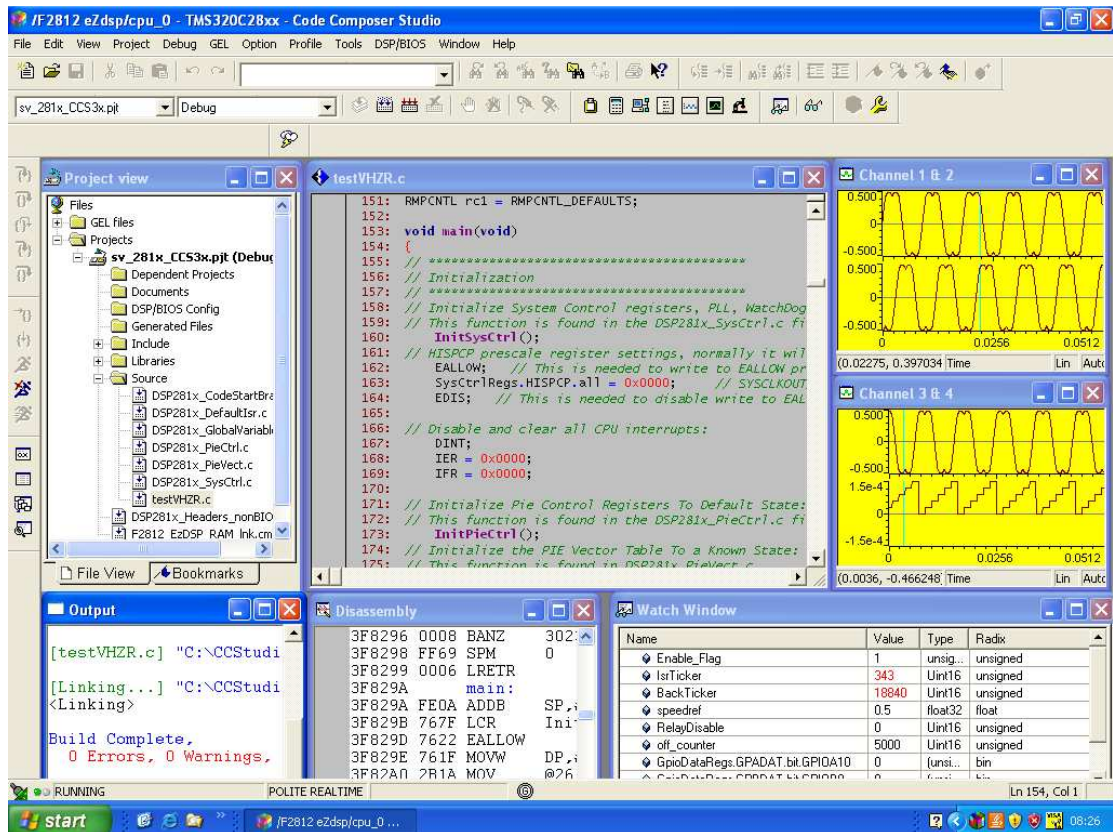
Figure 8.1. A screen shot of a project developed in Code Composer Studio

The developed source files follow the general flowchart which is shown in Figure 8.2. Programs start by initializing the necessary features and peripherals of the DSP. The initialization part defines and initializes the software variables, constants and specific registers. The initialized registers are watchdog timer registers, event manager registers, clock registers. Some of these registers are redefined in the rest of the program depending upon the developed algorithm. Once the initialization is finished the main function enters into an infinite loop without any function. At this point the program waits for the interruption events and calls the interrupt subroutines. An interrupt is enabled and its respective timer is activated to allow the ADC to sample at specific intervals. Then, the timer used for triggering interrupts has to start and initiate ADC conversion. The actual controlling action will be done within the main loop and the Interrupt Service Routine (ISR).

119
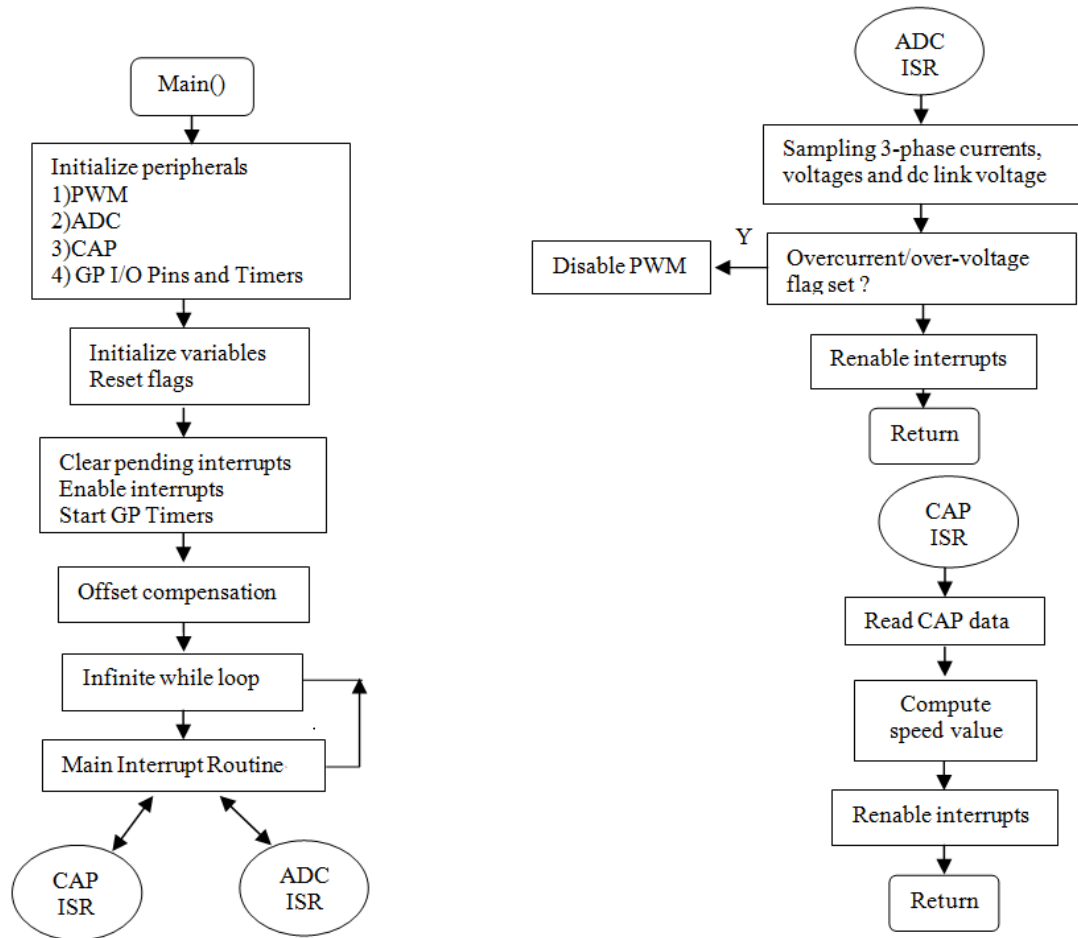
Figure 8.2. The basic program flow diagram

The open loop V/Hz controller was developed at first to ensure the developed inverter and peripheral hardware are working correctly. The outputs of the Hall Effect current, voltage and speed sensors were monitored with the CRO to ensure everything was working correctly. From this simple test it was concluded that the basic software structure and peripheral setup was fully functional for DTC algorithm.

8.2 Implementation of the Modified Space Vector Pulse Width Modulation for ZSI

The practical implementation of the space vector pulse width modulation (SVPWM) for the two-level z-source inverter (ZSI) is discussed in this section.

The main idea of the SVPWM is that F2812 should approximately and continuously synthesize the rotating reference voltage by using the eight combinations of inverter

120

switching vectors. Therefore, the frequency of the output voltage is same as that of the reference voltage.

By rearranging the equation (6.11) according to the Figure 6.1 for sector 1,

$$V_{ref,d} = MV_{max} \cos\alpha = d_1|V_1| + d_2|V_2|\cos 60°$$

$$V_{ref,q} = MV_{max} \sin\alpha = d_2|V_2|\sin 60° \tag{8.1}$$

where d denotes duty ratio, M denotes the modulation index and Vmax is the maximum value of the desired phase voltage.

By normalizing the voltages with the maximum phase voltage; Vmax=1 and $|V_1|=|V_2|= 2/\sqrt{3}$.

Then, the duty ratios can be derived as,

$$d_1 = M \sin(60° - \alpha)$$

$$d_2 = M \sin(\alpha) \tag{8.2}$$

Since the F2812 operates based on the fixed point system, in order to calculate the sin function, the F2812 needs a table of sinusoidal values. Because the d-q decomposition is identical for the six sectors as shown in Figure 8.3, a 60° sine look-up table is sufficient. In order to complete one revolution, the sine table must be cycled through six times. After selecting two adjacent basic vectors and calculating their possessing times including shoot-through times, the next step is the selection of the switching pattern.
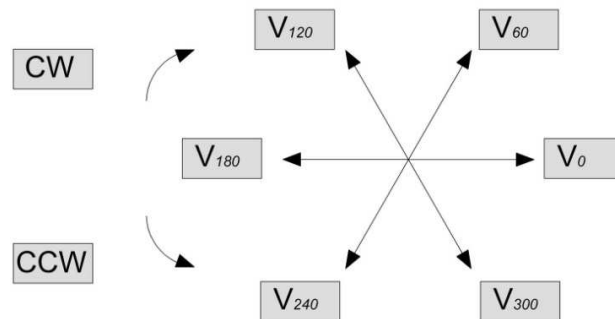
Figure 8.3.   Switching pattern of SVPWM, CW refers to clockwise and CCW refers to counterclockwise

At the beginning and at the end of the each switching period, a zero vector is activated by turning off all upper switches, and in the middle of the switching pattern, a zero vector is activated by turning on all of the upper switches. The different zero vectors are used in order to minimize the switching transitions. By using both zero vectors in the modulation algorithm, the F2812 can achieve better harmonic efficiency.

The developed SVPWM algorithm for ZSI is verified before proceeding through the experimental works. The developed SVPWM routine for ZSI is given in Appendix C. It was written in C and compiled using Code Composer Studio. It generates three sinusoidal references with a desired modulation index (M) and frequency by selecting the inverter sector and computing the switching duty cycles regarding the selected shoot duty ratio. Then, it configures out six PWM generators to work at the selected switching frequency.

To go through step by step simulation, the zero shoot-through duty ratio is selected at first. The developed SVPWM algorithm for ZSI is given in Figure 8.4. According to the developed algorithm, the following are steps in the main program:

1) Configure the timers and compare units for symmetric PWM.

2) Input desired shoot through duty ratio, speed and direction of rotation

3) Obtain the magnitude of reference voltage vector V_{ref} (based on constant V/Hz profile).

The following are the steps in the interrupt driven modified SVPWM routine for ZSI:

1) Obtain the theta by integrating the command speed.

2) Obtain the sine and cosine of theta

3) Determine which sector V_{ref} is in.

4) Decompose V_{ref} to obtain d_1, d_2, d_{sh} and d_0 as compare values.

5) Determine the switching pattern and load the obtained compare values into corresponding compare registers.
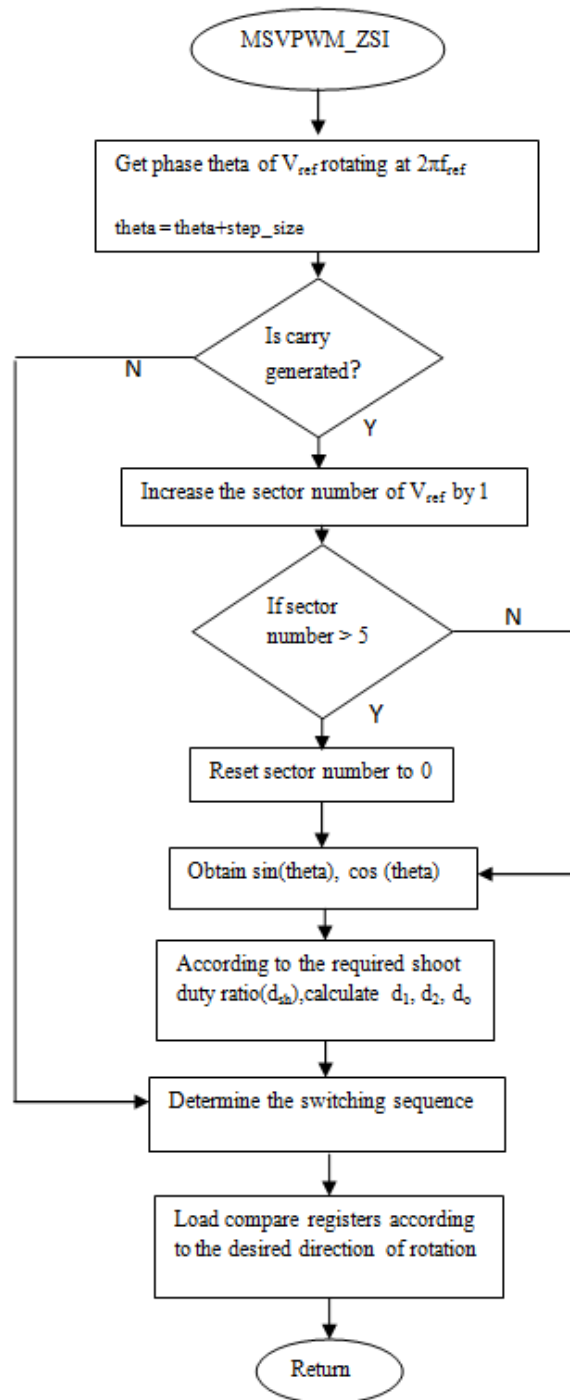
Figure 8.4. The developed SVPWM algorithm for ZSI

Throughout the experimental studies the waveform measurements are conducted with a 200 MHz four channel Tektronix TPS2024 Series Digital Storage Oscilloscope (DSO). The obtained PWM outputs related to the upper switches were monitored by DSO can be seen in Figure 8.5 for each sector.
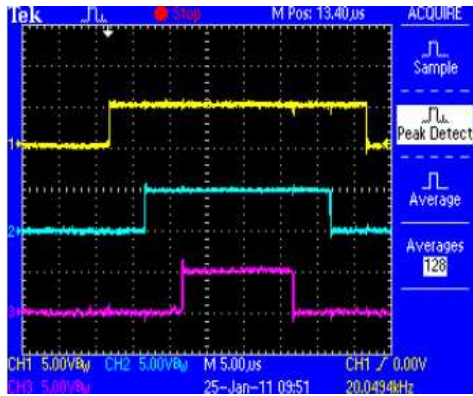
Sector1
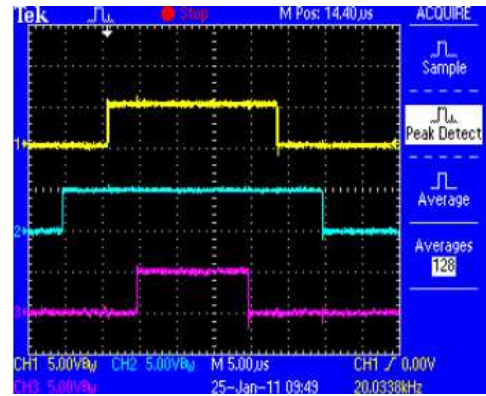
Sector 2
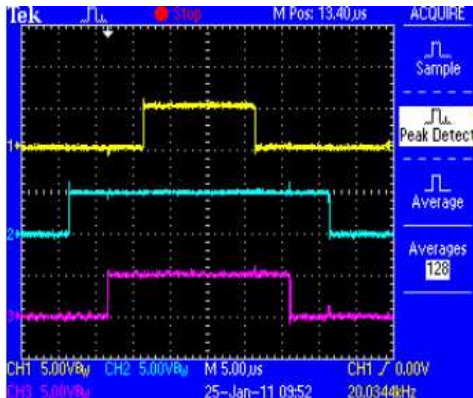
Sector 3
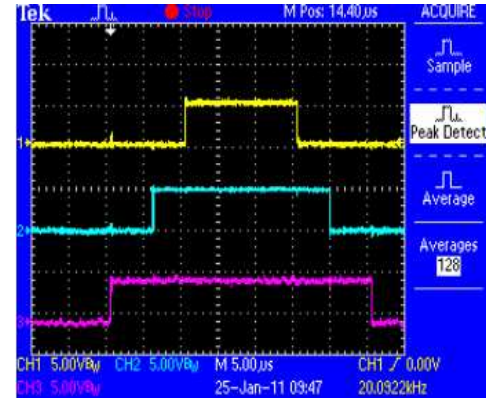
Sector 4
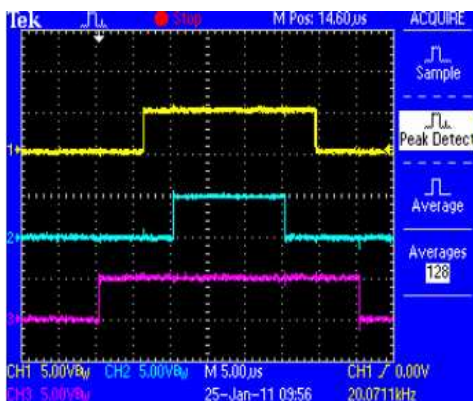
Sector 5
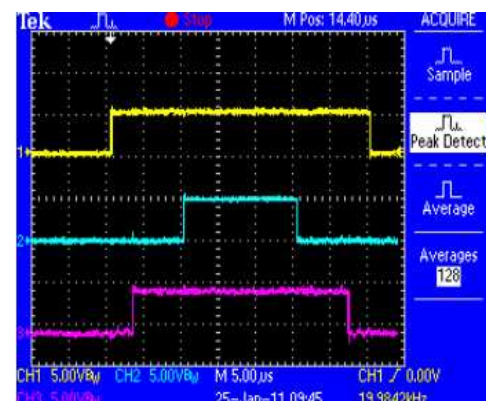
Sector 6

Figure 8.5. The obtained 20kHz PWM outputs related to the upper switches for each sector with the zero shoot-through duty ratio and M=0.4

A simple low–pass RC filter circuit to filter out the high frequency components was also used for further verification of the generated PWM signals. The R and C values were chosen as R = 4.7 kΩ and C = 100 nF. The selected cut–off frequency are lower than the PWM frequency. This low–pass filter is connected to the PWM outputs of the TMS320F2812 and the filtered version of the PWM signals were also monitored by the digital oscilloscope. The difference between two filtered gate signals produces a line-to line output voltage which is free of harmonics as shown in Figure 8.6 by red line.
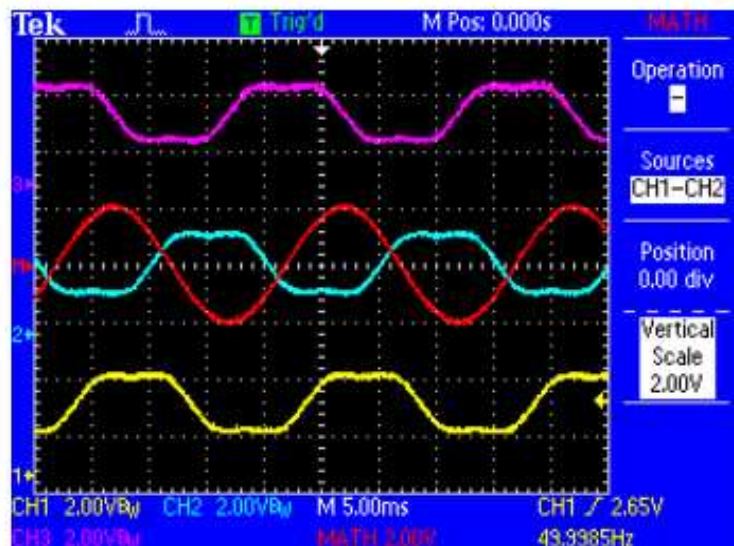
Figure 8.6. The low-pass filtered form of the generated PWM waveforms to form a 50Hz and M=0.4 three-phase voltages having positive sequence (Yellow-phase A, Blue- phase B, Purple- phase C)

The filtered waveforms shown on the oscilloscope are the same shape as the one shown in WatchWindow of CCStudio in Figure 8.7. In the watch window screen shot, the bottom figure shows the sector numbers of the generated rotating reference voltage vector.
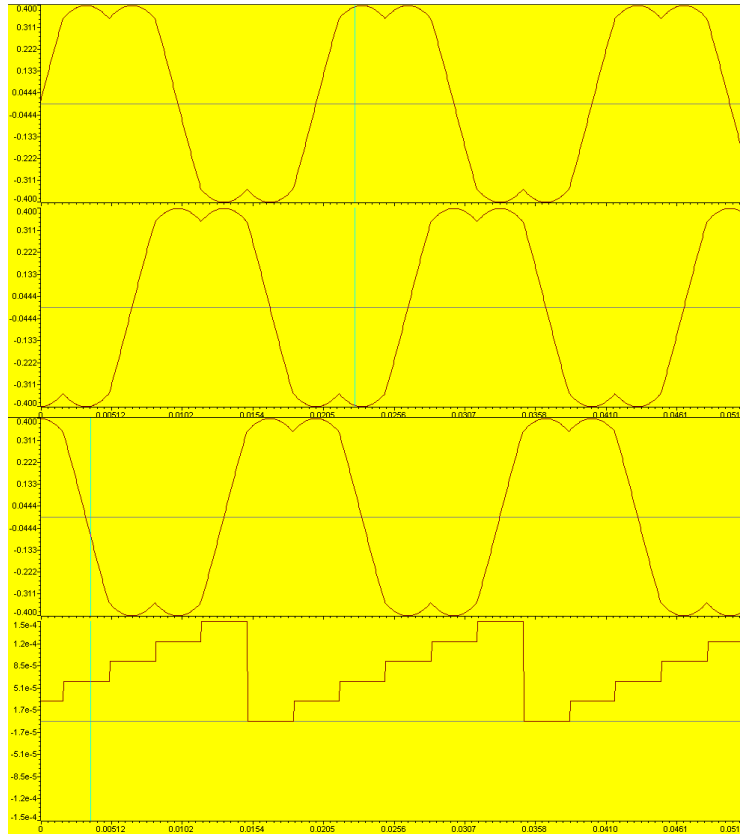
Figure 8.7. The watch window screen shot for positive sequence voltage generation; the first three show phase to neutral three-phase voltages at 50Hz and M=0.4 and the last one shows the sector numbers traced

Note that, the order of the sector numbers shows that a vector is rotating in the counterclockwise (CCW) direction indicating the positive sequence.

The filtered forms of the generated PWM signals were also monitored by the digital signal oscilloscope and CCStudio Watch Window for negative sequence voltage generation. They are shown in Figure 8.8 and Figure 8.9, respectively.
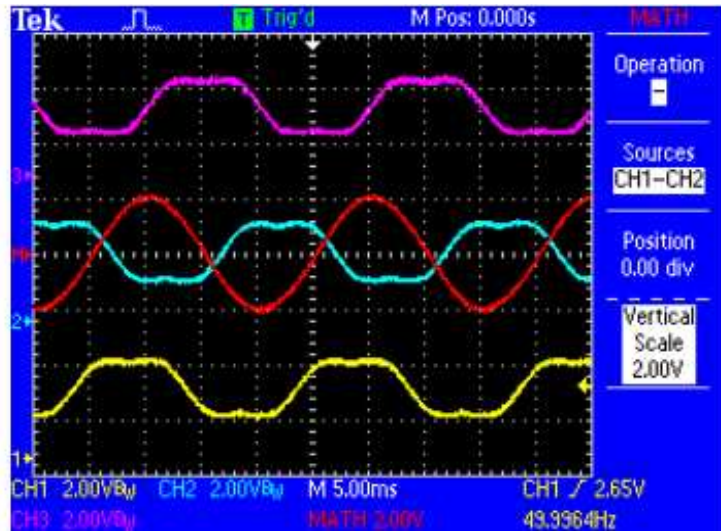
Figure 8.8. The low-pass filtered form of the generated PWM waveforms to form a 50Hz and M=0.4 three-phase voltages having negative sequence (Yellow-phase A, Blue- phase B, Purple- phase C)
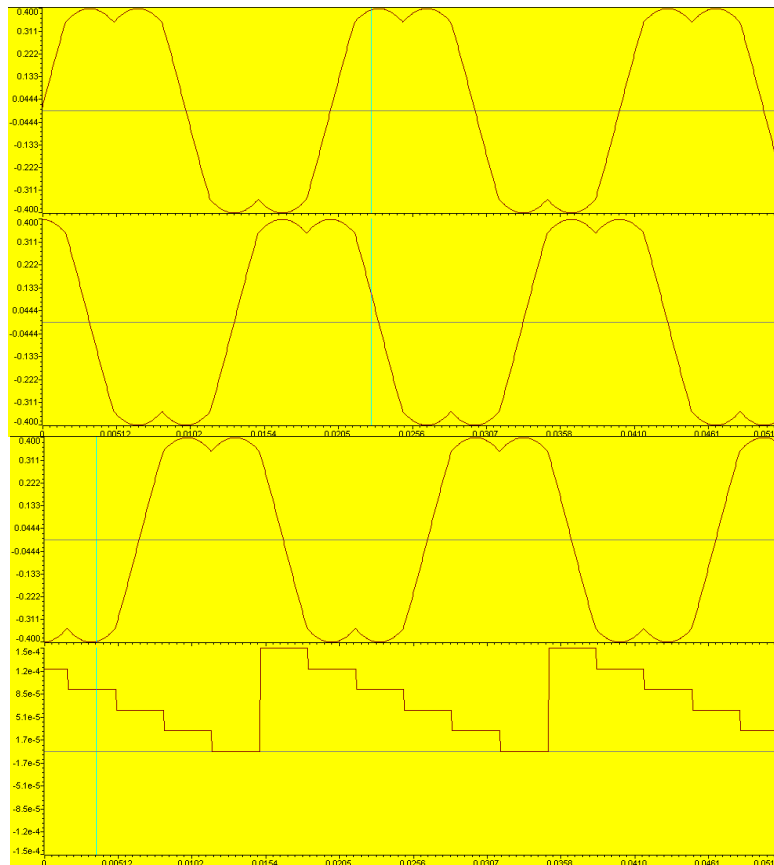
Figure 8.9. The watch window screen shot for sequence voltage generation; the first three show phase to neutral three-phase voltages at 50Hz and M=0.4 and the last one shows the sector numbers traced

After verifying the written program for zero shoot through state, a shoot duty ratio of 0.25 was applied to PWM generation algorithm. The generated pulses related to the two legs of the inverter bridge; PWM1, PWM4, PWM3, PWM6 pulses are shown in Figure 8.10 for four sectors. The filtered forms of the signals related to upper switches are also monitored in DSO as given in Figure 8.11. According to these figures, the shoot-through states are evenly and symmetrically located in each phase as intended.
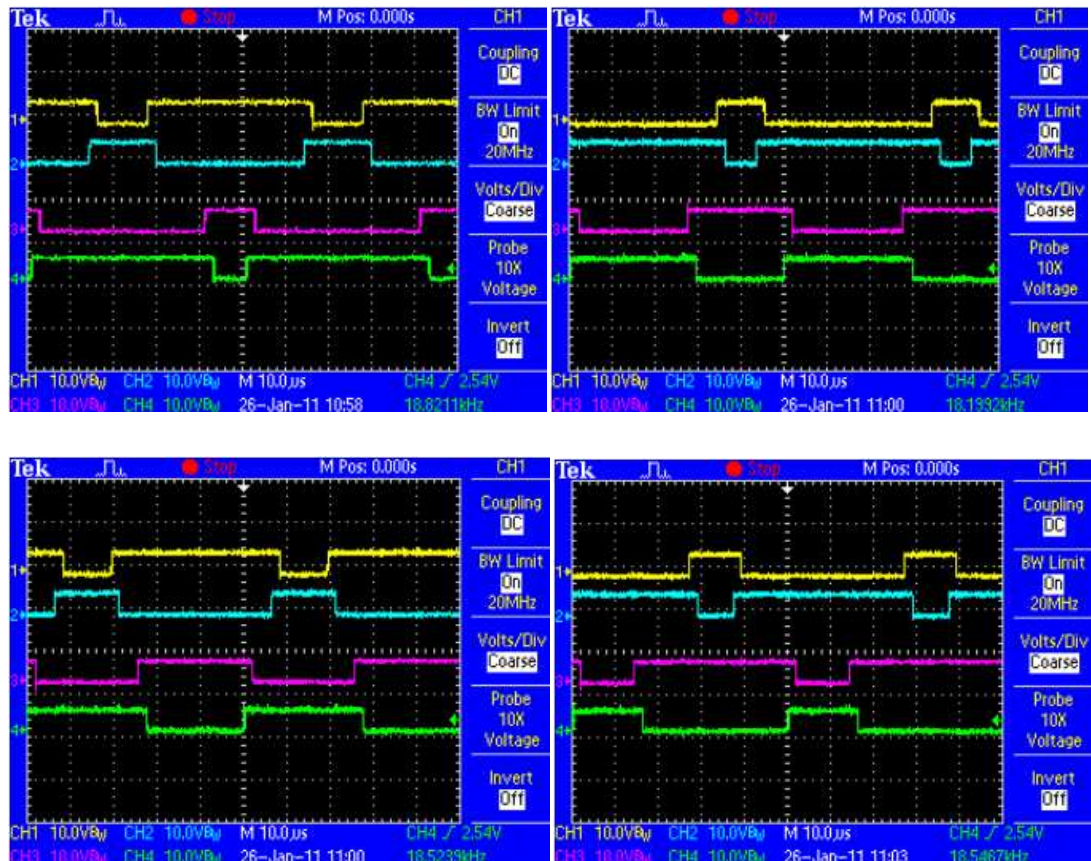
Figure 8.10. The generated PWM pulses related for the two leg (PWM1, PWM4, PWM3, PWM6) with a shoot-through duty ratio of 0.25 at 20kHz
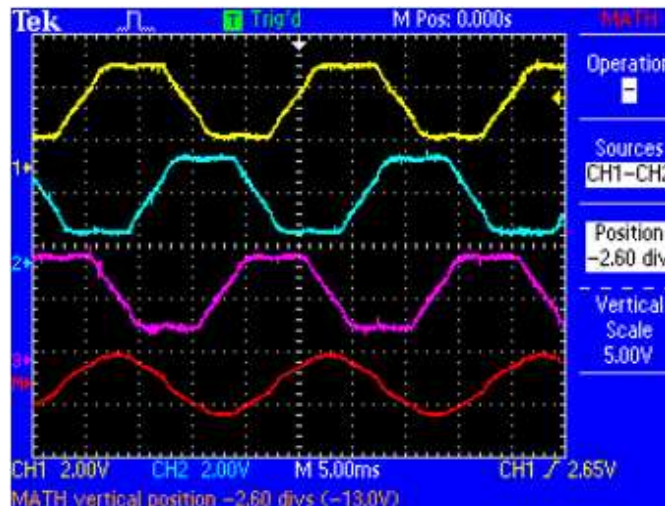
Figure 8.11. The low-pass filtered form of the generated PWM waveforms to form a 50Hz and M=0.4 three-phase voltages with a shoot-through ratio of 0.25

According to the DSO waveforms obtained with zero and non-zero shoot-through duty ratios, the generated PWM pulses are symmetric according to the same center and at the both ends switching signals are low and in the middle all PWM signals are high. Therefore, the obtained waveforms show that the developed source code implemented in TMS320F2812 generates the switching signals for z-source inverter in an intended manner.

8.3 V/Hz Control Implementation

The open loop V/Hz control is a basic control method, providing a variable frequency drive for applications like fan and pump at a reasonable cost. The objective is to control the machine speed while keeping the magnitude of the stator flux constant by serving the highest torque capability in a wide range [30]. While this type of control is very good for many applications, it is not well suited to applications that require higher dynamic performance.

This method is based on the steady-state equivalent circuit as shown in Figure 8.12 [30, 109].
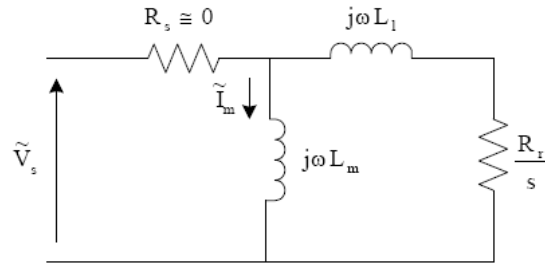
Figure 8.12. Simplified steady-state equivalent circuit of induction motor

In this figure, if the stator resistance is assumed to be zero and the stator leakage inductance is embedded into the rotor leakage inductance, then the air gap flux can be approximated by the stator voltage to frequency ratio. This equation is given by equation (8.3), assuming that the motor is operating in the linear magnetic region, so that Lm is constant.

$$\psi_m \cong L_m I_m = \frac{V_s}{jw} \Rightarrow \psi_m \propto \frac{V_s}{f} \tag{8.3}$$

To maintain the air gap flux at its rated value the voltage and frequency should be varied in the same proportion [30]. After providing the ratio between voltage and frequency remains constant then the maximum torque can be applied throughout the motors speed range.

Varying the supply voltage and frequency in proportion so that the stator flux remains constant maintains the shape of the torque-speed curve but shifts it along the speed axis. This effect is illustrated with the blue lines in Figure 8.13. This graph has mainly two frequency regions; the constant torque region which exists at frequencies from zero Hz up to a base frequency value, the constant power region which occurs at frequencies above the base frequency.
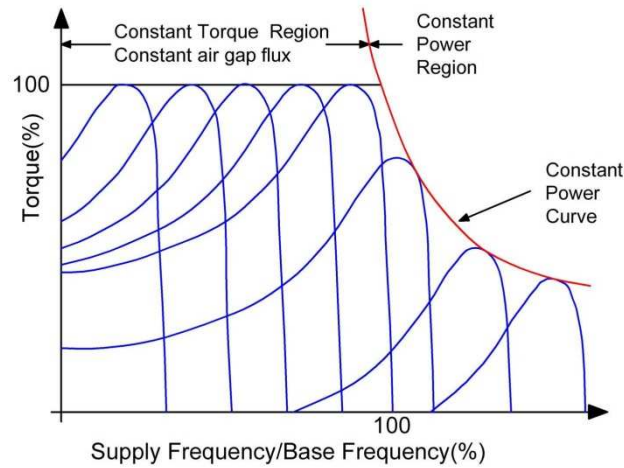
Figure 8.13.Torque-speed characteristics of an induction motor [69]

In the constant torque region, voltage and frequency are varied proportionately; this maintains constant flux and the pull out torque also remains constant. Motors mainly operate in this region. At frequencies above base frequency, operation is limited by the constant power curve. At frequencies above base frequency, with rated voltage, the air gap flux decreases and so does the torque. Because the motor flux is lower than at base conditions, this operation is also known as field-weakened (constant power) operation.

At frequencies above the rated frequency, the constant V/Hz ratio should not be used, because the voltage has to be fixed at a maximum value to avoid insulation breakdown at stator windings.

Furthermore, at low frequencies, the voltage drop caused by the stator resistance cannot be neglected. To compensate for this voltage drop below a certain frequency, some boost voltage is required. The voltage boost is often applied at frequencies lower than 20Hz to produce full-load torque. The applied voltage boost may be a constant value as shown in Figure 8.14.
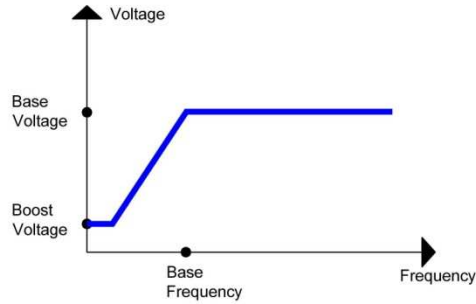
Figure 8.14. V/Hz profile with constant boost

However, the required boost voltage depends on the motor and the load characteristics, so using a fixed boost can produce undesirable results especially for different loading conditions. For example, assume a motor having a stator resistance of 1.5Ω and full-load current of 20A is rated at 380V /50Hz. The airgap voltage per Hz is calculated as 7,6 without taken into account the stator voltage drop and as 7 with stator voltage drop. If the motor is operated at full-load at 6Hz, the required voltage is 72V considering the voltage drop on the stator resistance. The required voltage boost can be reached with a 12 V/Hz.

For the no load case again for 6 Hz operation, the required voltage is 42V. Using the same fixed voltage boost value, causes applying an excess of 30V, which may results in saturating the iron core and overheating of motor. Therefore, the stator voltage compensation is used instead of a fixed boost to improve the torque response during low speed regions without the risk of saturation and overheating. This was accomplished by sensing motor current and automatically adjusting the voltage boost in proportion to the motor current.

The block diagram of the developed open loop V/Hz is presented in Figure 8.15. The slip compensation is not needed since the no-load speed of LIM is close to synchronous speed.
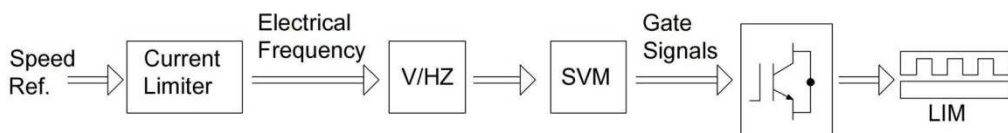
Figure 8.15. Block diagram of V/Hz control

The developed software timing diagram and flowchart are given in Figure 8.16 and Figure 8.17, respectively.
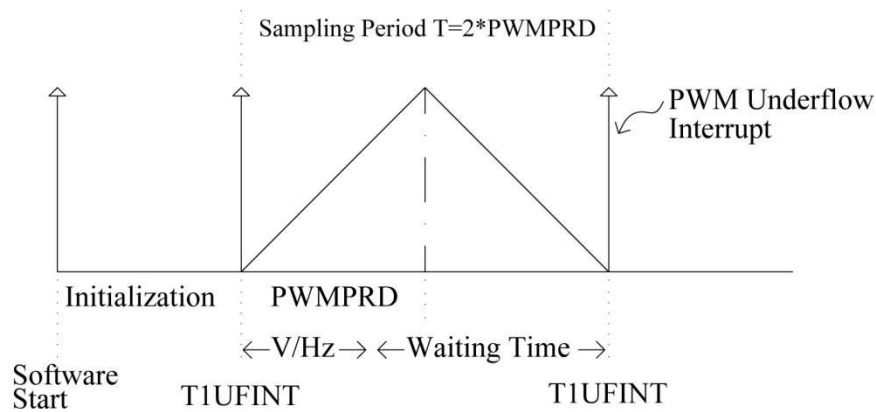
Figure 8.16. Software timing diagram for V/Hz implementation

The constituted Timer1 Underflow (T1UFINT) interrupt module handles the whole V/F algorithm. It is periodically computed according to the selected fixed PWM period value. The sampling period Ts of 50μs (20 kHz) is established by setting the timer1 period to 3750 (PWMPRD=3750). This timer is set in up-down count mode and generates a periodical interrupt on timer1 underflow event. The goal of the T1UFINT is to update the stator voltage reference according to the set frequency command.

A current limiter monitors the motor current and reduces the frequency command when the current exceeds a predetermined value. A boost voltage is not added to V/Hz profile to compensate for the stator voltage absorbed by the stator resistance at low speed, instead IR compensation is done. The V/Hz block converts the frequency command to voltage reference for SVM block by using (8.4).

voltout = _IQmpy(_IQ(1.7408),absfreq) + _IQmpy(_IQ(0.1296),iMag)   (8.4)

where voltout, absfreq, iMag are all pu values.

The generated voltage is limited to its rated value in case of working in the field weakening region. By using this computed voltage and the selected frequency, the SVM block generates the gate signals for the inverter.
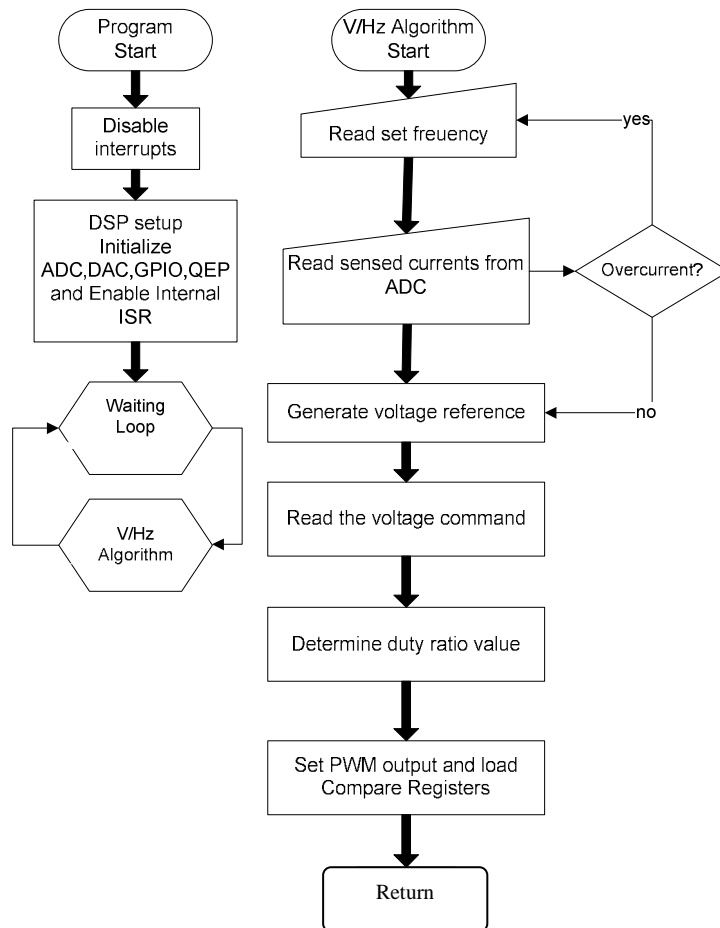
Figure 8.17. Software flowchart for V/Hz implementation

Initial value of the frequency set value is also important. When the motor is operating in the solid line portion of the torque-speed curve, the motor current is directly proportional to motor torque. However, other than the solid region, if the motor is line started, the current inrush will be approximately 600% of full load current. To ensure that the drive system is not require 120% of rated current, the drive is started at a low frequency about 1-2 Hz and then increase speed by increasing frequency linearly by this way the motor always operate on the solid portion of the torque-speed curve.

Since the V/Hz control method is based on the steady state motor model, it cannot achieve the adequate dynamic performance. This can be considered as the basic drawback of the scalar control method. However, whether a V/Hz control or direct torque control is applied to an asynchronous motor, the applied voltage is tied to the

applied frequency through the magnetic flux capacity of the motor so the rated flux cannot be exceeded.

8.4 DTC Implementation

The developed DTC algorithm has two control loops; the inner one consist of the flux & torque estimators, hysteresis control and an inverter voltage selector, the outer one is the speed control. The motor speed is measured by using HAMLIN 55075 hall-effect sensor through CAP1 input of DSP. The speed controller is implemented with traditional PI type controller. Its resulting output signal constitutes the reference for torque control. An inertia compensator is also included to reduce the deviations due to acceleration or deceleration of the inertia [110]. The torque reference generated by the outer control loop is passed to the inner controller. In presented system three phase motor currents, voltages and DC link voltage are measured by LEM sensors and processed by A/D converter.

Based on the measured voltages and currents, the inner loop performs a coordinate transformation to get the estimating torques or fluxes. In the developed DTC program, thrust and flux estimations are also represented by using the per unit system like the motor currents, voltages which are stored as a Q15 fraction for normalization. Besides preventing from overflow, the usage of pu values also allows the same controller to be used for any motor regardless of its parameters. The pu model of the linear induction motor defines the stator current and flux to be equal to one when the drive has reached its nominal speed under nominal load. According to the well-known base values, the flux and thrust equations given in (2.8) and (2.10) are normalized. The stator flux and thrust equations are rewritten as in (8.5) and (8.6) to be used in DSP programming.

$$\frac{d}{dt}\overline{\psi}_{s,pu} = T_n(\overline{v}_{pu} - R_{s,pu}\,\overline{i}_{s,pu}) \tag{8.5}$$

where Tn is expressed in absolute unit.

$$F_{e,pu} = \overline{\psi}_{sd,pu}\overline{i}_{sq,pu} - \overline{\psi}_{sq,pu}\overline{i}_{sd,pu} \tag{8.6}$$

The written DTC subroutine is given in Appendix C. It was tested in terms of the correctness of the voltage and current ADC readings of the motor obtained by running 7.5kW, 380V,Y-connected motor at no-load. Figure 8.18 shows the screen shot of the developed program and Figure 8.19 shows the ADC readings of the per-unit (pu) values of the alpha and beta components of motor phase currents and voltages which are generated by using Clarke transformation.
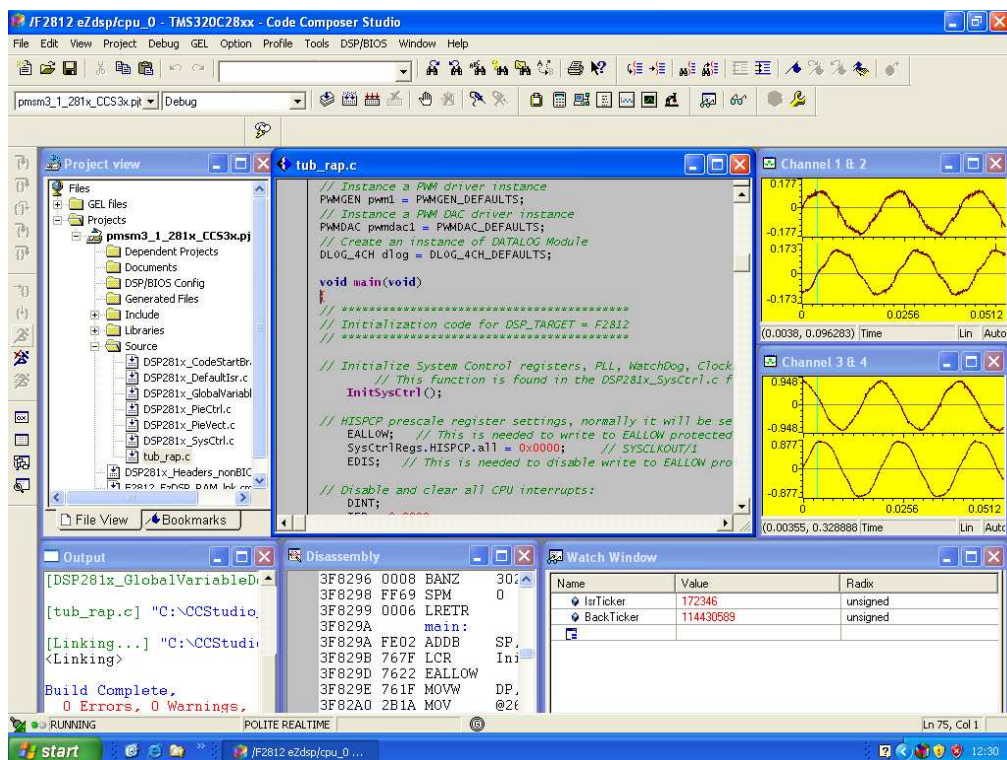
Figure 8.18. The screen shot of the developed DTC program working under CCStudio3. e while watching per-unit (pu) values of the alpha and beta components of motor phase currents and voltages
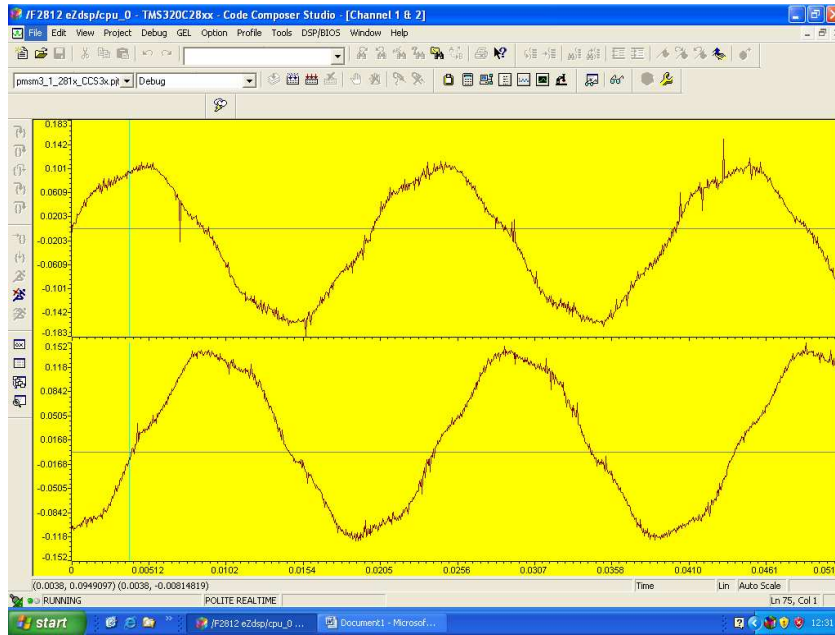
(a)

Per-unit (pu) values of the alpha and beta components of motor phase currents which were 1.8A rms
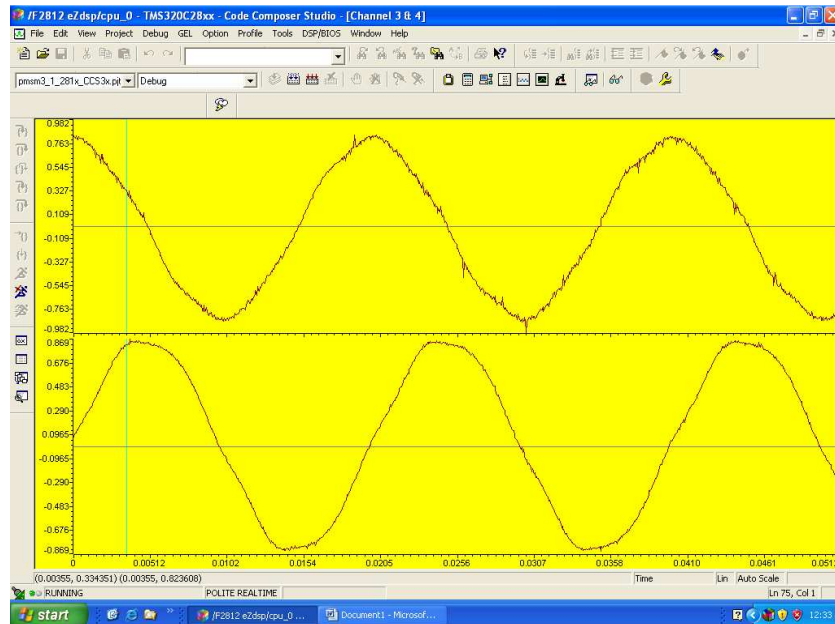
(b)

Per-unit (pu) values of the alpha and beta components of motor phase voltages which were 220V rms

Figure 8.19. ADC readings of the motor currents and voltages under no-load

1.8A rms for rated current of 15A refers to 0.12 pu peak value which was verified in Figure 8.18.a except from noise on. 220V rms for rated voltage of 250V rms refers to 0.9 pu peak value which was also verified in Figure 8.18.b. The noisy view of the currents mostly results from the reading of too small current with the LA-100P current sensor which is most suitable around 100A peak measurements.

After verifying that the ADC readings are much closer to their real values, the flux is calculated from these current and voltage readings. However, it was not easy as embedding only the integral equation given in (2.10). In real world, the noises; dc offsets in the measurements, digital approximation errors driving an ordinary integration equation into saturation. To overcome this problem, low pass filtered based integration is preferred as explained in chapter 5. Figure 8.20 shows screen shot of the developed program while running. The obtained results related to the estimation of the alpha and beta components of the flux and its sector are presented in Figure 8.21. Notice that, the estimated flux components are oriented 90 degrees from each other that as should be theoretically.
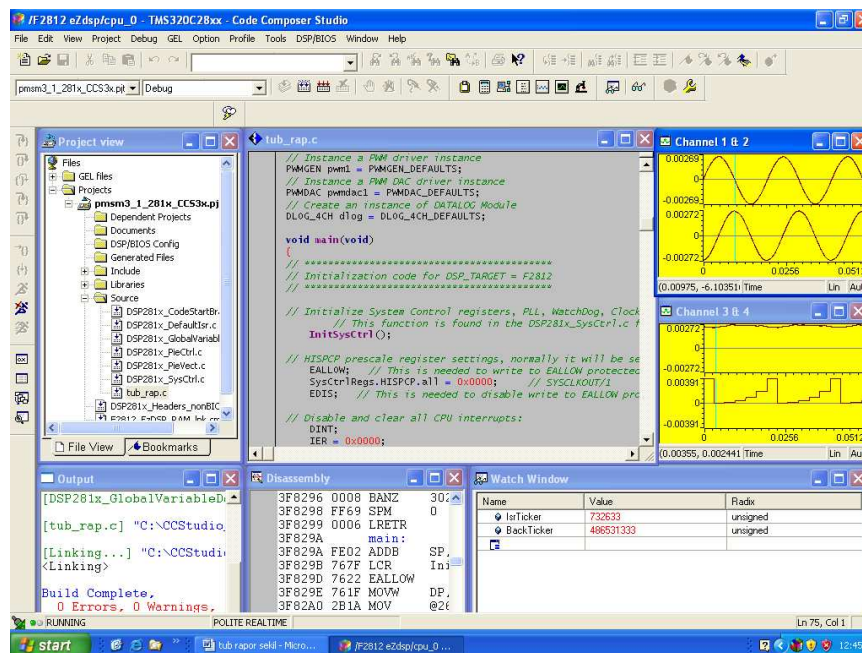
Figure 8.20. The screen shot of the developed DTC program working under CCStudio3. while watching per-unit (pu) values of the alpha and beta components of flux and its sector

138
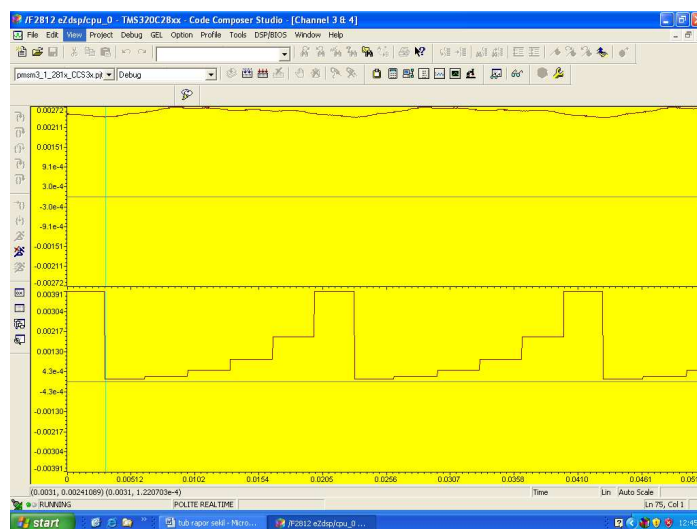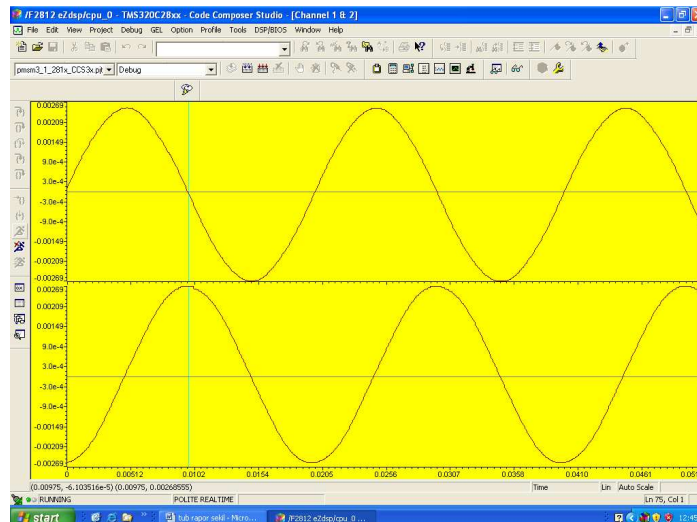
Figure 8.21. Per-unit (pu) values of the alpha and beta components of flux and its sector

By comparing this estimated stator flux and thrust pu values with their reference ones, the inner loop determines increments or decrements of stator flux and thrust via a hysteresis comparator according to the switching voltage table. All internal data of DSP is sent through a D/A converter and displayed in the scope for control purposes.

Figure 8.22 shows a flowchart of the DTC program. The developed program is started by initializing the necessary features and peripherals of the DSP. The rest of the application can be thought of as a sequence of three operations:

Voltage, currents and measurement through ADC

- DTC algorithm
- PWM generation
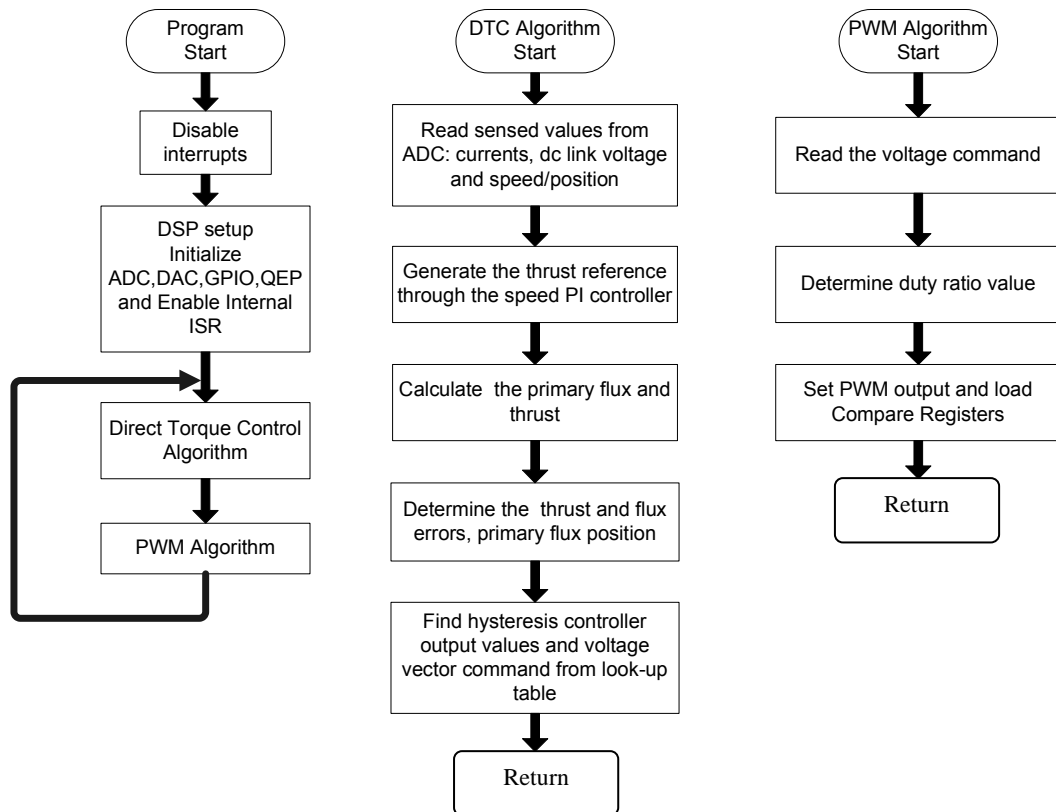
Figure 8.22. Simplified flowchart diagram of DTC

For a stable operation of hysteresis based DTC, 25us time is elapsed in the inner control. This type of operation becomes practical with TMS320F2812 technology. The outer speed control loop is calculated once per millisecond to obtain new thrust reference value. The detailed flow chart diagram of DTC subroutine is shown in Figure 8.23.

Symmetrical PWM is used in the control implementation. By this method, the general purpose timer is set in the up-down continuous mode where its counter register starts counting from zero up to the value stored in the timer period register, then it counts down to zero. Period register timer value is set to make the period of the up-down counting equal to the switching period of the drive.

```
                              ┌─────────┐
                              │DTC start│
                              └────┬────┘
                                   │
        ┌──────────────────────────┴──────────────────────────┐
        │              Calculate ids,iqs,vds,vqs               │
        │                                                      │
        │   ⎡X_d⎤   2 ⎡ coswt   cos(wt−2π/3)  cos(wt+2π/3)⎤⎡X_a⎤ │
        │   ⎢   ⎥ = ─ ⎢                                   ⎥⎢X_b⎥ │
        │   ⎣X_q⎦   3 ⎣−sinwt −sin(wt−2π/3) −sin(wt+2π/3)⎦⎣X_c⎦ │
        └──────────────────────────┬──────────────────────────┘
                                   │
        ┌──────────────────────────┴──────────────────────────┐
        │          Calculate ψ_ds, ψ_qs using LPF approach     │
        │                                                      │
        │   ψ̄_{ms(k)}^{est} = ───────((V̄_ms − Ī_ms R_s)T_s     │
        │                     1+T_s ω_c                         │
        │                     + ψ̄_{ms(k−1)}^{est})             │
        └──────────────────────────┬──────────────────────────┘
                                   │
        ┌──────────────────────────┴──────────────────────────┐
        │                 Add compensation term                │
        │                                                      │
        │  ψ_ds = ψ_qs^{est} ω_c/ω_e + ψ_ds^{est}              │
        │  ψ_qs = −ψ_ds^{est} ω_c/ω_e + ψ_qs^{est}             │
        └──────────────────────────┬──────────────────────────┘
                                   │
        ┌──────────────────────────┴──────────────────────────┐
        │           Calculate the frequency of stator flux     │
        │                                                      │
        │            ψ_{ds(k−1)}ψ_{qs(k)} − ψ_{ds(k)}ψ_{qs(k−1)}│
        │   ω_{e(k)} = ─────────────────────────────────────   │
        │                     (ψ_ds^2 + ψ_qs^2)T_s             │
        └──────────────────────────┬──────────────────────────┘
```
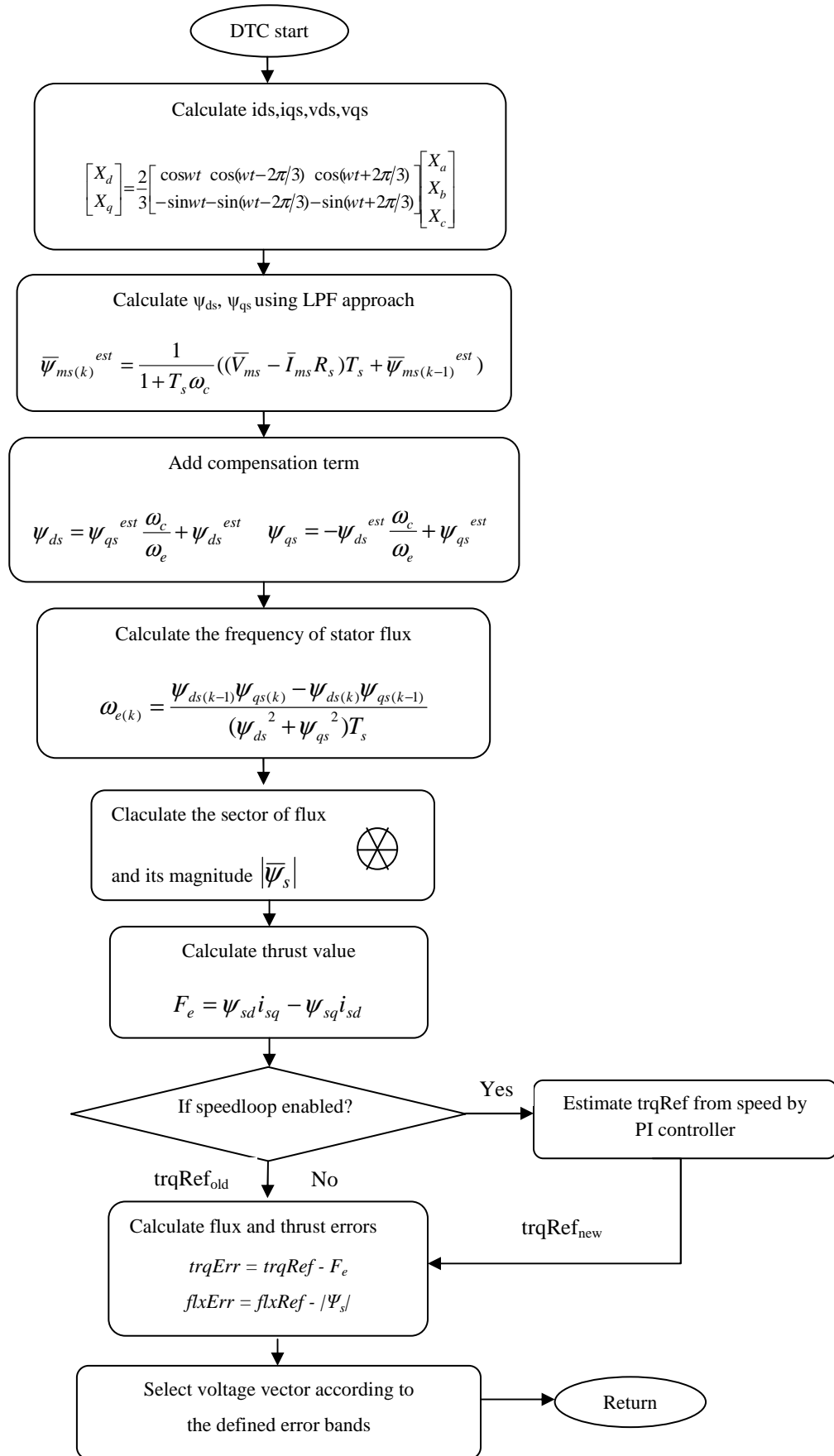
The compare register is set to match the duty ratio value and it decides the active duration time of the PWM output. When the value of timer count register during counting up period matches the value stored in the compare register, the PWM output is set active and it stays in this state until the value of the count register during down counting matches the compare register value as shown in Figure 8.24.
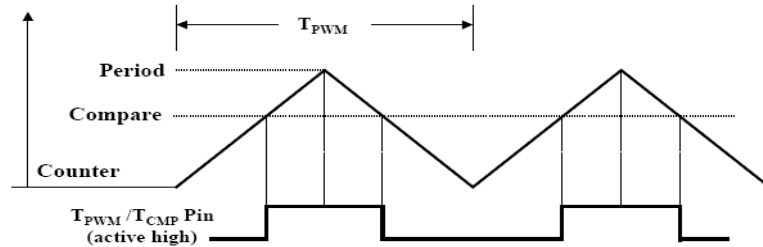
Figure 8.24. Symmetric PWM Waveform [105]

The polarity of the PWM outputs is set active high (AH) to match the gate drive requirement. The programmable dead band feature of the PWM generator is also used to prevent shoot. According to the datasheet, IRGPS60B120KDP IGBT has a maximum 800-ns turn off delay time that makes the selection of dead band of 2 μs reasonable to ensure safe operation of the inverter.

The flux reference is chosen in accordance with the load level. When the rated torque is required, rated stator flux should be developed. Since the motor under no-load conditions draws as little as 50% of its rated magnetizing current, a lightly loaded motor does not need rated stator flux to produce the required torque [110]. Thoughtlessly selected the stator flux reference causes excessive heating that lowers the efficiency.

8.5 Summary

In this chapter, the algorithms mentioned in the preceding chapters using the TMS320F2812 eZdsp are introduced. A brief description of the dsp implementation platform is also given. The developed control strategy using DSP is based on generation of necessary gate pulses by processing input signals and adding user interface. The core control routines used in the DSP software are described, tested by building the related 'C' code and the test results are presented.

CHAPTER 9

EXPERIMENTAL WORK

This chapter is related with the results taken and the problems countered during experimental study. At first, the generated three-phase voltages were given to resistive load to be ensured with the developed DSP program and hardware set-up. Figure 9.1 shows the generated 50Hz phase to neutral voltage waveforms with and without low pass filter at the inverter end with a modulation index of 0.5 under 30V dc link voltage. The switching frequency is at 5kHz.
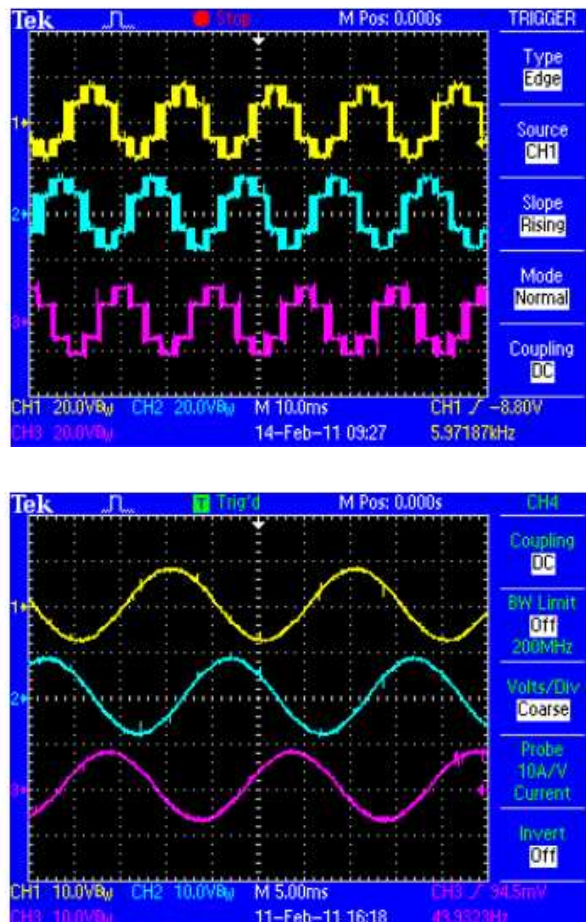
Figure 9.1. The generated phase to neutral voltages M= 0.5, f= 50Hz, Vdc= 30V
without/with LC filter at the inverter end

However, with the increase in dc link voltage, EMI became a major concern when DSP frequently reset caused by a trip signal in spite of no real fault condition. This is nuisance tripping occurs even at 40V dc link level. The unwanted interfering signal captured by digital signal oscilloscope (DSO) under 48V dc link seen in Figure 9.2 may come from noise sources via a radiation through space as electromagnetic waves, or by conduction.
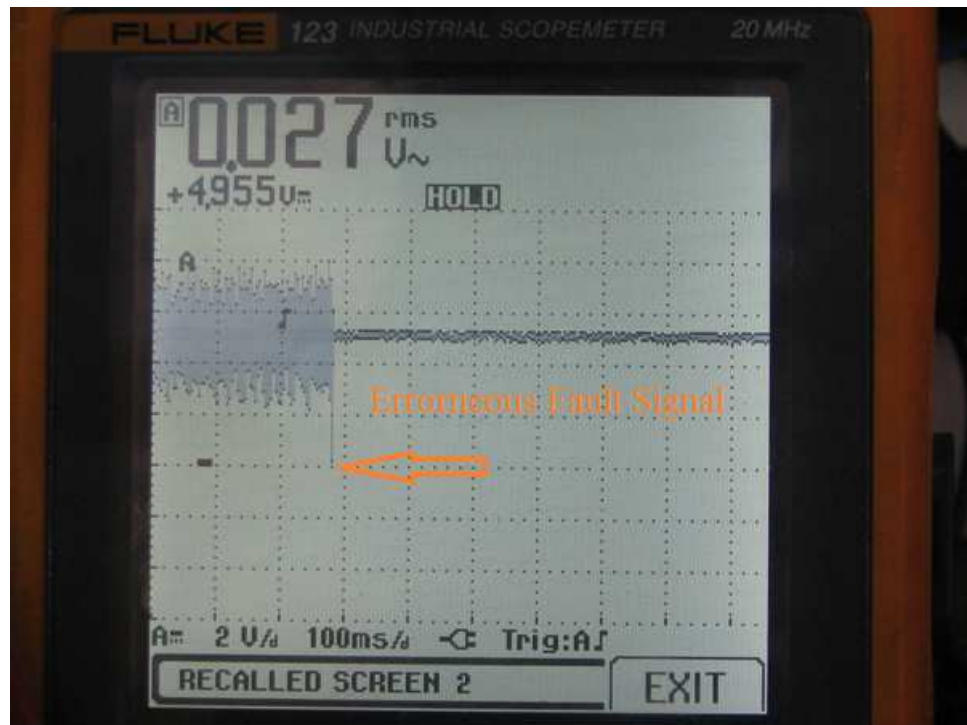
Figure 9.2.   DSO capture of the signal at the fault detection pin showing nuisance tripping related to EMI problem at 48V dc link

From the figure, the noise occurs in the form of narrow pulse associated with the PWM switching actions. Since the noise pulses are different from the real protection signals which are hold by latches in the fault detection circuit, a kind of digital filter was added in software to eliminate narrow pulses of which width less than 500ns.

With this noise elimination method, the system works well with the input dc voltage about 63V. The generated phase to neutral voltages at the low-pass filter end and at the inverter end is shown in Figure 9.3. The modulation index is 0.5 and the reference frequency is set to 50 Hz. The output voltage waveforms at the end of the LC filter are very clear as shown by yellow, blue and purple traces but for phase C at the inverter end shown by green line is so noisy because of the resistive nature of the

load. The red line shows the line-line voltage. Experimental results show that the amplitude of the output voltage is about 18V which is very close to the calculated theoretical value.
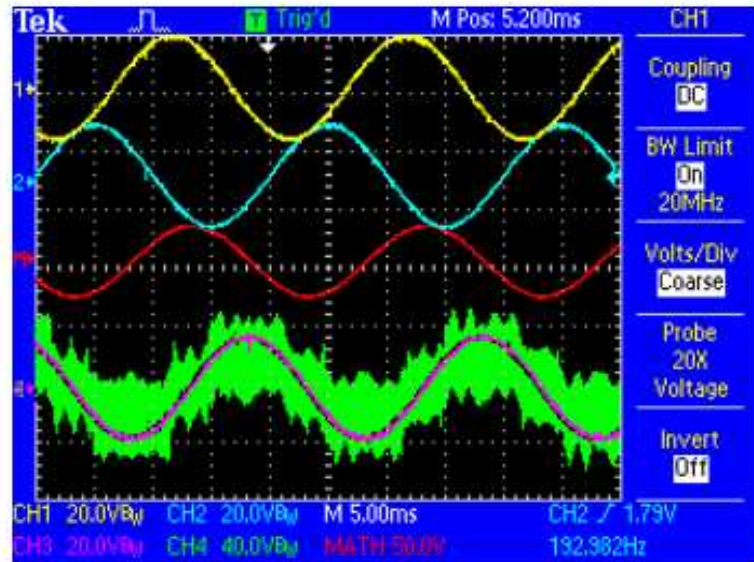
Figure 9.3. The generated phase to neutral voltages M= 0.5, f= 50Hz, Vdc= 63V

However, the elimination of the narrow pulses was not a solution to the noise problem above 68V. After understanding the EMI immunity of the developed control system is not acceptable, several precautions were taken against EMI to ensure the success of the drive system.

9.1 Electromagnetic Interference (EMI)

EMI results from the switching systems in which the current or voltage changes rapidly. The higher the switching dv/dt and di/dt is, the higher EMI emission will be. Therefore, high voltage / high current power supplies, power converters, contactors and motor-drives can cause serious electromagnetic disturbances. These affect the operation of the susceptible devices such as DSP's, PLCs or I/O modules.

EMI can be radiated through space as electromagnetic waves, or it can be conducted along a cable. Conduction can take the form of common-mode or differential-mode currents. In differential-mode, the currents are equal and opposite on the two wires. Common-mode currents are almost equal in amplitude on the two lines, but travel in the same direction. These currents are mainly caused by the coupling of radiated

EMI to the power lines and by stray capacitive coupling to the body of the equipment [111,112].

The conducted EMI noise in a PWM inverter are mainly due to the many small capacitive couplings exist in the drive systems as shown in Figure 9.4 [112,-114].
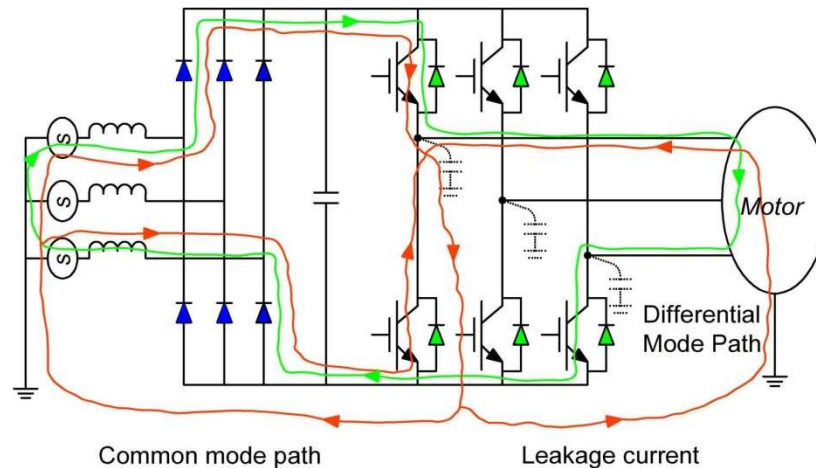
Figure 9.4. Common mode and differential mode noise paths in PWM drive
(modified from [112])

The design measures for EMI protection should be considered even in designing the circuits, which cannot be added afterwards. For example, to minimize the inductive coupling, it is good practice to keep PCB tracks as short and wide as possible, especially for power supply lines in which the signal tracks which carry fast changing currents. Other than PCB design, the taken precautions to minimize the EMI problem are listed as in the following;

- Power circuit (rectifier, dc link filter, inverter) part is not share the same metallic cabinet with control circuit including TMS320F2812 board as seen in Figure 9.5. Both parts are screened individually and the cabinets and cabinet doors are properly earthed. By this way noisy and clean leads were separated from each other as shown in Figure 9.6.

146
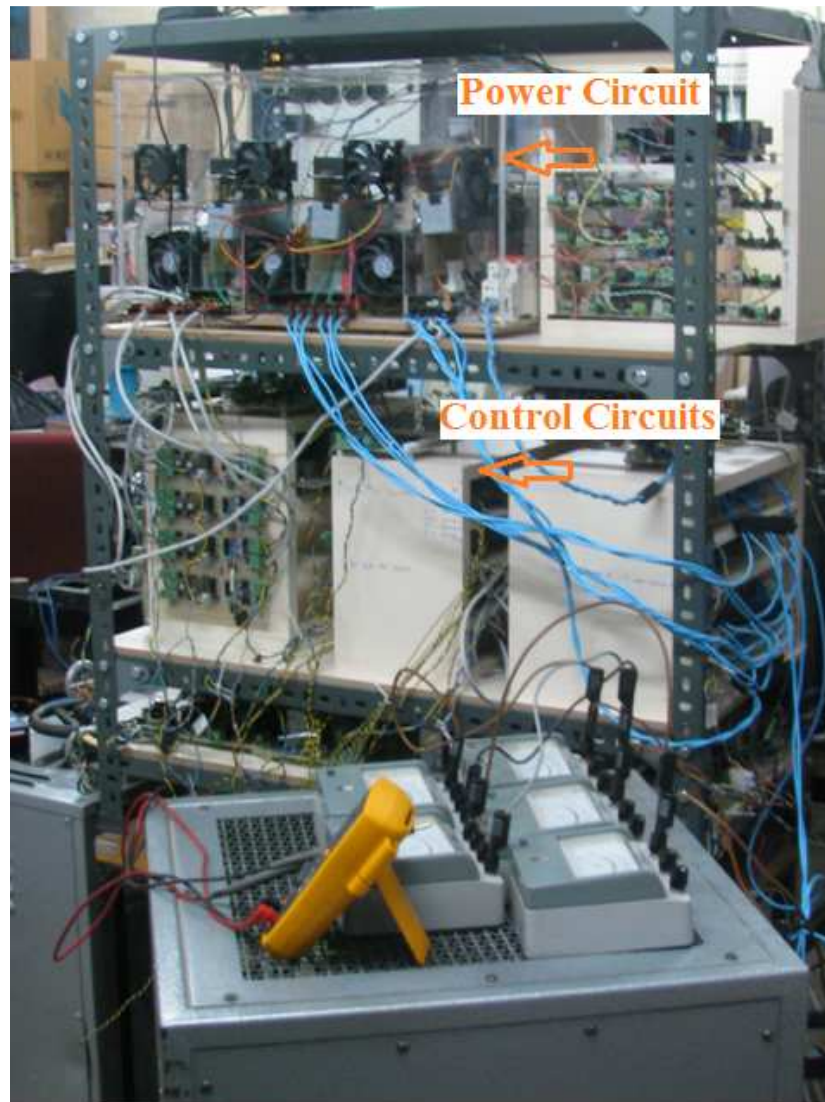
Figure 9.5. Experimental set-up view before countermeasures were taken against EMI

Shielded power cables are also used between two cabinets and both ends of the shields are grounded at 360º in order to suppress EMI/RFI. To allow the entrance of the cables connected to the controller, holes are made in the side of the enclosures. The size of the holes is small enough so that the shielding ability of the enclosure is not distorted. The length of the hole is smaller than the wavelength of EMI.
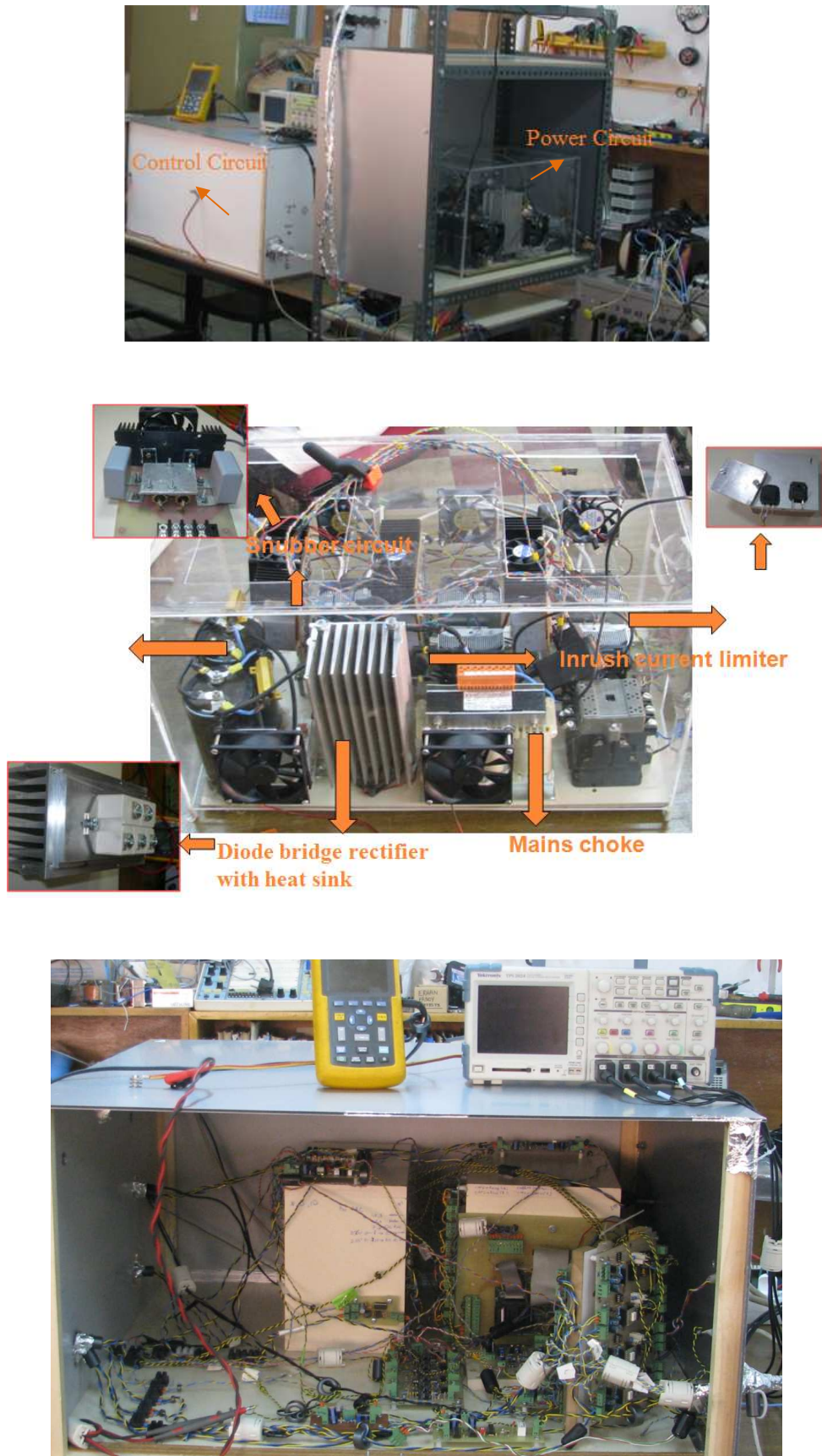
Figure 9.6. Experimental set-up view after countermeasures were taken against EMI

- Line filter as shown in Figure 9.7 is added on the input side of the three phase rectifier after the variac to reduce the effect of noise coming from commercial power line. It comprises of a toroidal ferrite, capacitance of the order of 0.1 µF, and two capacitors of the order of nF, a resistance of the order MΩ and a varistor to protect from over voltage.
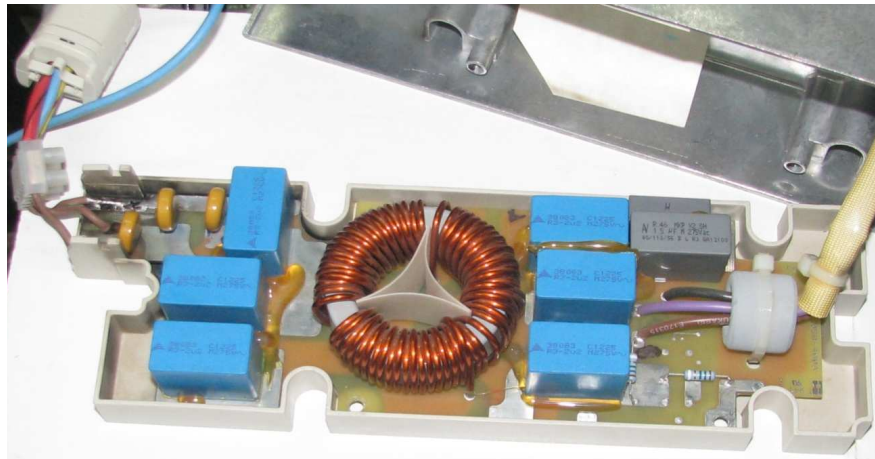
Figure 9.7. The photo of the three-phase line filter

- A power line filter is connected in the inputs of linear power supplies of control circuit cards. This filter can prevent EMI/RFI of the circuit with other adjacent circuits.
- Decoupling capacitors are placed between the supply rail and ground as near as possible to each alone standing logic IC.
- Since the usage of the long cables is more susceptible to EMI than the short cables, the cables are kept as short as possible.
- Cables are also filtered using ferrite cores possibly. Ferrite is general term for a class of non-conductive ceramics. They are especially effective in damping of high frequency oscillations above 1 MHz. To maximize their effect, the wire through the ferrite core is wrapped two times to attenuate high frequencies.
- RC filter and metal oxide varistor (MOV) for contactor coil and suppressor diode for dc relay coil are used for reducing EMI.

- The cable length between the inverter and the motor is kept as short as possible and the chassis of the motor was grounded for safety reasons during experimental study.

For the motors rated at 380V, the required DC bus voltage is about at 550 V. With the short rise and fall times of IGBTs, the rate of change of the VSI output voltage reaches approximately 0.5-11 kV/µs.

The short motor cables can be considered as resistors with 50 Hz. However, in case of PWM IGBT inverter having short rise and fall times typically in the range of 0.05-1µs, the long cables represent shunt capacitances and stray inductances similar to the transmission lines as shown in Figure 9.8 [112].
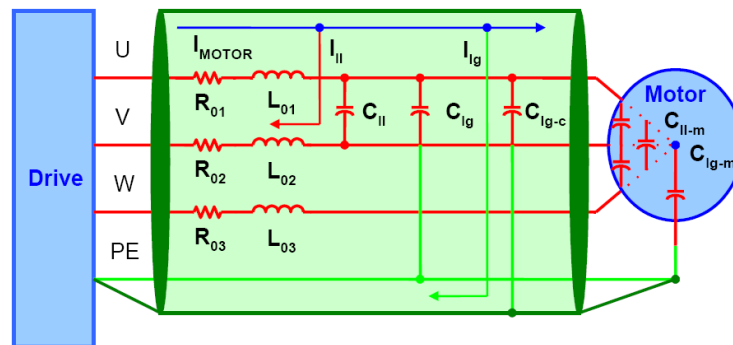
Figure 9.8. Transmission line equivalent circuit of long cables [112]

According to transmission line theory, a forward travelling pulse is either partially or fully reflected at the receiving end depending on the impedance mismatch in the system [114]. When the motor impedance is greater than the characteristic line impedance; the voltage is reflected from the motor back toward the inverter. Therefore, voltage doubling at the motor terminals may occur with long cables and IGBT's with small rise times. This over-voltage transient has been known to cause premature failure of the motor and cable insulation in many installations [114]. The critical cable lengths for various rise times are given in Table 9.1.

Table 9.1. Minimum cable length after which voltage doubling occurs at motor terminals. ([115])

Pulse rise time	Critical cable length
0.1 µs	6 m
0.5 µs	39 m
1 µs	59 m
2 µs	118 m
3 µs	177 m
5 µs	295 m

Additionally, the charging and discharging of the stray capacitances of the cable with steep changing of the inverter output voltage cause excessive peak currents. Particularly, the charging current of these stray capacitors causes over current faults.

The usage of dV/dt filter is one of the solutions to protect the system from the destructive effects of peak voltages facilitated by long cable runs between the inverter and motor.

Other than generating the voltage spikes on the motor terminals, the rectangular voltage forming characteristics of an inverter bring about the additional losses in the motors caused by the high frequency current ripple. These problems are solved by installing a low pass filter at the output terminal of the inverter.

A three-phase LC filter shown in Figure 9.9 is selected in this thesis due to its simplicity.
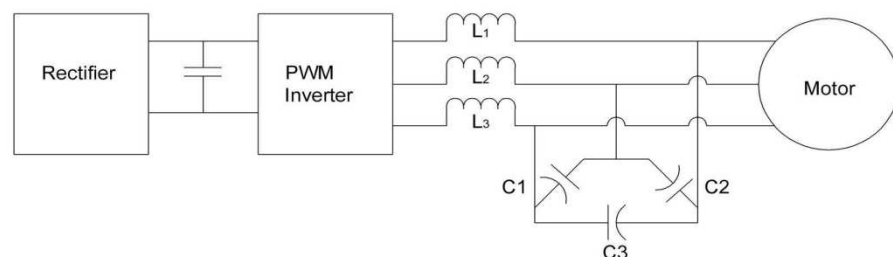
Figure 9.9. LC filter connection diagram

In designing the LC filter, different design criteria can be considered. These criteria may include resonance frequency, filter size, cost and losses. In our case, the design is a compromise between the filtering performance and the cost.

As a rule of thumb, for a fundamental frequency of 50Hz, the resonance frequency has to be at least 500Hz and the PWM frequency of the inverter has to be at least 5 kHz [116, 117].

According to the general LC filter output equations, the resonance frequency is calculated by (9.1).

$$f_r = \frac{1}{2\pi\sqrt{L_f C_f}} \tag{9.1}$$

The filter capacitor provides a low-impedance path for high-frequency currents. These currents are limited mainly by the filter inductor. Capacitor value is calculated by (9.2) to keep the max dV/dt at motor's terminal within the limits required by the design specifications of dv/dt.

$$C \geq \frac{i_{peak,motor}}{\frac{dv}{dt}max} \tag{9.2}$$

Another design criterion is the voltage drop in the filter inductor. The voltage drop will be significant is the fundamental frequency is high.

Even though capacitor and the inductor values planned to use are 40 uF and 1.2 mH, since 8uF and 15mH inductor were available in the laboratory, so they were used forming 460 Hz resonance frequency LC filter.

The frequency of the output waveform is planned to change from 20 to 100 Hz. Therefore, the minimum resonance frequency of the filter should be 1000Hz which is suitable for the switching frequency of 15 kHz.

The sinusoidal LC filter may not require an additional resistor if the inverter output voltage does not include significant harmonics near the system resonance frequency. Furthermore, the motor impedance can be considered as a damping resistance. Unfortunately, the LC filter also may produce some problems, namely the resonance frequency, the common mode voltage on the motor terminals against the ground. The damping resistance in series with the filter capacitor is alleviated this resonance phenomenon.

- A common mode current is also caused by the cable asymmetries [118, 119]. If the cables are oriented in a totally symmetric fashion providing equal capacitors and inductors like in Figure 9.10, then there is less contribution to common mode current.
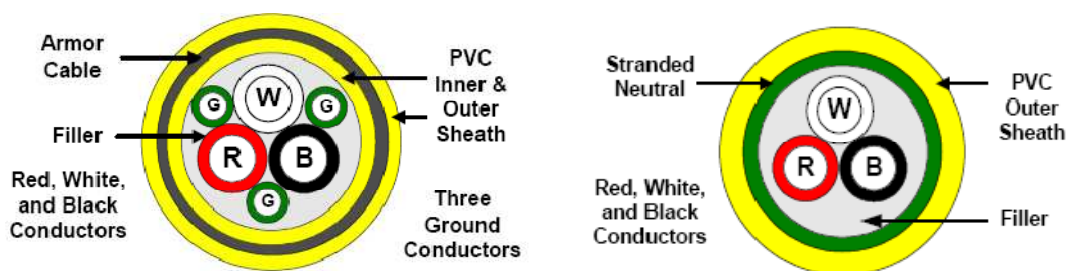
Figure 9.10. Symmetrical cable [112]

When the four wires cabling as shown in Figure 9.11 is used as in this study, the capacitance and inductance balance is distorted, and as a result of this considerable common mode current is induced.
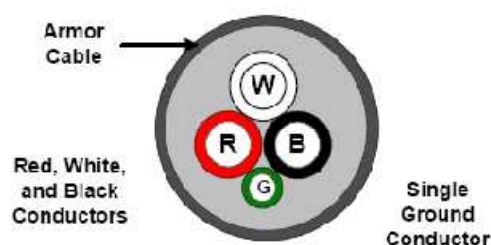
Figure 9.11. Unsymmetrical cable [112]

The improvement after the taken EMI countermeasures mentioned above are observed clearly on the signal at the fault detection pin as given in Figure 9.12 in contrast to Figure 9.2, both were captured at 60V dc link.
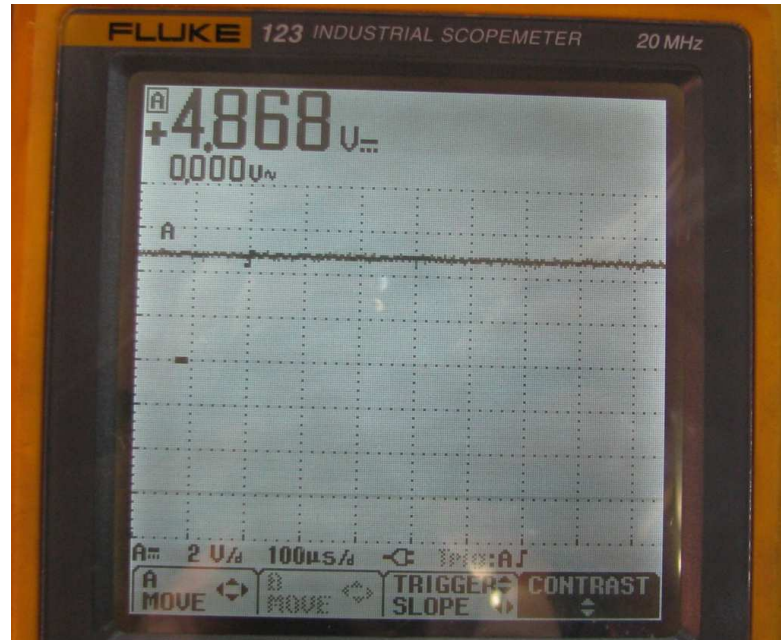
Figure 9.12. DSO capture of the signal at the fault detection pin at 60V dc link
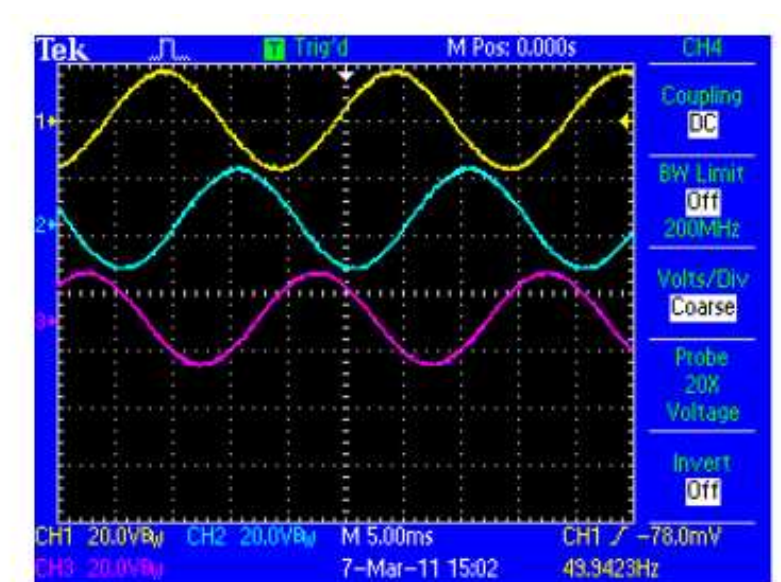
Figure 9.13. The generated phase to neutral voltages M= 0.5, f= 50Hz, Vdc= 60V

After examining that the systems worked satisfactorily at a low voltage (60V), the DC voltage was increased in steps of 30V up to 250V. However, noise still comes out with increasing voltage. When the DC bus voltage reaches 250V, an increased noise level on the fault detection signal is clearly seen as shown in Figure 9.14.
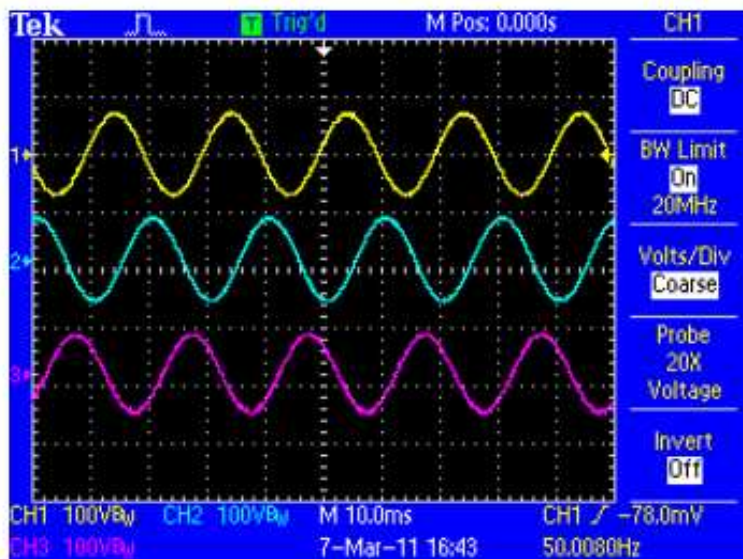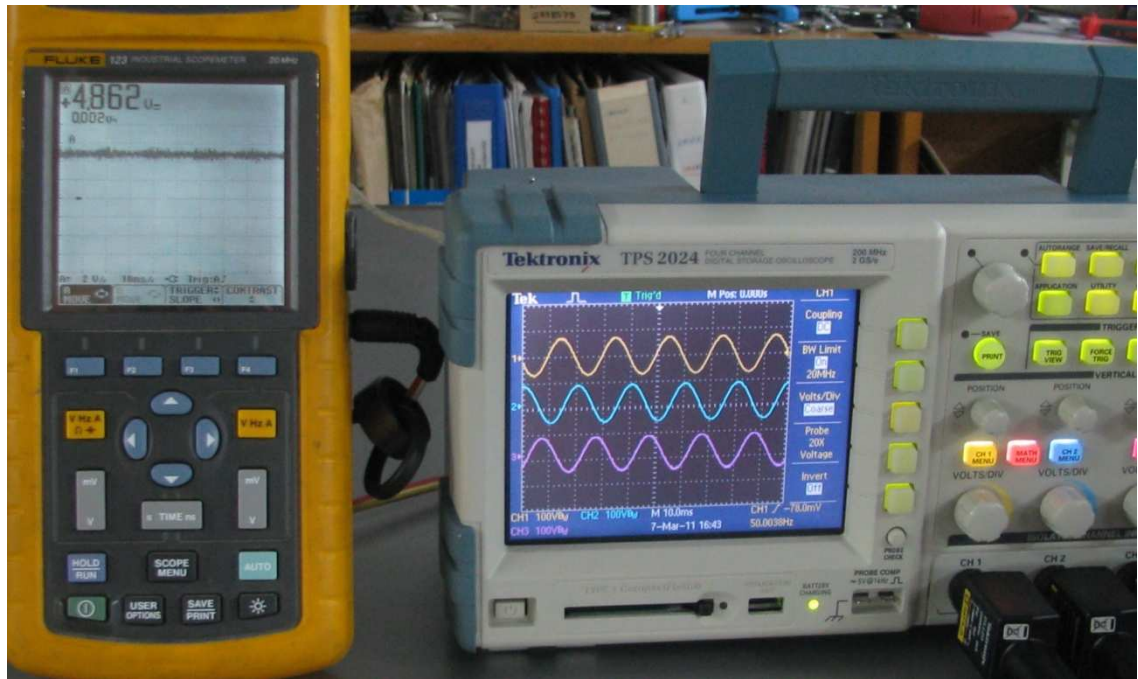
Figure 9.14. DSO captures showing the signal at the fault detection pin at 250V dc link and the generated 3-phase voltage signals after LC filtering with countermeasures were taken against EMI

After increasing the dc link voltage to 275V, the gate resistor of the lower IGBT in the middle leg was burn out. The problem is the peak power capability of the gate resistor was not enough to carry the peak current flowing in the gate-emitter circuit. During turn-on process the gate driver circuit is trying to charge the input capacitance of the IGBT (4300 pF) from 0 to 18V in 50ns. According to (9.3), this process might causes 1.548A flowing through 0.75W, 10Ω gate resistor.

$$I_{g,peak} = \Delta V . C / \Delta t \qquad\qquad (9.3)$$

To decrease the peak turn-on current, the gate resistor for IGBT is increased to 15Ω and the positive bias supply voltage is decreased to 15V. By doing that EMI emissions are further reduced. It is better to use surge proof, metal film resistors.

After putting the control circuits into the cabinet, the gate driver circuit is away from the inverter. Although the gate-emitter signals are transferred through twisted cables, about 55 cm long distances may lead to a higher inductance in the gate-emitter circuit. Since as stated in [120] is that every 1 cm of 0.5 mm od wire has an inductance of 7.26 nH, an assumption of 100 nH stray inductance in the gate-emitter circuit with a di/dt of 30A/μs would be generate a surge voltage voltage of 3V. This can be result in a reduction in the applied gate emitter bias voltage below 15V and hence an increase in rise time of IGBT. Moreover, depending on the stray inductance and the input capacitance of the IGBT, reflection can be occur in the IGBT side causing gate-emitter voltage to rise above its rated value. This phenomenon is also improved by paralleling a 10 KΩ resistor between the gate-emitter terminals of an IGBT. Furthermore, the distance between the gate driver and the IGBTs is kept as close as possible. However, the use of fiber optic cable is the most reliable solution but it is not preferred due to its cost problem.

After LC filtering with taken countermeasures against EMI, DSO captures showing the three-phase input currents of the rectifier and voltage and current waveforms of motor are presented in Figure 9.15.a, Figure 9.15.b and Figure 9.15.c, respectively. The dc link voltage is 250V, the modulation index is 0.5 and the reference frequency is set to 25 Hz. All of them satisfy the theoretical expectations.
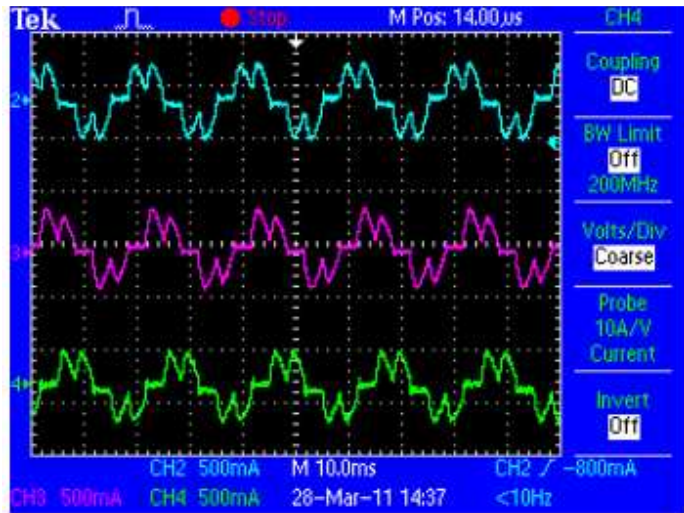
Figure 9.15.a. 3-phase diode bridge rectifier current waveforms, f=25Hz
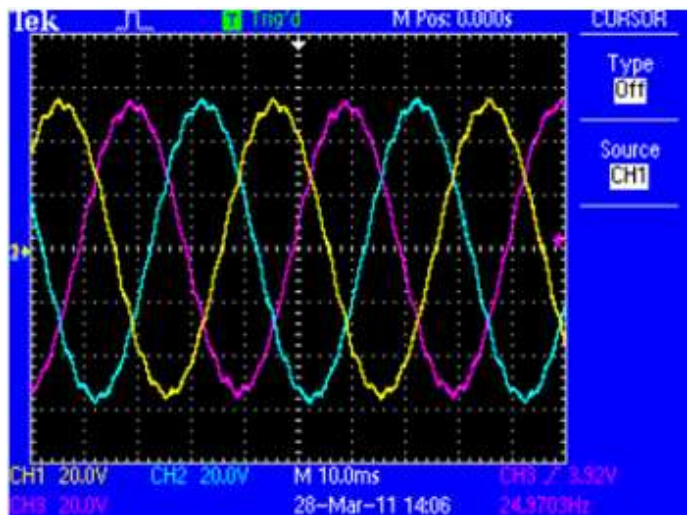
Figure 9.15.b. 3-phase motor voltage waveforms signals after LC filtering showing
the signal at 250V dc link, f=25Hz
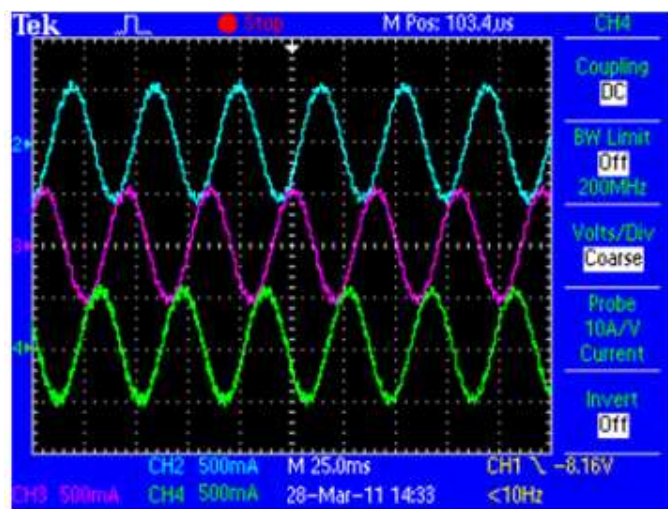
Figure 9.15.c. 3-phase motor current waveforms signals, f=25Hz

157

9.2 Results Related with ZSI Experiment

The developed Z-Source inverter prototype used in the experiment is shown in Figure 9.16. The Z-source network has the following parameters: $L_1=L_2=2.3mH$, $C_1=C_2=3300\mu F$. The inductors and capacitors are oversized in the prototype for possible regenerative operation. There cannot be any DC capacitors right across the inverter in the shoot-through states. With using a traditional snubber circuit, a huge loss will occur during the shoot through, thus the traditional snubber circuit cannot be applied in ZSIs. A special snubber circuit is implemented in order to reduce the overshoot as shown in Figure 9.16. During experiment, the switching frequency is at 5 kHz and the modulation index is selected as 0.85.
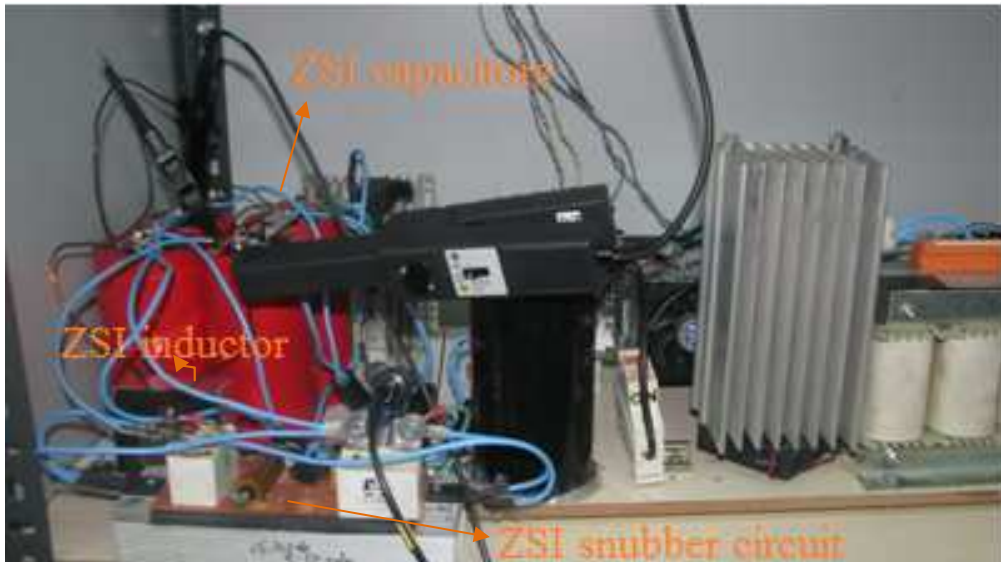
Figure 9.16. Z-source view

The experimental results are presented for two cases: the non-shoot-through mode and the shoot-through mode.

i) Results during normal operation (non-shoot-through mode):

For the first case shown in Figure 9.17, the input dc voltage is adjusted at 28V. For the second case shown in Figure 9.18, the input dc voltage is adjusted at 50V. As expected, the z-source capacitor voltage is the same as the input dc voltage for both cases. The z-source input current is less than 0.5A since no boost is applied. The voltage across the inverter bridge is close to 28V for the first case and 50V for the second case.
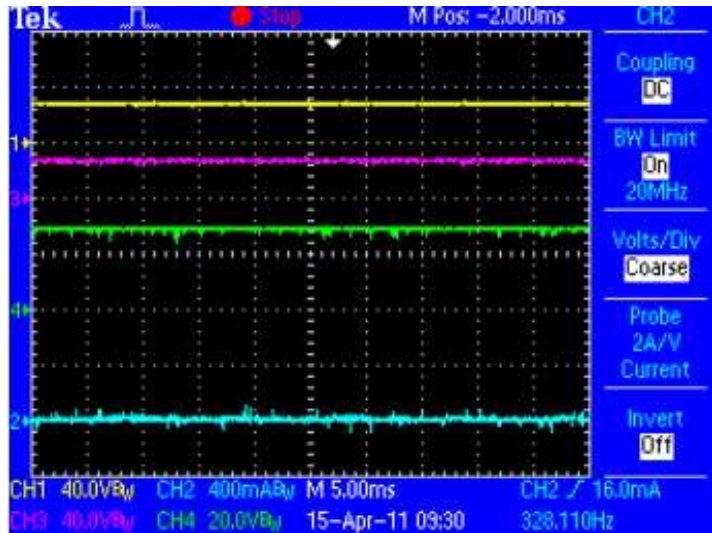
Figure 9.17. Results with no boost at 28V (yellow: input dc voltage, purple: Z-source capacitor voltage, green: inverter input voltage, blue: Z-source input current)
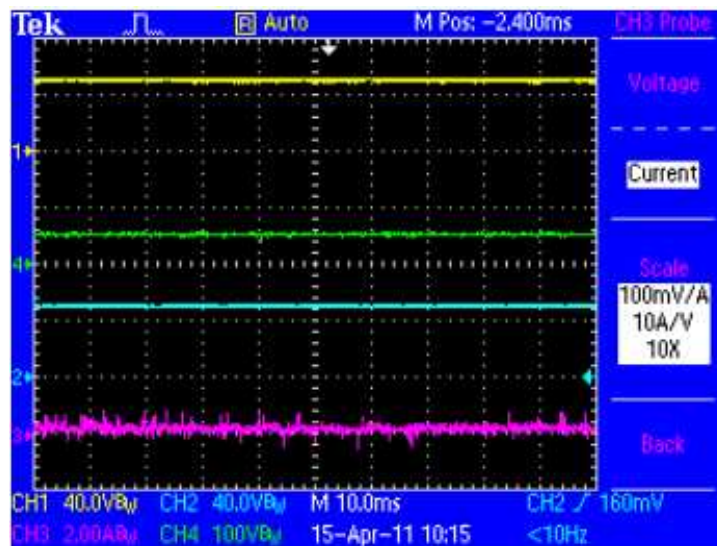
Figure 9.18. Results with no boost at 50V (yellow: input dc voltage, green: Z-source capacitor voltage, blue: inverter input voltage, purple: Z-source input current)

Based on the experimental results, without shoot-through, the inverter operates just as a traditional inverter, where the capacitor voltage equals the input voltage as expected.

ii) Results with Boost Mode:

The shoot-through duty ratio of 0.18 is selected at first for 50V dc-link voltage. The pair of switching signals showing the shoot time belonging to the middle leg is given in Figure 9.19. According to the switching pattern of ZSI generated by using the Table 6.1, for a 5kHz switching frequency 6 shoot period is seen in the bridge voltage as shown in Figure 9.19. The inverter bridge voltage is equal to zero during shoot times and equal to the peak value defined by the boost factor given by (6.8) during non-shoot-through state.
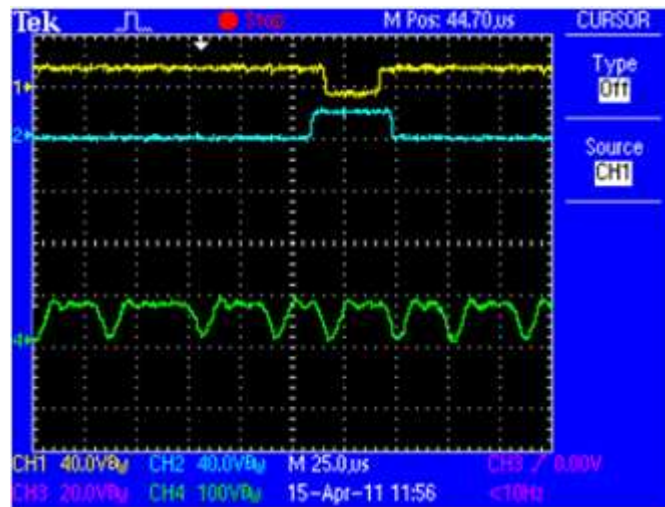
Figure 9.19.The inverter bridge voltage at the shoot periods

The obtained results with a boost factor of 1.56 are shown in Figure 9.20.
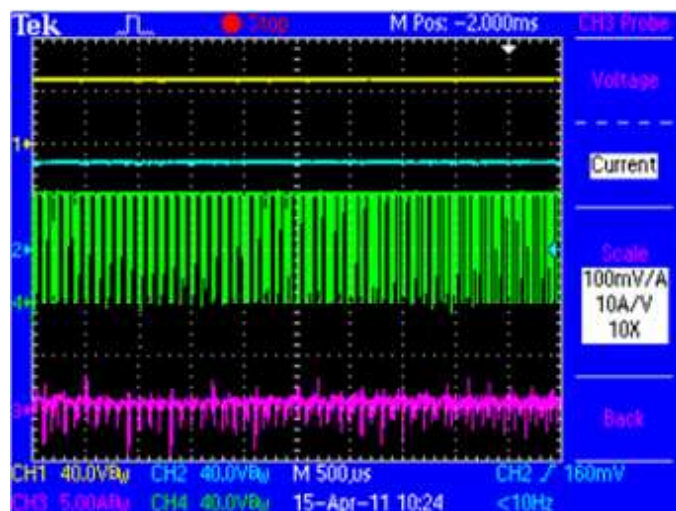
Figure 9.20. Results with shoot through duty ratio of 0.18 at 50V dc input voltage (yellow: input dc voltage, blue: Z-source capacitor voltage, green: inverter input voltage, purple: Z-source input current)

160

According to Figure 9.20, the average of the dc link voltage of the bridge inverter is shown by blue line is about 64V which is the expected theoretical value calculated by (6.7) and the peak value of the pulsating dc-link inverter voltage is very close to 78V which is the expected theoretical value calculated by (6.8).

As a second case, the result obtained with a boost factor of 1.9 is shown in Figure 9.21. The average of the dc link voltage of the bridge inverter is shown by blue line is 72V which is very near to the expected theoretical value calculated by (6.7) and the peak value of the pulsating dc-link inverter voltage is very close to 95V which is the expected theoretical value calculated by (6.8).
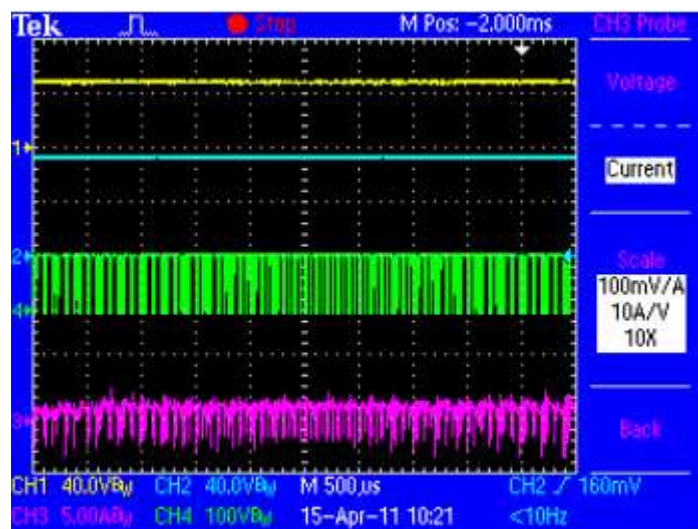
Figure 9.21. Results with shoot through duty ratio of 0.235 at 50V dc input voltage (yellow: input dc voltage, blue: Z-source capacitor voltage, green: inverter input voltage, purple: Z-source input current)

From Figure 9.21, the increase in the input current of z-source inverter is clearly seen as anticipated.

It is successfully demonstrated that the Z-source inverter operating in boost mode with shoot-through can greatly boost the dc link voltage as desired.

Furthermore, Z-source inverter produces PWM voltage waveforms just like the traditional inverter. Thus, a LC filter is added after the inverter to achieve sinusoidal waveform. The filter parameters are $L = 25$ *mH* and $C = 8uF$.

The experimental results are given for a 50V dc link voltage in Figure 9.22 for no boost and Figure 9.23 with 1.9 boost conditions.
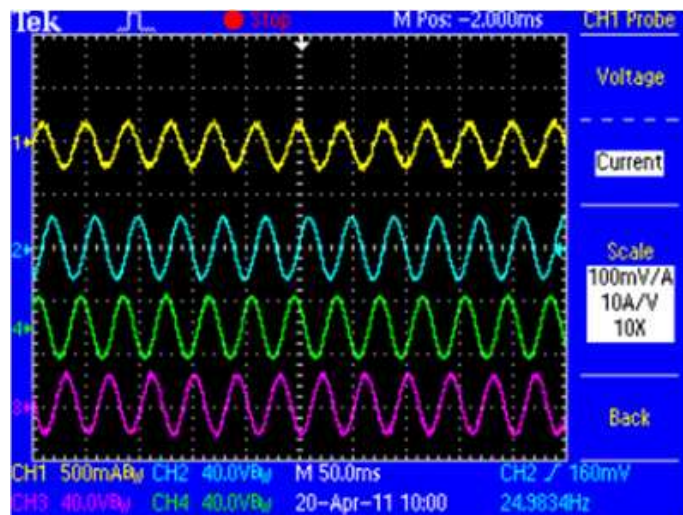
Figure 9.22. Motor voltages and current waveforms without boost
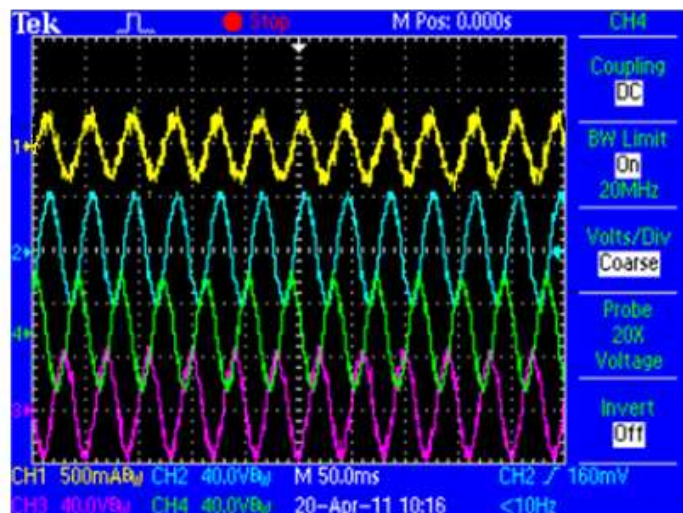
Figure 9.23. Motor voltages and current waveforms with B=1.89

According to the simulation results, the obtained motor voltages and current at the end of the LC filter are sinusoidal, which confirms that the Z-source inverter will produce low harmonics with a boost capability.

9.3 Summary

A prototype has been built to further verify the operation, theoretical relationships of voltage boost of the presented z-source LIM drive system. Experimental results verified the effectiveness of the implemented z-source inverter based on V/Hz control strategy using fixed-point DSP TMS320F2812. With the developed z-source inverter based on V/Hz control, the AC voltage applied to LIM is no longer limited and is boosted 90% which is beyond the limit achieved by conventional VSI. The obtained waveforms clearly demonstrate that the dc capacitor voltage can be boosted and maintained to a desired level, which is the average input inverter voltage. The results obtained with the prototype z-source inverter circuit are slightly differed from those obtained from theoretical calculations due to the power losses on the circuit components in the experiment circuit.

CHAPTER 10

CONCLUSIONS

The objective of this thesis is to analyze, design and realize a flexible z-source inverter based LIM drive system. The developed system is based on ezDSPTMS320F2812, all the required experimental hardware components including power circuit and interface circuits. To solve this task, both theoretical and practical system are designed, simulated and constructed.

The mathematical model of LIM is necessary in order to obtain better control performance. In chapter 2, the LIM mathematical model are given with an analogy to rotary induction motor and the related Matlab/Simulink model have been presented. Actually, the operation principles of LIM are similar to the traditional rotary induction motor. However, LIM's control characteristics are a bit more complicated due to finite length of its primary. As a result of this feature, LIM has an end effect phenomenon causing attenuation in air-gap flux also in thrust. For achievement of better LIM control, the end effect is considered in mathematical modelling of LIM. The LIM mathematical model with end-effect is developed in stationary reference frame and the developed model is simulated by using Matlab/Simulink. The detractive influence of the increased supply frequency, the decreased seconder resistance on thrust is shown in chapter 4 by means of simulation results.

The direct thrust control (DTC) is chosen as vector control method for LIM. In DTC method, flux linkage and electromagnetic thrust are controlled directly and independently by hysteresis controllers and selection of optimum inverter switching modes. In this control concept, flux and torque control loop is required. In addition, DTC requires only one parameter, primary resistance, among the motor's all parameters during a control operation. In this thesis, DTC of LIM is mathematically investigated and its simulation model is developed.The performance of direct thrust controlled LIM

drive with different hysteresis band amplitudes for thrust and stator flux is simulated with Matlab/Simulink. It has been deduced that the width of the hysteresis bands influences the drive performance in terms of flux and torque ripples, current harmonics and switching frequency of the power device. According to simulation results, hysteresis band for stator flux mainly influences the stator current; on the other hand, hysteresis band for thrust mainly affects the switching frequency. Consequently, it is better to choose the small hysteresis band for flux for reducing the current harmonics by considering their heating effect and small hysteresis band for thrust to reduce thrust pulsations with using high-speed switching devices and processors.

A method for better flux/thrust estimation for DTC is proposed in considering the end effect phenomenon of LIM and its viability is proven by using Matlab/Simulink. Furthermore, the ordinary flux estimation algorithm based on open loop integration does not work well practically due to the presence of noise and dc offsets. Offset errors in the measured voltages and currents are mainly resulting from the analog signal conditioning circuits and sensors. The problem arises from the interfacing of sensor-generated signals with the A/D input of DSP. Since ezDSPTMS320F2812 accepts analog input signals in the range 0-3.3V, a dc offset of 1.5V is added to the ac signal produced by the sensor. However, the dc offsets at the A/D input differ due to different voltage drops on wires or connectors. In order to alleviate this effect, a software routine is developed for calibrating the offset for each ADC channel. The signal is sampled 30000 times before motor starting and the no-load offset for each channel is obtained.

Furthermore, in chapter 5 the flux estimation algorithm has been modified to work on a real system for digital approximation and measurement errors as explained. A discrete form of the low-pass filter is used instead of the pure integrator in stator flux estimation to prevent the integral instability. Moreover, the stator flux magnitude and phase angle errors compensation are also accomplished.

Z-source inverter based LIM drive was not dealt with before in the literature. This recently developed inverter structure is used to overcome the problems in the traditional voltage source inverters. It employs a unique impedance network coupled with the inverter main circuit to the dc voltage that is rectified from mains ac voltage. This new

power conversion topology is studied as a step up converter in the dc link which converts the input dc voltage to a higher output dc voltage for three phase inverter bridge. Furthermore, the reliability of the voltage source inverter is improved, since there is no need for the dead times to avoid miss-gating from EMI that causes the destruction of the v-source inverter.

Throughout the study, the steady state mathematical analysis of ZSI is completed and the related simulation results are also presented in chapter 6. The simulation results closely agree with the theoretical calculations because both theoretical analyses and simulations have been conducted under ideal conditions.

The hardware design procedure for LIM drive system is presented in chapter 7. The capability of each developed hardware circuit and the guidelines for selecting the required circuit components are explained in detail. The experimental control design details and flow charts to implement the control algorithms are presented in chapter 8. The developed experimental set-up is adaptable to any DSP controlled motor control system.

The obtained experimental results with the developed prototype circuit related with ZSI based on V/Hz control are presented. The operation of the ZSI and the effectiveness of the voltage boost are verified by experimental results. With the developed z-source inverter based on V/Hz control, the AC voltage applied to LIM is no longer limited and is boosted 90% which is beyond the limit achieved by conventional v-source inverter. The results obtained in the prototype circuit have slightly differed from those obtained from theoretical calculations. The reason for this is the power losses on the circuit components in the experimental circuit. The forward voltage drop on the input diode of z-source inverter led to power losses because it carried all the input current. Additionally, the current through the z-source capacitors are also the source of power losses. Thus, the usage of lower ESR capacitors would also increase the efficiency. Furthermore, it is observed that the line current and voltage contains much less harmonics because of both the Z source inductors and capacitors compared with traditional VSI.

Prototype LIM drive system is designed and constructed to realize the experiments. The program developments for ZSI based LIM drive on ezDSPTMS320F2812 are completed and tested for V/Hz control and DTC. However, the developed prototype drive unit efficiency needs to be increased especially in terms of common mode voltage noise reduction. The important consequences of this study are that the application of ZSI based LIM drive becomes practical and viable with a low cost, and also better flux/thrust estimations are achieved for LIM.

10.1. Future Work

The simulations and experimental works of the studied methods show promise for future works. Because of circuit construction limitations, the developed methods could not be tested over a wide voltage ranges. Therefore, the experimental work is required to implement the developed techniques in the entire voltage range of LIM.

EMI problem is very important aspect of the motor drive system. The switching pattern of the three-phase inverter IGBT's also causes the pulsed nature of DC link current with different amplitudes and different durations. The conducted EMI noise from inverter switching is directly caused by the pulsating DC link current. Concerning the real plant application of the motor drive, EMI causes a nuisance tripping of the inverter by influencing the control circuits. How to solve the EMI effectively by using soft-switching techniques, hardware improvements by using smd circuit construction and laminated dc busbar design for minimizing the stray inductance of the dc link should be a topic of the future work.

To reduce the thrust and flux ripples, an improved DTC algorithm for LIM in which the application of the voltage vector having variable duty period in accordance with the error status in each sector could be realized practically.

The online primary resistance measurement algorithm can be developed and embedded into DTC and V/Hz software programs. Sensorless operation of the LIM drive system could be introduced. It will reduce the number of sensors used in the system. This will lead to a lower cost of the whole system.

APPENDIX A

THE PARK TRANSFORMATION

In the late 1920s, R.H. Park introduced a revolutionary approach to electric machine analysis [31]. He formulated a change of variables which replaced variables such as voltages, currents, and flux linkages associated with fictitious windings rotating with the rotor called direct-quadrature. Main reason, why to transform three phases a,b,c system to dq0 is to simplify description of system. Instead of equation for each phase, there will be only, two dimensional system with direct- and quadrature-axis. It has the unique property of eliminating all time varying inductances from the voltage equations of three-phase ac machines due to the rotor spinning.

The transformation from $X_{abc} = \begin{bmatrix} X_a \\ X_b \\ X_c \end{bmatrix}$ (three-phase coordinates) to $X_{dq} = \begin{bmatrix} X_d \\ X_q \end{bmatrix}$ (dq rotating coordinates) is obtained through the multiplication of the vector X_{abc} by the transformation matrix T:

$$X_{dq} = T \cdot X_{abc} \tag{A.1}$$

where X represents any stator quantity to be transformed.

Park's transformation matrix T established according to Figure A.1 transforms three-phase quantities (voltage, current, flux linkage, etc.) into two-phase quantities developed on a rotating dq0 axes system, whose speed is w [31].

168
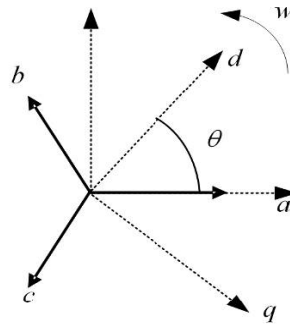
Figure A.1. Relationship between the dq and the abc quantities [31]

Assuming a balanced three-phase system (no zero sequence component), a three-phase vector representation transforms to dq vector representation (zero-axis component is 0) through the transformation matrix T, defined as:

$$T = \frac{2}{3}\begin{bmatrix} \cos wt & \cos(wt - 2\pi/3) & \cos(wt + 2\pi/3) \\ -\sin wt & -\sin(wt - 2\pi/3) & -\sin(wt + 2\pi/3) \end{bmatrix} \qquad (A.2)$$

The inverse transformation is calculated as:

$$X_{abc} = T^{'} \cdot X_{dq} \qquad (A.3)$$

The inverse transformation matrix is defined as:

$$T^{'} = \begin{bmatrix} \cos wt & -\sin wt \\ \cos(wt - 2\pi/3) & -\sin(wt - 2\pi/3) \\ \cos(wt + 2\pi/3) & -\sin(wt + 2\pi/3) \end{bmatrix} \qquad (A.4)$$

If an inverse Park transformation is made over the two axis of the static plane the resulting vector will contain the alpha - beta coordinates and then if the Clarke inverse transformation is done to that new vector, there will be a vector with three coordinates with the three desired sinusoidal signals.

169

APPENDIX B

INTERNAL CIRCUITRY OF HCPL-316J
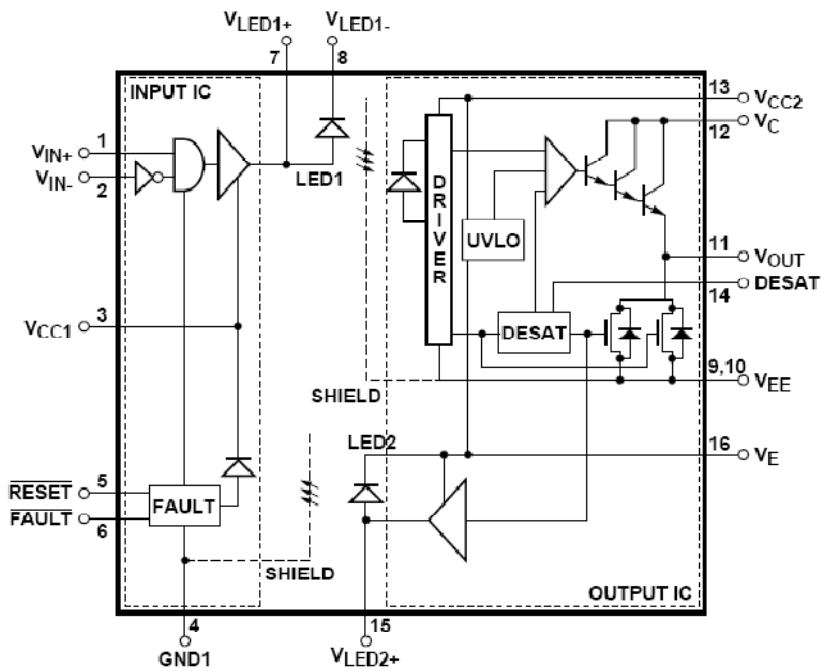
Figure B.1. Internal circuitry of HCPL-316J (datasheet)

The outputs (V_{OUT} and FAULT) of the HCPL-316J are controlled by the combination of V_{IN}, UVLO and a detected IGBT Desat condition.

Table B.1. Output control of HCPL-316J

V_{IN+}	V_{IN-}	UVLO ($V_{CC2} \cdot V_E$)	Desat Condition Detected on Pin 14	Pin 6 (FAULT) Output	V_{OUT}
X	X	Active	X	X	Low
X	X	X	Yes	Low	Low
Low	X	X	X	X	Low
X	High	X	X	X	Low
High	Low	Not Active	No	High	High

SOURCE CODES of SVM ROUTINE FOR ZSI AND DTC ROUTINE

```
//=======================================================================
// SVM routine for ZSI
//=======================================================================
void Mmysv(_iq gain, _iq freq, _iq freqmax, _iq tsh)
{       _iq tempduty;
        _iq tx, ty;
        if (freq < _IQ(0))
                {freq =  labs(freq);
                 cw = 1;
                 sectora = 5 - sector;
                 }
        else {cw = 0;
                 sectora = sector ;}
        stepangle = _IQmpy(freq,freqmax);
// Calculate new angle alpha
        alpha = alpha + stepangle;
        entryold = entrynew;
        if (alpha >= _IQ(1.0))
                alpha = alpha - _IQ(1.0);
        entrynew = alpha;
        ty = _IQsin(_IQmpy(entrynew ,pi_third));          // ty = sin(NewEntry)
        tx = _IQsin(pi_third - _IQmpy(entrynew,pi_third));    // tx = sin(60-NewEntry)
// Determine which sector
    if  (entrynew - entryold < 0)
    {     if (sector == 5)
                sector = 0;
          else
                sector = sector + 1;
    }
        tx = _IQmpy(_IQ(0.5),tx);
        ty = _IQmpy(_IQ(0.5),ty);
         if (tx + ty >Ts)
                {       tx = _IQmpy(tx, _IQdiv(Ts,(tx+ty)));
                        ty = _IQmpy(ty, _IQdiv(Ts,(tx+ty)));    }
        tz = _IQmpy(_IQ(0.5),(Ts-tx-ty));
        if (tsh >_IQmpy(_IQ(0.6667), tz))
                        tsh = _IQmpy(_IQ(0.6666), tz);
         switch (sector)
        { case 0://Sector 1 calculations
                da = tz- _IQmpy(_IQ(1.5),tsh);
                db = tz + tx - _IQmpy(_IQ(0.5),tsh);
                dc = tz + tx + ty + _IQmpy(_IQ(0.5),tsh);
                daL = tz-_IQmpy(_IQ(0.5),tsh);
```

```
                dbL = tz + tx + _IQmpy(_IQ(0.5),tsh);
                dcL = tz + tx + ty + _IQmpy(_IQ(1.5),tsh);
                break;
        case 1:  // Sector 2 calculations
                db = tz - _IQmpy(_IQ(1.5),tsh);
                da = tz + ty - _IQmpy(_IQ(0.5),tsh) ;
                dc = tz + tx + ty + _IQmpy(_IQ(0.5),tsh);
                dbL = tz - _IQmpy(_IQ(0.5),tsh);
                daL = tz + ty + _IQmpy(_IQ(0.5),tsh) ;
                dcL = tz + tx + ty + _IQmpy(_IQ(1.5),tsh);
                break;
        case 2:  // Sector 3 calculations
                db = tz - _IQmpy(_IQ(1.5),tsh);
                dc = tz + tx - _IQmpy(_IQ(0.5),tsh);
                da = tx + ty + tz + _IQmpy(_IQ(0.5),tsh);
                dbL = tz - _IQmpy(_IQ(0.5),tsh);
                dcL = tz + tx + _IQmpy(_IQ(0.5),tsh);
                daL = tx + ty + tz + _IQmpy(_IQ(1.5),tsh);
                break;
        case 3:  // Sector 4 calculations
                dc = tz - _IQmpy(_IQ(1.5),tsh);
                db = tz + ty - _IQmpy(_IQ(0.5),tsh);
                da = tx + ty + tz + _IQmpy(_IQ(0.5),tsh);
                dcL = tz-_IQmpy(_IQ(0.5),tsh);
                dbL = tz + ty + _IQmpy(_IQ(0.5),tsh);
                daL =  tx + ty + tz + _IQmpy(_IQ(1.5),tsh);
                break;
        case 4:  // Sector 5 calculations
                dc = tz- _IQmpy(_IQ(1.5),tsh);
                da = tx + tz-_IQmpy(_IQ(0.5),tsh);
                db = tx + tz + ty + _IQmpy(_IQ(0.5),tsh);
                dcL = tz-_IQmpy(_IQ(0.5),tsh);
                daL = tx + tz + _IQmpy(_IQ(0.5),tsh);
                dbL = tx + tz + ty + _IQmpy(_IQ(1.5),tsh);
                break;
        case 5:  // Sector 6 calculations
                da = tz - _IQmpy(_IQ(1.5),tsh);
                dc = ty + tz-_IQmpy(_IQ(0.5),tsh);
                db = tz +tx+ty+_IQmpy(_IQ(0.5),tsh);
                daL = tz-_IQmpy(_IQ(0.5),tsh);
                dcL = ty + tz + _IQmpy(_IQ(0.5),tsh);
                dbL = tz +tx+ty+_IQmpy(_IQ(1.5),tsh);
                break;
        } //end of switch case
// Convert the unsigned GLOBAL_Q format (ranged (0,1)) -> signed GLOBAL_Q format
(ranged (-1,1))
// Then, multiply with a gain .
        da = _IQmpy(_IQ(3.99999),(da-_IQ(0.5)));
        daL = _IQmpy(_IQ(3.99999),(daL-_IQ(0.5)));
        db = _IQmpy(_IQ(3.99999),(db-_IQ(0.5)));
        dbL = _IQmpy(_IQ(3.99999),(dbL-_IQ(0.5)));
        dc = _IQmpy(_IQ(3.99999),(dc-_IQ(0.5)));
        dcL = _IQmpy(_IQ(3.99999),(dcL-_IQ(0.5)));
        if (cw)
        {    tempduty = dc;
```

172

```
                    dc = db;
                    db = tempduty;
                    tempduty = dcL;
                    dcL = dbL;
                    dbL = tempduty;
                }
    } // END OF void Mmysv(_iq gain, _iq freq, _iq freqmax, _iq tsh)


//=====================================================================
// DTC Algorithm
//=====================================================================
interrupt void MainISR(void)
{ // Verifying the ISR
    IsrTicker++;
while (AdcRegs.ADCST.bit.SEQ1_BSY == 1)
            { };
        adc[0] = AdcRegs.ADCRESULT0;
        adc[1] = AdcRegs.ADCRESULT1;
        adc[2] = AdcRegs.ADCRESULT2;
        adc[3] = AdcRegs.ADCRESULT3;
        adc[4] = AdcRegs.ADCRESULT4;
        adc[5] = AdcRegs.ADCRESULT5;
        adc[6] = AdcRegs.ADCRESULT6;
        adc[7] = AdcRegs.ADCRESULT7;
        adc[8] = AdcRegs.ADCRESULT8;
        for (i=0;i<6;i++)
        ChOut[i] = read_ADCb(off[i], adc[i], ChGain[i]);
        for (i=6;i<9;i++)
        ChOut[i] = read_ADCu(off[i], adc[i], ChGain[i]);
//------------------------------------------------------------------------
// Clarke transformation
iAlpha = _IQmpy((_IQ15toIQ((int32)ChOut[0]) -
_IQmpy(_IQ(0.5),_IQ15toIQ((int32)ChOut[1]))-
_IQmpy(_IQ(0.5),_IQ15toIQ((int32)ChOut[2]))),_IQ(0.66666667));
iBeta = _IQmpy(( _IQ15toIQ((int32)ChOut[1]) -
_IQ15toIQ((int32)ChOut[2])),_IQ(0.57735)); vAlpha =
_IQmpy((_IQ15toIQ((int32)ChOut[3]) - _IQmpy(_IQ(0.5),_IQ15toIQ((int32)ChOut[4]))-
_IQmpy(_IQ(0.5),_IQ15toIQ((int32)ChOut[5]))),_IQ(0.66666667));
vBeta = _IQmpy(( _IQ15toIQ((int32)ChOut[4]) -
_IQ15toIQ((int32)ChOut[5])),_IQ(0.57735)); // 1/sqrt(3) = 0.57735026918963
iMag = _IQsqrt(_IQmpy(iAlpha,iAlpha) + _IQmpy(iBeta,iBeta));
vMag = _IQsqrt(_IQmpy(vAlpha,vAlpha) + _IQmpy(vBeta,vBeta));
//------------------------------------------------------------------------
// DClink voltage
vdcMag = _IQ15toIQ((int32)ChOut[6]);
//------------------------------------------------------------------------
///flux approximation Rs=0.126 pu with filter
oldflxalpha = flxAlpha;
emfalpha=vAlpha-_IQmpy(iAlpha ,_IQ(0.126));
emfalpha = _IQmpy(_IQ(2*PI*BASE_FREQ),emfalpha); //Global Q 22
flxAlpha=oldflxalpha+_IQmpy(_IQ(T),emfalpha);
//flxAlpha=_IQmpy(_IQ(0.9922),flxAlpha);
oldflxbeta = flxBeta;
flxAlpha=_IQmpy(Clpf,flxAlpha);
emfbeta=vBeta-_IQmpy(iBeta ,_IQ(0.126));
```

173

```
emfbeta = _IQmpy(_IQ(2*PI*BASE_FREQ), emfbeta); //Global Q 22
flxBeta=oldflxbeta+_IQmpy(_IQ(T),emfbeta);
 //flxBeta=_IQmpy(_IQ(0.9922),flxBeta);
flxBeta=_IQmpy(Clpf,flxBeta);
//Flx Magnitude
//flxMag=_IQsqrt(_IQmpy(flxAlpha,flxAlpha)+_IQmpy(flxBeta,flxBeta));
//Compensation Term
oldtFlxalpha = tFlxalpha;
tFlxalpha=_IQmpy(_IQ(0.5),flxBeta)+flxAlpha;
oldtFlxbeta = tFlxbeta;
tFlxbeta=flxBeta-_IQmpy(_IQ(0.5),flxAlpha);
//Flx Magnitude
tFlxmag=_IQsqrt(_IQmpy(tFlxalpha,tFlxalpha)+_IQmpy(tFlxbeta,tFlxbeta));
tetanew=_IQatan2PU(tFlxbeta, tFlxalpha);
K1= _IQ21(400);   //K1 = 1/(fb*T)
if ((tetanew <= MAX_LIMIT)&(tetanew > MIN_LIMIT))
omg = _IQmpy(K1,(tetanew - tetaold));
else
omg=_IQtoIQ21(omgf);
K3=_IQ(0.99995);
K2=_IQ(0.00005);
omg = _IQmpy(K2,_IQtoIQ21(omgf))+_IQmpy(K3,omg);
 if (omg>_IQ21(1))
omgf= _IQ(1);
else if (omg<_IQ21(-1))
omgf= _IQ(-1);
else
 omgf= _IQ21toIQ(omg);
tetaold=tetanew;
// Calculate Clpf
Clpf = _IQmpy(_IQmpy (_IQ(0.5),_IQ(T)),omgf);
Clpf = _IQdiv(_IQ(0.9999), Clpf);
// -------------------------------------------------------------------------------
//         Calculate flux vector sector
        a = _IQ(1.73);
        b = _IQmpy(_IQ(-1),_IQ(1.73));
        flxr = tFlxalpha;
        flx2s = _IQmpy(a, tFlxbeta) - tFlxalpha;
        flx2t = _IQmpy(b, tFlxbeta) - tFlxalpha;
        if (flxr >= _IQ(0)) sectora = 0x008C;
        else sectora = 0x0070;
        if (flx2t >= _IQ(0)) sectorc = 0x00E0;
        else sectorc = 0x001C;
        if (flx2s >= _IQ(0)) sectorb = 0x0038;
        else sectorb = 0x00C4;
        sector = sectora & sectorb & sectorc;
// -------------------------------------------------------------------------------
//       Flux error
        flxErr = flxRef - tFlxmag;
        if (flxErr > Hbflx) flxi=1;
        else if (flxErr < ((-1)*Hbflx)) flxi = 0;
// -------------------------------------------------------------------------------
// Calculate torque
        trq = _IQmpy(tFlxalpha,iBeta) - _IQmpy(tFlxbeta,iAlpha);
// -------------------------------------------------------------------------------
```

174

```
//  Connect inputs of the RMP_CNTL module and call the Ramp control
//  calculation function.
        rc1.TargetValue = _IQ(SpeedRef);
        rc1.calc(&rc1);
// ------------------------------------------------------------------------
//   Connect inputs of the PID_REG3 modules and compute the PID speed controller.
   if (SpeedLoopCount == SpeedLoopPrescaler)
{       pid1_spd.Ref = rc1.SetpointValue;
         pid1_spd.Fdb = speedpu;
        pid1_spd.calc(&pid1_spd);
        trqRef = pid1_spd.Out;
        SpeedLoopCount = 1;
   }
   else SpeedLoopCount ++;
// ------------------------------------------------------------------------
//        Torque error and Torque hysteresis control
        trqErr = trqRef - trq;
        if (trqErr > Hbtrq) trqi = 1;
        else if (trqErr < ((-1)*Hbtrq)) trqi = -1;
        else trqi = 0;
// ------------------------------------------------------------------------
// Vector finding algorithm
        if ((trqi == 1) && (flxi == 1))   vector = sector << 1;
        if ((trqi == 1) && (flxi == 0))   vector = sector << 2;
        if ((trqi == -1) && (flxi == 1))  vector = sector >> 1;
        if ((trqi == -1) && (flxi == 1))  vector = sector >> 2;
        if (vector < 0x0004)      vector = vector << 6;
        if (vector > 0x0080)  vector = vector >> 6;
        oddsector = (sector & 0x0004)|(sector & 0x0010)|(sector & 0x0040);
        if ((trqi == 0) && (flxi == 1) && (sector == oddsector))
                                              vector = 0x0000;
        if ((trqi == 0) && (flxi == 1) && (sector != oddsector))
                                              vector=0x00FC;
        if ((trqi == 0) && (flxi == 0) && (sector == oddsector))
                                              vector = 0x00FC;
        if ((trqi == 0) && (flxi == 0) && (sector != oddsector))
                                              vector = 0x0000;
//------------------------------------------------------------------------
//Current Limiting
   if (flxAlpha < flxLimlow)
          {     if (iMag > iLimit1) vector = 0x0000;
                if (iMag > iLimit2) vector = 0x0004;
          }
//------------------------------------------------------------------------
// Counting the number of vector changings
        if (vector != vector_old){
                vctchange ++;
                vector_old = vector; }
//------------------------------------------------------------------------
// Counting the frequency of pwm
        pwm_freq_counter ++;
        if (pwm_freq_counter == 20000){        //20000*50us=1s
                pwm_freq_counter = 0;
         pwm_freq = vctchange;
         vctchange = 0;}
```

```
//------------------------------------------------------------------------
// HCPL RESET
   GpioDataRegs.GPADAT.bit.GPIOA10 = 1; // fault cleaning for HCPL
         DELAY_US(RESET_usDELAY);                // Delay constant for 5 ms
         GpioDataRegs.GPADAT.bit.GPIOA10 = 0; // Indicates no fault for HCPL
//------------------------------------------------------------------------
// Sending the vector state to gate drive circuit
//------------------------------------------------------------------------
switch (vector){
case 0x0004:
              EvaRegs.CMPR1=0;
              EvaRegs.CMPR2=PeriodMax;
              EvaRegs.CMPR3=PeriodMax;
              break;
case 0x0008:
              EvaRegs.CMPR1=0;
              EvaRegs.CMPR2=0;
              EvaRegs.CMPR3=PeriodMax;
              break;
case 0x0010:
              EvaRegs.CMPR1=PeriodMax;
              EvaRegs.CMPR2=0;
              EvaRegs.CMPR3=PeriodMax;
              break;
case 0x0020:
              EvaRegs.CMPR1=PeriodMax;
              EvaRegs.CMPR2=0;
              EvaRegs.CMPR3=0;
              break;
case 0x0040:
              EvaRegs.CMPR1=PeriodMax;
              EvaRegs.CMPR2=PeriodMax;
              EvaRegs.CMPR3=0;
              break;
case 0x0080:
              EvaRegs.CMPR1=0;
              EvaRegs.CMPR2=PeriodMax;
              EvaRegs.CMPR3=0;
              break;
case 0x0000:
              EvaRegs.CMPR1=PeriodMax;
              EvaRegs.CMPR2=PeriodMax;
              EvaRegs.CMPR3=PeriodMax;
              break;
case 0x00FC:
              EvaRegs.CMPR1=0;
              EvaRegs.CMPR2=0;
              EvaRegs.CMPR3=0;
              break;
default:
              EvaRegs.ACTRA.all = 0x0000;
       break;
}    //switch (vector){
 // ------------------------------------------------------------------------
//    Connect inputs of the PWMDAC module
```

176

```
    PwmDacCh1 = (int16)_IQtoIQ15(flxAlpha); //PWM7
    PwmDacCh2 = (int16)_IQtoIQ15(flxBeta);  //PWM9
    PwmDacCh3 = (int16)sector;              //PWM11
    pwmdac1.update(&pwmdac); // Call update function for pwmdac1
// -------------------------------------------------------------------------
//   Connect inputs of the DATALOG module
    DlogCh1 =(int16)_IQtoIQ15(tFlxalpha);
    DlogCh2 =(int16)_IQtoIQ15(tFlxbeta);
    DlogCh3 =(int16)sector;
    DlogCh4 =(int16)sector;
    dlog.update(&dlog);  // Call the DATALOG update function.
//-------------------------------------------------------------------------
    AdcRegs.ADCTRL2.bit.RST_SEQ1 = 1;       // Reset SEQ1
    AdcRegs.ADCST.bit.INT_SEQ1_CLR = 1;             // Clear INT SEQ1 bit
    AdcRegs.ADCTRL2.bit.EVA_SOC_SEQ1 = 1;
    EvaRegs.EVAIMRA.bit.T1UFINT = 1;// Enable more interrupts from this timer
    EvaRegs.EVAIFRA.all = BIT9;//
    PieCtrlRegs.PIEACK.all |= PIEACK_GROUP2;
}        //end of interrupt void MainISR(void)
```

REFERENCES

[1]   Boldea I., Nasar S. A. (1997). *Linear electric actuators and generators.* Cambridge University Press, UK.

[2]   Sung J. H., Nam K. (1999). A new approach to vector control for a linear induction motor considering end effects. *IEEE Conf. Rec. in IAS Annu.Meeting*, 2284–2289.

[3]   Lee J. H., Ahn S. C., and Hyun D. S. (1998). Dynamic characteristic analysis of vector controlled LIM by finite element method and experiment. *IEEE Conf. Rec. in IAS Annu. Meeting*, 799–806.

[4]   Kwon B., Woo K., and Kim S. (1999). Finite element analysis of direct thrust controlled linear induction motor. *IEEE Trans. Magn.*, 35, 1306–1309.

[5]   Kang, G. and Nam, K. (2005). Field-oriented control scheme for linear induction motor with the end effect. *IEE Proc. Electr. Power Appl.,* 152.

[6]   Lin, F.-J. and Lee, C.-C. (2000). Adaptive Backstepping Control for linear induction motor drive to track periodic references. *IEE Proc. Electr. Power Appl.,* 147.

[7]   Silva da E. F., Santos dos E. B., Machado, P. C. M. and Oliveira de M. A. A. (2003). Vector contol of linear induction motor. *IEEE. ICIT,* Mairbor, Slovenia, 518-523.

[8]   Dolinar D., Stumberger G., and Grcar B. (1998). Calculation of the linear induction motor model parameters using finite elements. *IEEE Trans. Magn.*, 34, 5, 3640–3643.

[9]   Mirsalim M., Doroudi A., and Moghani J. S. (2002). Obtaining the operating characteristics of linear induction motors: A new approach. *IEEE Trans. Magn.*, 38, 2, 1365–1370.

[10]   Zhang Z., Eastham T. R., and Dawson G. E. (1993). LIM dynamic performance assessment from parameter identification. *IEEE IAS Annu. Meeting Conf. Rec*, 2, 1047–1051.

[11]   Faa-Jeng L., Shieh Hsin-Jang, Shyu K., and Huang P. (2004). On-line gain tuning IP controller using real coded genetic algorithm. *Electric Power System Research 72*, 157-169.

[12]   Lin F.J., and Rong-Jong W. (2001). Hybrid control using recurrent fuzzy neural network for linear induction motor servo drive. *IEEE Trans. On Fuzzy Systems*, 9, 1,102-115.

[13]   Faa-Jeng L., Rong-Jong W., Wen-Der C., and Shu-eng H. (2002). Adaptive backstepping control using recurrent neural network for linear induction motor drive. *IEEE Trans. On Industrial Electronics*, 49, 1,134-145.

[14]   Hu J., Wu B. (1998). New Integration Algorithms for Estimating Motor Flux over a Wide Speed Range. *IEEE Trans. on Power Electronics*, 13, 5, 969-977.

[15]   Hurst Kevin D., Habetler T. G., Griva G., Profumo F. (1998). Zero-Speed Tacholess IM Torque Control: Simply a Matter of Stator Voltage Integration. *IEEE Transactions on Industry Applications*, 34, 4, 790-795.

[16]   Nik Idris N.R:, Yatim A.M. (2002). An Improved Stator Flux Estimation in Steady-State Operation for Direct Torque Control of Induction Machines. *IEEE Transactions on Industry*, 38, 1, 110-116.

[17]   Holtz J., Quan J. (2003). Drift- and Parameter-Compensated Flux Estimator for Persistent Zero-Stator-Frequency Operation of Sensorless- Controlled Induction Motors. *IEEE Transactions on Industrial Applications, 39,4, 1052-1060.*

[18]   Lascu C., Boldea I., Blaabjerg F. (2000). A Modified Direct Torque Control for Induction Motor Sensorless Drive. *IEEE Transactions on Industry Applications,* 36, 1, 122-130.

[19]   Rodic M., Jezernik K. (2002). Speed Sensorless Sliding Mode Torque Control of Induction Motor. *IEEE Transactions on Industrial Electronics*, 49, 1, 87-95.

[20]   Habetler T. G., Profumo F., Pastorelli M. and Tolbert L. M. (1991). Direct torque control of induction machines using space vector modulation. *IEEE Conference Record of the Industry Applications Society Annual Meeting,* 1, 428-436.

[21]   Mir S., and Elbuluk M. E. (1995). Precision torque control in inverter-fed induction machines using fuzzy logic. *IEEE-IAS Annual Meeting*, 396- 401.

[22]   Bird G., and Zelaya De La Parra H. (1997). Fuzzy logic torque ripple reduction for DTC based AC drives. *IEEE Electronic Letters*, 33, 17, 1501-1502.

[23]   Martins C.; Roboam X.; Meynard T. A. and Caryalho A. S. (2002). Switching frequency imposition and ripple reduction in DTC drives by using a multilevel converter. *IEEE Trans. Power Electronics*, 17, 2, 286-297.

[24]   Gieras, J. F. (1994). *Linear Induction Drives*. Oxford Science Publications.

[25]   Bucci G., S. Meo, A. Ometto, and M. Scarano, (1994). The control of LIM by a generalization of standard vector techniques, *Proc. of IEEE IAS*, pp. 623-626.

[26]   Yamamura, S. (1978). *Theory of Linear Induction Motors.* University of Tokyo Press.

[27]   Boldea I., Nasar Syed A. (2001).*The Induction Machine Handbook.* CRC Press

[28]   Wildi T. (2002). *Electrical Machines, Drives, and Power Systems*. 5th ed. Upper Saddle River, NJ: Pearson Education, Inc.

[29]   Ong, Chee-Mun. (1998). *Dynamic simulation of electric machinery: using Matlab/Simulink.* Prentice Hall PTR.

[30]   Bose, Bimal K. (2001). *Power electronics and AC drives*. Prentice Hall.

[31]   Krause Paul C., Wasynczuk O., Sudhoff Scott D. (2002). *Analysis of electric machinery and drive systems*. Wiley-IEEE Press.

[32]   Takahashi I. and Nogushi T. (1986). A new quick response and high efficiency control strategy of an induction motor. *IEEE Trans. On Ind. Appl.*, 22, 7, 820-827.

[33]   Baader U., Depenbrock M., Gierse G. (1989). Direct self control of inverters-fed induction machine: A basis for Speed Control without Speed Measurement. *IEEE Industry Applications Society Annual Meeting,* 1, 486 – 492.

[34]   Buja G. and Kazmierkowski M. P. (2004). Direct torque control of pwm inverter-fed ac motors-a survey. *IEEE Trans. on Industrial Electronics*, 51, 4.

[35]   ABB Corporation Power Electronics System Products, http://www.abb-drives.com/StdDrives/RestrictedPages/Marketing/Documentation/files/PRoducts/DTCTechGuide1.pdf

[36]   Wai R. J. and Lin F. J. (2001). Adaptive recurrent-neural-network control for linear induction motor. *IEEE Trans. Aerosp. Electron. Syst.*, 37, 4, 1176-1192.

[37]   Liu J., Lin F., Yang Z, Zheng Trillion Q. (2006).Field oriented control of linear induction motor considering attraction force & end-effects. *IEEE Power Electronics and Motion Control Conference,* 1, 1 – 5.

[38]   Gastli, A. (2002). Improved field oriented control of an LIM having joints in its secondary conductors. *IEEE Transactions on Energy Conversion,* 17, 349 – 355.

[39]   Rathore A.K., Mahendra S.N. (2004). Simulation of secondary flux oriented control of linear induction motor considering attraction force & transverse edge effect. *9th IEEE International Power Electronics Congress, 158-163*.

[40]   Delli Colli, V., Marignetti, F., Scarano, M., Radulescu, M.M. (2003). Implementation of an improved direct thrust and flux control for linear induction motors. *IEEE International Electric Machines and Drives Conference,* 1, 488 – 493.

[41]   Itoh K., Kubota H. (2005). Thrust ripple reduction of linear induction motor with direct torque control. *Proceedings of the Eighth International Conference on Electrical Machines and Systems,* 1, 655 – 658.

[42]   Leonhard W. (2001). *Control of Electrical Drives*. Berlin: Springer.

[43]   Buja G. and Casadei D. (1997). DTC-based strategies for induction motor drives. *IECON '97 23rd International Conference on Industrial Electronics, Control and Instrumentation*, 4, 1506-1516.

[44]   Casadei D., Grandi G., Tani A. (1997). Analytic Investigation of Torque and Flux Ripple in DTC Schemes for Induction Motors. *Proc. IEEE IECON'* 97, 552-556.

[45]   Casadei D., Grandi G., Serra G., Tani A. (1994). Effect of flux and torque hysteresis band amplitude in direct torque control of induction motor. IEEE-IECON'94 Conf. Rec., 299-304.

[46]   Casadei D., Serra G., Tani A., and Zari L. (2006). Assessment of direct torque control for induction motor drives. *Bulletin of the Polish Academy of Technical Sciences*, 54, 3.

[47]   Kang J-K., Chung D-W and Sul S.K. (1999). Direct torque control of induction machine with variable amplitude control of flux and torque hysteresis bands. *International Conference on Electric Machines and Drives IEMD'99*, 640-642.

[48]   Duncan J. and Eng C. (1983). Linear induction motor-equivalent- circuit model. *Proc. IEE,* 130, Pt. B, 1, 51-57.

[49]   Matsumiya, T. and Tagagi, K. (1971). End effect and equivalent circuit of linear induction machine. *J. IEE. Japan*, 91, 117-127.

[50]   Dawson Grahame E., Eastham Anthony R. and Gieras Jacek F. (1986). Design of Linear Induction Drives by Field Analysis and Finite: Element Techniques. IEEE. *Trans. on Ind.Appl.*, IA-22, 5, 865-873.

[51]   da Silva E.F., dos Santos C.C., Nerys J.W.L. (2004). Field oriented control of linear induction motor taking into account end-effects. *IEEE International Workshop on Advanced Motion Control*, 689-694.

[52]   da Silva E.F., Machado P.C.M., de Oliveira M.A.A. (2003). Dynamic model for linear induction motors. *IEEE International Conference on Industrial Technology*, 1,478-482.

[53]   Lai Yen-Shin, Chen Jian-Ho. (2001). A new approach to direct torque control of induction motor drives for constant inverter switching frequency and torque ripple reduction. *IEEE Transaction on Energy Conversion,* 16, 220-227.

[54]   Nik Rumzi N I., Adbul H M Y. (2002). An improved stator flux estimation in steady-state operation for direct torque control of induction machines. *IEEE Trans. on Industry Application*, 38, 1, 110-116.

[55]   Hurst K. D., Habetler T. G., Geriva G., Profumo F. (1998). Zero-Speed tacholess IM torque control: Simply a matter of stator voltageintegration. IEEE Tran. Ind. Appl., 34, 4, 790- 795.

[56]   Kuo-kai S., Shang Li-J., Chen Hwang-Z. and Jwo Ko-W. (2004). Flux compensated direct torque control of induction motor drives for low speed operation. *IEEE Trans. on Power Electronics*, 19, 6, 1608-1613.

[57]   Luukko J., Niemela M., Pyrhonen J. (2003). Estimation of the flux linkage in a direct-torque-controlled drive. *IEEE Trans. on Industrial Elec*, 50, 2, 283-287.

[58]   Texas Instruments. (2000). *High performance direct torque control induction motor drive utilising TMS320C31 digital signal processor.* encon.fke.utm.my/nikr/ti.pdf

[59]   Xiamnin Ma Youlin Gui. (2002). Extended Kalman filter for speed sensorless DTC based on DSP *Intelligent Control and Automation. IEEE Proceedings of the 4th World Congress*, 119-122.

[60]   Pai, D., Mangsuli, P.R., Rao, N.J. (2000). Nonlinear observer based sensorless direct torque control of induction motor. *Power Electronics and Motion Control Conference. Proceedings IPEMC 2000, 440-445.*

[61]   Shin Myoung-H., Hyun Dong-S., Cho Soon-B., Choe Song-Y. (2000). An improved stator flux estimation for speed sensorless stator flux orientation control of induction motors *IEEE Transactions on Power Electronics*, 312 – 318.

[62]   Lascu, C., Boldea, I. and Blaabjerg, F. (1998). A modified direct torque control (DTC) for induction motor sensorless drive. *IEEE Industry Applications Conference, 1998.Thirty-Third lAS Annual Meeting*, 1, 415-422.

[63]   Griva G., Habetler Thomas G, Profumo F. (1998). Stator resistance tuning in a stator flux field oriented drive using an instantaneous hybrid flux estimator. *IEEE Transactions on Power Electronics*, 13, 1, 125-133.

[64] Mitronikas E D., Safacas A N., Tatakis E C. (2001). A new stator resistance tuning method for stator-flux-oriented vector-controlled induction motor drive. *IEEE Trans.on Industrial Elec.*, 48, 6, 1148-1157.

[65] http://www.allaboutcircuits.com/vol_1/chpt_12/6.html, visited on July 23, 2010.

[66] *NEMA Insulation Classes* http://www.engineeringtoolbox.com/nema-insulation-classes-d_734.html, visited on July 23, 2010.

[67] Chapuis, Y.A. and Roye D. (1998). Direct torque control and current limitation method in start up of an induction machine. *IEE Conf. Power Electronics and Variable Speed Drives*, 451-455.

[68] Juhasz Gy, Halasz S.and Veszpremi K. (2000). New aspects of a direct torque controlled induction motor drive. *IEEE International Conference on IT*, 1, 43-48.

[69] Mohan N. (2001).*Advanced electric drives*. Mnpere.

[70] Choi J.W., Yong S.I., Sul S.K. (1994). Inverter output voltage synthesis using novel dead time compensation. *IEEE Applied Power Electronics Conference and Exposition*, 1, 100 – 106.

[71] Jeong, S. and M. Park. (1991). The analysis and compensation of dead-time effects in pwm inverters. *IEEE Trans. On Industrial Electronics*, 38, 108-114.

[72] Kang J-K., Chung D-W and Sul S.K. (1999). Direct torque control ofinduction machine with variable amplitude control of flux and torquehysteresis bands. *International Conference on Electric Machines and Drives IEMD'99*, 640-642.

[73] Okumus H. I.¸, Aktas M. (2010). Adaptive hysteresis band control for constant switchingfrequency in DTC induction machine drives. *Turk J Elec Eng & Comp Sci*, 18, 1.

[74] Mir S., and Elbuluk M. E. (1995). Precision torque control in inverter-fedinduction machines using fuzzy logic. *IEEE-IAS Annual Meeting*, 396-401.

[75] Bird I. G., and De La Parra Zelaya H. (1997). Fuzzy logic torque ripplereduction for DTC based AC drives. *IEEE Electronic Letters*, 33, 17, 1501-1502.

[76] Li Y., Shao J. and Si B. (1997). Direct torque control of induction motors forlow speed drives considering discrete effect of control and dead-time timing of inverters. *IEEE-IAS Annual Meeting*, 781-788.

[77] Casadei D., Serra G., Tani A., Zarri L., Profumo F. (2003). Performance analysis of a speed-sensorless induction motor drive based on a constant-switching-frequency DTC scheme. *IEEE Transactions on IndustryApplications*, 39, 2, 476-484.

[78] Peng F. Z., Joseph A., Wang J., Shen M., Chen L. (2005). Z-Source inverter for motor drives. *IEEE Trans. on Power Elec.*, 20, 4, 857-863.

[79] Peng F. Z., Yuan X., Fang X., and Qian Z. (2003). Z-source inverter for adjustable speed drives. *IEEE Power Electronics Letters*, 1(2), 33–35.

[80] Peng F. Z. (2003). Z-Source Inverter. *IEEE Transactions on Industrial Applications*, 39, 2, 504-510.

[81]   Justus Rabi B. and Arumugam R. (2005). Harmonics study and comparison of Z-source inverter with traditional inverters. *American Journal of Applied Sciences,* 2 (10), 1418-1426.

[82]   Holland K., Shen M., Peng F. Z. (2005). Z-source inverter control for traction drive of fuel cell – battery hybrid vehicles. *IEEE Industrial Applications Conference*, 3, 1651-1656.

[83]   Senthilkumar, R., Bharanikumar, R.; Jerom, J., Bannari. (2007). Z-source inverter for UPS application. *IEEE International Conference on Intelligent and Advanced Systems, 2007. ICIAS 2007,* 835 – 839.

[84]   Jin-Woo J.; Keyhani, A. (2007). Control of a fuel cell based z-source converter. *IEEE Transactions on Energy Conversion,* 22, 2, 467 – 476.

[85]   Ding X., Qian Z., Xie Y., Peng F. Z. (2006). A novel z-source rectifier. *IEEE Power Electronics Specialists Conference*, 1-5.

[86]   Zhang F., Fang X., Peng F. Z., Qian Z. (2006). A new three phase AC-AC z-source converter. *IEEE Applied Power Electronics Conference and Exposition*, 123-126.

[87]   Zare, F., Firouzjaee, J.A. (2007). Hysteresis band current control for a single phase z-source inverter with symmetrical and asymmetrical z-network. *Power Conversion Conference - Nagoya, 2007. PCC '07,* 2-5, 143 – 148.

[88]   Gao Z., Shen K., Wang J., Chen Q. (2010). An improved control method for inductive load of z-source inverter. *IEEE Power and Energy Engineering Conference (APPEEC), 2010 Asia-Pacific,* 28-31,1-4.

[89]   van der Broeck H.W., Skudelny H.-C., and Stanke G.V.(1988). Analysis and realization of a pulsewidth modulator based on voltage space vectors. *IEEE Transactions on Industry Applications*, 24, 142-150.

[90]   Vinh T., Chun T., Ahn J., Lee H. (2007). Algorithms for controlling both the DC boost and AC output voltage of z-source inverter. *IEEE Transactions on Industrial Electronics,* 54, 5, 2745 – 2750.

[91]   Yu Tang, Shaojun Xie, Chaohua Zhang, Zegang Xu. (2009). Improved Z-Source Inverter With Reduced Z-Source Capacitor Voltage Stress and Soft-Start Capability. *IEEE Transactions on Power Electronics,* 24, 2, 409 – 415.

[92]   Erickson Robert W., Maksimovic D. (2001). *Fundementals of Power Electronics*. Kluwer Academic Publishers.

[93]   Rockwell Automation. *Line reactors and AC drives*. http://www.ab.com/drives/techpapers/Line%20Reactors%20and%20AC%20Drives1.pdf

[94]   Barnes M. (2003). *Practical variable speed Drives and power electronics*, Elsevier.

[95]   Rashid Muhammad H. (2001). *Power electronics handbooks,* Academic Press.

[96]   Mitsubishi Semiconductors. *Application notes on general considerations for IGBT and intelligent power modules.*

[97]   International Rectifier. *Snubber considerations for IGBT applications,* Zhang Y., Sobhani S., Chokhawala R. http://ciecfie.epn.edu.ec/Automatizacion/Materias/ConversoresEstaticos/Snubbers%20for%20IGBTs.pdf.

[98]   Allegro Micro Systems, Inc. Application Report. *Isolated open loop current sensing using Hall effect technology in an optimized magnetic circuit.* Richard Dickinson & Shaun.

[99]   Texas Instruments. Application Report. (2002). *Analysis of the Sallen-Key architecture.* James Karki.

[100] Texas Instruments. Application Report. (2001). *FilterPro MFB and Sallen-Key Low-Pass Filter Design Program.* John Bishop, Bruce Trump, R. Mark Stitt,

[101] Fuji Electric Device Technology Co. Application Note. *Gate drive circuit design.* http://www.fujielectric.com/device/semi/pdf/REH984/REH984_07.pdf

[102] Fuji Electric Device Technology Co. IGBT Modules Application Manual (2004). *Protection circuit design.*

[103] Texas Instruments. Literature number SPRS174K. (2004). *TMS320F28x digital signal processors data manual.*

[104] Texas Instruments. Literature number SPRU60B. (2004). *TMS320F28x analog-to-digital converter (ADC) reference guide.*

[105] Texas Instruments. Literature number SPRU65. (2002). *TMS320F28x event manager (EV) peripheral reference guide.*

[106] Texas Instruments. Literature number SPRC085. (2010) *TMS320F28x Fixed point math (qmath) library Reference Guide.*

[107] Lapsley P., Bier J., Shoham A. and Lee E.A. (1997). *DSP processor fundamentals: architectures and features*, IEEE Press, New Jersey.

[108] Texas Instruments. *C28x teaching materials.* Bormann F.

[109] Texas Instruments. Literature number SPRC080. (2003). *F281x digital motor control library.*

[110] Nash James N. (1997). Direct torque control, induction motor vector control without an encoder. *IEEE Transactions on Industry Applications*, 33, 2, 333-341.

[111] Ott H. W.(1988). *Noise reduction techniques in electronics systems.* John Wiley &Sons.

[112] Skibinski, G.L., Kerkman, R.J., Schlegel, D. (1999). EMI emissions of modern PWM AC drives. *IEEE Industry Applications Magazine*, 5, 6, 47-81.

[113] Zare, Firuz. (2009). EMI in modern AC motor drive systems. IEEE EMC Society Newsletters**,** summer, 222, 53-58.

[114] Persson E. (1992). Transient Effects in Application of PWM Inverters to Induction Motors. *IEEE Trans. Ind. Applicat.*, 28, 1095— 1100.

[115] Jouanne von A. and Enjeti P. (1997). Design Considerations for an Inverter Output Filter to Mitigate the Effects of Long Motor Leads on ASD Applications. *IEEE Trans. Ind. Appl.*, l, 33, 1138— 1145.

[116] Xiyou, C., Bin, Y., and Yu, G. (2002). The engineering design and the optimization of inverter output RLC filter in AC motor drive system. *Proc. IEEE IECON'02* Sevilla, Spain. .175–180.

[117] van der Broeck, H. and Loef, C. (1995). Use of LC filters in hard switching PWM inverter drives. In *Proc. EPE'95*, Sevilla, Spain.

[118] NEMA Standards Publication. (2001).*Application Guide for ac Adjustable Speed Drive Systems.*

[119] Bentley John M. and Link Patrick J. (1997). Evaluation of Motor Power Cables for PWM AC Drives. *IEEE Transactions on Industry Applications,* 33(2) , 342-358.

[120] Analog Devices. *Hardware Design Techniques*, http://www.analog.com/library/analogdialogue/archives/39-06/Chapter%209%20Hardware%20Design%20Techniques%20F.pdf

CURRICULUM VITAE

PERSONAL INFORMATION

Surname, Name: Etoğlu Süslüoğlu Berrin

Nationality: Turkish (TC)

Date and Place of Birth: 4 January 1977, Diyarbakır

Marital Status: Married

Phone: +90 342 317 2116

Fax: +90 342 360 1103

email: susluoglu@gantep.edu.tr

EDUCATION

Degree	Institution	Year of Graduation
MS	University of Gaziantep	2004
BS	METU	2000
High School	Manisa Lisesi	1995

WORK EXPERIENCE

Year	Place	Enrollment
2001- Present	University of Gaziantep	Res. Asst.

FOREIGN LANGUAGES

English

PUBLICATIONS

1- Berrin Susluoglu, Vedat M. Karsli, Improved current control strategy for shunt active power filter, IEEE 2nd Power and Energy Conference, PECon 2008, 1-3 Dec. 2008 Page(s):1379 - 1382.

2- Berrin Susluoglu, Vedat M. Karsli, Uç Etkili Lineer Asenkron Motorun Matlab/Simulink ile Modellenmesi, ELECO-2008.

3- Berrin Susluoglu, Vedat M. Karsli, Direct Thrust Controlled Linear Induction Motor Including End Effect, IEEE 13th Power Electronics and Motion Control Conference, EPE-PEMC 2008, 1-3 Sept. 2008 Page(s):850 - 854.

4- Berrin Susluoglu, Vedat M. Karsli, A Comparative Study of SAPF with Two Different Current Control Strategies, ELECO-2007 International Conference on Electrical and Electronics Engineering, Bursa / Turkey.

5- Vedat M. Karsli, Mehmet Tümay, Berrin Susluoglu, An Evaluation of Time Domain Techniques for Compensating Currents of Shunt Active Power Filters, ELECO-2003 International Conference on Electrical and Electronics Engineering, Bursa/ Turkey.